Time-Frequency Analysis of Systems with Changing Dynamic Properties

Thesis by

Samuel Case Bradford V

In Partial Fulfillment of the Requirements

for the Degree of

Doctor of Philosophy

California Institute of Technology

Pasadena, California

2006

(Defended July 19, 2006)

Acknowledgements

Many thanks to my advisor, Tom Heaton, for his valuable guidance as I worked through this research. Always enthusiastic, I am very grateful to him for helping me expand on aspects of my thesis that I found intriguing, and for applying his insight to my studies.

I am also indebted to my thesis committee, Rob Clayton, John Hall, Monica Kohler, and particularly Jim Beck, for their patience and advice.

Large portions of my thesis are dependent on digitized data, and as such I would like to acknowledge the many organizations who have assisted with the collection and digitization of data: NSMP for digitization of Millikan Library film records, CGS for Imperial County Services Building records, SCEDC for Southern California seismic data, USC for Millikan Library records (I would like to thank Professor Todorovska and Professor Trifunac for other appreciated discussions), USGS for the Millikan Library dense instrumentation network, and the PBIC for the loan of instruments/recorders for the Broad Center ambient vibration test.

My thesis has benefitted from the support of the entire Thomas Building – including Carolina Oseguera, Julie Wolf, Swami Krishnan, Jeff Scruggs, Andy Guyader, Judy Mitrani-Reiser, Sam Feakins-Daly, Alex Taflanidis, and my officemate Jing Yang. In particular, the experimental guidance of Javier Favela, the thoughtful editing of Anna Olsen, and the many contributions of Matt Muto made this a stronger work.

Special thanks to Georgia Cua and John Clinton, for the good times and companionship, and I am grateful as well to John for the technical foundation upon which much of my research depends.

In a larger sense, the support and understanding of my family has helped me through the years, and I would like to thank my parents (Clete and Teri and Ken and Jessica) and grandparents (Amber and Carl and Julia) for their encouragement to pursue my goals.

Finally, my deepest thanks are reserved for my patient wife, Charlotte.

Abstract

Time-frequency analysis methods transform a time series into a two-dimensional representation of frequency content with respect to time. The Fourier Transform identifies the frequency content of a signal (as a sum of weighted sinusoidal functions) but does not give useful information regarding changes in the character of the signal, as all temporal information is encoded in the phase of the transform. A time-frequency representation, by expressing frequency content at different sections of a record, allows for analysis of evolving signals. The time-frequency transformation most commonly encountered in seismology and civil engineering is a windowed Fourier Transform, or spectrogram; by comparing the frequency content of the first portion of a record with the last portion of the record, it is straightforward to identify the changes between the two segments. Extending this concept to a sliding window gives the spectrogram, where the Fourier transforms of successive portions of the record are assembled into a time-frequency representation of the signal. The spectrogram is subject to an inherent resolution limitation, in accordance with the uncertainty principle, that precludes a perfect representation of instantaneous frequency content. The wavelet transform was introduced to overcome some of the shortcomings of Fourier analysis, though wavelet methods are themselves unsuitable for many commonly encountered signals.

The Wigner-Ville Distribution, and related refinements, represent a class of advanced time-frequency analysis tools that are distinguished from Fourier and wavelet methods by an increase in resolution in the time-frequency plane. I introduce several time-frequency representations and apply them to various synthetic signals as well as signals from instrumented buildings.

For systems of interest to engineers, investigating the changing properties of a system is typically performed by analyzing vibration data from the system, rather than direct inspection of each component. Nonlinear elastic behavior in the force-displacement relationship can decrease the apparent natural frequencies of the system – these changes typically occur over fractions of a second in moderate to strong excitation and the system gradually recovers to pre-event levels. Structures can also suffer permanent damage (e.g., plastic deformation or fracture), permanently decreasing the observed natural frequencies as the system loses stiffness. Advanced time-frequency representations provide a set of exploratory tools for analyzing changing frequency content in a signal, which can then be correlated with damage patterns in a structure. Modern building instrumentation allows for an unprecedented investigation into the changing dynamic properties of structures: a framework for using time-frequency analysis methods for instantaneous system identification is discussed.

Contents

List of Figures

List of Tables

Chapter 1

Introduction

Modern digital seismology has advanced considerably in recent years. As seismic instrumentation systems have become more sensitive and accurate, stations have been deployed in civil engineering structures such as buildings, bridges, and dams, allowing for an unprecedented investigation into their dynamic properties. The fields of civil/structural engineering and earthquake engineering have benefitted greatly from this increased instrumentation of structures. 24-bit digitization systems, now commonplace, allow for the analysis of strong earthquake motions and ambient vibrations on the same instrument, with a signal-to-noise ratio of over 100 for typical ambient vibration levels. When these instruments and digitization systems are combined with a continuous telemetry and storage system, such as that found in the Southern California Seismic Network, building behavior can be observed over a timespan of seconds, hours, days, weeks, months, or even years; this provides a rich data set for investigations into changes in the dynamic properties of these buildings.

Transform methods are fundamental in understanding signals from a wide variety of fields. Scientists and engineers are often restricted to studying systems through signals associated with these systems (vs. physically inspecting the components of the system), and the properties of the signal are typically difficult to identify in the time-domain. Transforming the signal into the frequency domain via the Fourier Transform identifies the frequency content of the signal, which is often more useful than time-domain information for investigation of dynamic properties. A Fourier Transform of a time series (such as an earthquake record from an instrumented structure) contains

information regarding the frequency content of the signal, but it cannot resolve the exact onset of changes in natural frequency, as temporal information is contained only in the phase of the transform. Comparing a Fourier Transform of the first portion of the record with a later portion reveals information about the evolution of the dynamic properties, but decreases the frequency resolution of each portion of the record – this idea is at the heart of the spectrogram. By applying the Fourier Transform with a running window, a properly constructed spectrogram is better able to resolve temporal evolution of frequency content. However, there is a trade-off in time resolution versus frequency resolution in accordance with the uncertainty principle.

I present a mathematical foundation for analyzing the evolution of frequency content in a signal and apply these techniques to synthetic records from linear and nonlinear finite element models. These analysis techniques are then applied to records from instrumented structures, with examples drawn from forced vibration tests, ambient vibrations, and buildings damaged during historical earthquakes. Many of these techniques are adaptations of the Wigner-Ville Distribution, which is one of the oldest and most fundamental time-frequency representations. As investigations into instrumented structures are dependent on digital signal processing, applying advanced signal processing tools to this data allows for a deeper understanding of the system's evolution with time.

When Does a Structure Change Stiffness?

Many signals contain non-stationary components or represent a system with changing dynamic properties; an example of such a system is the behavior of instrumented buildings under earthquake excitation. During earthquake motions, typical buildings undergo an apparent loss of stiffness due to nonlinearity in the force-displacement response. This temporary decrease in natural frequency can be quite large and occurs rapidly – typically over a few seconds during strong shaking. (Nonlinearity in the force-displacement relationship creates a lower effective (secant) stiffness; for a single degree of freedom oscillator with stiffness k and mass m, the natural frequency ω is

given by $\omega = \sqrt{k/m}$.) Buildings also can experience a permanent loss of stiffness based on damage, e.g., Figure 1.1 shows the behavior of Caltech's Millikan Library since construction, with a significant change in natural frequencies (see also Clinton et al. (2006), Bradford et al. (2004), Favela (2004)). Moderate to large earthquakes have permanently changed the natural frequencies of the structure since construction in the 1960s, for a total decrease of $\sim 10\%$ in the NS fundamental mode, and more than 20% in the fundamental EW mode. The temporary decrease in natural frequency during the events is even larger, though the building recovers shortly after the event.

Changes in the dynamic properties of instrumented structures motivated initial investigations into estimating the dynamic properties of a system during an event, as well as identifying the onset of permanent changes.

System Identification and Time-Frequency Analysis

System identification, as described in Beck (1996), is composed of three major steps: 1. specify the mathematical structure for the system; 2. estimate the model parameters from measurements made on the system; and 3. evaluate whether the model is adequate for its intended purpose. To this end, several parametric system identification techniques, such as Caltech's MODE-ID software, perform an effective parameterization of a given signal. Parametric techniques, however, require a parameterization, which can be non-unique, and there may not be *a priori* an obvious choice for choosing parameters of an evolving system.

Detailed reviews of the state of system identification (e.g., Beck (1996), Doebling et al. (1996), Todorovska and Trifunac (2006a)) have identified several sources of modeling and implementation difficulties, including: the presence of factors that mimic damage, such as the effects of soil-structure interaction on the measured frequencies; high redundancy in civil engineering structures, resulting in a low sensitivity when damage is localized; modeling uncertainties; uncertainties in training data if data is recorded under different conditions than an event; incomplete damage scenarios in the parameterization; and sparse sensor distribution in a real system. Reducing

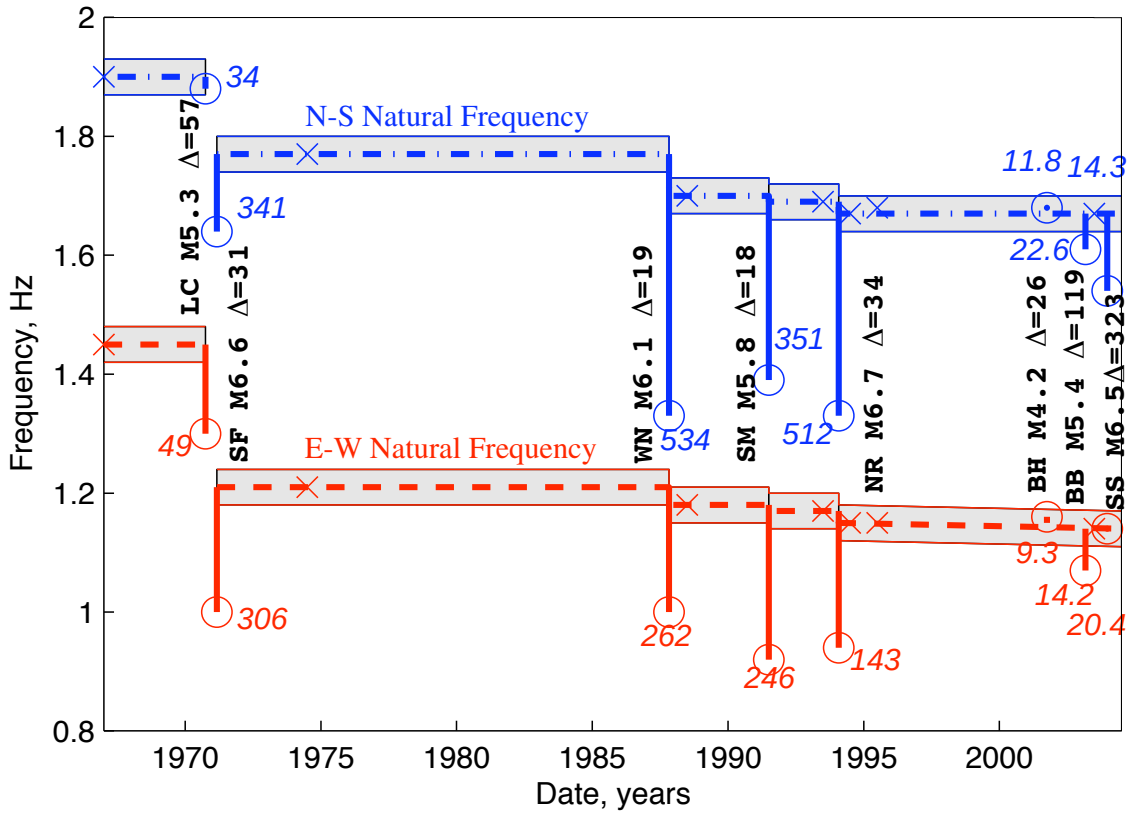

Figure 1.1: Historical behavior of Millikan Library - EW (red) and NS (blue) fundamental frequencies since construction. Crosses indicate frequencies from forced vibration tests. Circles indicate estimates from recorded earthquakes, and the associated numbers in italics are peak acceleration values recorded for the event (cm/s^2). Dashed lines represent the observed natural frequencies of the library, and the shaded region is the likely variance from such factors as weather conditions, weight configuration of the shaker used for forced vibration tests, and experimental error. Note the significant drop in observed frequencies during the events and the permanent decrease in both the EW and NS natural frequencies. [Earthquake Abbreviations: LC: Lytle Creek, SF: San Fernando, WN: Whittier Narrows, SM: Santa Monica, NR: Northridge, BH: Beverly Hills, BB: Big Bear, SS: San Simeon] (Adapted from Clinton et al. (2006).)

the effects of these factors generally requires that the operator have some knowledge about the system and its properties.

Time-frequency analysis, exploring system behavior through the exploration of the behavior in the time-frequency plane, provides important insight into the dynamic properties of a system. Wandering natural frequencies can be extracted from the ridges of a 2D representation, and the onset of changes in the dynamic properties can be further correlated with physical properties of the system such as deformation, damage, peak velocity, etc. While these methods can be used as a starting point for parameterization in the general system identification sense, they also by themselves provide interesting information regarding the character and extent of changes in the apparent natural frequency of systems. Changes in physical properties are typically represented in the time-frequency plane as changes in the observed natural frequency of some signal of interest.

Chapter 2

Time-Frequency Representations

In this Chapter I present a mathematical background for time-frequency representations of signals, with a selection of different techniques and examples. It is necessary to discuss the concept of instantaneous frequency, which in some literature is defined as the derivative of the phase of the complex signal – that is, for $\varphi(t)$ as the phase of the signal $x(t)$, the quantity $\varphi'(t)$ is elsewhere referred to as the instantaneous frequency (e.g., Bracewell (2000)). This terminology is misleading, as I am primarily investigating signals with more than one frequency component at each time instant. Interpreting $\varphi'(t)$ (a scalar value) as a *mean* instantaneous frequency is a better physical interpretation, and I reserve the term "instantaneous frequency" to refer to the frequency distribution in a signal at each instant, which will in general not be a single scalar value.

The Wigner-Ville Distribution and related transformations provide a new method for extracting instantaneous frequency information from signals. This chapter provides the mathematical foundation for the research described in Chapters 3 and 4. After motivating the concept of a Time-Frequency Representation (TFR) for a signal, I give examples of common distributions, with discussions of their applicability. In general, there is not one time-frequency analysis method that is suitable for all signals. The method must be selected based on the character of the signal and the information of interest in the signal. I present several sample signals with evolving frequency content along with a selection of time-frequency methods and a discussion of the methods in the context of identifying frequency content in the time-frequency

plane. For each of the techniques presented in Sections 2.4 through 2.11, there is a corresponding sample signal in Section 2.12 that demonstrates some of the advantages and shortcomings of the method.

Many of the advanced time-frequency analysis techniques presented here were developed for the analysis of complex signals, while the data from instrumented systems is real (representing some measured property of a physical system). Using the analytic associate of a real signal improves the results of transformations such as the Wigner-Ville Distribution (Boashash, 1988). The analytic associate $x(t)$ of a signal $s(t)$ is defined such that $x(t) \equiv s(t) + i\mathcal{H}[s(t)]$, where $\mathcal{H}[s(t)]$ is the Hilbert Transform[1] of the signal $s(t)$. In this thesis, TFR techniques are applied to the analytic associates of real signals unless noted otherwise – in particular, $x(t)$ is generally the complex-valued analytic associate of some real-valued time signal of interest.

For a time-frequency representation of a signal $x(t)$, $\text{TFR}(t, \omega)$, the goal is to estimate the strength of the frequency ω at time t. As the uncertainty principle precludes a perfect simultaneous description of time and frequency (Section 2.2), all TFR representations are by necessity approximations to instantaneous frequency. These approximations vary in accuracy, and there are further obstacles to interpreting a general TFR as an energy distribution in the time-frequency plane. One serious obstacle is that the Wigner-Ville Distribution and related distributions are in general not positive for all values of time and frequency, negating the energetic interpretation of amplitude in the time-frequency plane. However, even with negative values, there is still an intuitive association between amplitude in the time-frequency plane and locations of energy in the signal. I introduce the term pseudo-energy to describe the time-frequency amplitudes from a TFR. As this pseudo-energy is not necessarily positive, the physical interpretation of amplitude as energy is flawed. However, pseudo-energy is valid as an approximation to energy in the time-frequency plane; high values imply high energy and low/negative values imply low energy. Thus, describing the

[1]The Hilbert Transform is sometimes referred to as a "quadrature filter" and the transformed signal as the "quadrature signal." Running the transform four times will return the signal to the original signal, as each transformation shifts real frequencies by $\pi/2$ and negative frequencies by $-\pi/2$.

distribution of pseudo-energy in the time-frequency plane is a useful approximation to the distribution of energy at each instant, and time-frequency representations can be interpreted as approximate energy even in cases where the representation is not entirely positive.

2.1 Frequency Content of Non-Stationary Signals

The Fourier Transform (FT) of a signal decomposes the original signal into harmonic components, identifying the spectral content of the signal. This process allows for system identification in terms of the natural frequencies and corresponding mode shapes, which are directly related to the physical properties of the system. However, when analyzing signals with evolving frequency content, the amplitude of the FT does not give the full information regarding the behavior of the system (Bracewell, 2000). A sample signal with evolving frequency is shown in Figure 2.1(a), along with the amplitude of the FT of the signal. While the FT correctly identifies the main components of the signal, it allows for neither a straightforward identification of the onset of each signal component nor an identification of which frequency component arrived first. All such temporal information is contained in the phase of the transform, but cannot be easily extracted for system identification purposes.

In Figure 2.2, I introduce a Time-Frequency Representation (TFR) of the synthetic signal. This representation creates a frequency estimate at each instant in the signal and a more thorough understanding of the evolution of the natural frequency. If the signal represents the behavior of a system, then changing frequency content can be correlated with the evolving properties of a system (e.g., changing stiffness, damage to a structural component).

To create the time-frequency representations in Figure 2.2, a sliding window is used to split the signal into segments, and the Fourier Transform of each segment is then assembled into the final time-frequency matrix. Two windowing widths are presented to emphasize the trade-off in temporal resolution versus frequency resolution. In the top figure, a wide window is used, and the coarse temporal resolution of the

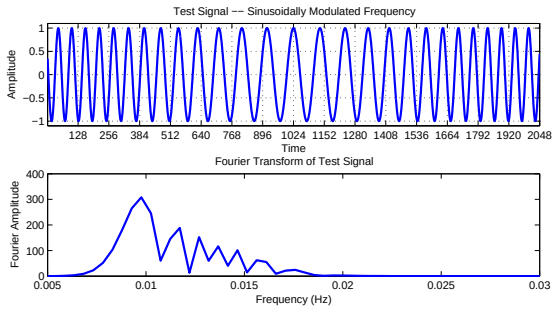

(a) Sample signal with evolving frequency, and Amplitude of the Fourier Transform – note that the Fourier Transform, while correctly identifying the components of the signal, does not allow for a straightforward interpretation of frequency evolution.

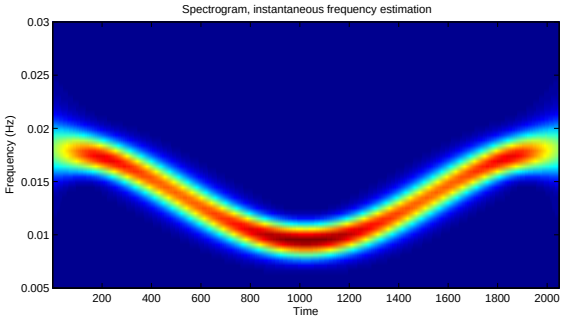

(b) Spectrogram. this distribution has limited resolution and takes on a "blocky" structure due to the trade-off between temporal resolution and frequency resolution in the time-frequency plane. However, this representation clearly captures information about progression of the mean frequency during the signal.

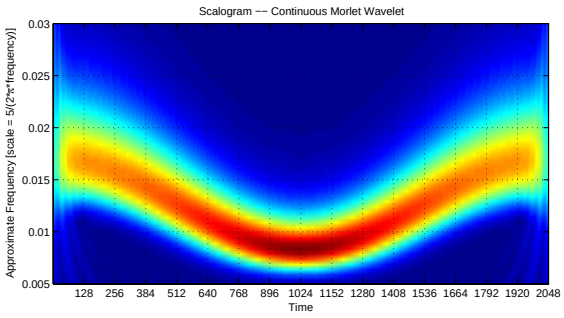

(c) Scalogram of sample signal (Continuous Morlet Wavelet). Wavelet transformations create a time-*scale* representation, where scale has an approximate equivalency to frequency.

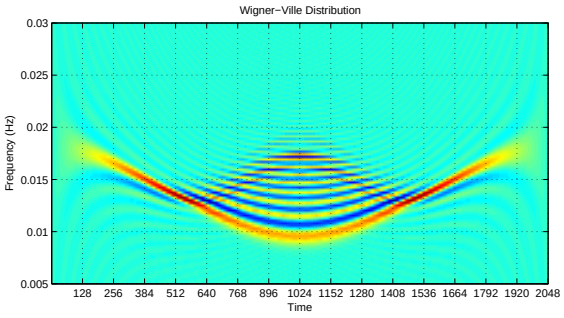

(d) Wigner-Ville Distribution for the sample signal. Note that resolution of the signal is quite crisp, though the strong interference terms make this method unsuitable for general signal analysis.

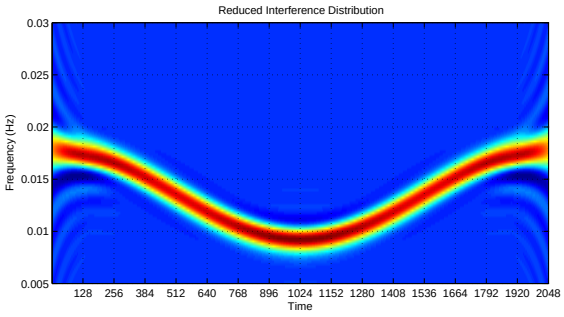

(e) Reduced Interference Distribution for the sample signal.

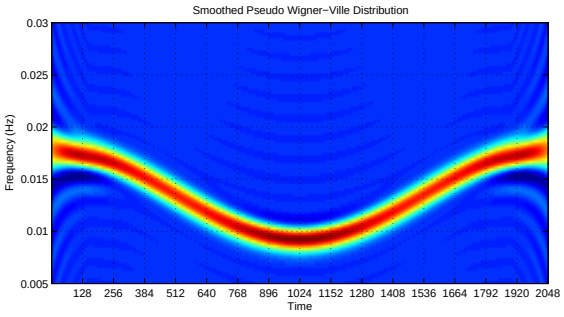

(f) Smoothed Pseudo Wigner-Ville Distribution for the sample signal

Figure 2.1: Selected Time-Frequency Representations: (a) Sample signal, (b) Spectrogram (Section 2.4), (c) Scalogram (Section 2.5), (d) Wigner-Ville Distribution (Section 2.7), (e) Reduced Interference Distribution (Section 2.9), and (f) Smoothed Pseudo Wigner-Ville Distribution (Section 2.10).

representation is immediately obvious . In the second figure, a narrower window is used which increases the temporal resolution, and it is now easier to identify the evolution of the frequency content contained in the signal; however, the narrow window decreases the maximum frequency resolution for each slice. Both of these windowing choices smear information in the time-frequency plane along the time and frequency axes. The third spectrogram plot in Figure 2.2 is an instantaneous frequency representation, an improvement over the methods in the first two plots. This method still leaks energy along both axes, but closely matches the theoretical frequency content, shown in the fourth plot. This instantaneous spectrogram, also presented in Figure 2.1(b), still has a noticeable block-like structure, a result of the inability of this method to create a true instantaneous energy estimation. The uncertainty principle (Section 2.2) precludes a TFR with perfect resolution in both time and frequency, but various methods have been proposed that can create useful representations for instantaneous frequency content.

In time-frequency representations, the goal is to create a distribution which correctly identifies energy in the time-frequency plane. For the spectrogram example, the information in the time-frequency plane closely matches that of the theoretical components of the signal, shown in the last plot of Figure 2.2. However, the spectrogram method introduces some further complications for analyzing the temporal evolution of the frequency content of the signal. A long time window will smear the time-frequency information across the time axis, changing the perceived duration and onset of a signal component. A shorter time window, while improving temporal resolution, decreases the maximum resolution along the frequency axis. Temporal resolution and frequency resolution are inversely proportional in accordance with the uncertainty principle, which limits the effective resolution of all time-frequency representations.

Another method for analyzing the instantaneous spectrum of a signal is to decompose it into different bases: one such choice is the wavelet transformation. The Continuous Wavelet Transform (CWT) creates a scalogram – a time-*scale* representation of the signal, where the scale of the wavelet bases has an intuitive association

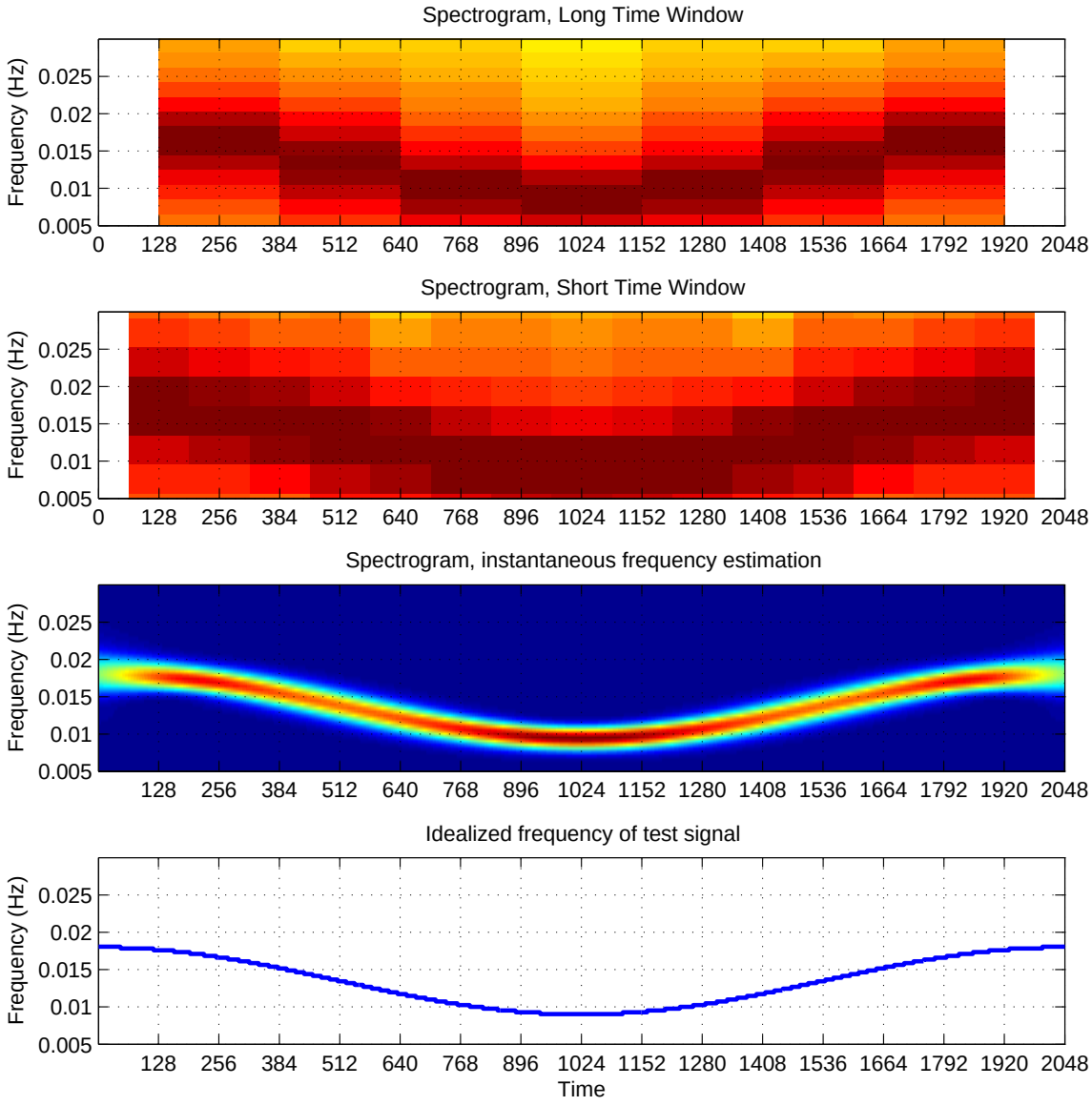

Figure 2.2: Comparison of spectrogram methods for sample signal: Spectrogram (long time window), spectrogram (short time window), spectrogram (instantaneous frequency estimation, using a Hanning windowing technique), and theoretical frequency content of the signal. These plots demonstrate the typical trade-off in time resolution against frequency resolution. A longer Fourier Transform window improves the frequency resolution, but will also smear the signal along the time axis; a shorter window will improve temporal resolution at the cost of frequency resolution.

with frequency. Wavelet methods by virtue of their localized nature have some advantages for time-frequency analysis of non-stationary signals as compared with Fourier methods. Figure 2.1(c) demonstrates the use of the wavelet transform on our test signal, though the frequency axis is only an approximation based on the scale of the wavelet transform. Again, the time-frequency information roughly matches that of our known frequency distribution.

Shortcomings of the spectrogram and scalogram methods motivated further refinements into creating an accurate time-frequency representation. Figures 2.1(d)-(f) briefly present members of a different family of time-frequency methods. These methods are described in more detail in later sections, as indicated in the caption.

2.2 Uncertainty Principle in Temporal and Frequency Resolution

The inverse relationship between temporal resolution and frequency resolution has been formalized as the Heisenberg-Gabor Uncertainty Principle.

The uncertainty principle as applied to quantum physics ("Heisenberg Uncertainty Principle" or "Heisenberg Indeterminacy Principle") refers to the relationship between certain canonically related quantum observables, such as position and momentum.[2] Briefly, if you measure the momentum of a particle p to within an accuracy of Δp, then you cannot resolve the position x more accurately than $\Delta x = h/\Delta p$, where h is Plank's constant, $\sim 6.63x10^{-34} Joule \cdot seconds$ (Feynman et al., 1966), such that:

$$\Delta x \cdot \Delta p \geq h. \tag{2.1}$$

An analogous inequality can be formulated for time and frequency resolution. The standard proof offered in many textbooks (Flandrin (1999), Qian (2002), and others)

[2]This is a separate principle from the observer effect, which states that observation of a system changes the phenomenon being observed.

is straightforward, depending on the definition of the Fourier Transform, Parseval's Formula (Equation 2.2), and the Cauchy-Schwarz Inequality (Equation 2.6).

For vectors $a(t)$ and $b(t)$ (with Fourier Transforms $A(\omega)$ and $B(\omega)$), the definition of the convolution operator leads to Parseval's Formula:

$$\int_{-\infty}^{+\infty} a(t)b^*(t)dt = \frac{1}{2\pi}\int_{-\infty}^{+\infty} A(\omega)B^*(\omega)d\omega. \tag{2.2}$$

If $a(t) = b(t)$ (implying $A(\omega) = B(\omega)$), then Equation 2.2 becomes:

$$\int_{-\infty}^{+\infty} |b(t)|^2\, dt = \frac{1}{2\pi}\int_{-\infty}^{+\infty} |B(\omega)|^2\, d\omega. \tag{2.3}$$

Parseval's Formula implies a conservation of energy between the time domain and frequency domain (the form of Equation 2.3 is also referred to as the Plancherel Formula (Mallat, 1999)).

For the case of a derivative, $\frac{d}{dt}b(t) \leftrightarrow i\omega B(\omega)$:

$$\int_{-\infty}^{+\infty} \left|\frac{db}{dt}(t)\right|^2 dt = \frac{1}{2\pi}\int_{-\infty}^{+\infty} \omega^2 \,|B(\omega)|^2\, d\omega. \tag{2.4}$$

I will also require the Cauchy-Schwarz Inequality, which for functions $a(t)$ and $b(t)$ can be expressed as:

$$|\langle a, b\rangle|^2 \leq \langle a, a\rangle \cdot \langle b, b\rangle\,, \tag{2.5}$$

where $\langle\,\cdot\,,\cdot\,\rangle$ denotes an inner product. For the usual integral ($\mathbf{L_2}$) inner product for complex-valued functions, Cauchy-Schwarz implies that:

$$\left|\int a(t)b(t)\,dt\right|^2 \leq \int |a(t)|^2\,dt \cdot \int |b(t)|^2\,dt. \tag{2.6}$$

With these formulas, I can now derive the uncertainty in temporal and frequency resolution for a signal, $x(t)$, (Fourier Transform $X(\omega)$). I begin with the assumption of finite energy:

$$\mathbb{E}_x = \int_{-\infty}^{\infty} |x(t)|^2 dt < +\infty. \tag{2.7}$$

Without loss of generality I can further define the axes such that:

$$\int_{-\infty}^{\infty} t|x(t)|^2 dt = 0, \tag{2.8}$$

$$\int_{-\infty}^{\infty} \omega|X(\omega)|^2 d\omega = 0. \tag{2.9}$$

Taking the second moment as a measure of time and frequency support (temporal duration and frequency bandwidth):

$$\Delta t^2 = \int_{-\infty}^{\infty} t^2|x(t)|^2 dt, \tag{2.10}$$

$$\Delta \omega^2 = \int_{-\infty}^{\infty} \frac{1}{2\pi}\omega^2|X(\omega)|^2 d\omega, \tag{2.11}$$

$$= \int_{-\infty}^{\infty} \left|\frac{dx}{dt}(t)\right|^2 dt. \qquad \text{(Equation 2.4.)} \tag{2.12}$$

Simply multiplying Equations 2.10 and 2.12 gives:

$$\Delta t^2 \Delta \omega^2 = \int_{-\infty}^{\infty} t^2|x(t)|^2 dt \cdot \int_{-\infty}^{\infty} \left|\frac{dx}{dt}(t)\right|^2 dt. \tag{2.13}$$

Applying the Cauchy-Schwarz inequality of Equation 2.6 to the right-hand side of Equation 2.13 gives:

$$\int_{-\infty}^{\infty} t^2|x(t)|^2dt \cdot \int_{-\infty}^{\infty} \left|\frac{dx}{dt}(t)\right|^2 dt \geq \left|\int_{-\infty}^{\infty} t\, x^*(t)\frac{dx}{dt}(t)dt\right|^2 \tag{2.14}$$

Take $|I|^2$ to be the right hand side of Equation 2.14 such that:

$$I = \int_{-\infty}^{\infty} t\, x^*(t)\frac{dx}{dt}(t)dt, \tag{2.15}$$

$$I = [t\, x^*(t)x(t)]_{-\infty}^{+\infty} - \int_{-\infty}^{\infty}\left[t\, x(t)\frac{dx^*}{dt} + x^*(t)x(t)\right]dt, \tag{2.16}$$

$$I = \left[t\,|x(t)|^2\right]_{-\infty}^{+\infty} - \int_{-\infty}^{\infty}|x(t)|^2dt - \int_{-\infty}^{\infty} t\, x(t)\frac{dx^*}{dt}(t)dt, \tag{2.17}$$

$$I = 0 - 1 - I^*, \qquad \text{(Valid only if } \left[t\,|x(t)|^2\right] \to 0 \text{ as } t \to \infty) \tag{2.18}$$

$$\implies I + I^* = -1, \tag{2.19}$$

$$\implies \text{Real}\{I + I^*\} = 2\text{Real}\{I\} = -1, \tag{2.20}$$

$$\implies \text{Real}\{I\} = -\frac{1}{2}, \tag{2.21}$$

$$\implies (\text{Real}\{I\})^2 = \frac{1}{4} \leq I^2. \tag{2.22}$$

The restriction in Equation 2.18 is necessary for this form of the proof, though the final result is valid for all $x \in \mathbf{L_2}(\mathbb{R})$ (Mallat, 1999). From Equation 2.13, 2.14 ,and 2.22:

$$\Delta t^2\Delta\omega^2 \geq |I|^2 \geq (\text{Real}\{I\})^2 = \frac{1}{4}. \tag{2.23}$$

Finally, the time-frequency analog to the Heisenberg Principle, the Heisenberg-Gabor Uncertainty Principle:

$$\Delta t \cdot \Delta\omega \geq \frac{1}{2}. \tag{2.24}$$

The uncertainty principle of Equation 2.24 holds as an equality if the Cauchy-Schwarz relationship of Equation 2.14 is an equality – implying that $x'(t) = C\, t\, x(t)$

for some constant C, that is, $x(t)$ is a Gaussian function, $x(t) = Ae^{-\alpha t^2}$ for some value A and $\alpha > 0$. For all other functions, the uncertainty principle is an inequality, providing a limit on the resolution in the time-frequency plane.

2.3 Support & Marginal Conditions

When creating a time-frequency representation, the ultimate goal is for information in the time-frequency plane to represent properties of the original signal. As such, the frequency content portrayed by the TFR ought to match the frequency content of the original signal, and the temporal variations in amplitude should be properly represented along the time axis. Information in the time-frequency plane which is properly aligned in both time and frequency is "supported," and one way to classify support in the time-frequency plane is through the marginal and total energy conditions:

$$\int_{-\infty}^{+\infty} TFR_x(t,\omega)\, d\omega = |x(t)|^2, \qquad \text{Frequency Marginal Condition} \tag{2.25}$$

$$\int_{-\infty}^{+\infty} TFR_x(t,\omega)\, dt = |X(\omega)|^2, \qquad \text{Time Marginal Condition} \tag{2.26}$$

$$\int_{-\infty}^{+\infty}\int_{-\infty}^{+\infty} TFR_x(t,\omega)\, dt\, d\omega = \mathbb{E}_x, \qquad \text{Total Energy Condition} \tag{2.27}$$

where $X(\omega)$ is the Fourier Transform of $x(t)$, and $\mathbb{E}_x$ is the total energy of signal $x(t)$. Satisfying the marginal conditions states that the integral of the TFR along the time axis is equal to the power spectrum of the signal (the squared Fourier Transform), while the integral along the frequency axis gives the squared envelope of the original time series – the energy condition states that the total area of the TFR, the double integral across time and frequency, is the energy contained in the original signal. These conditions have an intuitive appeal, as they imply a limitation on the extent of the signal in the time-frequency plane. In an ideal representation, a signal of short duration would have a narrow representation along the time axis, and the frequency content would be localized to the frequency of the signal. The total energy condition is also a useful property, particularly for the situation where the TFR is being used

as an instantaneous energy estimate – bounded energy makes for a more meaningful physical interpretation.

The marginal conditions are important criteria for constructing a TFR, though these conditions are neither necessary nor sufficient for the construction of useful representations.[3] For a graphical example of the time and frequency marginal conditions, please see Section 2.13.3, and Figures 2.43 and 2.44.

2.4 Short-Time Fourier Transform & Spectrogram

Recall that the Fourier Transform of $x(t)$, $X(\omega)$, is defined as:

$$X(\omega) = \int_{-\infty}^{\infty} x(t)e^{-i\omega t}dt. \tag{2.28}$$

For a signal with evolving frequency content, the Fourier Transform does not give information regarding the temporal evolution of changes in character of the signal. However, the Fourier Transform of the first portion of the record can be easily compared with the Fourier Transform of the last portion of the record, revealing the frequency content in each portion. A logical extension of this concept is to window the original signal and compute a running Fourier Transform, or Short-Time Fourier Transform (STFT):

$$STFT(t,\omega) = \int_{-\infty}^{\infty} x(u)h^*(u-t)e^{-i\omega u}du, \tag{2.29}$$

where $h(t)$ is a windowing function, which can be a boxcar, Hanning window, or other short-time window that applies the Fourier Transform of Equation 2.28 to the selected portion of the signal. The spectrogram, $SP(t,\omega)$, is the squared amplitude

[3]For example, the spectrogram and scalogram (Sections 2.4 and 2.5) are useful representations that do not satisfy these marginal conditions. The WVD (Section 2.7) satisfies the marginal conditions, but it contains interference terms which make it unsuitable as an instantaneous energy estimate.

of the STFT:

$$SP(t,\omega) = \left[\int_{-\infty}^{\infty} x(u)h^*(u-t)e^{-i\omega u}du\right]^2. \tag{2.30}$$

The uncertainty principle in time-frequency representations applies to spectrogram methods, but it is also useful to discuss the spectrogram in terms of redundancy. In signals representing discretely sampled observations of a system, the integral formulation of Equation 2.28 is recast as the Discrete Fourier Transform:

$$\hat{X}[n] = \sum_{m=0}^{M-1} \hat{x}[m]e^{-2\pi mn/N} \qquad n = 0, 1, 2, \ldots, N-1, \tag{2.31}$$

where $\hat{x}[m]$ is the discrete signal ($\hat{A}$ will represent the discrete version of A) and $\hat{X}[n]$ is the corresponding Discrete Fourier Transform. Equation 2.29 is then replaced with the Discrete Short-Time Fourier Transform:

$$\begin{aligned}\widehat{STFT}[m,n] &= \sum_{k=0}^{L-1} \hat{x}[m]\hat{h}^*[k-m]e^{-2\pi kn/N} \\ &= STFT(t,\omega)|_{t=m\Delta t,\,\omega=2\pi n/(L\Delta t)},\end{aligned} \tag{2.32}$$

with $\hat{h}^*[k] = h^*(k\Delta t)$ as a discrete windowing function of length L, and $\widehat{STFT}[m,n]$ as the discrete Short-Time Fourier Transform.

When discussing these discrete representations, some basic relations govern the amount of independent values present in a signal and its transform. For a discrete vector $x[n]$ with length N (even), the Discrete Fourier Transform results in a complex vector of length $N/2$ (properly, the Fourier Transform is of length N, with a redundant mirroring about $\omega = 0$ which reduces the effective length of the vector to $N/2$). This complex vector has $N/2$ amplitude values and $N/2$ phase values for a total of N pieces of unique information – it is a linear transform with no redundancy. When considering the *amplitude* of the Fourier Transform, as in the STFT and spectrogram, there is an apparent loss of 50% of the information in the signal. The phase of the complex value is typically discarded, leaving an amplitude vector of length $N/2$. A non-redundant

discrete STFT will be restricted to J-by-K matrices where $J \times K = N/2$. A vector of length $N = 4096$, for example, could be composed of an 8-by-256 matrix, a 32-by-64 matrix, a 128-by-16 matrix, etc., all of total size 2048 ($N/2$). The 8-by-256 matrix has 8 segments along the time domain, each with a frequency resolution of 256 points across the frequency axis; all information in the first segment is smeared across the first 1/8th of the TFR. The 128-by-16 matrix would have 128 segments along the time domain, representing much finer temporal information, but with a resolution along the frequency axis of only 16 points across the entire frequency range.

This limitation on resolution in time and frequency is another way to interpret the fundamental restrictions of the uncertainty principle, as an increase in resolution along the time axis is only possible by decreasing the resolution along the frequency axis. In practice, spectrograms are created with redundant information, and time-windowing parameters are selected to localize the expression of energy in the time-frequency plane. As the window impinges upon a portion of the record, the frequency content of the portion is reflected in the time-frequency plane, which will smear information forwards and backwards along the time axis. Taking a shorter window localizes information in time at the cost of a wider representation along the frequency axis.

2.5 Continuous Wavelet Transform & Scalogram

Another familiar transformation is the Wavelet Transform, which can be extended to a Time-Frequency representation by means of the Continuous Wavelet Transform (CWT):

$$CWT(t,a) = \frac{1}{\sqrt{a}} \int_{-\infty}^{\infty} x(u)\Psi\left(\frac{u-t}{a}\right) du, \tag{2.33}$$

where a is the scale (dilation factor) for the analyzing wavelet, Ψ. To create the wavelet transformation, the original wavelet is smoothly shifted over the full signal (dilating and contracting as necessary), creating a scale estimate for each instant of the original signal. Different wavelet families have been proposed (e.g., Harr, Mexican Hat, Meyer, Daubechies) with various mathematical properties (Mallat, 1999). For

the continuation of this thesis, I will make use of the Morlet Wavelet for wavelet transform methods, defined as a Gaussian tapered cosine.

$$\Psi_{morlet}(t) = e^{-\frac{t^2}{2}} cos(5t). \tag{2.34}$$

The squared amplitude of the CWT is the scalogram:

$$SCALOGRAM(t,a) = \frac{1}{a}\left[\int_{-\infty}^{\infty} x(u)\Psi\left(\frac{u-t}{a}\right) du\right]^2. \tag{2.35}$$

In wavelet representations, the identification of "frequency" is only possible as an approximation. Low scales represent a compressed wavelet with rapidly changing details, which corresponds to high frequencies. Similarly, high scales represent slowly changing signals with low frequencies. For the Morlet Wavelet, scale and frequency are related by $frequency \approx \frac{5/2\pi}{scale}$. The Morlet Wavelet is a Gaussian-tapered cosine wave, and the frequency approximation reflects the frequency of the cosine portion of the wavelet.

Wavelets and the Continuous Wavelet Transform are well suited to detect changes in a signal that occur over a short timespan, and these methods have been used with great success for detecting anomalies in signals. Using wavelet techniques, it is possible to identify, with great precision, the exact temporal onset of "spikes" or "knocks" in a signal, as well as correct for long-period drifting of a signal (Boashash, 2003).

A wavelet is in general not monochromatic in terms of frequency content. For example, the Morlet Wavelets in Figure 2.3 are the basis used for the wavelet transforms in this thesis. Each of these wavelets has the same general shape, but they are expanded/dilated by their scale: at lower scales (higher frequencies) the true frequency content of a wavelet becomes poorly defined.

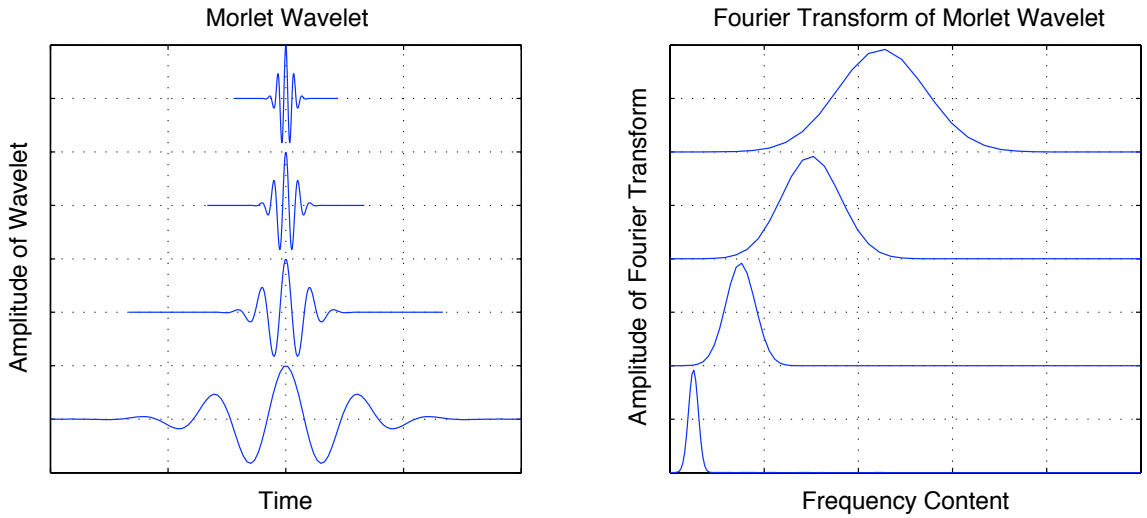

Figure 2.3: Morlet wavelet and equivalent frequency content at different "scale" values. The Morlet wavelet is one family of wavelets based on a Gaussian-tapered cosine. The scale of the wavelet represents the dilation/expansion, which has an approximate inverse relationship to the frequency content of the wavelet (*frequency* $\approx \frac{5/2\pi}{scale}$). By definition, wavelets are not monochromatic, and wavelet transformations create a time-*scale* representation (hence "scalogram") rather than a time-frequency representation. For higher frequencies (lower scale values), the bandwidth of the frequency content grows proportionally to the center frequency of the wavelet. This creates a diffuse frequency approximation at high frequencies.

2.6 Gabor Transform

The Gabor Transform is a discrete transformation, similar in structure to the STFT (Section 2.4). By reducing the redundancy of the STFT, the Gabor transform is equivalent to the information contained in an ideal discrete STFT, sampled along a lattice of $n = \lambda L$ and $\omega = \frac{\mu}{W}$:

$$\begin{aligned} GABOR_x(\lambda, \mu) &= \sum_{n=-\infty}^{\infty} x(n) G^*(n - \lambda L) \mathrm{e}^{-i(\mu/W)(n-\lambda L)}, \\ &= STFT_x(\lambda L, \frac{\mu}{W}), \quad \text{[as in Equation 2.32]} \end{aligned} \tag{2.36}$$

where $G(n)$ is a synthesis window, often chosen as a Gaussian window. Discretizing $n = \lambda L$ and $\omega = \frac{\mu}{W}$ gives a sampling factor of $\frac{W}{L}$; this is a measure of the information in the time-frequency plane. For $W = L$ the Gabor Transform is critically sampled, and there are as many points in the time-frequency plane as there are in the original signal $x(t)$. For $W < L$ the representation is undersampled (fewer points in the time-frequency plane), and for $W > L$ the representation is oversampled (more points in the time-frequency plane, a redundant distribution). In the case when $L = 1$, there is no temporal discretization, and the Gabor Transform reduces to the discrete STFT. The Gabor Transform is also analogous to a filterbank, uniformly sampled in frequency. When comparing the TFR results from the CWT and Gabor Transform, the Gabor Transform corrects the diffuse nature of the CWT, though the total structure is far coarser than the CWT.

2.7 Wigner-Ville Distribution

Recent signal processing advances have led to a new class of TFR tools. These new methods allow for distributions that function more accurately than the spectrogram method, though the uncertainty principle of Section 2.2 does preclude a *perfect* instantaneous frequency estimation at each point in the time-frequency plane.

The most fundamental of these TFR methods is the Wigner-Ville Distribution (WVD). Many other TFR methods (including the spectrogram and the scalogram) can be derived from the WVD, with a suitable choice of smoothing factors. For a signal, $s(t)$, with analytic associate $x(t)$, the Wigner-Ville Distribution, $WVD_x(t,\omega)$, is defined as:

$$WVD_x(t,\omega) = \int_{-\infty}^{+\infty} x(t+\frac{\tau}{2})x^*(t-\frac{\tau}{2})\mathrm{e}^{-i\omega\tau}\,d\tau. \tag{2.37}$$

E. Wigner, who first proposed this transformation (Wigner, 1932), was applying this equation to derive a joint representation of position and momentum in quantum mechanics – position and momentum are the standard examples of a canonically related pair. The Heisenberg Uncertainty Principle (Section 2.2) maintains that at the quantum level the accuracy of a measurement in position is inversely related to the accuracy of the measurement in momentum. In the field of signal processing, the inverse relationship between temporal and frequency resolution is analogous to the inverse relationship between quantum measurements of momentum and position.

In general, the "Wigner Distribution" of a signal $x(t)$ is defined as above (Equation 2.37), while the "Wigner-Ville Distribution" is defined as the Wigner Distribution when the function $x(t)$ is the analytic associate (also "analytic signal" or "complex signal") of the signal of interest, $s(t)$. This naming convention reflects the contributions of J. Ville (Ville, 1948), who independently developed this equation and applied it to the analysis of complex (analytic) signals (Boashash, 2003).

The WVD is an entirely real-valued function which satisfies the marginal conditions (Section 2.3), and for certain classes of signals it has ideal resolution in time and frequency. Interference terms and negative values, however, are significant obstacles to using the WVD as a system identification tool for general signals (Bracewell, 2000). The function $x(t)$ appears twice in the integral, as x and x^*, which makes the distribution "bilinear" or "quadratic." Cross-term interference from the quadratic $x(t+\frac{\tau}{2})x^*(t-\frac{\tau}{2})$ term in the WVD generates highly oscillatory interference when there are multiple frequency components in a signal. This interference can have an amplitude larger than the expression of the auto terms, and typically ranges from

extreme negative to extreme positive values. Negative values in the time-frequency plane, under an instantaneous energy interpretation of the WVD, would correspond to negative energy; this negates the physical interpretation of the WVD as representing the energy content of a signal. However, the satisfaction of the marginal conditions and many other desirable properties have led to an interest in improving the accuracy of the WVD as a time-frequency representation, primarily by reducing the effects of the interference terms on the final result.

Note that the WVD is similar to the Fourier Transform, though instead of transforming the original signal, the kernel of the WVD contains a type of autocorrelation term (in this case, the phase lag of the ambiguity function, or "properly symmetrized covariance function" (Flandrin and Martin, 1997)). The Ambiguity Function, $AF_x(\tau, \nu)$, is the 2-D Fourier Transform of the WVD and has the expression:

$$AF_x(\tau, \nu) = \int_{-\infty}^{+\infty} x(t + \frac{\tau}{2}) x^*(t - \frac{\tau}{2}) \mathrm{e}^{-i\nu\tau}\, dt, \tag{2.38}$$

which is the same form as the WVD in Equation 2.37, but with integration with respect to t instead of τ. This transformation is not always real valued and is often used as a cross-AF to determine correlation functions between different states.

2.8 Classes of Time-Frequency Representations

Many useful time-frequency representations can be expressed in the form of a suitably smoothed Wigner-Ville Distribution. It is useful to define some classes of TFRs, such as Cohen's Class and the Affine Class. Representations in Cohen's Class satisfy time-shift and frequency-shift invariance, and representations in the Affine Class satisfy time-shift and scale-shift invariance:

$$\text{Time Shift Covariance} \quad : \quad \left[\begin{array}{rcl} (S_\tau X)(\omega) & = & e^{i\omega\tau} X(\omega) \\ \Rightarrow \; T_{S_\tau X}(t,\omega) & = & T_X(t-\tau,\omega), \end{array} \right. \tag{2.39}$$

$$\text{Frequency Shift Covariance} \quad : \quad \left[\begin{array}{rcl} (M_\nu X)(\omega) & = & X(\omega-\nu) \\ \Rightarrow \; T_{M_\nu X}(t,\omega) & = & T_X(t,\omega-\nu), \end{array} \right. \tag{2.40}$$

$$\text{Scale Shift Covariance} \quad : \quad \left[\begin{array}{rcl} (C_a X)(\omega) & = & \frac{1}{\sqrt{|a|}} X(\omega/a) \\ \Rightarrow \; T_{C_a X}(t,\omega) & = & T_X(at,\omega/a). \end{array} \right. \tag{2.41}$$

In this notation, T_{AX} is the time-frequency representation $T(t,\omega)$ applied to the transformed signal AX ($S_\tau X$ is a constant time shift operator, $M_\nu X$ is a constant frequency shift operator, and $C_a X$ is a scale shift operator). There are many covariance properties: a TFR satisfies a covariance property if it preserves (or is "covariant to") a transformation on a signal (e.g., for time and frequency shifts on a signal, the time-frequency representation of a shifted signal is the shifted time-frequency representation of the original signal). The unsmoothed WVD satisfies all three of these covariance properties and is therefore a member of both Cohen's Class and the Affine Class. In the following sections I describe some of the most basic covariance properties. Further investigations into covariance properties are presented in Papandreou-Suppappola (2003).

2.8.1 Cohen's Class

The spectrogram and Wigner-Ville Distribution are members of the general class of time-frequency representations known as Cohen's Class. It the most general form, a time-frequency representation in Cohen's Class, $TFR_C(t,\omega)$, can be represented by:

$$TFR_C(t,\omega) = \frac{1}{2\pi} \int_{-\infty}^{+\infty} \int_{-\infty}^{+\infty} \int_{-\infty}^{+\infty} x\left(u+\frac{\tau}{2}\right) x^*\left(u-\frac{\tau}{2}\right) \Gamma(\theta,\tau) e^{-i(\theta t+\omega t-\theta u)}\, du\, d\tau\, d\theta, \tag{2.42}$$

with different kernel functions $\Gamma(\theta, \tau)$. This is equivalent to a smoothed Wigner-Ville Distribution (c.f. Equation 2.37), such that:

$$\begin{aligned} TFR_C(t,\omega) &= \int_{-\infty}^{+\infty}\int_{-\infty}^{+\infty} WVD_x(u,\nu) f_C(t-u,\omega-\nu)\, du\, d\nu, \\ f_C(t,\omega) &= \int_{-\infty}^{+\infty}\int_{-\infty}^{+\infty} \Phi_C(u,\nu) e^{-i\omega u} e^{i\nu t}\, du\, d\nu, \end{aligned} \tag{2.43}$$

where $f_C(t,\omega)$ and $\Phi_C(t,\omega)$ are kernel functions (either f_C or Φ_C uniquely defines the representation). For $f_C = \delta(t)\delta(\omega) \leftrightarrow \Phi_C = 1$, Equation 2.43 reduces to the WVD. For $f_C = WVD_x(-t,-\omega) \leftrightarrow \Phi_C = AF_x(-t,-\omega)$ (the WVD or Ambiguity Function (Equation 2.38) for the time/frequency reversed signal), Equation 2.43 reduces to the spectrogram (c.f. Equation 2.30). This smoothed WVD formulation, for different kernel properties, makes it straightforward to design time-frequency representations satisfying useful properties.

Cohen's class is equivalently defined as representations satisfying the time-shift and frequency-shift covariances of Equations 2.39 and 2.40, since representations that satisfy these properties can always be expressed in the form of Equation 2.42 or 2.43.

2.8.2 Affine Class

The scalogram and Wigner-Ville Distribution are members of the Affine Class, distributions that satisfy time-shift and scale-shift covariance (Equations 2.39 and 2.41). As in the formulation of Cohen's Class, any time-frequency representation in the Affine Class, $TFR_A(t,\omega)$, can be expressed as:

$$\begin{aligned} TFR_A(t,\omega) &= \int_{-\infty}^{+\infty}\int_{-\infty}^{+\infty} WVD_x(u,\nu) f_A(\omega(t-u),\nu/\omega)\, du\, d\nu, \\ f_A(\gamma,\lambda) &= \int_{-\infty}^{+\infty}\int_{-\infty}^{+\infty} \Phi_A(\alpha,\beta) e^{-i\beta\lambda} e^{i\alpha\gamma}\, d\alpha\, d\beta. \end{aligned} \tag{2.44}$$

For $f_A(\gamma,\lambda) = \delta(\gamma)\delta(\lambda+1)$, TFR_A is the WVD of the signal; for $f_A(\gamma,\lambda) = WVD_\phi(-\gamma,-\lambda)$, the WVD of a time/frequency reversed wavelet, TFR_A reduces to the scalogram (c.f. Equation 2.35).

2.9 Reduced Interference Distribution

The Reduced Interference Distribution (RID) has some advantages over the standard Wigner-Ville Distribution. The RID and WVD are both time-frequency distributions in Cohen's general class, but reduced interference methods are better suited to transient, non-stationary signals, as well as reducing the quadratic interference that complicates interpretation of the Wigner-Ville Distribution. In general, a "Reduced Interference Distribution" refers to any distribution that reduces the expression of the cross-terms relative to the auto-terms in a quadratic TFR representation; the RID given here is one particular member of a broad class of such representations.

The Reduced Interference Distribution, $RID(t,\omega)$, with kernel $R_x(t,\tau)$, based on a time series $s(t)$ with analytic associate $x(t)$, is defined as:

$$\begin{aligned} RID(t,\omega) &= \int_{-\infty}^{\infty} h(\tau) R_x(t,\tau) \mathrm{e}^{-i\omega\tau} d\tau, \\ R_x(t,\tau) &= \int_{-\frac{|\tau|}{2}}^{+\frac{|\tau|}{2}} \frac{g(\nu)}{|\tau|} \left(1+\cos\tfrac{2\pi\nu}{\tau}\right) x\left(t+\nu+\tfrac{\tau}{2}\right) x^*\left(t+\nu-\tfrac{\tau}{2}\right) d\nu. \end{aligned} \tag{2.45}$$

Note the similarity to the WVD (Equation 2.37) in general form, with the addition of a smoothing kernel in R_x. In this formulation, $h(\tau)$ is a time-smoothing window, and $g(\nu)$ is a frequency-smoothing window. The smoothing windows can be adjusted to fit specific needs, see Appendix C for selected software packages with RID implementations. I have presented a RID formulation for a Hanning window of $[(1+cos(2\pi\nu/\tau))/2]$. Other common smoothing kernels include binomial, bessel, and triangular (or "bartlett") windows (http://tftb.nongnu.org/, 2006; Boashash, 2003). For different choices of kernel, the formulation of $R_x(t,\tau)$ will change, but it will retain its general auto-correlation structure.

2.10 Smoothed Pseudo Wigner-Ville Distribution

Another distribution intended to reduce the expression of interference terms in the WVD is the Smoothed Pseudo Wigner-Ville Distribution (SPWVD):

$$SPWVD_x(t,\omega) = \int_{-\infty}^{\infty} h(\tau) \int_{-\infty}^{\infty} g(u-t)x(u+\tau/2)x^*(u-\tau/2)\,du\,\mathrm{e}^{-i\omega\tau}d\tau. \quad (2.46)$$

"Pseudo" refers here to the smoothing function $h(\tau)$, a frequency-smoothing window in the time domain that removes the need to integrate the WVD from $-\infty$ to ∞ as well as reducing cross-term interference (at the expense of decreased resolution). "Smoothed" is in reference to the time-smoothing function $g(t)$. In the form of Equation 2.42, $\Phi_C = \tilde{h}(\omega)g(t)$, a separable equation that allows for independent control of resolution in the time and frequency axes.

2.11 Other Time-Frequency Representations

The following TFRs, as members of Cohen's Class, can be expressed as a smoothed WVD, as in Equation 2.42. When selecting a smoothing function, it is possible to parameterize f_C such that it is a function of the product of t and ω, $f_C(t,\omega) = \tilde{f}_C(t\omega)$, and $\tilde{f}_C(0) = 1$. Representations in this subclass automatically satisfy scale shift covariance (Equation 2.41), the time and frequency marginal conditions (Equations 2.26 and 2.25), and also reduce the expression of interference. The Choi-Williams Distribution (Section 2.11.1) and Born-Jordan Distribution (Section 2.11.2) satisfy these properties, and the Zhao-Atlas-Marks Distribution (Section 2.11.3) is a refinement of the Born-Jordan distribution which sacrifices satisfaction of the marginal conditions for a smoother distribution along the frequency axis. This is by no means an exhaustive list of time-frequency representations, but rather a brief description of selected distributions that have well-defined kernels and that are commonly used in the signal processing community.

2.11.1 Choi-Williams

The Choi-Williams Distribution (Equation 2.47) reduces interference between arbitrary components and in general eliminates the expression of interference from cross-terms:

$$CW_x(t,\omega) = 2\int_{-\infty}^{\infty}\int_{-\infty}^{\infty}\sqrt{\frac{\alpha}{16\pi\tau^2}}e^{-\nu^2\alpha/(16\tau^2)}x\left(t+\nu+\frac{\tau}{2}\right)x^*\left(t+\nu-\frac{\tau}{2}\right)e^{-i\omega t}d\nu\,d\tau. \tag{2.47}$$

The Choi-Williams Distribution preserves interference horizontally and vertically, causing a ripple effect when there are auto-terms with the same time or frequency value. As α goes to zero, the Choi-Williams Distribution reduces to the Wigner-Ville Distribution. Increasing values of α reduces the expression of cross-terms, but also begins to interfere with the expression of the auto-terms. As in most time-frequency representations, there is a trade-off in implementing this distribution.

As a member of Cohen's Class, the Choi-Williams Distribution can be expressed as in Equation 2.42 with $\Phi_C = e^{-\left[\frac{\pi\omega t}{\alpha}\right]^2}$, a Gaussian function of $(t\omega)$.

2.11.2 Born-Jordan

The Born-Jordan Distribution (Equation 2.49) preserves time and frequency support, with the kernel $\Phi_C(t,\omega) = \frac{sin(\pi\omega t)}{\pi\omega t}$, a sinc function of $(t\omega)$:

$$BORN\_JORDAN_x = \int_{-\infty}^{\infty}\frac{1}{|\tau|}\int_{t-|\tau|/2}^{t+|\tau|/2}x(u+\tau/2)x^*(u-\tau/2)\,du\,e^{-i\omega t}\,d\tau. \tag{2.48}$$

2.11.3 Zhao-Atlas-Marks

The Zhao-Atlas-Marks (ZAM) Distribution, Equation 2.49, also known as the "Cone-Shaped Distribution" from the shape of the region $|\tau| \geq 2|t|$ in the $t-\tau$ plane, again reduces interference between arbitrary components in the time-frequency plane. It is able to almost completely remove cross-term interference from auto-terms with the same frequency value ("horizontal" interference in the time-frequency plane) but

preserves interference from auto-terms with the same time value ("vertical" interference). This is a smoothed version of the Born-Jordan Distribution, filtered along the frequency axis:

$$ZAM_x(t,\omega) = \int_{-2t}^{2t} e^{-i\omega t} \int_{-\infty}^{\infty} x\left(u+\frac{\tau}{2}\right) x^*\left(u-\frac{\tau}{2}\right) f(t-u,\tau)du\,d\tau, \quad (2.49)$$

$$f(t,\tau) = \begin{cases} \frac{1}{\tau}e^{-\alpha\tau^2} & , \ |\tau| \geq 2|t| \\ 0 & , \ otherwise \end{cases}$$

The Cohen kernel for this distribution is $\Phi_C(t,\omega) = \frac{sin(\pi\omega t)}{\pi\omega t}e^{-\alpha t^2}$, which suppresses the Born-Jordan sinc function with the $e^{-\alpha t^2}$ term. As α in $f(t,\tau)$ increases, cross-terms are suppressed at the expense of interference with the character of auto-terms (again, only "vertical" interference, from auto-terms with different frequency components occurring at the same time instant). The ZAM Distribution has been extensively used in speech analysis (Qian, 2002) as an alternative to spectrogram methods.

2.12 Sample Signal with Transient Components

It is useful to apply these time-frequency analysis methods to a synthetic signal with known frequency content. The test signal in this section (Figure 2.4, along with the Fourier Transform) is composed of 5 main segments of 512 points each, for a total length of $N = 5 * 512 = 2560$:

1. Baseline signal which consists of a low frequency sine wave, plus noise,
2. Baseline plus a transient high-frequency component,
3. Baseline signal,
4. Baseline signal is doubled in amplitude, plus a transient intermediate-frequency component,
5. Baseline signal (doubled).

I present linear and logarithmic plots of various TFR methods for this sample signal. First I present traditional time-frequency representations (spectrogram, wavelets, Gabor transform) that may be more familiar to the engineering community, then modern quadratic TFRs and masked TFR methods. The kernel-smoothing done by modern TFR methods does a better job of removing the cross term interference than masking/overlay filtering methods, though these techniques do still have problems with positivity and time-frequency resolution. Each of these methods is subject to the fundamental restrictions of the uncertainty principle (Section 2.2), which limits the ultimate resolution in the time-frequency plane.

The Reduced Interference Distribution presented in Section 2.12.6 has certain properties that make it nearly ideal for the types of signals often encountered in seismology and civil engineering.

2.12.1 Spectrogram

The Spectrogram, with varying window lengths, shows the evolution of the frequency content of the signal. The two transient pulses and the baseline signal can be identified

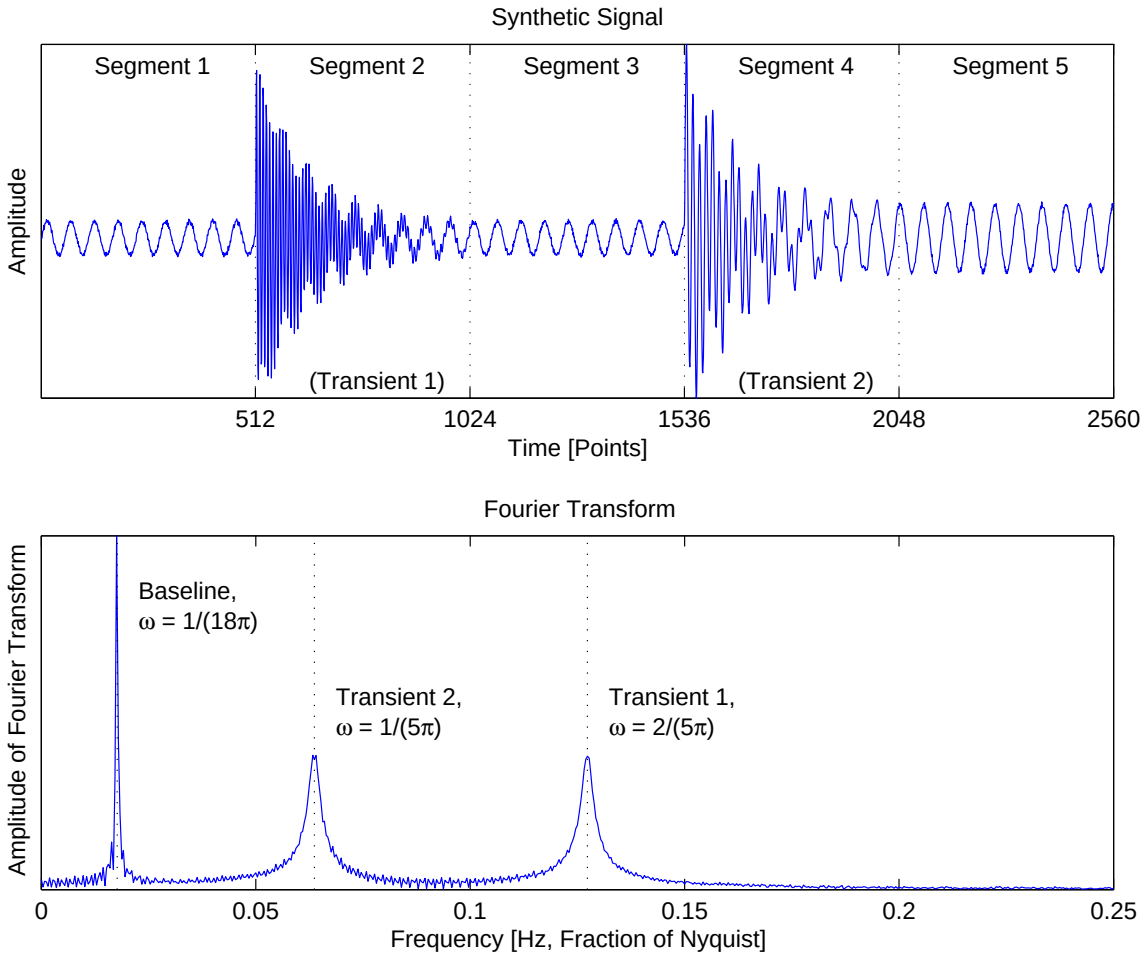

Figure 2.4: Test signal with transient components, five segments of different character – 1: Baseline signal (noisy sine wave), 2: Baseline with a high-frequency transient, which dies out by the end of the segment, 3: Baseline signal, 4: Baseline signal doubles in amplitude, with a intermediate frequency transient, which dies out by the end of the segment, 5: Baseline signal (doubled). The Fourier Transform correctly identifies the three main components of the record but does not provide information regarding the evolution of the signal's frequency content.

in the time-frequency plane, subject to the uncertainty relationship of Section 2.2. In these figures, the log plot alongside the linear plots allow for a more detailed investigation of the location of the energy in the Time-Frequency plane.

Of note in Figures 2.5 – 2.9 is the smearing of the transient signal components along the time axis. Energy in the time-frequency plane appears before the true temporal onset of the transient signals. The spectrogram, as a running Fourier Transform, extracts frequency content from the signal for a sliding window. However, the windowing involved in the Fourier Transform smears information such that the transient components appear in the time-frequency plane before their onset in the time series, as soon as the analysis window impinges on the transient. This is an artifact of the window used for calculating the Fourier Transform and represents one of the severe shortcomings in the spectrogram method for system identification. Identifying the onset of changes in the natural frequencies of a structure is necessary for the identification of changes in stiffness – and ultimately for correlating changes in dynamic properties with changes in physical properties of the system. The spectrogram, regardless of windowing length, is not able to create a joint time-frequency representation for the system without this uncertainty in resolution.

Figures 2.5 and 2.6 show sliding windows of 256 and 512 points, respectively. Each window overlaps the previous window by 50%. Choosing discrete windows reveals the "blocky" nature of the spectrogram method and emphasizes the trade-off in temporal vs. frequency resolution. The remaining spectrograms, Figures 2.7 – 2.9, are continuous spectrogram representations for different window sizes, obtained by shifting the window only one point at a time as the window moves along the original signal. This creates a smooth distribution, though the smearing of information in the time-frequency plane is still apparent at all window lengths. It is particularly useful to compare the linear plots in Figures 2.7 – 2.9. The transient peaks in Figure 2.7 are narrower in the time dimension and wider along the frequency dimension than the transient peaks in Figure 2.9. This is in agreement with earlier discussions of the canonical relationship between frequency resolution and temporal resolution. Though

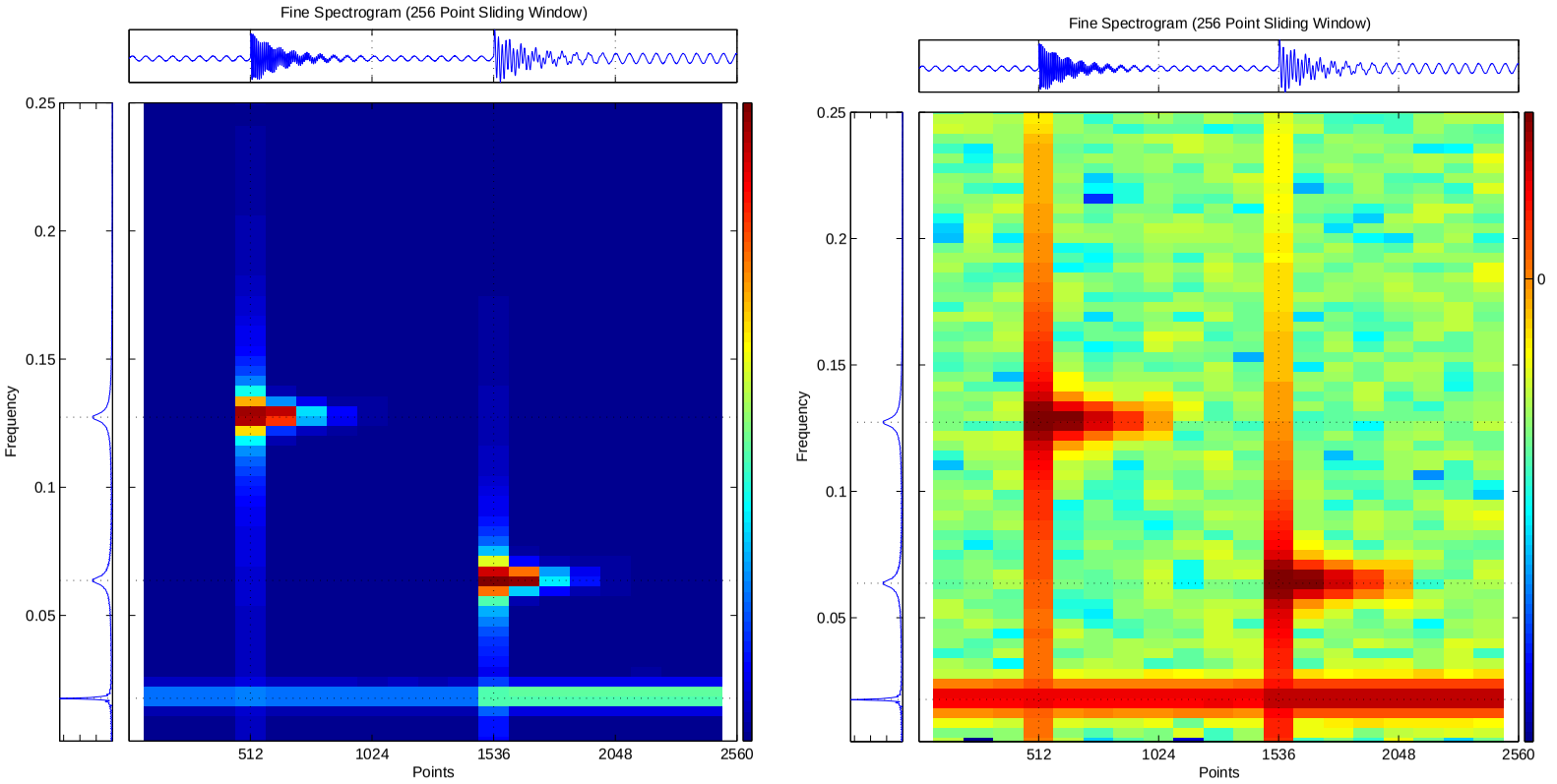

(a) Spectrogram

(b) Spectrogram, log10(abs())

Figure 2.5: Transient test signal, spectrogram, running window of 256 points. (Compare with Figure 2.6.) The information in the time-frequency plane is blocky and smeared in both time and frequency. The exact onset of the transient signals is impossible to determine, though it can be estimated with some accuracy.

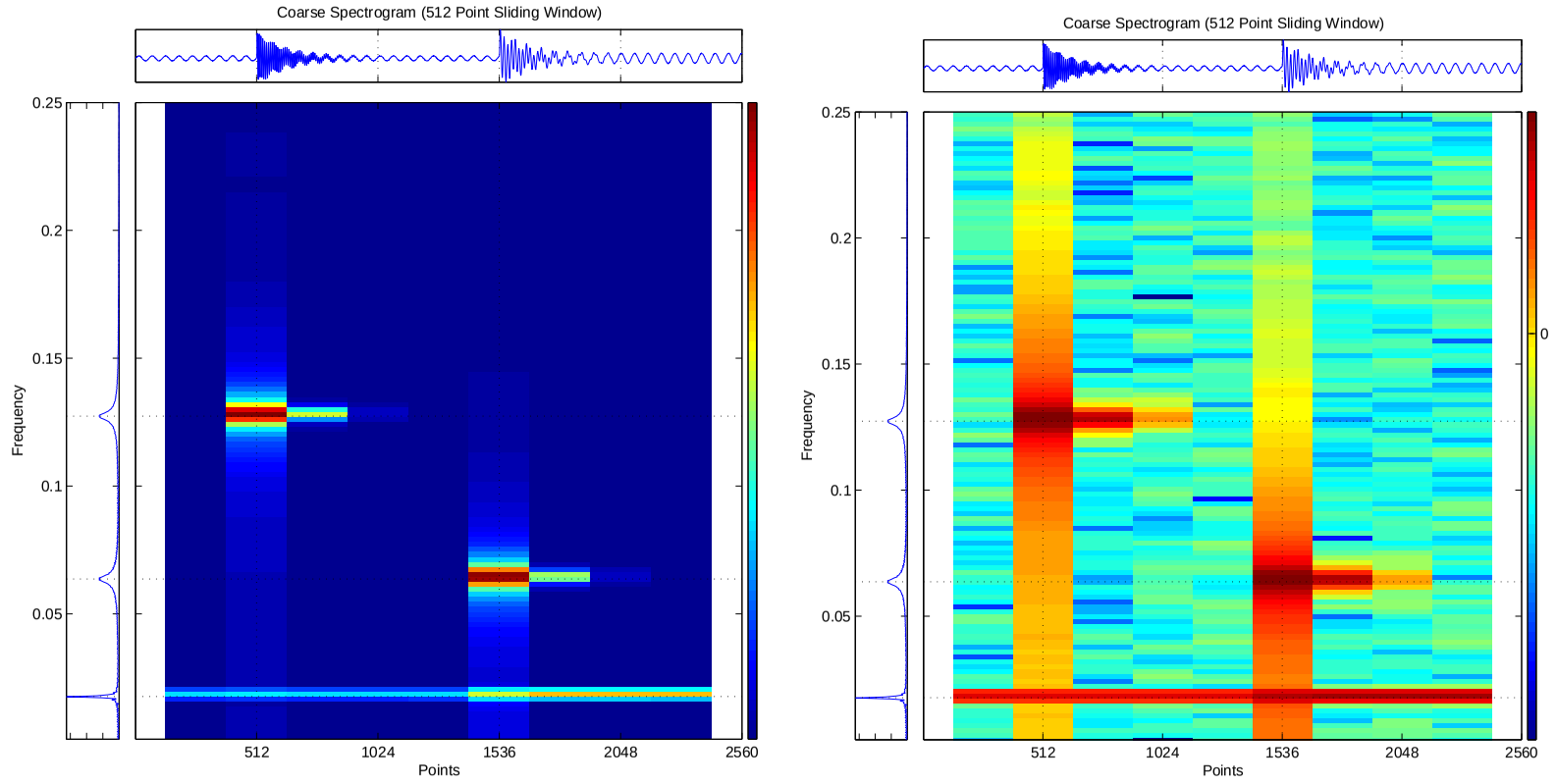

(a) Spectrogram

(b) Spectrogram, log10(abs())

Figure 2.6: Transient test signal, spectrogram, running window of 512 points. (Compare with Figure 2.5.) This window length has much better frequency resolution, but the temporal resolution is very coarse. The transient signals are thereby smeared across a wider time range, though they are much better represented in terms of frequency content.

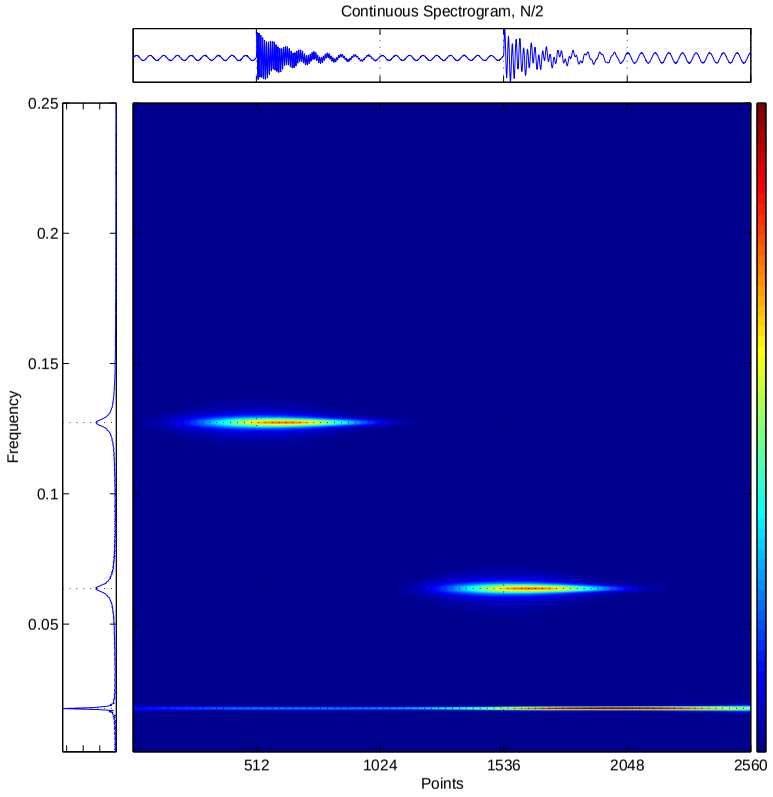

(a) Spectrogram

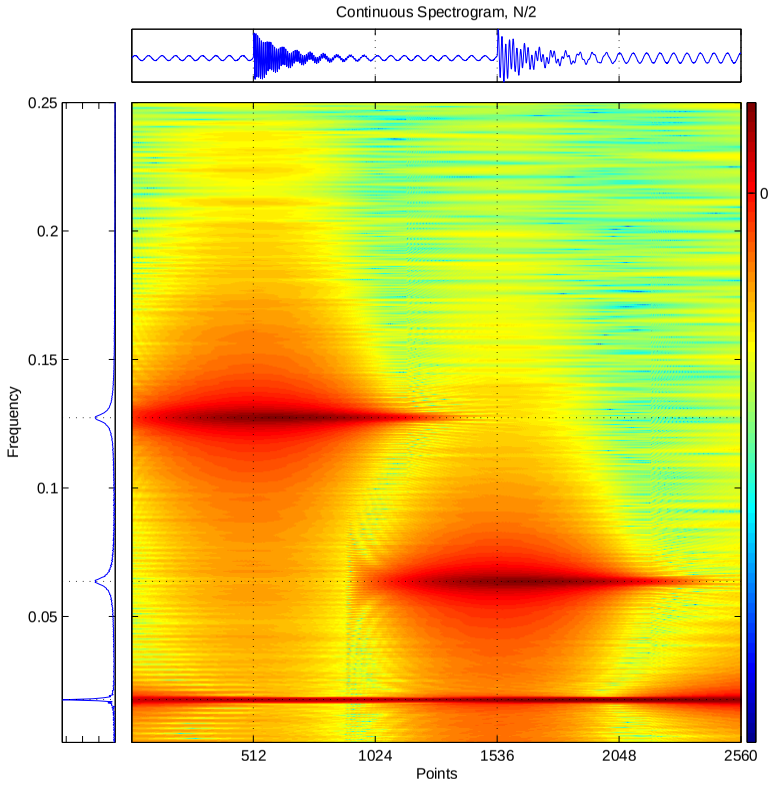

(b) Spectrogram, log10(abs())

Figure 2.7: Transient test signal, Continuous Spectrogram, window of N/2. The continous spectrogram implementation gives a frequency estimate for each point in the original record. This method still falls prey to the time/frequency resolution tradeoff of the typical spectrogram (Figures 2.5 and 2.6). The windowing involved with the STFT by definition smears the arrival of transient signals by a timespan proportional to the windowing function. Therefore, the transient signals appear in the time-frequency plane before the actual instant of their onset.

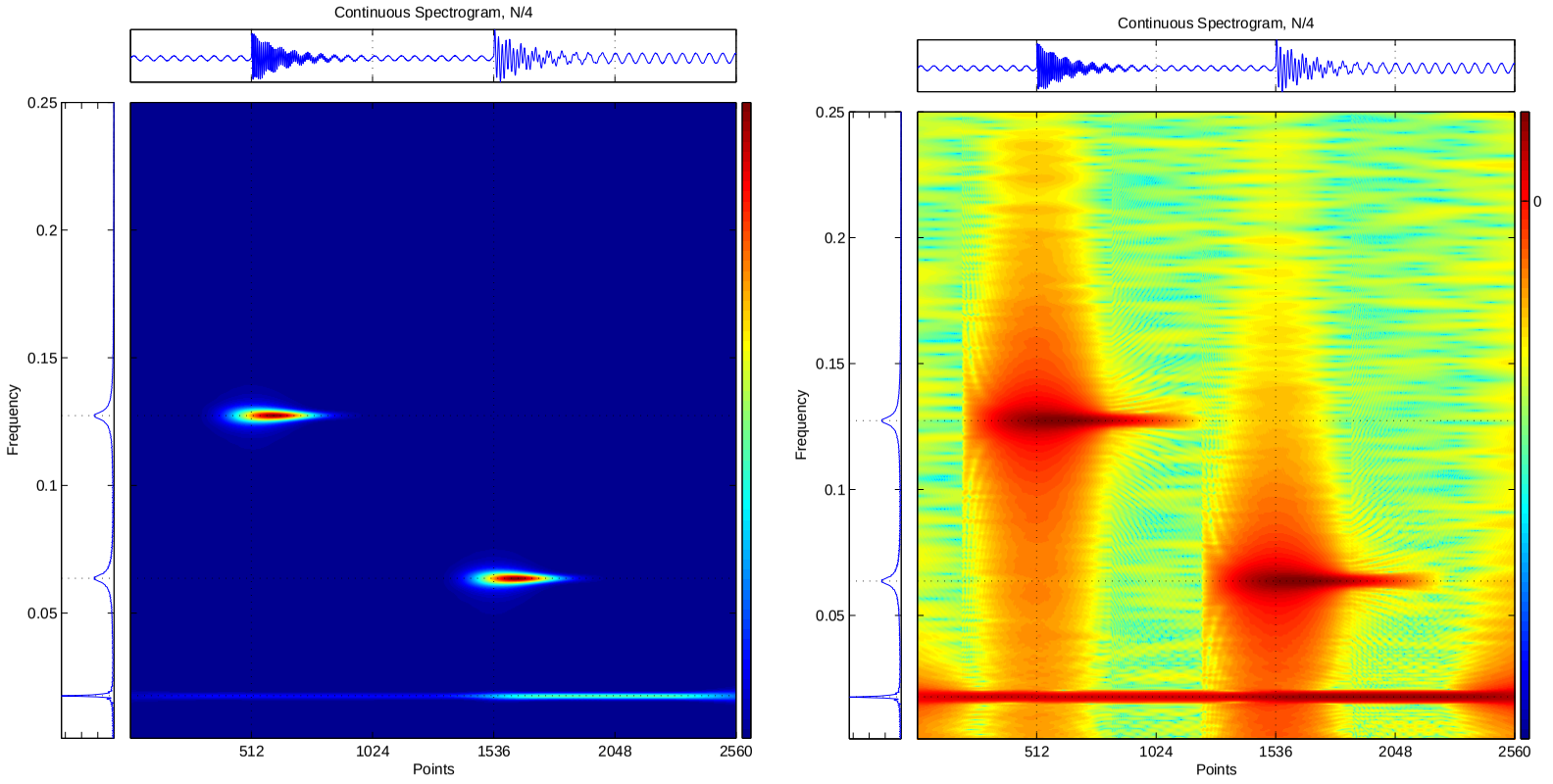

(a) Spectrogram

(b) Spectrogram, log10(abs())

Figure 2.8: Transient test signal, Continuous Spectrogram, window of N/4, as in Figure 2.7. For a shorter window, the temporal resolution increases, though information regarding the transient signals is still presenting before their arrival in the original signal.

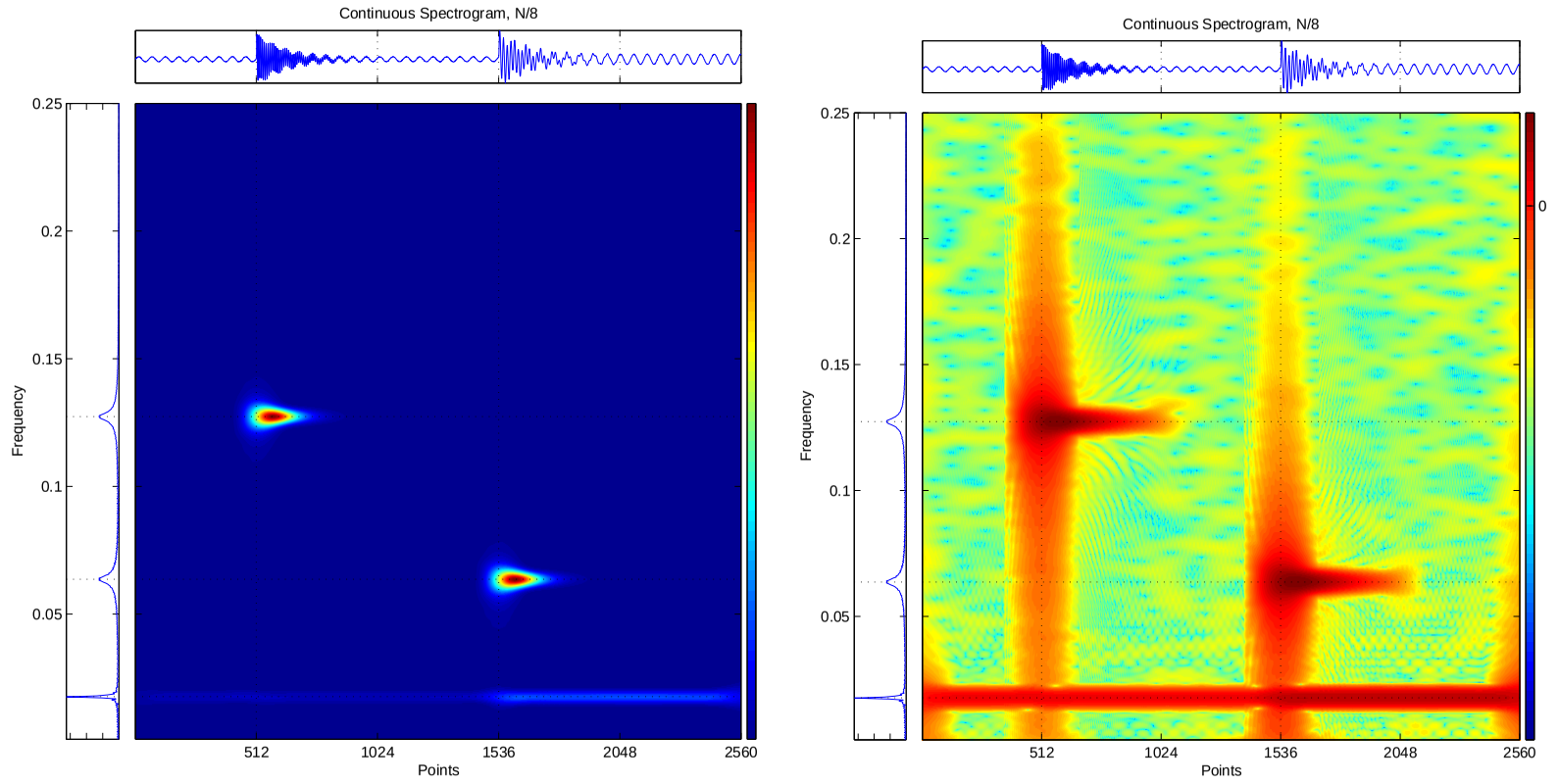

(a) Spectrogram

(b) Spectrogram, log10(abs())

Figure 2.9: Transient test signal, Continuous Spectrogram, window of N/8, as in Figure 2.7. For each successive decrease in window length, the temporal accuracy has increased at the expense of the accuracy of the frequency estimate in the time-frequency plane.

there is a gain in temporal accuracy for each decrease in window length (N/2 → N/4 → N/8), the frequency resolution at each level decreases by half as well.

2.12.2 Continuous Wavelet Transform

The CWT, shown in Figure 2.10, clearly shows the evolution of the properties of the signal. This wavelet implementation has more accurate temporal resolution than the spectrogram methods of Section 2.12.1, and the transient signals are matched in the time-frequency plane. However, the amplitude of the high-frequency component is lower than the intermediate component, and there is a diffuse smearing of the time frequency representation along the frequency axis – the scalogram is biased towards lower frequencies, and at higher scales the approximation between scale and frequency becomes less accurate.

Wavelet methods have much better temporal accuracy/support than the spectrogram methods, which can be seen in the onset of energy being limited to the temporal region where the transient signals appear. Even in the logarithmic plot, which magnifies the expression of energy, the transient signals are correctly located in the time-frequency plane. The attenuation of high frequencies becomes less apparent in the log plot, as both transient signals stand out clearly from the near-zero of the field. Some slight smearing is more noticeable for lower frequencies, which is an artifact of the inexact conversion from "scale" to "frequency." Of note is the sudden cutoff for the transient signals, which is not a windowing artifact; this sudden cutoff is an accurate depiction of the synthetic signal, as it was constructed from five distinct pieces. The first, third, and fifth segment of the record consist only of the baseline signal, and it is the excellent temporal resolution of the wavelet that leads to the crispness of the beginning and ending of these transient signals in the second and fourth segments.

The diffuse nature of this representation suggests (pseudo-)energy in the time-frequency plane at frequencies where there is no energy in the original signal. This is a serious shortcoming for this method despite the crisp temporal resolution.

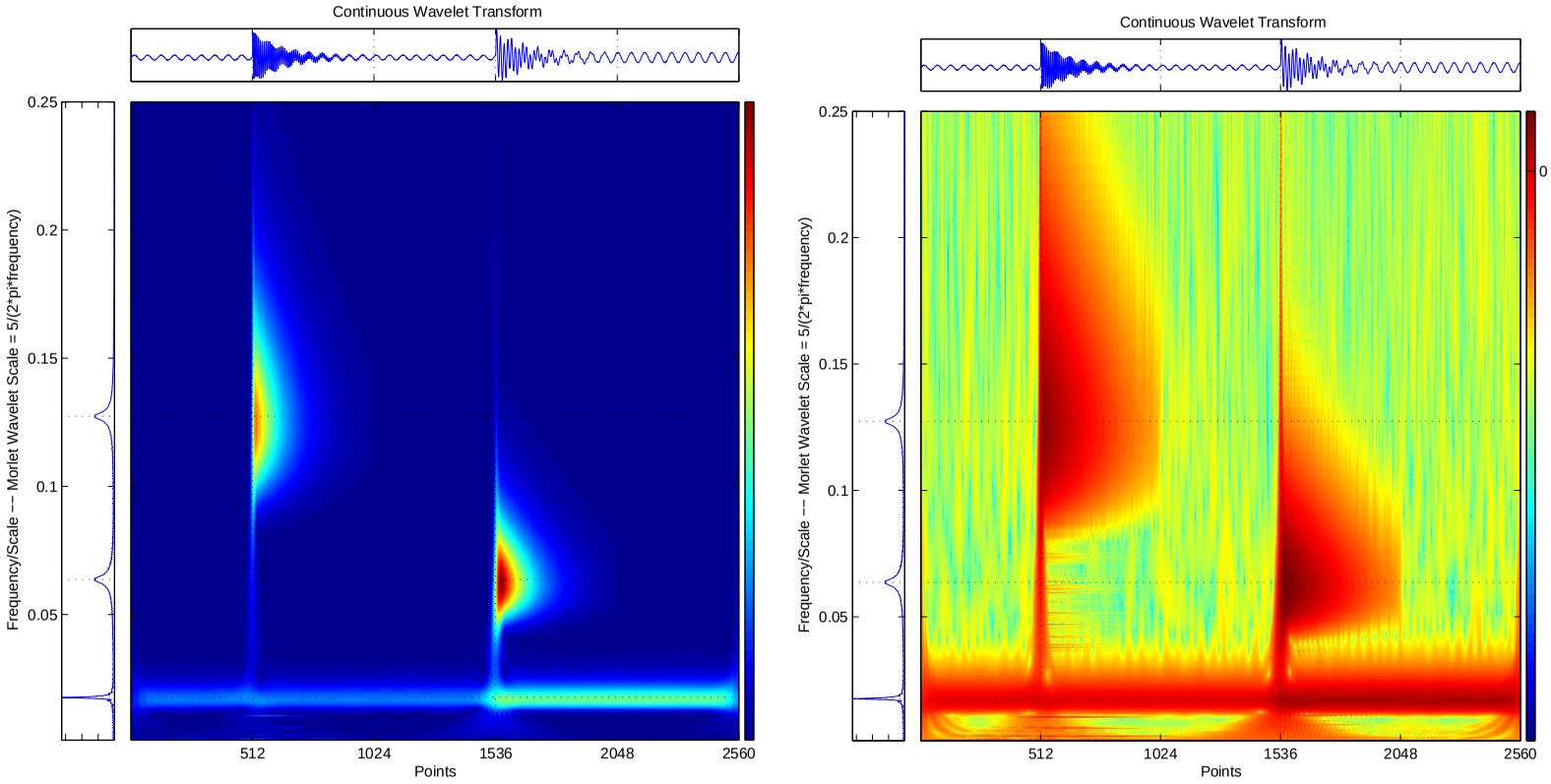

(a) Continuous Wavelet Transform

(b) Continuous Wavelet Transform, log10(abs())

Figure 2.10: Transient test signal, Continuous Wavelet Transform (Morlet Wavelet). The amplitude of this distribution is unevenly distributed around the known frequency in the signal, biased towards higher frequencies. The wavelet scalogram, in general, provides excellent temporal resolution. Unfortunately, interpreting the frequency content at each instant is not trivial, as the basis vectors for a wavelet transformation contain more than one frequency; the representation is limited to a frequency approximation based on the family of wavelet. The crisp cutoff in the log plot (at 1024 and 2048) is not a windowing artifact, but reflects the end of the transient signals. Each segment is 512 points, and there is no transient component in the first, third, or fifth interval.

2.12.3 Gabor Transform

The Gabor Transform (Equation 2.36) is a linear transformation that has several properties similar to the STFT and the CWT. As the Gabor Transform is evenly sampled in frequency, the Gabor Transform avoids the "spreading" associated with the CWT at high frequencies. The filterbank-like nature of the Gabor Transform provides superior temporal localization to the STFT. Figure 2.11 shows good resolution in the time-frequency plane, though the blocky nature of the Gabor Transform (similar to that of a coarsely sampled STFT) reduces the possible maximum resolution.

2.12.4 Wigner-Ville Distribution

The Wigner-Ville Distribution for the synthetic signal is shown in Figure 2.12. Interference from the cross-terms makes this distribution almost unusable for determining the instantaneous behavior of the signal. Cross-terms in the kernel of the WVD create interference terms between each component of the signal. These cross terms appear in the time-frequency plane directly between the auto terms – between each pair of auto terms is a region of highly oscillatory interference. As the WVD satisfies the marginal conditions (Section 2.3), these cross term interference patterns are completely removed by summing across the time (horizontal) or frequency (vertical) axis, even though the interference itself is not supported in time or frequency.

In Figure 2.12, the intermediate term at time ~ 1024 at a frequency of $\sim 0.095Hz$ is entirely from interference. Along the frequency subplot, the Fourier Transform shows that there is no energy in the signal at $.095Hz$, and the time-series subplot shows no transient signal beginning at time 1024. These interference terms are unsupported in the time-frequency plane and do not represent the true evolving frequency content of the signal. There are other interference terms midway between each of the transient peaks and the baseline peak (at $\sim 0.0725Hz$ between ~ 256 and ~ 1536, and at $\sim 0.04067Hz$ from ~ 768 to ~ 2048). The interference terms between the baseline and transients are stronger for the last section of the baseline, where the

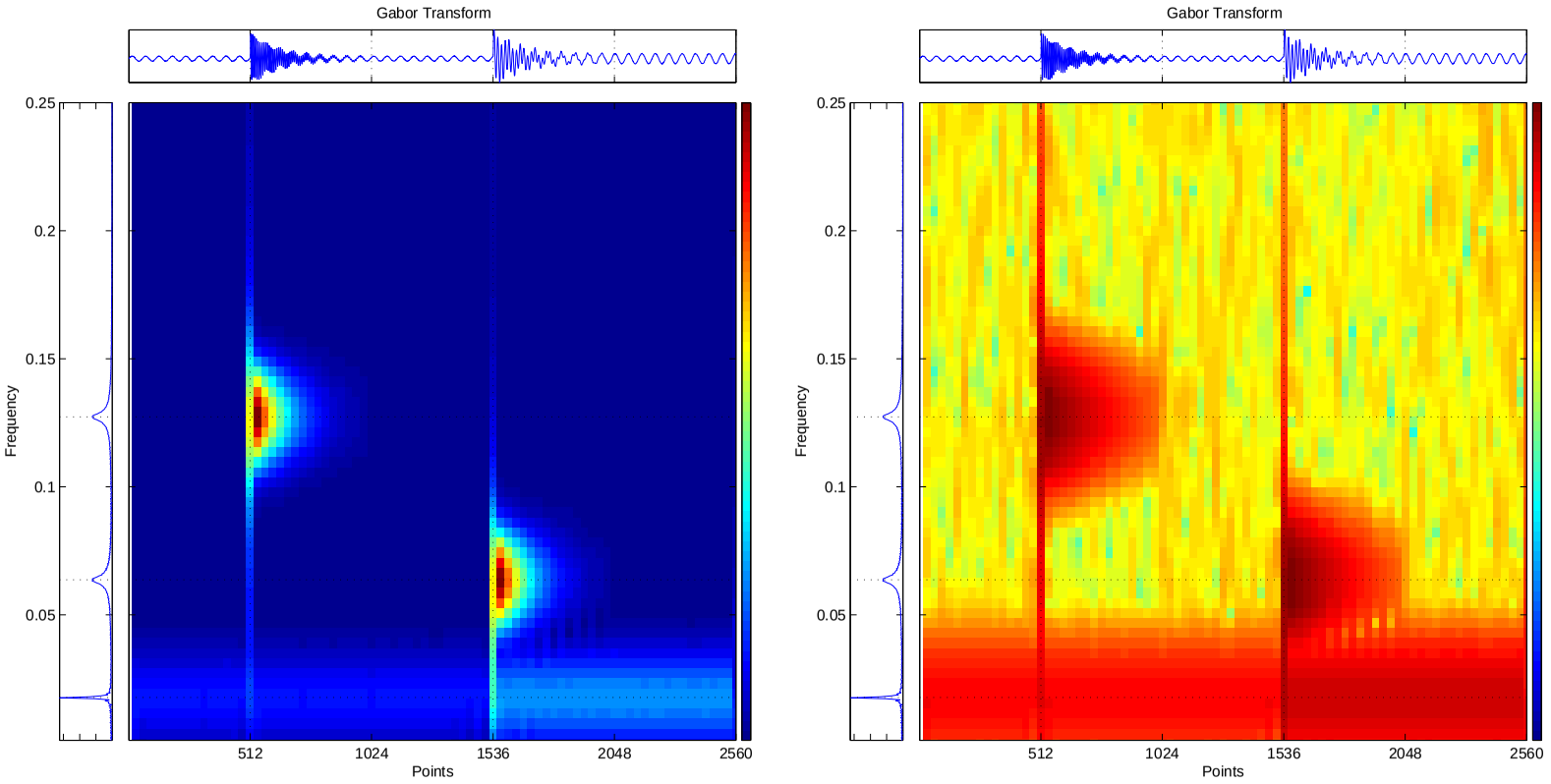

(a) Gabor Transform

(b) Gabor Transform, log10(abs())

Figure 2.11: Transient test signal, Gabor Transform. The Gabor Transform is equivalent to an ideally-sampled STFT, and can also be described as a filterbank with linear sampling across the frequency axis. The uniform sampling improves on the diffuse nature of the CWT and preserves resolution at higher frequencies.

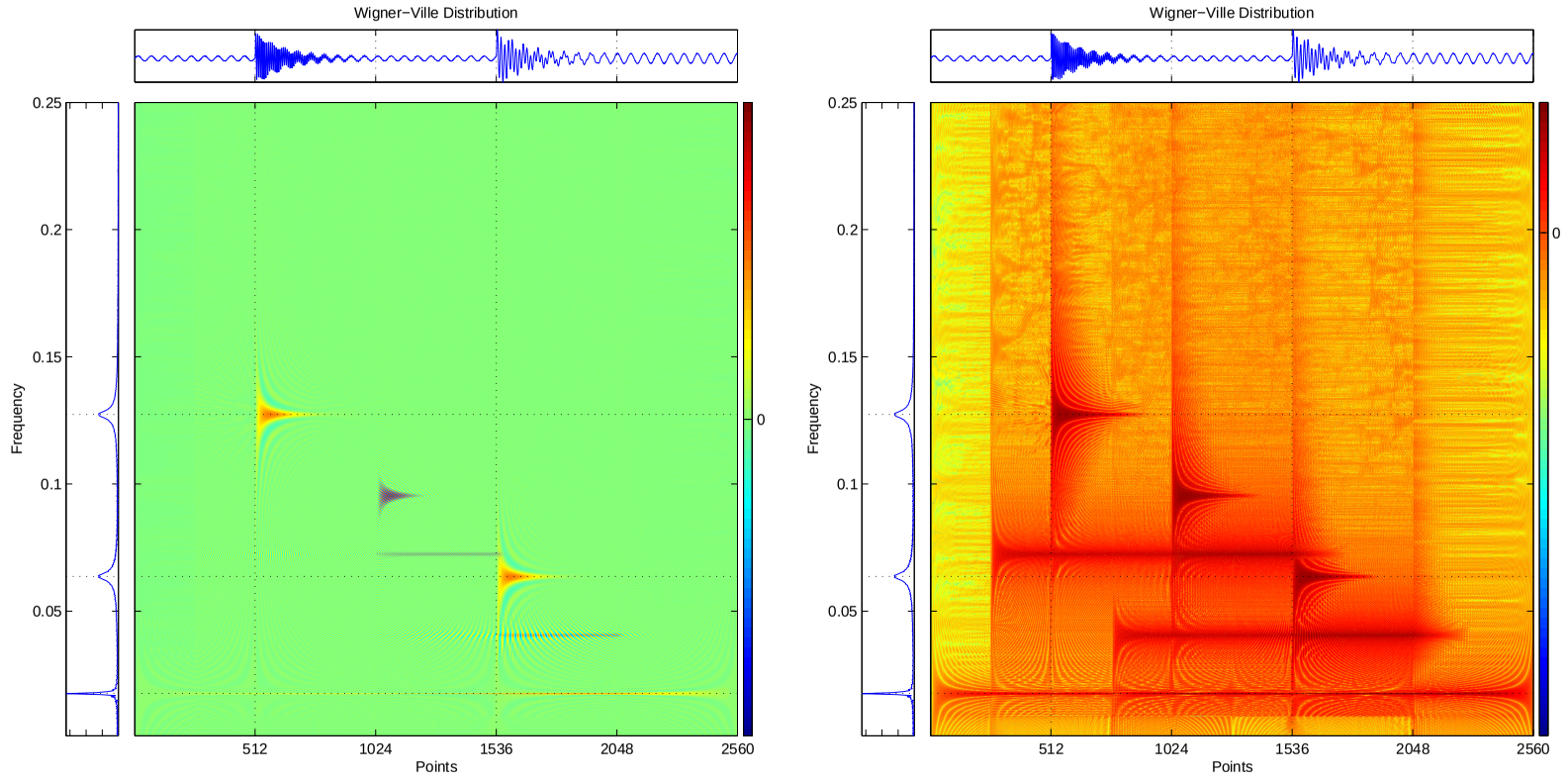

(a) Wigner-Ville Distribution

(b) Wigner-Ville Distribution, log10(abs())

Figure 2.12: Transient test signal, Wigner-Ville Distribution. In addition to oscillations near the peaks of the signal, there is cross-term interference located midway between each auto component of the signal – shifted in both time and frequency. The intermediate "pulse" at time ~ 1024 and $\sim 0.095Hz$ is entirely from interference between the two transient peaks. This interference term is unsupported in either time or frequency: it suggests energy at a frequency where there is known to be no energy, as shown in the Fourier Transform; and it suggests a temporal onset at an instant when there is no transient signal. There are other interference terms at $\sim 0.0725Hz$ between ~ 256 and ~ 1536, and at $\sim 0.04067Hz$ from ~ 768 to ~ 2048, representing interference between the transient terms and the baseline term.

baseline amplitude was doubled. Again, these terms are entirely interference, so this distribution does not accurately represent the character of the signal.

2.12.5 Smoothed Pseudo Wigner-Ville Distribution

The Smoothed Pseudo Wigner-Ville Distribution (SPWVD), Equation 2.46, Figure 2.13, reduces cross-term interference of the WVD. There are many ways of smoothing the WVD to obtain a more accurate TFR. The SPWVD is one of the most general formulations. Though the expression of the cross terms is reduced, the temporal accuracy is harmed by the smoothing process. The RID is a related method, with more accurate representation in the time-frequency plane.

2.12.6 Reduced Interference Distribution

The Reduced Interference Distribution (RID) reduces the expression of the interference terms found in the WVD. Reducing the expression of the cross-term interference is one of the primary goals in using quadratic TFR methods for signal processing. The RID has a smoothing function in both time (g) and frequency (h). I present several combinations of time and frequency window lengths in Figures 2.14 – 2.18. A longer window along the time axis smears information temporally, and a longer window along the frequency axis increases the bandwidth of the frequency information. In general form, the RID is similar to the SPWVD, though by adjusting the windowing functions, the RID has better temporal accuracy while avoiding the strongest expressions of cross-term interference.

In general, the smoothing functions of the RID need to be selected based on each individual signal being analyzed. There is no combination of window lengths that performs ideally for all signals, and the TFR method used must be adjusted based on the frequency content, the character of the signal, etc. However, RID window lengths of N/4 to N/10 will generally give good results for the signals commonly encountered in seismology and structural engineering, and in later sections I will be using windowing functions in this range.

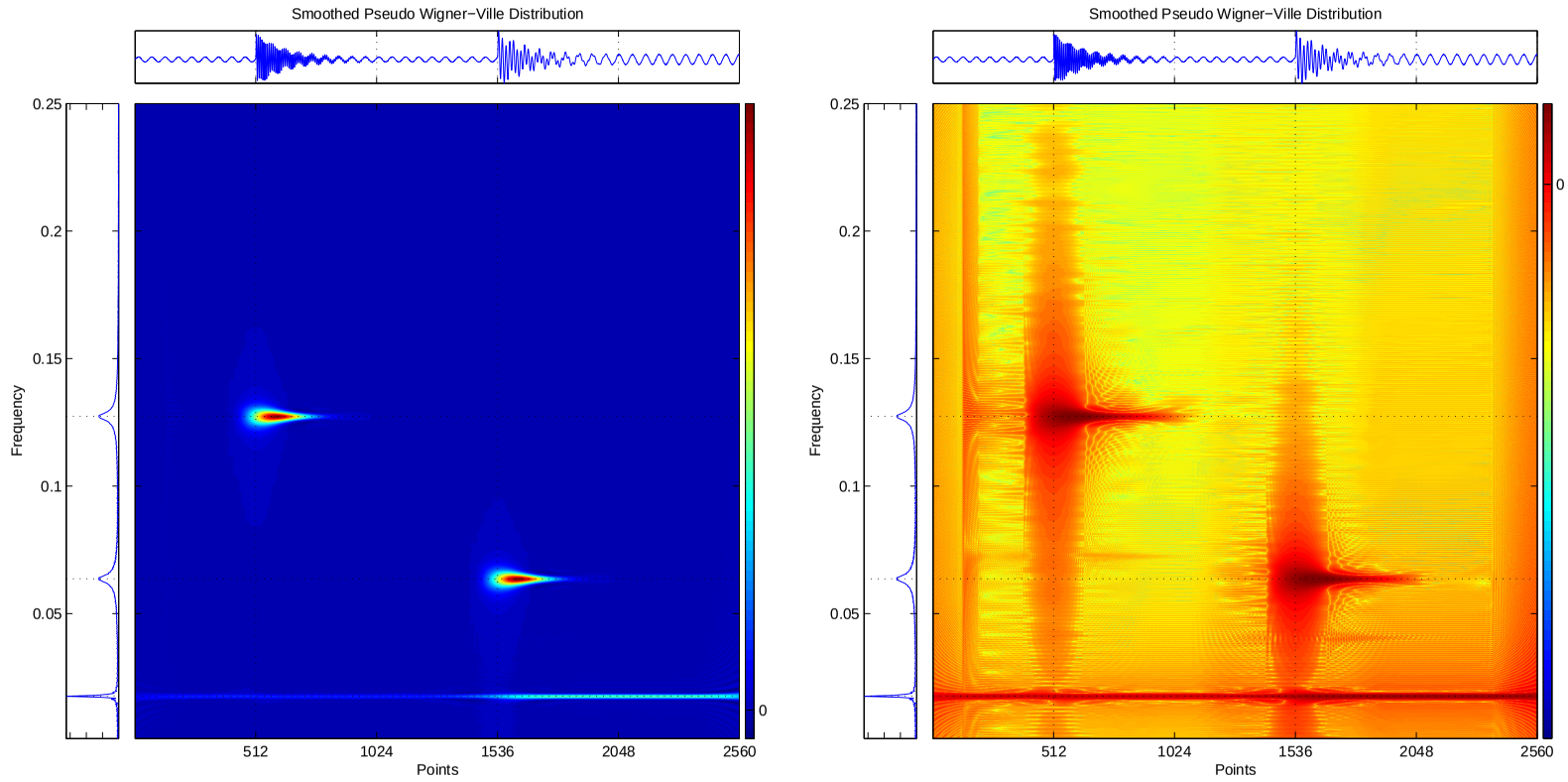

(a) Smoothed Pseudo Wigner-Ville Distribution

(b) Smoothed Pseudo Wigner-Ville Distribution, log10(abs())

Figure 2.13: Transient test signal, Smoothed Pseudo Wigner-Ville Distribution. By eliminating the cross-term interference, the SPWVD becomes a much more accurate representation of energy in the time-frequency plane. However, this formulation of the SPWVD brings the WVD closer to a spectrogram representation (c.f. Figure 2.9). The Reduced Interference Distribution is a related method for removing cross-term interference and in general has superior results (c.f. Figure 2.18).

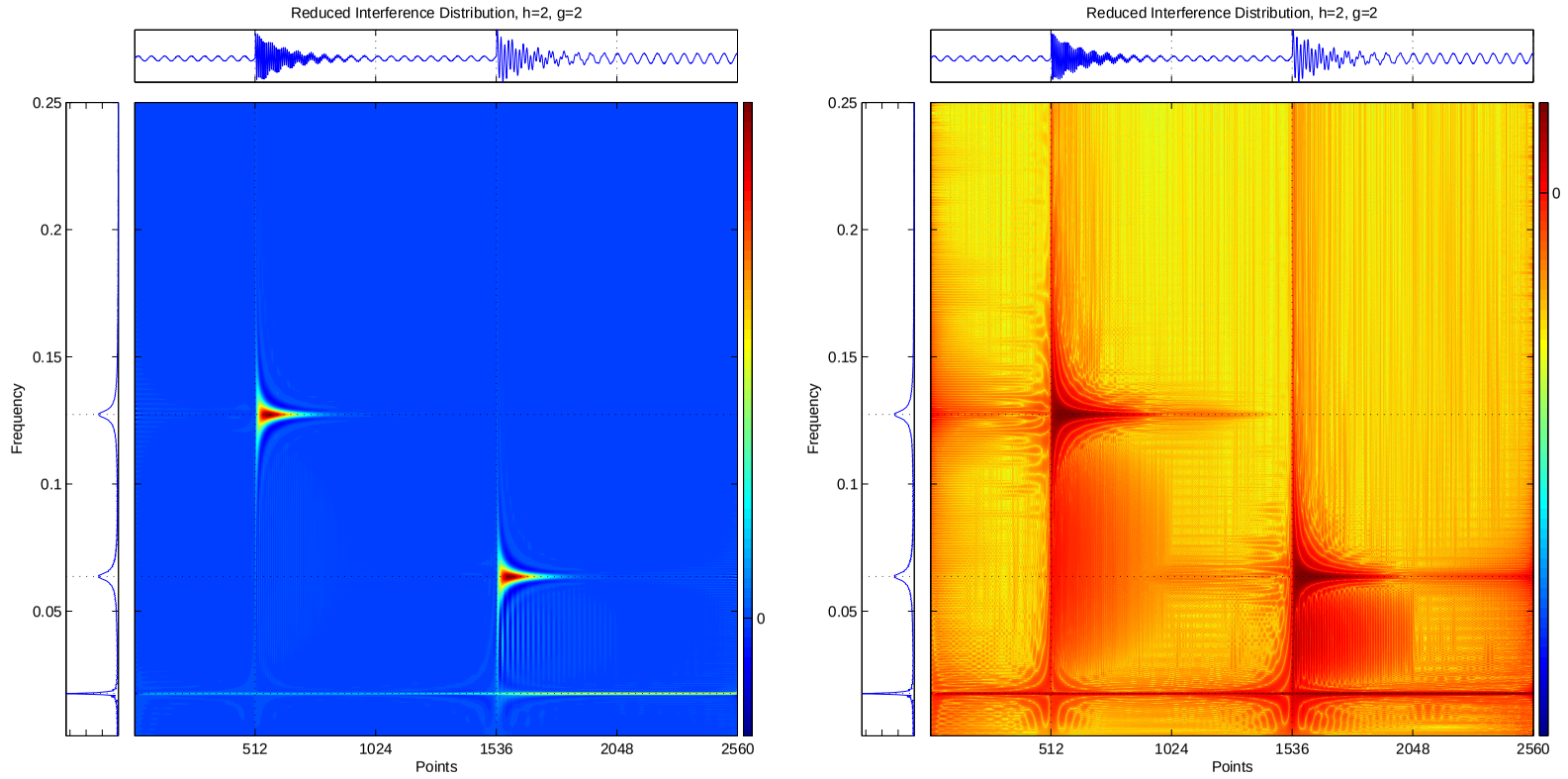

(a) Reduced Interference Distribution

(b) Reduced Interference Distribution, log10(abs())

Figure 2.14: Transient test signal, Reduced Interference Distribution, frequency window N/2, time window N/2. The RID has, in general, better temporal resolution than the SPWVD (Figure 2.13). Some residual interference appears between cross terms, but the general expression in the time-frequency plane is nearly ideal for this sample signal.

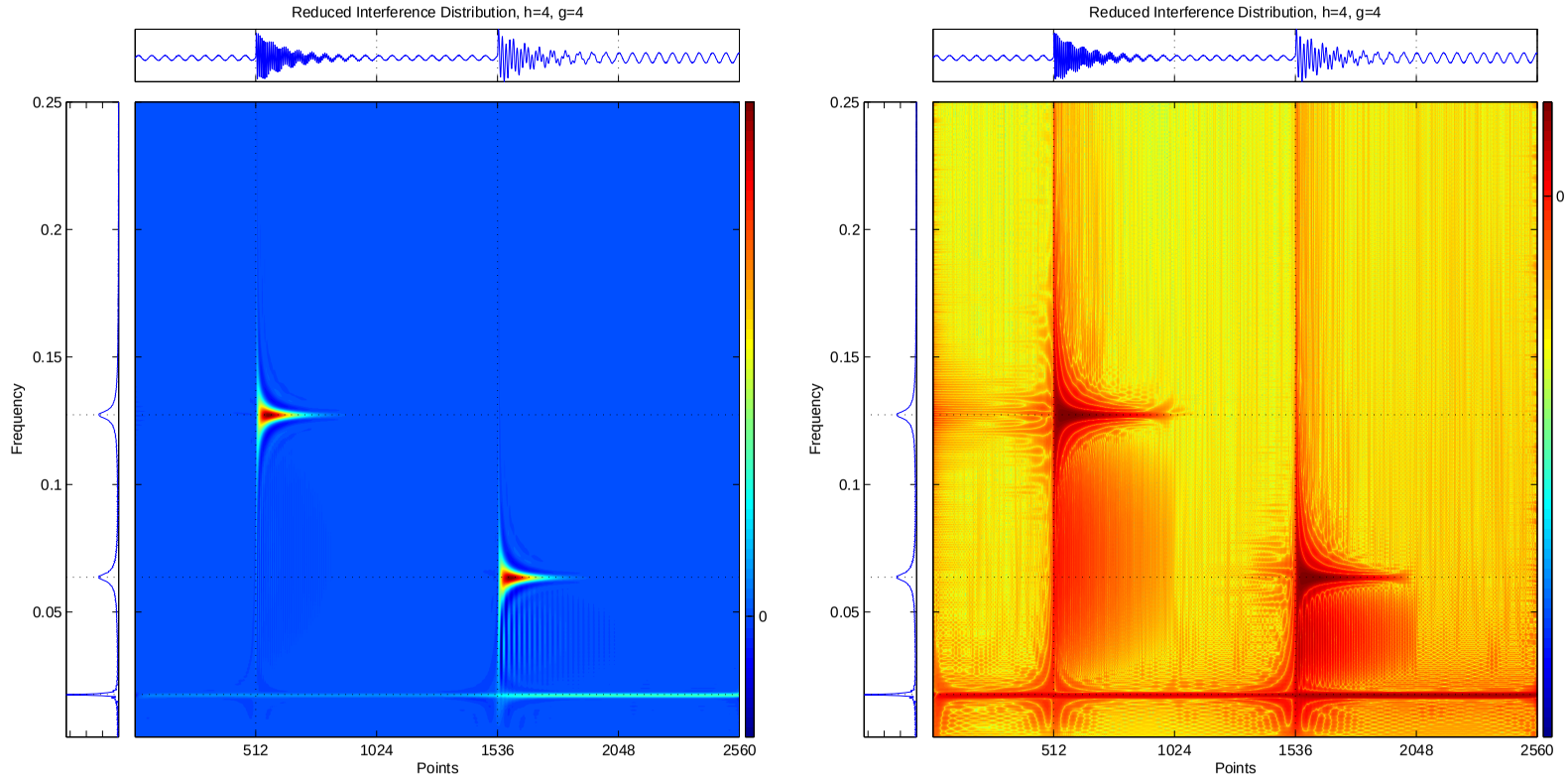

(a) Reduced Interference Distribution

(b) Reduced Interference Distribution, log10(abs())

Figure 2.15: Transient test signal, Reduced Interference Distribution, frequency window N/4, time window N/4. A shorter time and frequency windowing function gives better results than Figure 2.14.

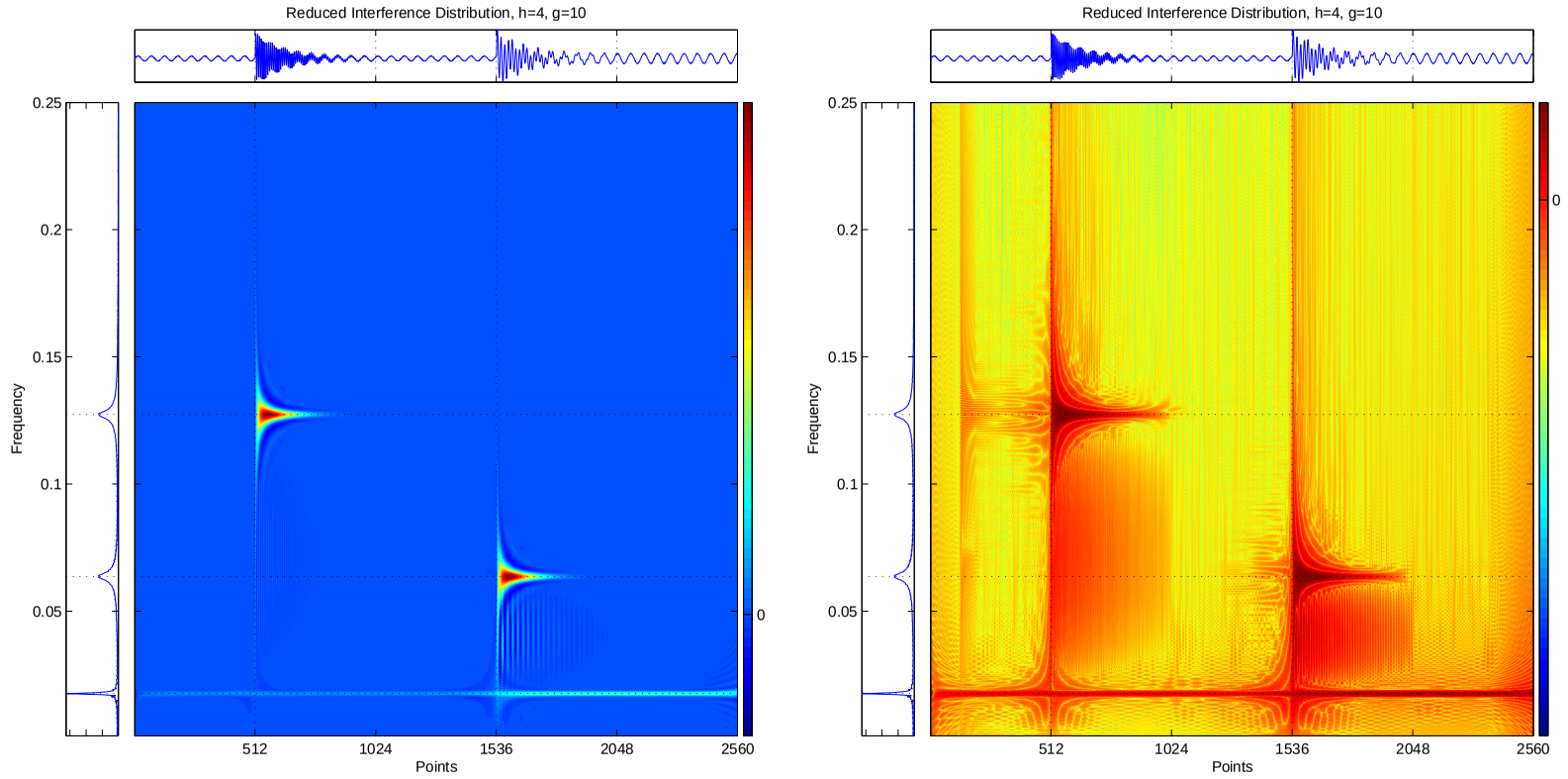

(a) Reduced Interference Distribution

(b) Reduced Interference Distribution, log10(abs())

Figure 2.16: Transient test signal, Reduced Interference Distribution, frequency window N/4, time window N/10. For completeness, I show several similar plots with different time and frequency window lengths. Lengths between N/4 and N/10, for both time and frequency, generally are suitable for seismic signals.

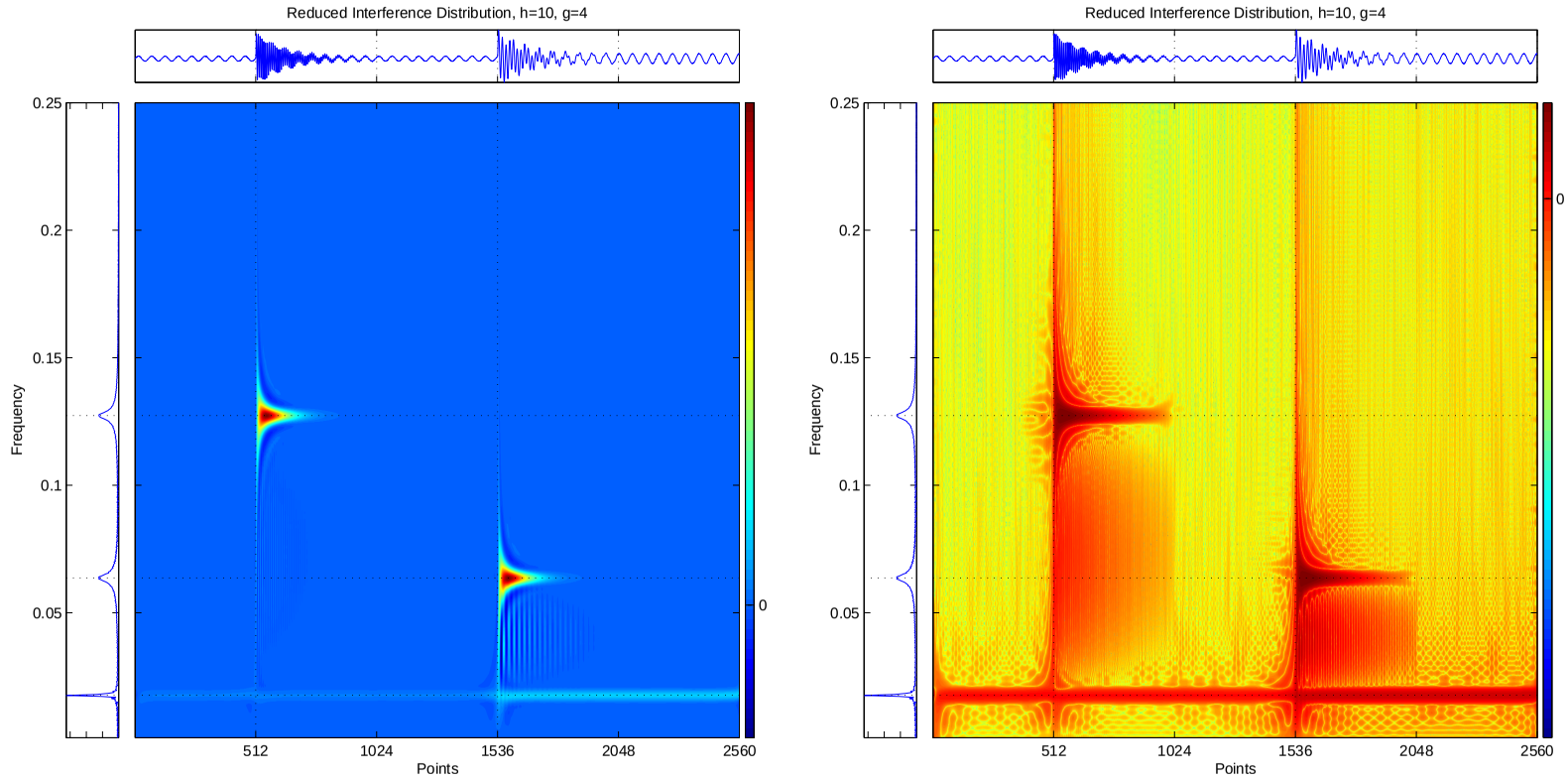

(a) Reduced Interference Distribution

(b) Reduced Interference Distribution, log10(abs())

Figure 2.17: Transient test signal, Reduced Interference Distribution, frequency window N/10, time window N/4. For completeness, I show several similar plots with different time and frequency window lengths. Lengths between N/4 and N/10, for both time and frequency, generally are suitable for seismic signals.

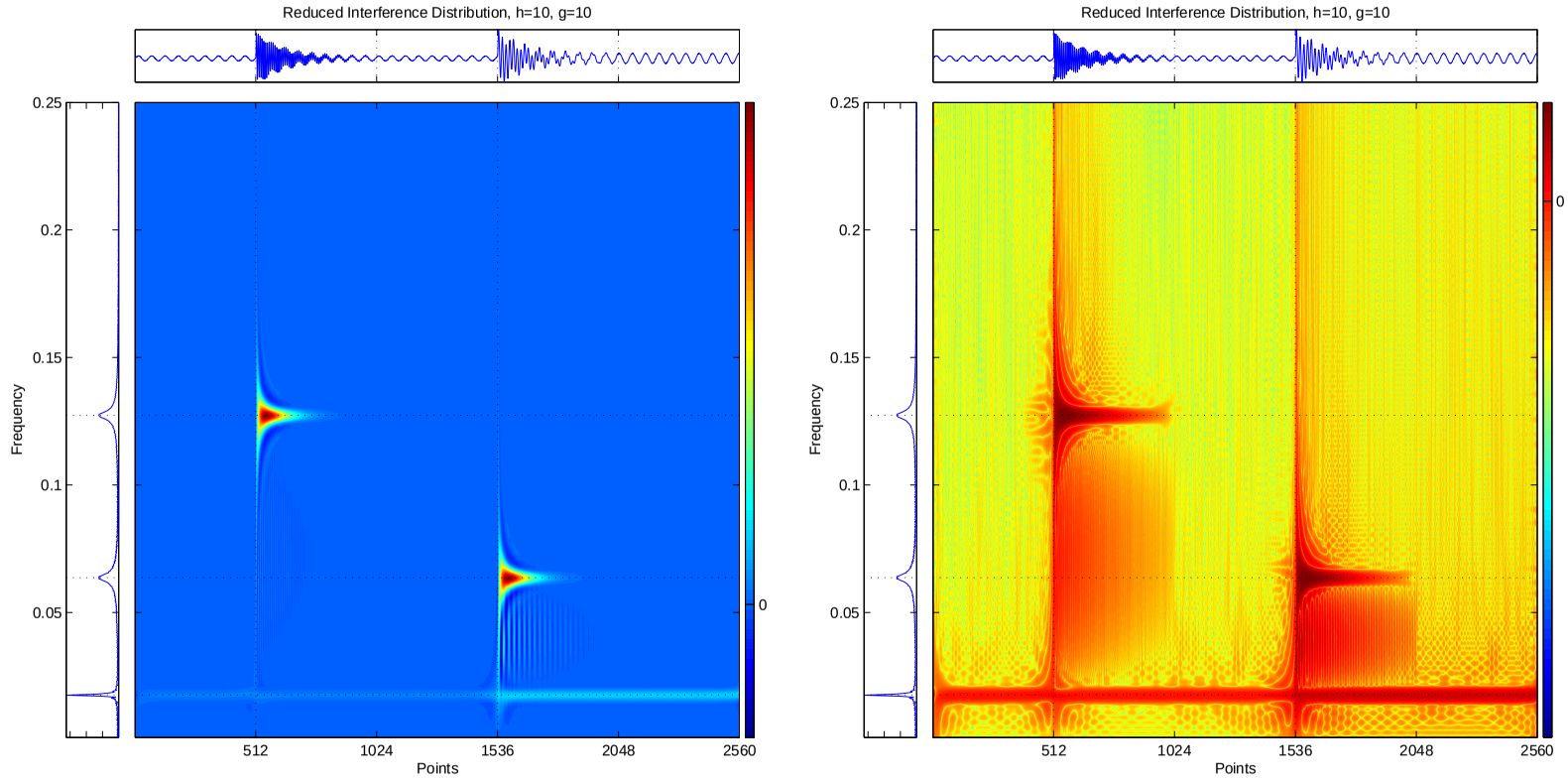

(a) Reduced Interference Distribution

(b) Reduced Interference Distribution, log10(abs())

Figure 2.18: Transient test signal, Reduced Interference Distribution, frequency window N/10, time window N/10. This is the shortest set of time and frequency windowing functions presented in this section. In general, window lengths need to be adjusted based on the character of the signal, though smoothing functions in the range of N/4 to N/10 are generally useful starting points.

2.12.7 Choi-Williams Distribution

The Choi-Williams Distribution (Figure 2.19), is similar to the RID, and is able to remove the cross-term interference nearly completely. The temporal behavior matches the RID, though the crisper temporal onset of the RID makes it better suited for general signal analysis.

2.12.8 Born-Jordan Distribution

The Born-Jordan Distribution (Figure 2.20) is another smoothed WVD, which removes many cross-terms while keeping the desired temporal and frequency resolution.

2.12.9 Zhao-Atlas-Marks Distribution

An additional smoothing term to the Born-Jordan Distribution results in the Zhao-Atlas-Marks (ZAM) Distribution (Figure 2.21). This smoothing adds interference terms, and the representation is more oscillatory than the RID for general signals.

2.12.10 Masked Wigner-Ville Methods

In an effort to reduce the effects of cross-term interference of the WVD, it is useful to investigate the character of the interference. As interference appears in the time-frequency plane midway between auto terms, a two dimensional (2-D) filter can be constructed that will preserve the expression of the auto terms and suppress the regions between the auto terms. Representations such as the spectrogram and scalogram have no interference terms, so they present themselves as logical candidates for a 2-D masking filter.

By overlaying these distributions with the WVD, the regions of low amplitude effectively minimize the expression of the oscillatory cross terms. Unfortunately, both the spectrogram and scalogram as 2-D masking filters impart their deficiencies to the final result, without completely eliminating the cross terms of the WVD. In particular, masking methods ultimately cannot remove cross-term interference that

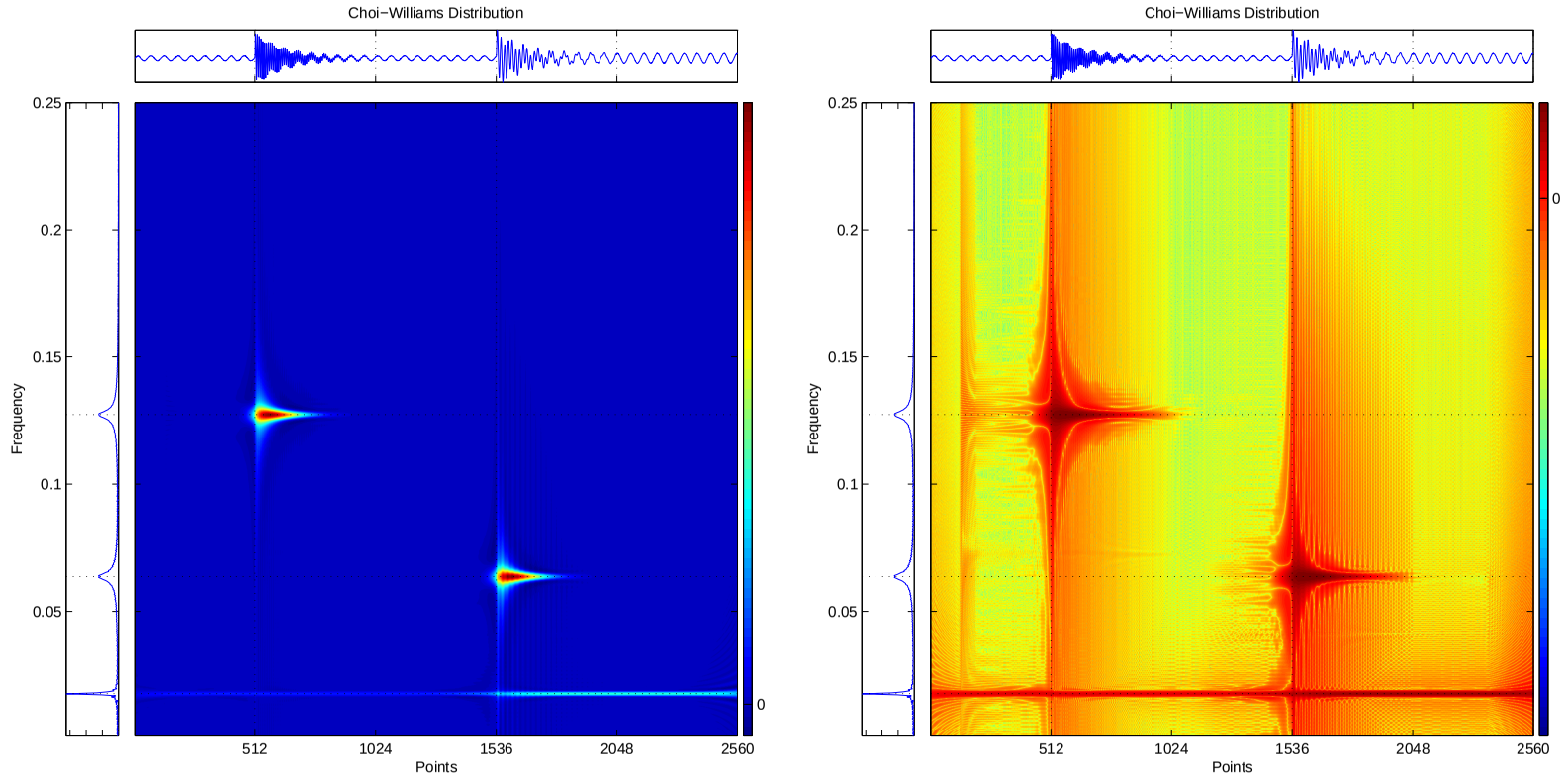

(a) Choi-Williams Distribution

(b) Choi-Williams Distribution, log10(abs())

Figure 2.19: Transient test signal, Choi-Williams Distribution. Temporal support is lost, as the transient signals appear before their instant of onset. Cross term interference, however, is cleanly removed when compared with the Reduced Interference Distribution (Section 2.12.6).

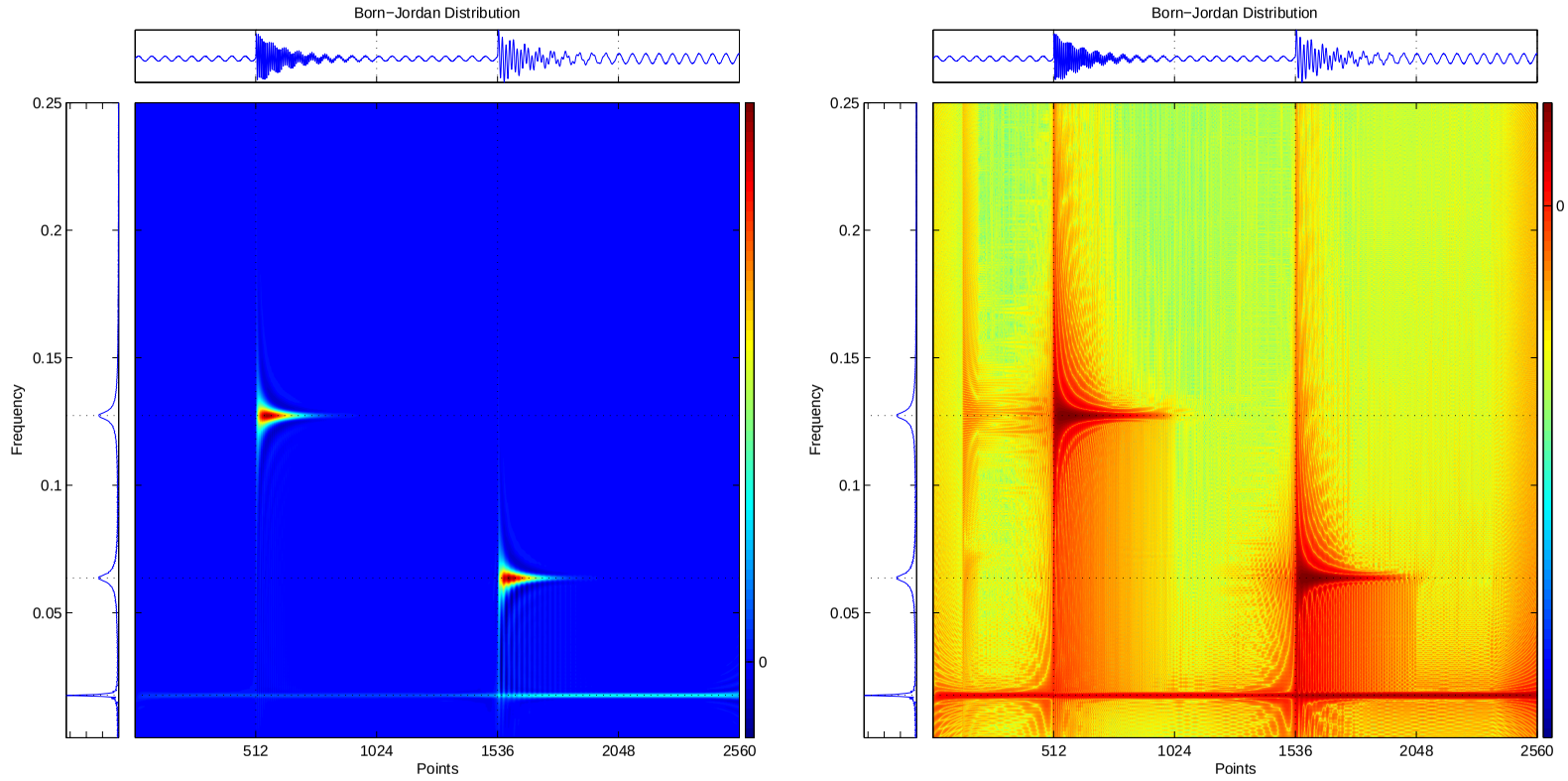

(a) Born-Jordan Distribution

(b) Born-Jordan Distribution, log10(abs())

Figure 2.20: Transient test signal, Born-Jordan Distribution. This representation is very similar to the Reduced Interference Distribution presented in Section 2.12.6. Interference between auto terms is preserved when there are multiple frequency components at each time instant, which is usually the case in signals of interest to seismology.

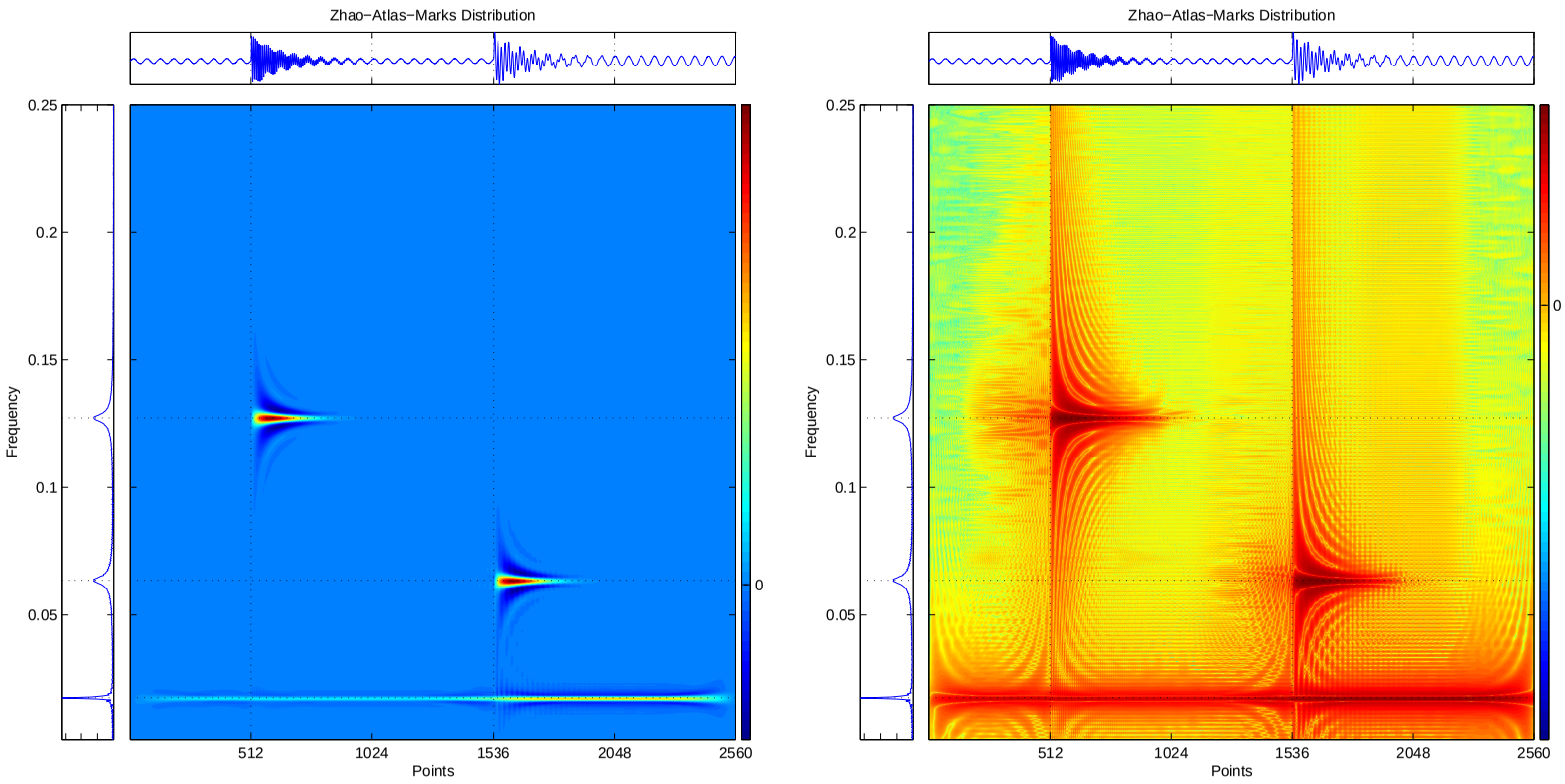

(a) Zhao-Atlas-Marks Distribution

(b) Zhao-Atlas-Marks Distribution, log10(abs())

Figure 2.21: Transient test signal, Zhao-Atlas-Marks Distribution. This distribution contains more oscillatory terms surrounding the auto terms than the Born-Jordan or Reduced Interference Distributions.

impinges on the expression of the auto terms, as they cannot distinguish between interference and the actual signal in these regions.

The scalogram overlay (scalogram as 2-D filter, Figure 2.22) is biased towards lower frequencies, and as such does not correctly identify the relative amplitudes of the two transient signals. The spectrogram overlay (spectrogram as 2-D filter) is presented for several window sizes (Figures 2.23 – 2.25), and the results are fairly accurate in the linear plot. The log plot, however, reveals considerable deviation from the ideal frequency representation for this signal. Interference in the time-frequency plane is merely reduced, not removed, and the onset of the transient components still arrive before their true onset in the time domain. These representations fail to accurately capture the evolution of the signal.

These two-dimensional overlay filtering methods have been investigated in the signal processing field as the "Masked WVD" (Boashash, 2003). The Masked WVD is exactly the use of the spectrogram as an overlay for the WVD. The consensus in the literature is that it is more effective to eliminate cross-term interference in the integral than to try to remove it with a filter/overlay afterwards. For a simple example of why this would be the case, one only need look at the time-frequency representations of a sample signal where the interference between the first transient term and the baseline signal impinges on the auto terms from the second transient term. There is no straightforward way to separate out the cross terms from the first transient and the baseline without damaging the character of the second transient term. The test signal approaches this case in the Morlet overlay plots (clearest in Figure 2.22(a) near point 1536 and frequency $.075Hz$), where the cross terms from the baseline signal and the high-frequency transient impinge on the intermediate transient and are correspondingly included even in the "wavelet-masked" version. In the seismic signals of interest to engineers, there are typically many closely spaced components of the signal, which makes the masked/overlay methods less effective than in a sample signal with clearly spaced frequency components.

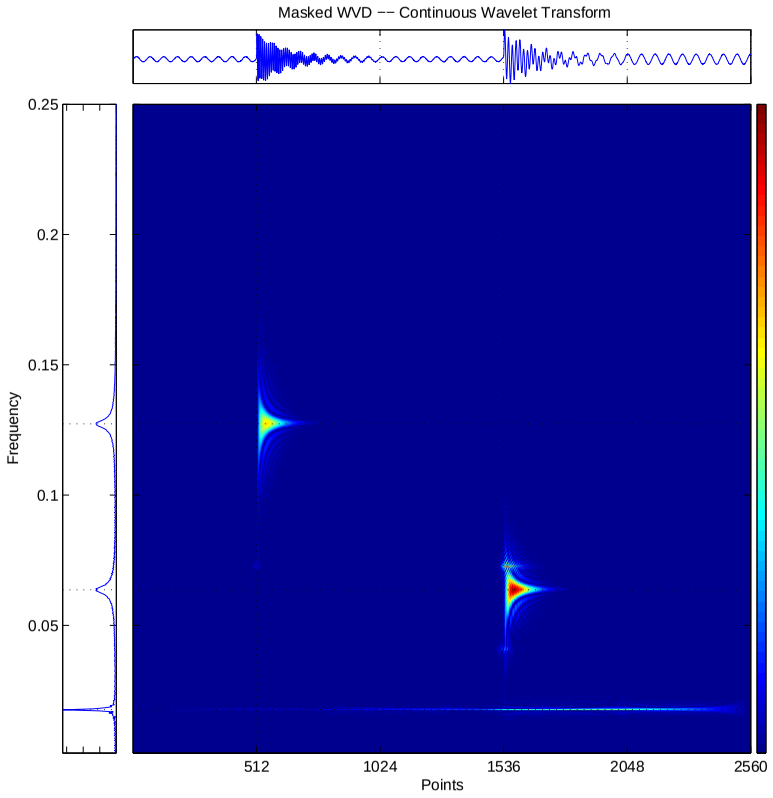

(a) Masked Wigner-Ville Distribution, CWT

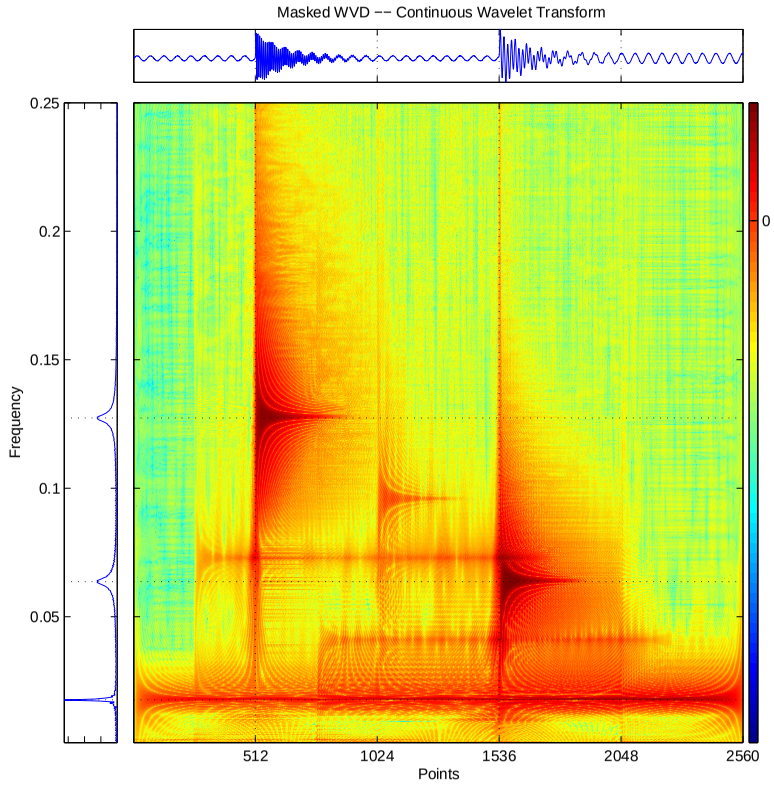

(b) Masked Wigner-Ville Distribution, CWT, log10(abs())

Figure 2.22: Transient test signal, Masked Wigner-Ville Distribution, Continuous Wavelet Transform (Morlet Wavelet). This does not remove the interference terms, as the WVD contains cross term oscillations that impinge on the region of auto terms. In general, other methods (such as the RID, CW, ZAM) reduce cross-term interference first, within the kernel of the transformation, leading to a better representation for a signal with many closely spaced frequencies.

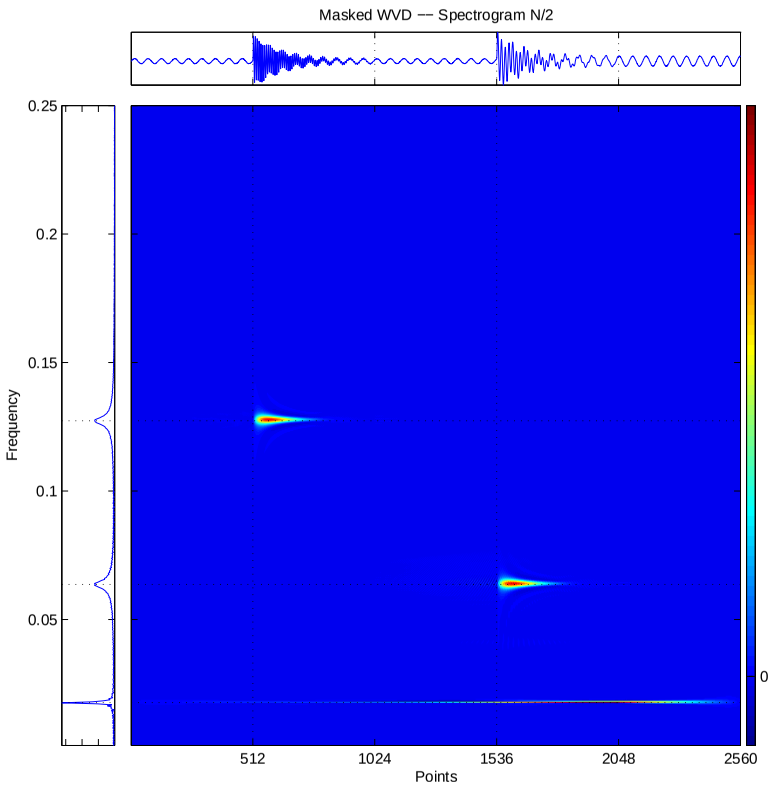

(a) Masked Wigner-Ville Distribution, Spectrogram N/2.

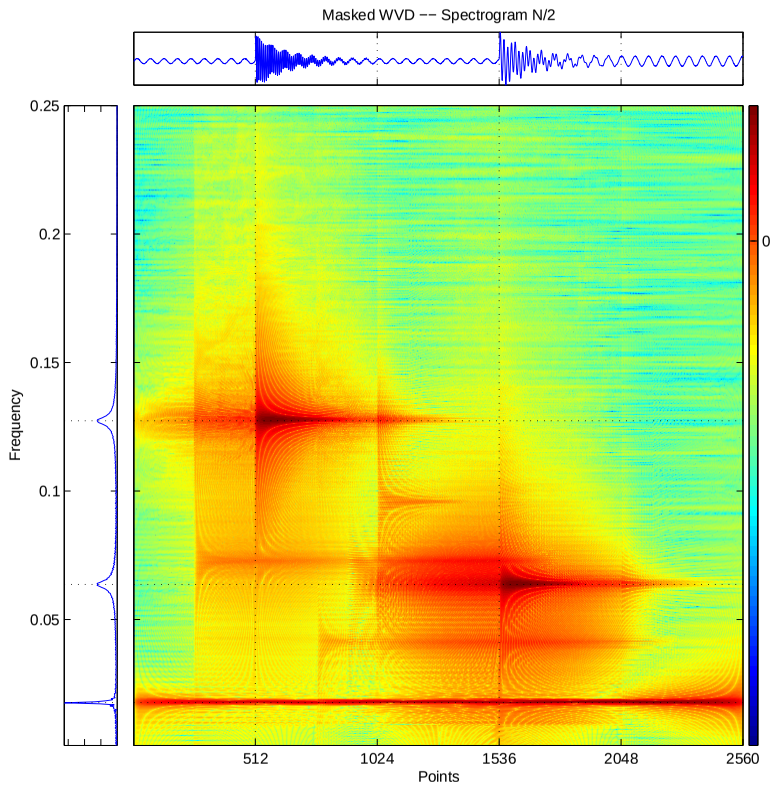

(b) Masked Wigner-Ville Distribution, Spectrogram N/2, log10(abs())

Figure 2.23: Transient test signal, Masked Wigner-Ville Distribution, Spectrogram N/2. This distribution has many of the characteristics desired from an ideal time-frequency representation. Using the spectrogram as a 2-D filter suppresses interference in the time-frequency plane in regions where there is little energy in the signal. The spectrogram is small but nonzero in the intermediate regions. Since the cross term interference of the WVD can be of large amplitude (in some cases larger than the auto terms), this method does not properly address the source of the interference, as seen in the plots of log amplitude. This representation preserves negative values.

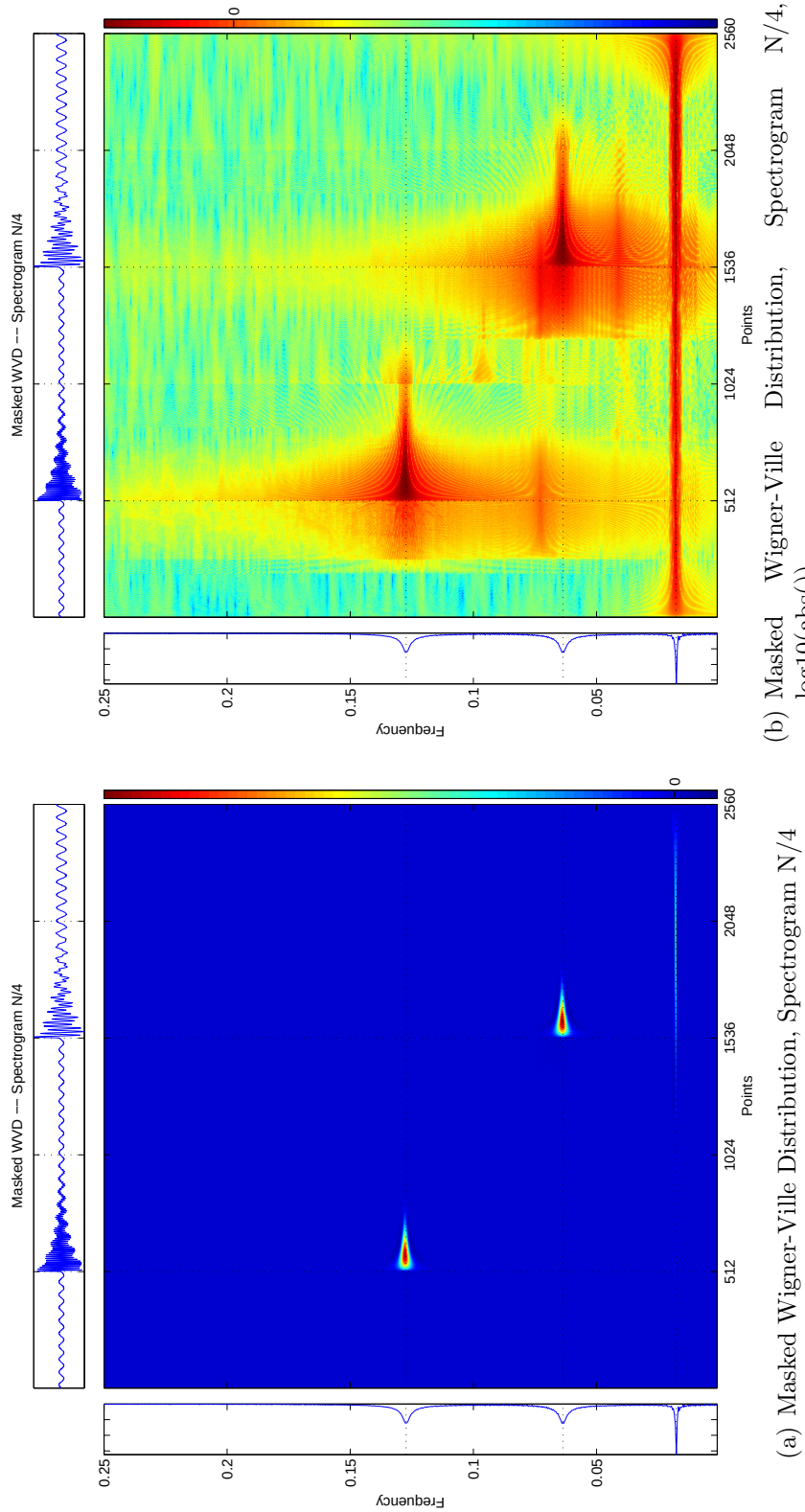

(a) Masked Wigner-Ville Distribution, Spectrogram N/4

(b) Masked Wigner-Ville Distribution, Spectrogram N/4, log10(abs())

Figure 2.24: Transient test signal, Masked Wigner-Ville Distribution, Spectrogram N/4, as in Figure 2.23.

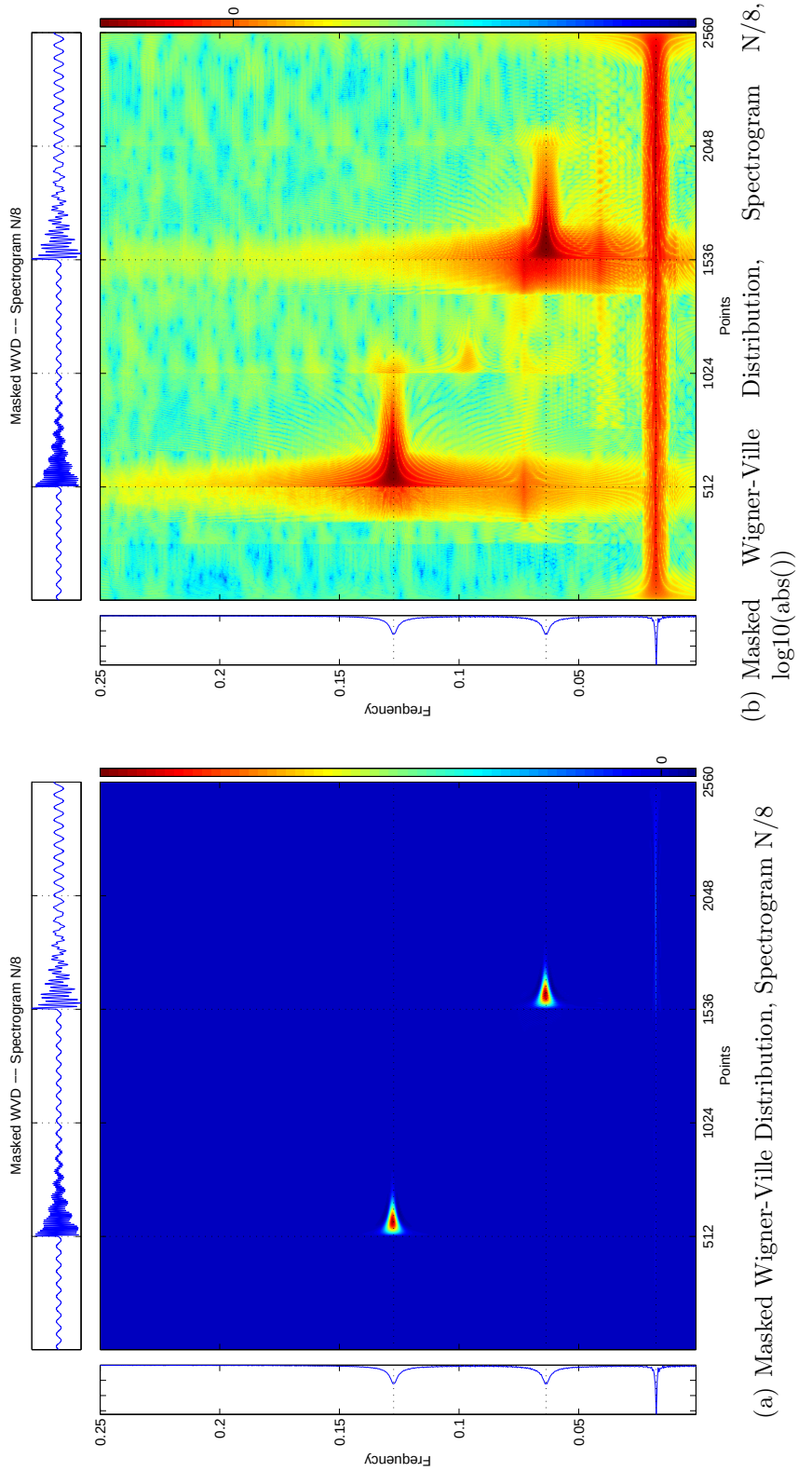

(a) Masked Wigner-Ville Distribution, Spectrogram N/8

(b) Masked Wigner-Ville Distribution, Spectrogram N/8, log10(abs())

Figure 2.25: Transient test signal, Masked Wigner-Ville Distribution, Spectrogram N/8, as in Figure 2.23.

2.12.11 Simple Masking Representation

The continuous wavelet transform (Sections 2.5 and 2.12.2) brings excellent temporal resolution across nearly the entire frequency range, and the spectrogram (Sections 2.4 and 2.12.1) method gives good temporal and frequency resolution. Combining them into a simple masking TFR provides an easy way to visually compare the results of other TFR methods. As it is composed of fundamental techniques that are more familiar to the engineering community, this example may help to illustrate the types of compromises necessary in creating a joint time-frequency representation.

This simple TFR has significant drawbacks: most obvious is the attenuation of higher frequency components. The scale/frequency transformation is an approximation, as the frequency content of a wavelet is somewhat diffuse and "leaks" across frequency ranges. Thus, the amplitudes of the two transient signals in the wavelet plot are different, while the area under the curve (energy integral) is approximately the same. (The higher frequency component is broader along the frequency axis, with a smaller peak; the lower frequency component is narrower along the frequency axis, with a higher peak.) When this is overlain with the spectrogram, the high-frequency transient signal is decreased relative to the medium-frequency transient – their amplitudes ought to be roughly the same given the character of the signal (c.f. the spectrogram plots of Section 2.12.1 and the Fourier Transform of the signal in Figure 2.4).

Figures 2.26 – 2.28 show Simple Masking TFR plots. The spectrograms are calculated using three different window lengths (N/2, N/4, and N/8), to again demonstrate the time-frequency resolution tradeoff inherent to the spectrogram method. The temporal accuracy of the CWT helps to attenuate the Spectrogram energy that was, non-physically, expressed before the temporal onset of the transient signals. The Spectrogram, in turn, helps to align the CWT more closely on the actual expressed frequencies of the signal. However, the shortcomings of both these methods are not removable by such simple methods. The CWT attenuation of high-frequency energy is a scaling that extends to the simple TFR, and the temporal lack of support for

the Spectrogram is strong enough that the CWT cannot completely suppress the expression of non-physical energy. The Gabor transform (Sections 2.6 and 2.12.3), as an ideally sampled spectrogram/scalogram representation, is more accurate than the simple masking representations.

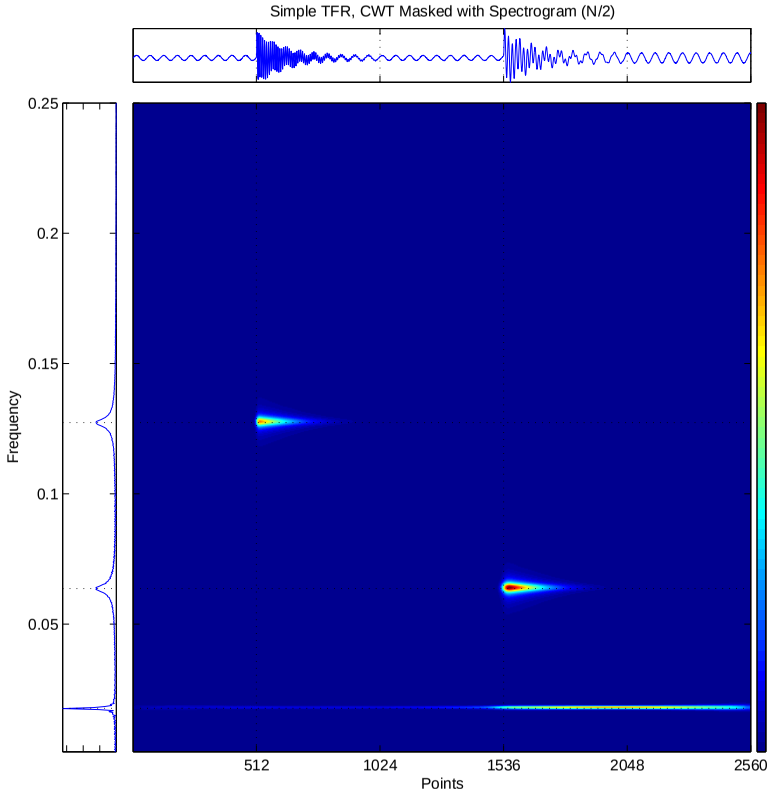

(a) Simple TFR, Scalogram and Spectrogram (N/2)

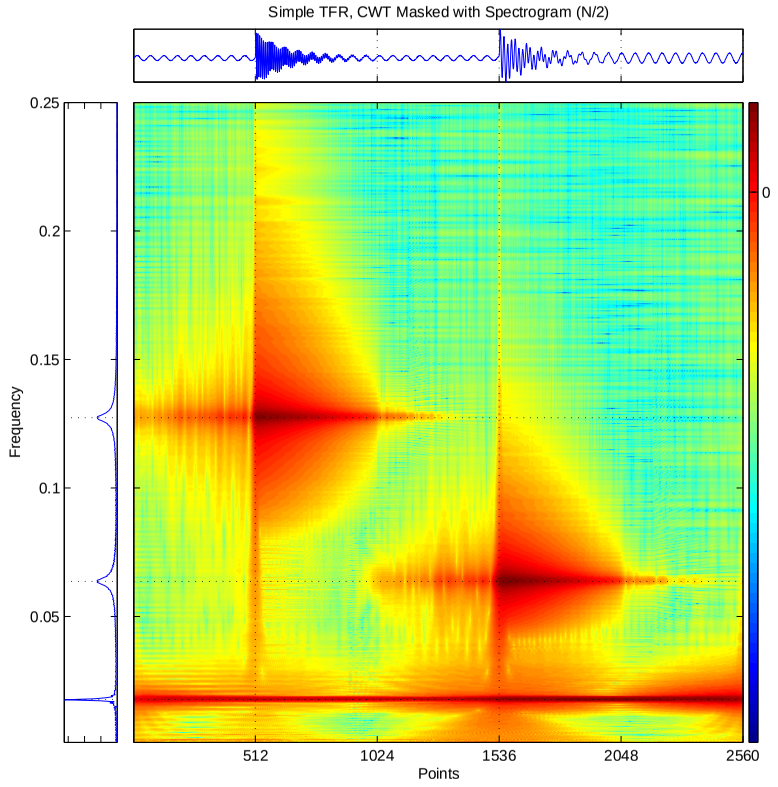

(b) Simple TFR, Scalogram and Spectrogram (N/2), log10(abs())

Figure 2.26: Transient test signal, Simple TFR, Scalogram and Spectrogram (N/2). Combining spectrogram and wavelet transform methods gives an estimate for the energy in the time-frequency plane. Each method has shortcomings and advantages, though these simple TFR methods are in general less useful than other established methods, and are presented here as an illustrative example only. In the linear plot, the temporal resolution seems suitable, though the amplitudes of the transient components are not equal. The logarithmic scaled plot shows more clearly the smearing along the time-axis.

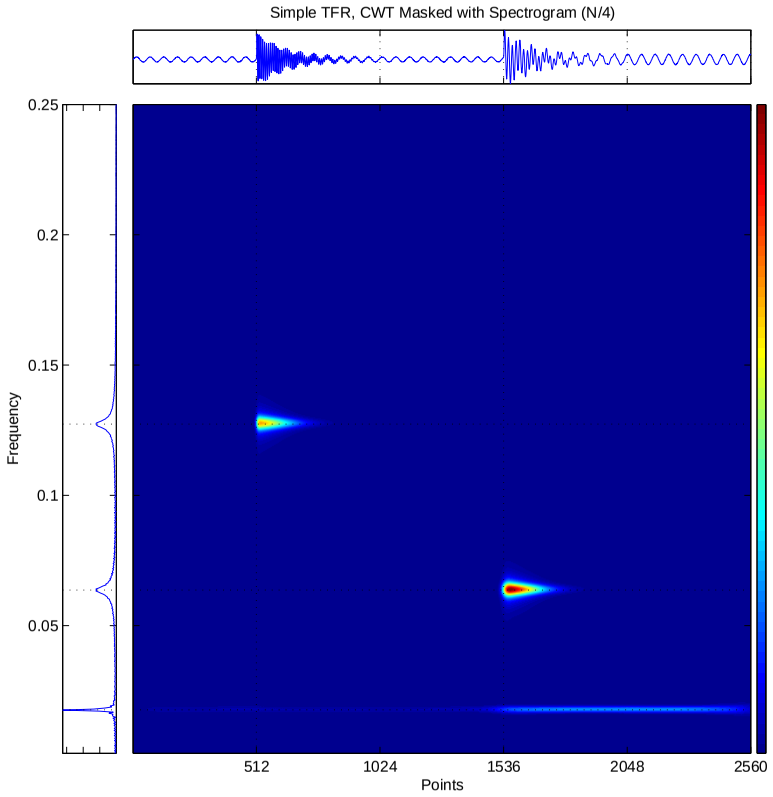

(a) Simple TFR, Scalogram and Spectrogram (N/4)

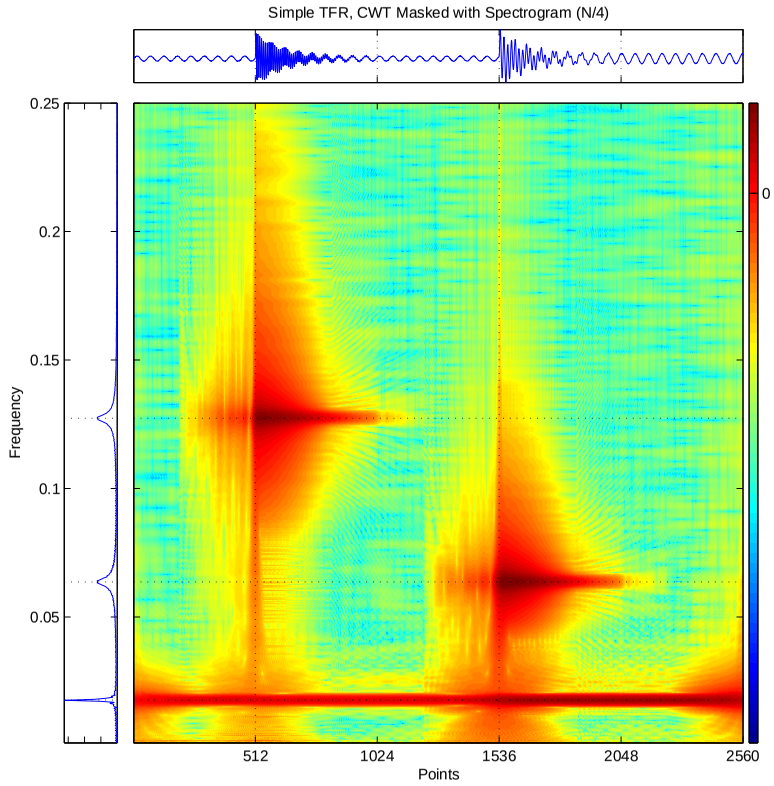

(b) Simple TFR, Scalogram and Spectrogram (N/4), log10(abs())

Figure 2.27: Transient test signal, Simple TFR, Scalogram and Spectrogram (N/4). As in Figure 2.26 for a finer spectrogram. A shorter window gives better temporal resolution, though there is still energy before the onset of the transient signals. Again, the wavelet method attenuates energy at high frequencies, so the transient terms do not have the same amplitudes.

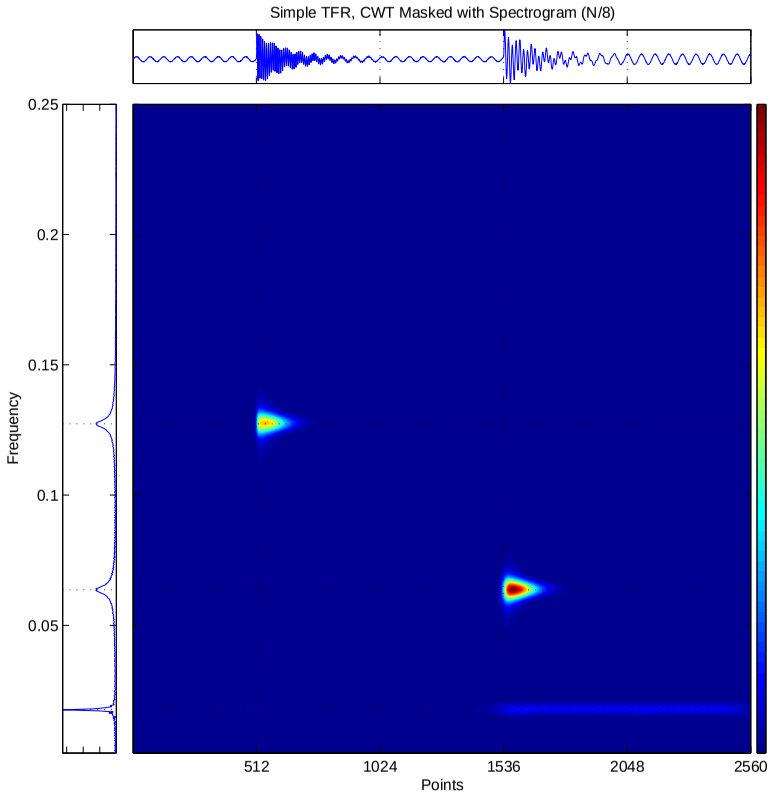

(a) Simple TFR, Scalogram and Spectrogram (N/8)

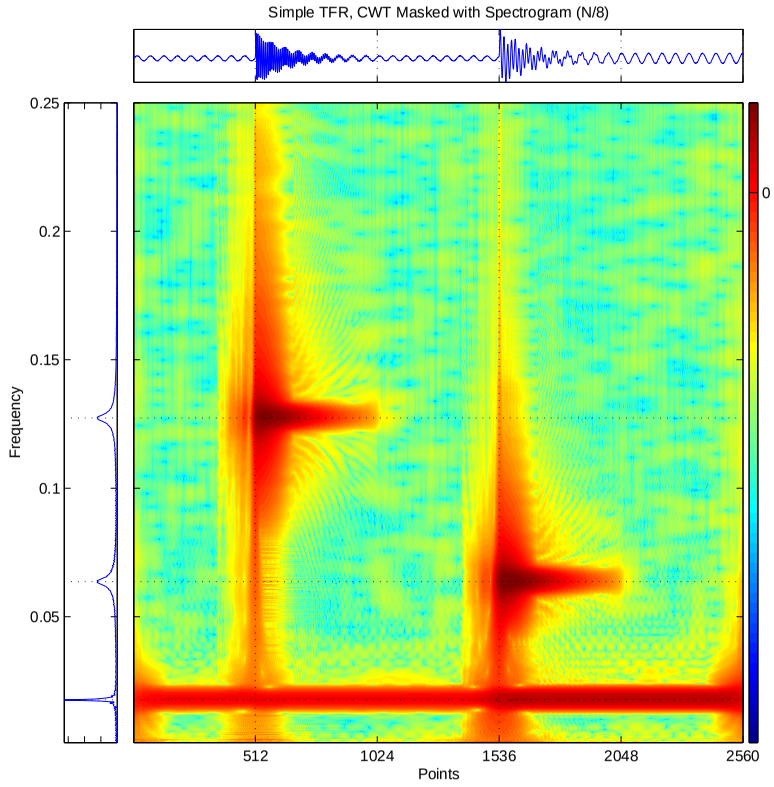

(b) Simple TFR, Scalogram and Spectrogram (N/8), log10(abs())

Figure 2.28: Transient test signal, Simple TFR, Scalogram and Spectrogram (N/8). As in Figure 2.26 for a finer spectrogram. At this level of spectrogram, the temporal resolution is more accurate, but still subject to uncertainty considerations. The Gabor transform, as an ideally sampled STFT (or alternately, as a linearly sampled wavelet filterbank) is in general the best linear time-frequency transform method, providing the best combination of time and frequency accuracy.

2.13 Further Examples

2.13.1 Chirp Function

Synthetic signals, with known frequency content, help to illustrate the representations created by the WVD. A chirp with linearly increasing frequency (Figure 2.29) is a useful example of a signal with changing frequency content. The WVD of this chirp, in Figure 2.30, identifies the instantaneous frequency of the original signal, though some interference is present. The interference is more clearly shown in the logarithmic plot of Figure 2.31.

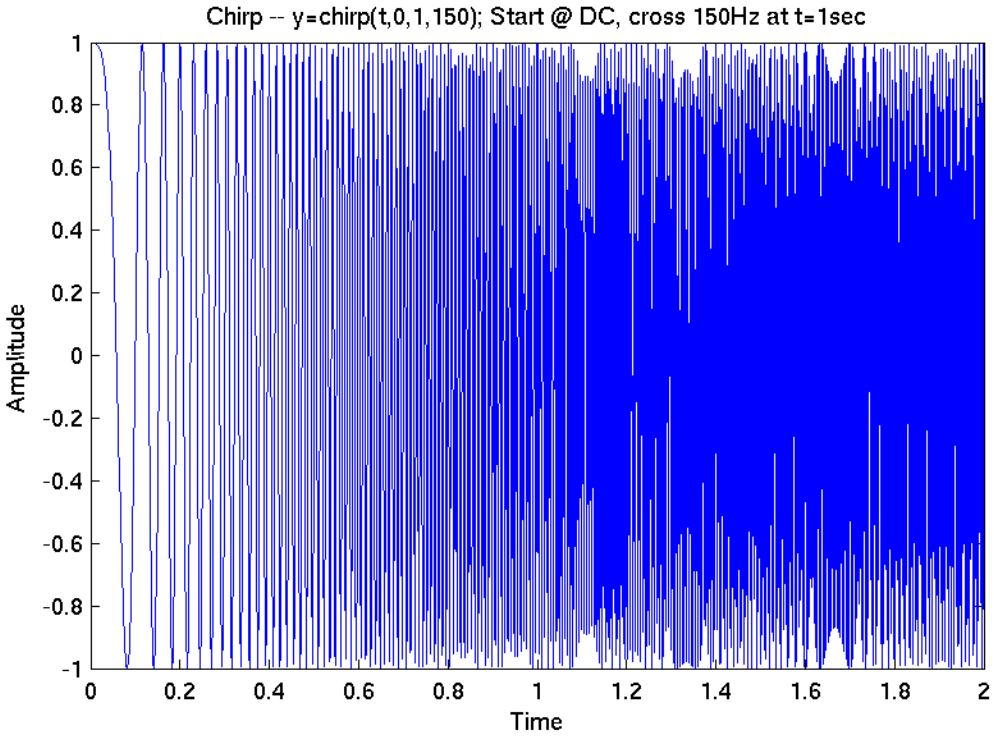

Figure 2.29: A chirp function with linearly increasing frequency content.

2.13.2 Double Chirp Function

The WVD has cross-term interference directly between locations of energy in the time-frequency plane. This interference is oscillatory in nature, and the Reduced

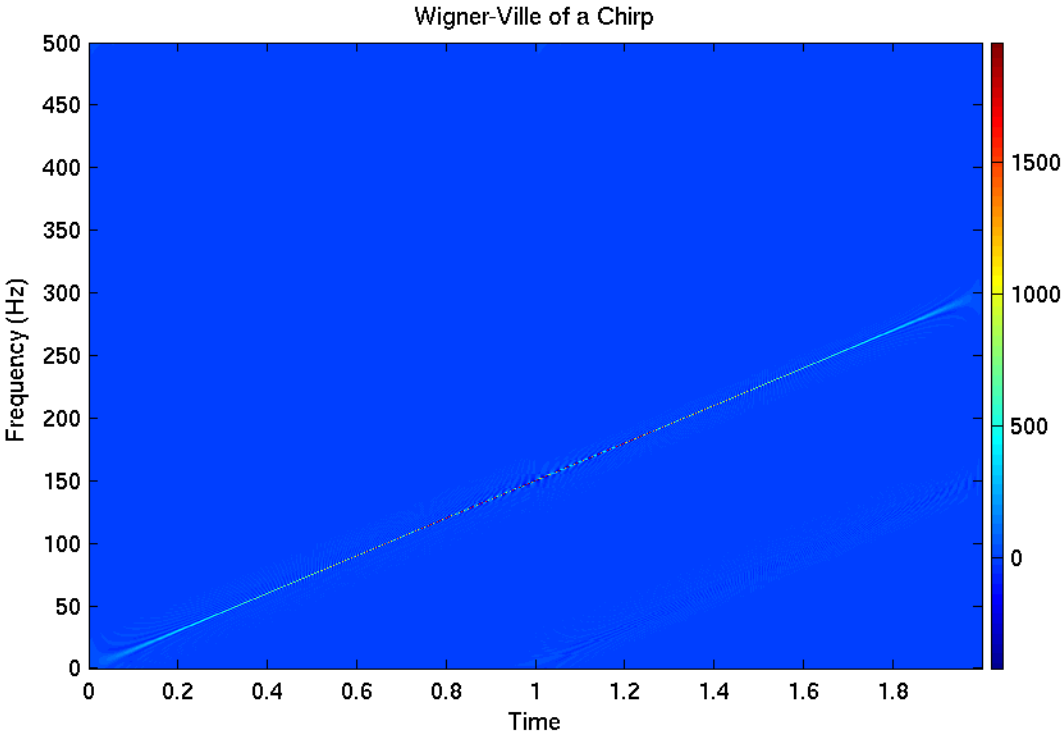

Figure 2.30: Wigner-Ville Distribution of Chirp Function. This is close to the actual instantaneous frequency content and represents intuitively the correct evolution of the frequency. Problems include a small amount of noise coming in underneath the signal (clearer in log plot) and also negative values along the line.

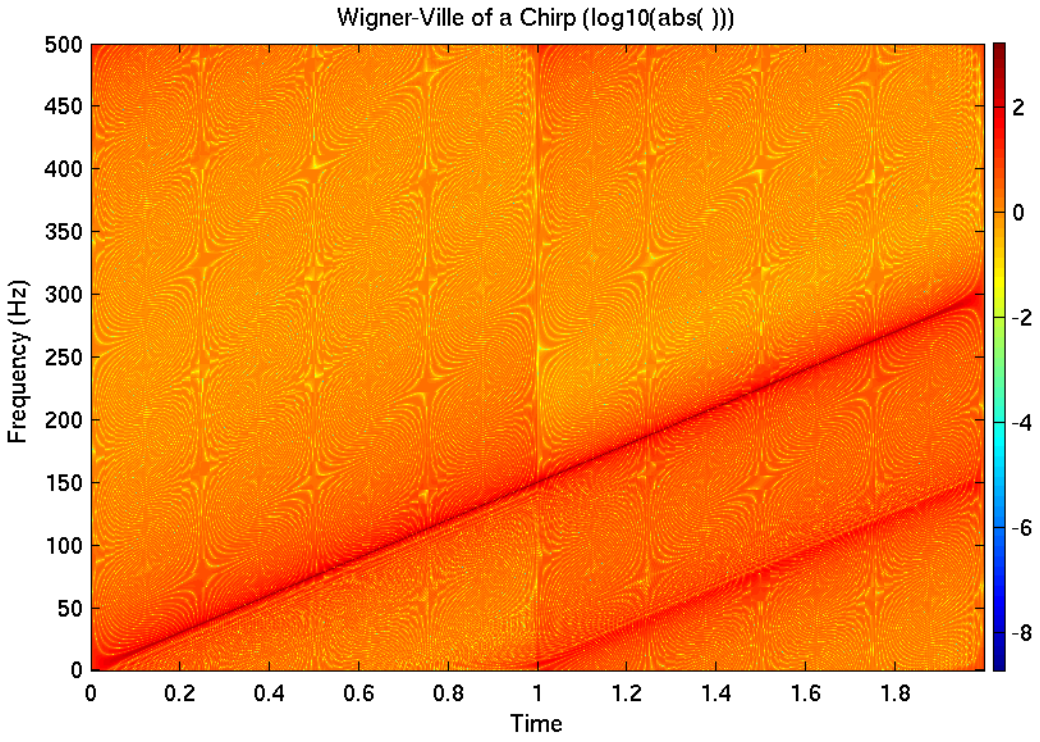

Figure 2.31: Wigner-Ville Distribution of Chirp Function, $(Log10(abs()))$. The interference terms are more apparent.

Interference Distribution (Section 2.9) aims to reduce the expression of the cross-terms relative to the auto-terms. A double chirp function, as in Figure 2.32, is an illustrative example. The frequency content of this signal is evolving with time: two

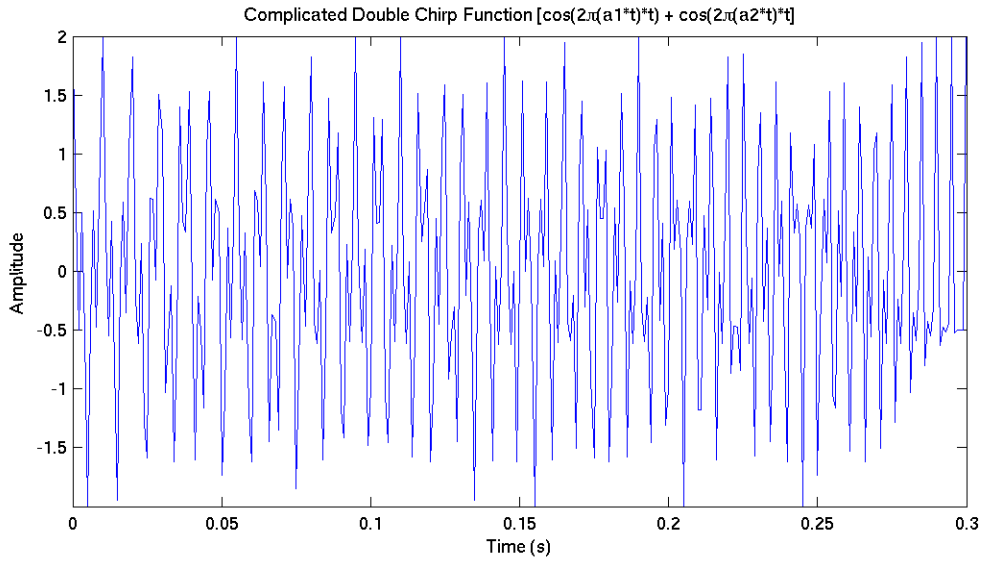

Figure 2.32: Double Chirp Function. This is a test function for identifying instantaneous frequency content of signals with changing frequencies. Sample Matlab script to generate this signal is available in Appendix C.

linear chirps separated in the time-frequency plane. The WVD is smoother than the spectrogram (Figure 2.33), with the shortcoming of interference terms that are not supported in time or frequency. The RID, however, has excellent resolution in time and frequency (Figures 2.34 and 2.35), without the large interference terms. The ability to resolve closely spaced signal components makes the RID suitable for many signal processing applications, including tracking evolving frequency content of a nonlinear system.

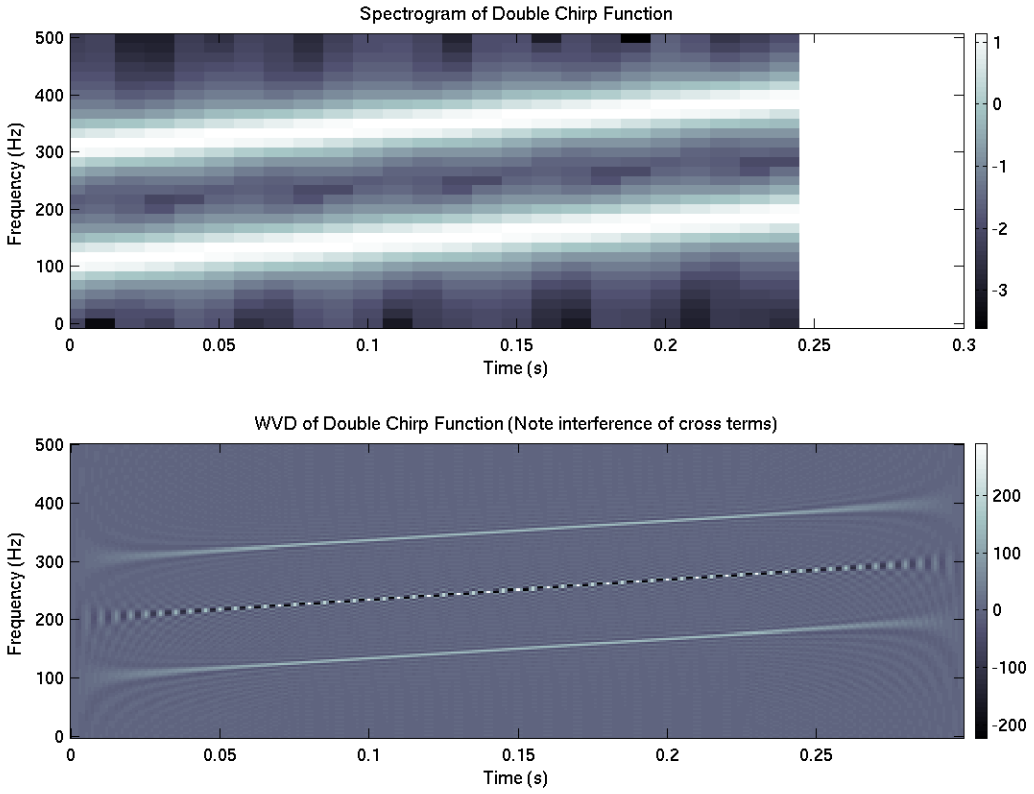

Figure 2.33: Spectrogram and WVD of double chirp function. Neither representation is accurate – the spectrogram is blocky, and the WVD has interference terms between the two signals. (Note the oscillatory nature of the interference terms.)

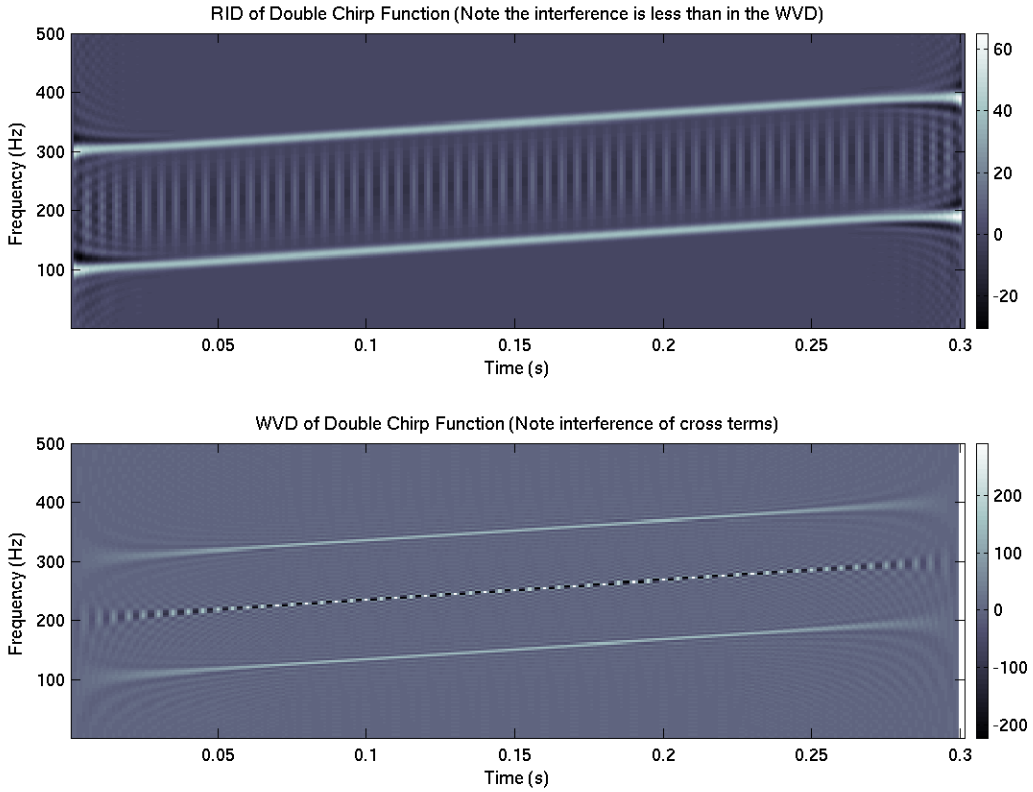

Figure 2.34: RID and WVD of double chirp function. The RID has a much clearer representation of the frequency content – very close to the known values at each instant. The interference is magnitudes smaller (clearer to see in the 3-D plots of Figure 2.35). Vertical striations remaining in the RID are small in amplitude and can be further reduced by refining the smoothing function.

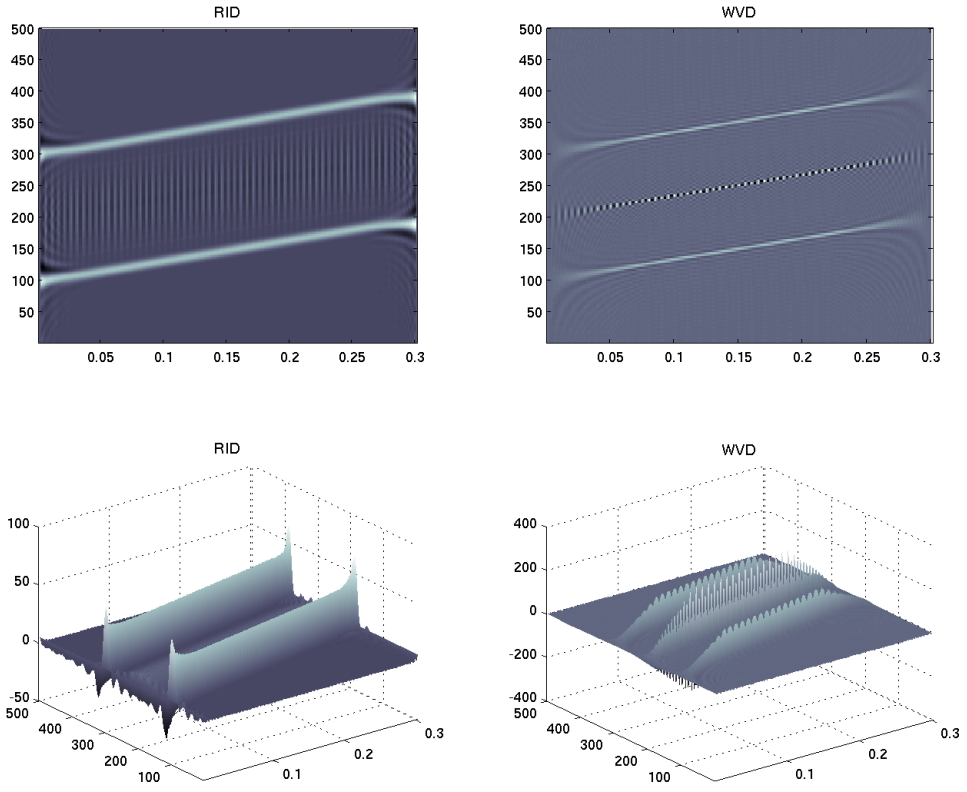

Figure 2.35: Double chirp function, 2-D and 3-D Plots of RID and WVD. These show the improvements of using the RID over the WVD. The 3-D plot presents more clearly the difference in relative amplitude of the cross term interference.

2.13.3 Millikan Library: 2005 Parkfield Earthquake

Time-Frequency Representations are an invaluable tool for investigating the evolving frequency content of a nonlinear system. As there is significant nonlinearity in the response of Caltech's Millikan Library (nonlinear-elastic and possibly plastic behavior), analysis of building records was the motivation for the time-frequency analysis techniques investigated in this thesis. For a sample time series I have selected an earthquake record from Caltech's Millikan Library. This building has nonlinear behavior for moderate levels of excitation (Clinton et al., 2006; Bradford et al., 2004) and the apparent natural frequency temporarily changes by nearly 10% during the Parkfield Event of 16 June 2005. There was no permanent change in the dynamic properties of Millikan Library from this event. As in the earlier synthetic signals, there is evolving frequency content. However, this signal has a very different energy distribution, with rapidly changing frequency content across a short timespan. Without clear separation of frequency components, time-frequency representations become more difficult to interpret, particularly with cross-term interference from the Wigner-Ville distribution and related distributions.

Figures 2.36 through 2.38 show continuous spectrograms for different windowing levels, and Figure 2.39 presents the continuous wavelet transform for comparison. The spectrogram and wavelet methods both have behavior that is less than ideal: the spectrogram smears information along the time and frequency axes, and the wavelet transform is very diffuse along the frequency axis. Figure 2.40 is the Wigner-Ville Distribution for the event (which is complicated by strong cross-term interference), and Figure 2.41 is the smoothed pseudo-Wigner-Ville Distribution, which is one technique for reducing the effects of cross-term interference in the WVD. Figure 2.42 presents a Reduced Interference Distribution, which has nearly ideal resolution in the time-frequency plane. The Wigner-Ville Distribution (and refinements such as the SPWVD and the RID) have crisp resolution in the time-frequency plane, and as such they are well suited to the analysis of records from buildings under earthquake excitation.

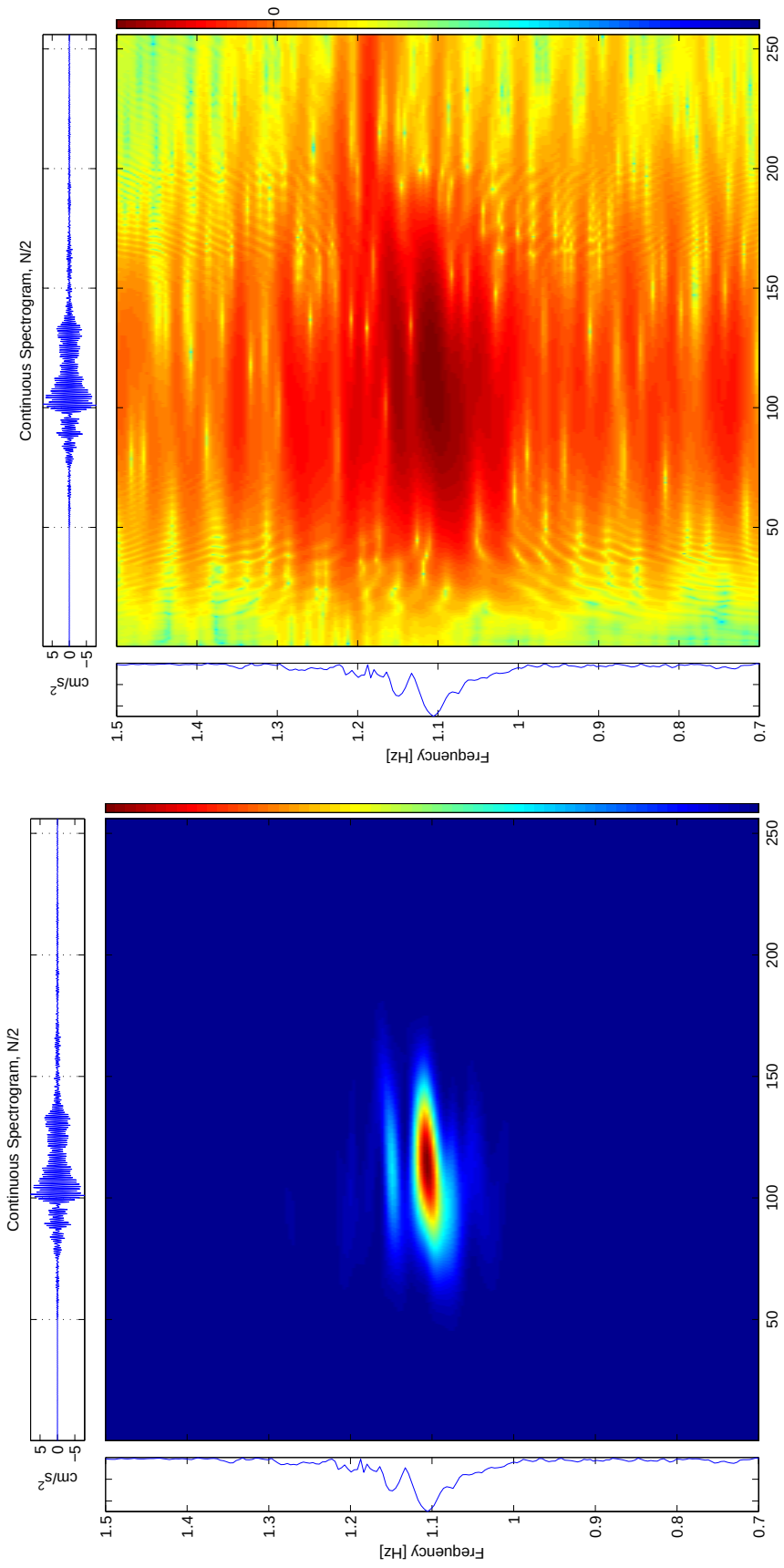

(a) Continuous Spectrogram, N/2

(b) Continuous Spectrogram, window of N/2, log10(abs())

Figure 2.36: Continuous Spectrogram, 2005 Parkfield Earthquake, Millikan Library record. Window of length N/2. For a longer window, information is smeared across the entire time axis. Energy shows up well before the onset of shaking at $t = 50$.

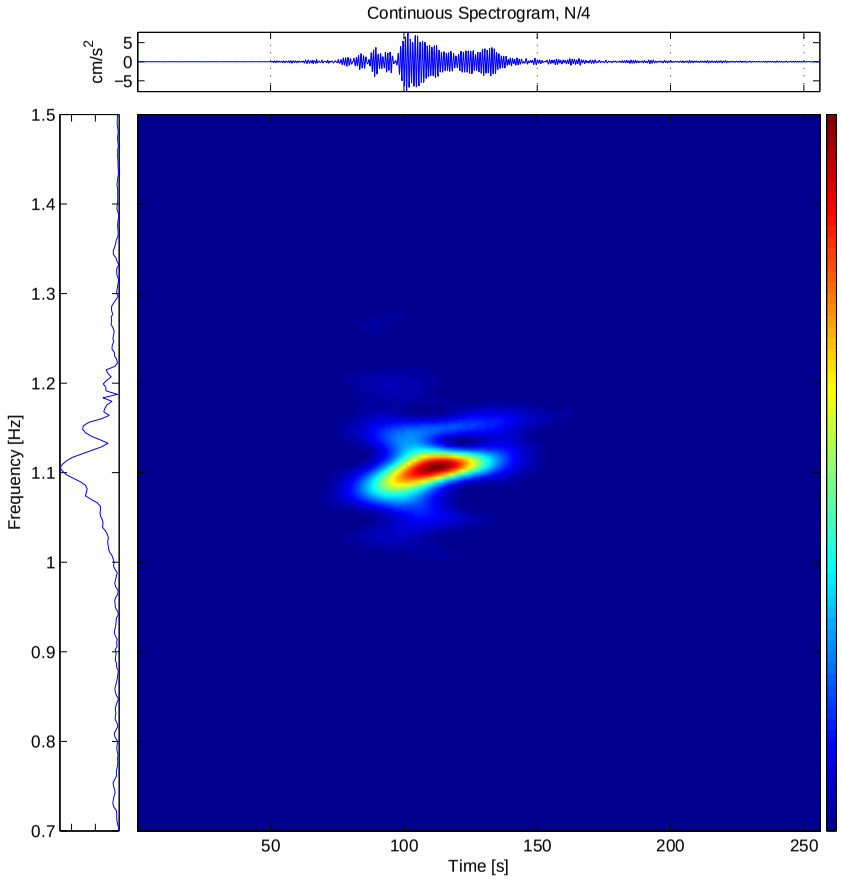

(a) Continuous Spectrogram, window of N/4

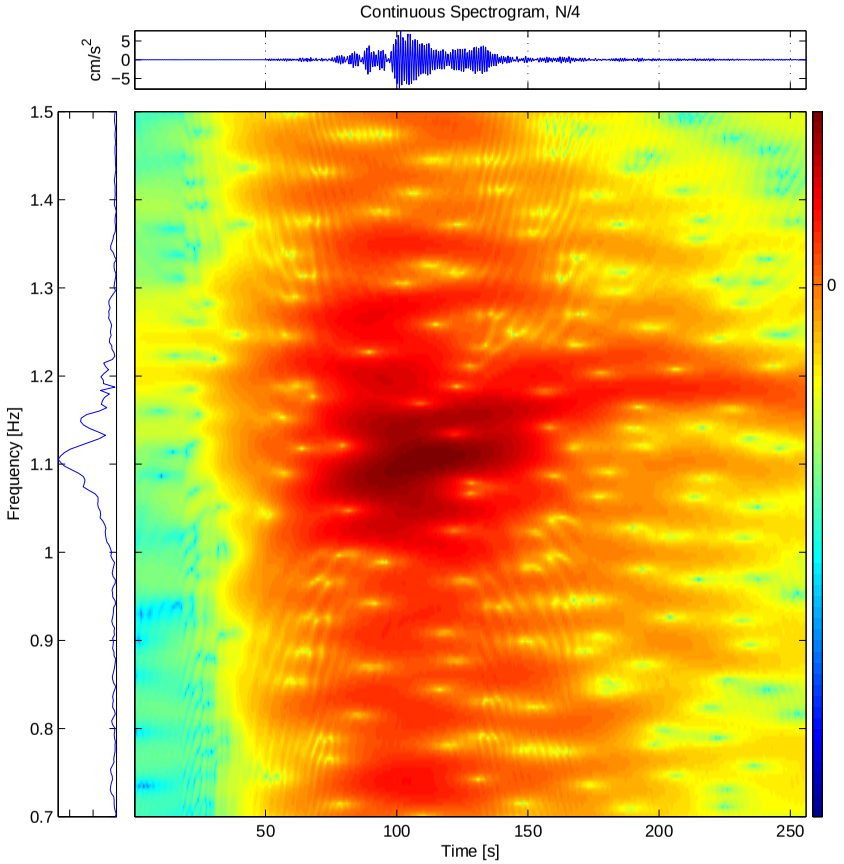

(b) Continuous Spectrogram, window of N/4, log10(abs())

Figure 2.37: Continuous Spectrogram, 2005 Parkfield Earthquake, Millikan Library record. As in Figure 2.36, with a window of length N/4. There is still energy appearing before the onset of shaking, but the shorter temporal window improves the representation.

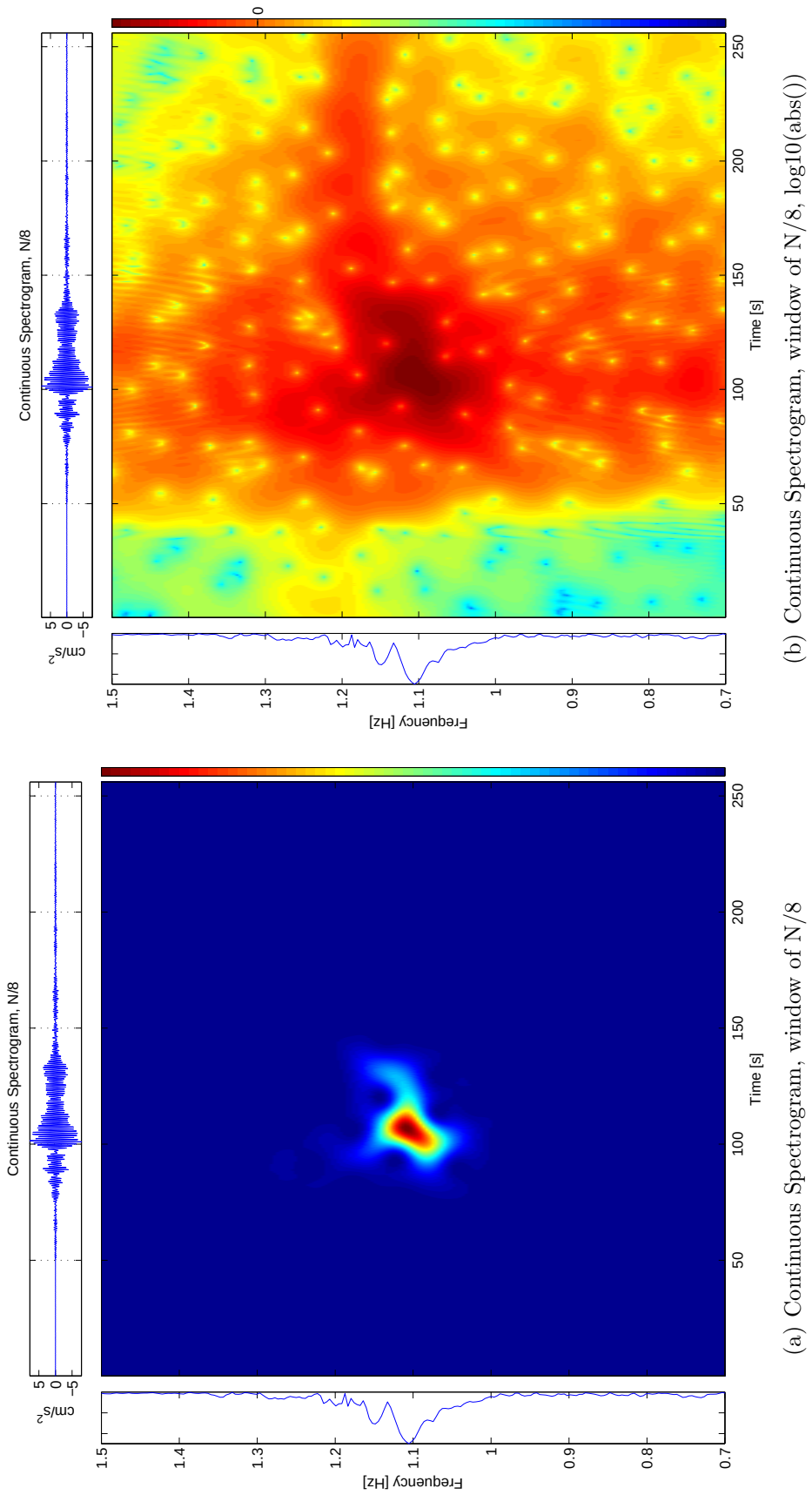

(a) Continuous Spectrogram, window of N/8

(b) Continuous Spectrogram, window of N/8, log10(abs())

Figure 2.38: Continuous Spectrogram, 2005 Parkfield Earthquake, Millikan Library record. As in Figure 2.36, window of length N/8. The onset of shaking at $t = 50$ is better indicated in the log plot – for a short window, the temporal resolution is increased at the expense of frequency resolution.

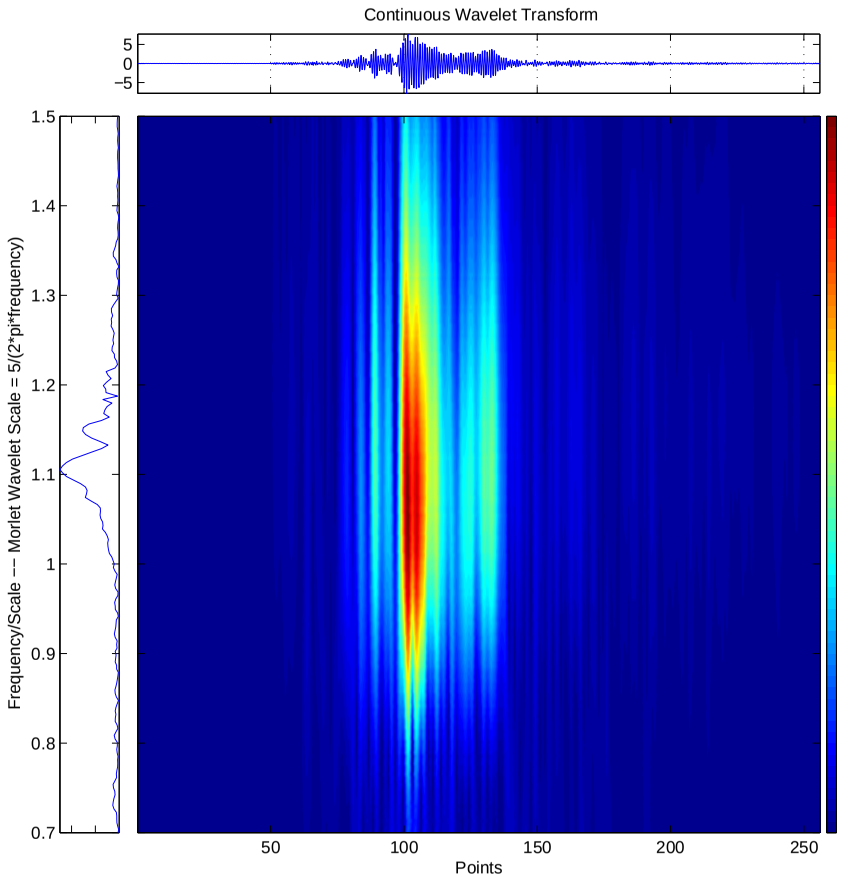

(a) Continuous Wavelet Transform

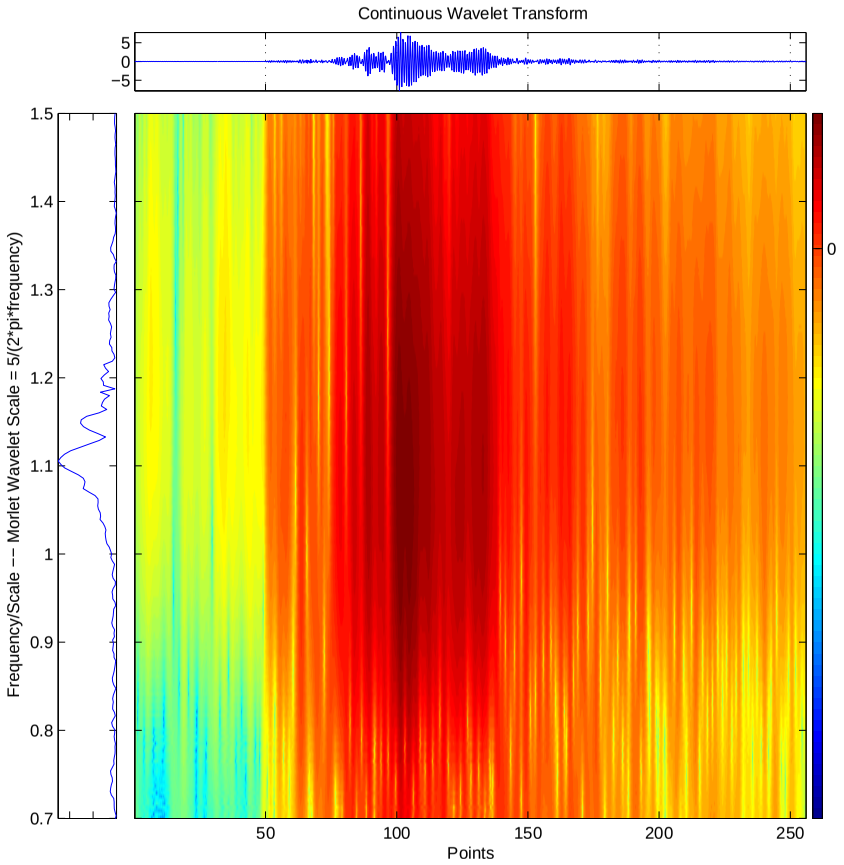

(b) Continuous Wavelet Transform, log10(abs())

Figure 2.39: 2005 Parkfield Earthquake, Millikan Library record. Continuous Wavelet Transform. Wavelet methods are more diffuse than the spectrogram methods, and it is very difficult to interpret the evolving frequency content of this signal. However, the onset of shaking at $t = 50$ is crisply indicated in the log plot, and it would be possible to estimate the peak frequency at each instant using this method.

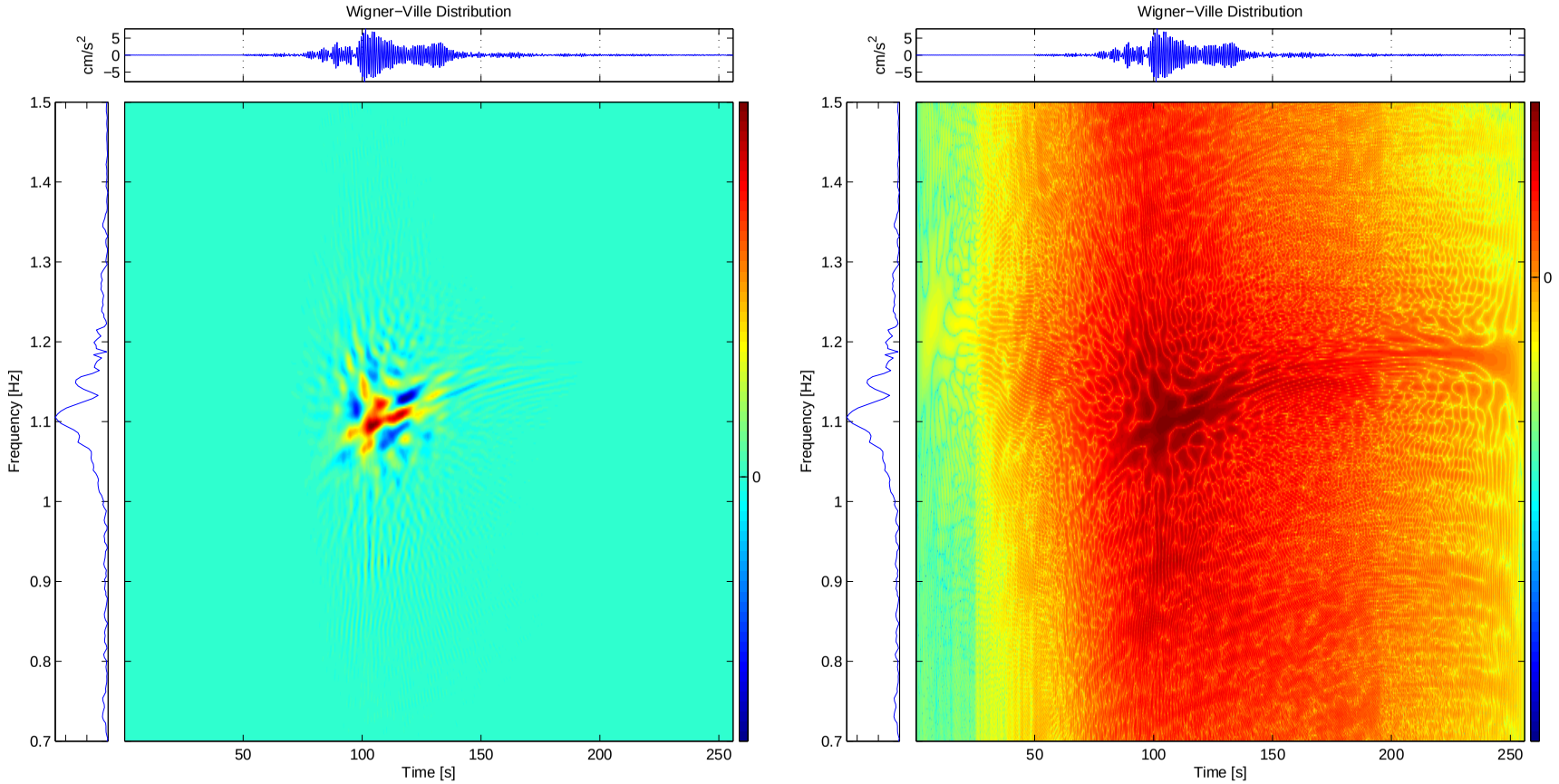

(a) Wigner-Ville Distribution

(b) Wigner-Ville Distribution, log10(abs())

Figure 2.40: 2005 Parkfield Earthquake, Millikan Library record. Wigner-Ville Distribution. Large-amplitude cross-terms complicate the interpretation of this distribution. The SPWVD (Figure 2.41) and RID (Figure 2.42) are refinements to the WVD.

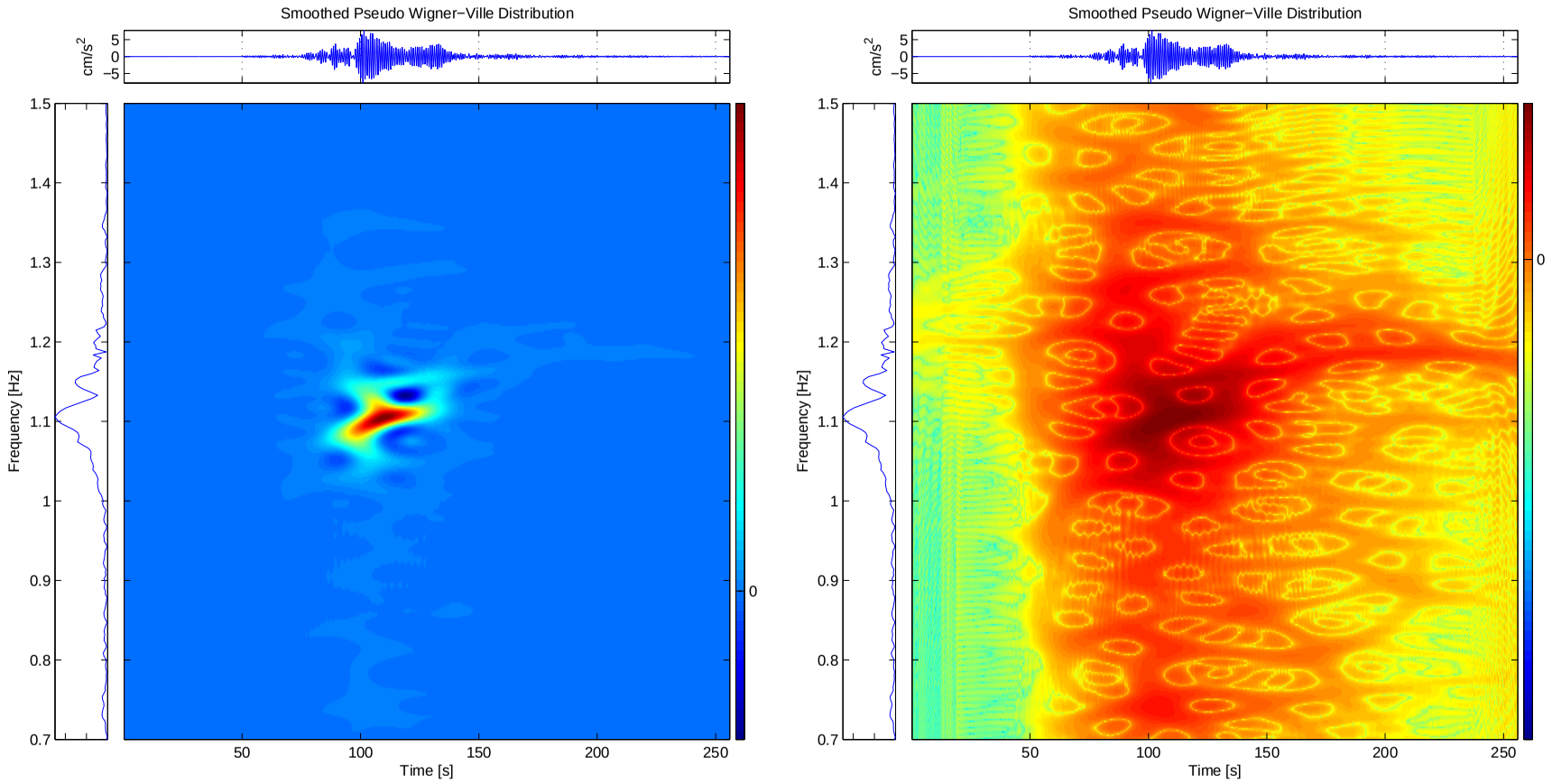

(a) Smoothed Pseudo Wigner-Ville Distribution

(b) Smoothed Pseudo Wigner-Ville Distribution, log10(abs())

Figure 2.41: 2005 Parkfield Earthquake, Millikan Library record. Smoothed Pseudo Wigner-Ville Distribution. The SPWVD is similar in character to the spectrogram of Figure 2.38. Smoothing the WVD to obtain the SPWVD reduces the expression of interference terms, but this smoothing also decreases the resolution in the time-frequency plane.

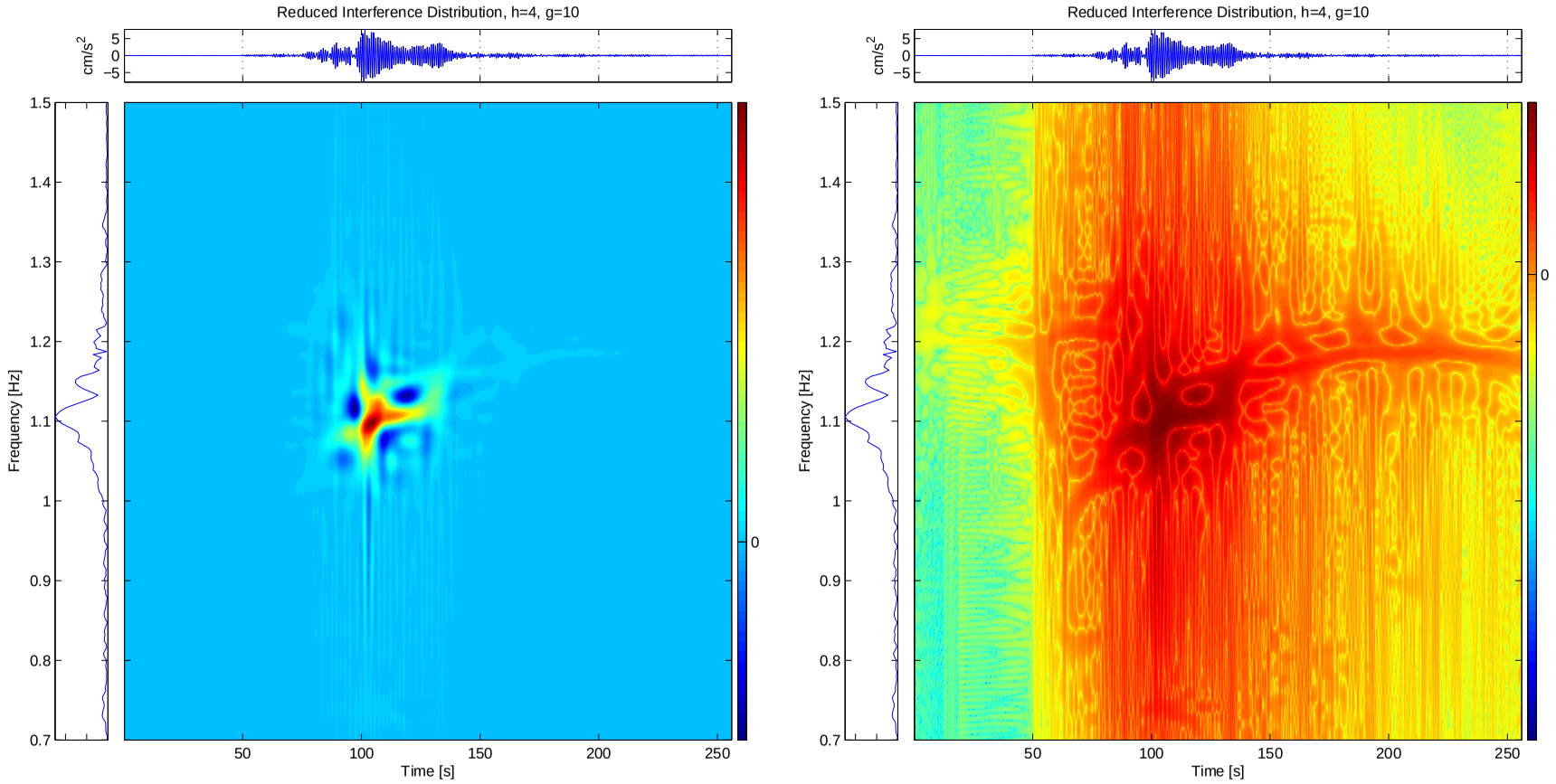

(a) Reduced Interference Distribution

(b) Reduced Interference Distribution, log10(abs())

Figure 2.42: 2005 Parkfield Earthquake, Millikan Library record. Reduced Interference Distribution. The RID is not entirely positive and still suffers from cross-term interference. But (pseudo-)energy is nearly perfectly located in the time-frequency plane, and the RID is in general a good approximation to the instantaneous frequency content of a signal. The onset of shaking is clearly indicated at $t = 50$.

In Section 2.3, I presented a brief description of the "marginal conditions," a mathematical characterization for the extent of energy in the time-frequency plane. The Wigner-Ville Distribution, though it contains oscillatory interference and large negative values, satisfies the marginal conditions as seen graphically in Figures 2.43 and 2.44. Summing across the frequency axis (the frequency integral of the time-frequency plane) gives the squared envelope of the original time series, and summing across the time axis (the time integral of the time-frequency plane) gives the squared Fourier Transform of the original signal. The oscillatory terms impart no *net* negative values when integrated along the time or frequency axis. The marginal conditions are satisfied in part because the interference terms in the WVD are highly oscillatory – large negative values tend to appear closely spaced with large positive values, such that if they are summed horizontally or vertically they add to zero. This justifies smoothing of the WVD as in the SPWVD and RID, where some limited smoothing of the WVD reduces the expression of interference terms.

Figure 2.43 shows the WVD for the Parkfield event, along with the plots graphically illustrating the marginal conditions. At the top of the figure is the original time series, and to the right is the Fourier Transform of the record. Along the left side of the plot are the squared Fourier Transform and the time integral of the WVD. At the bottom of the plot are the frequency integral of the WVD and the squared time series. The integrals and the squared Fourier Transform / Amplitude are presented separately in Figure 2.44, plotted on the same axis to confirm that the WVD satisfies the marginal conditions for this record.

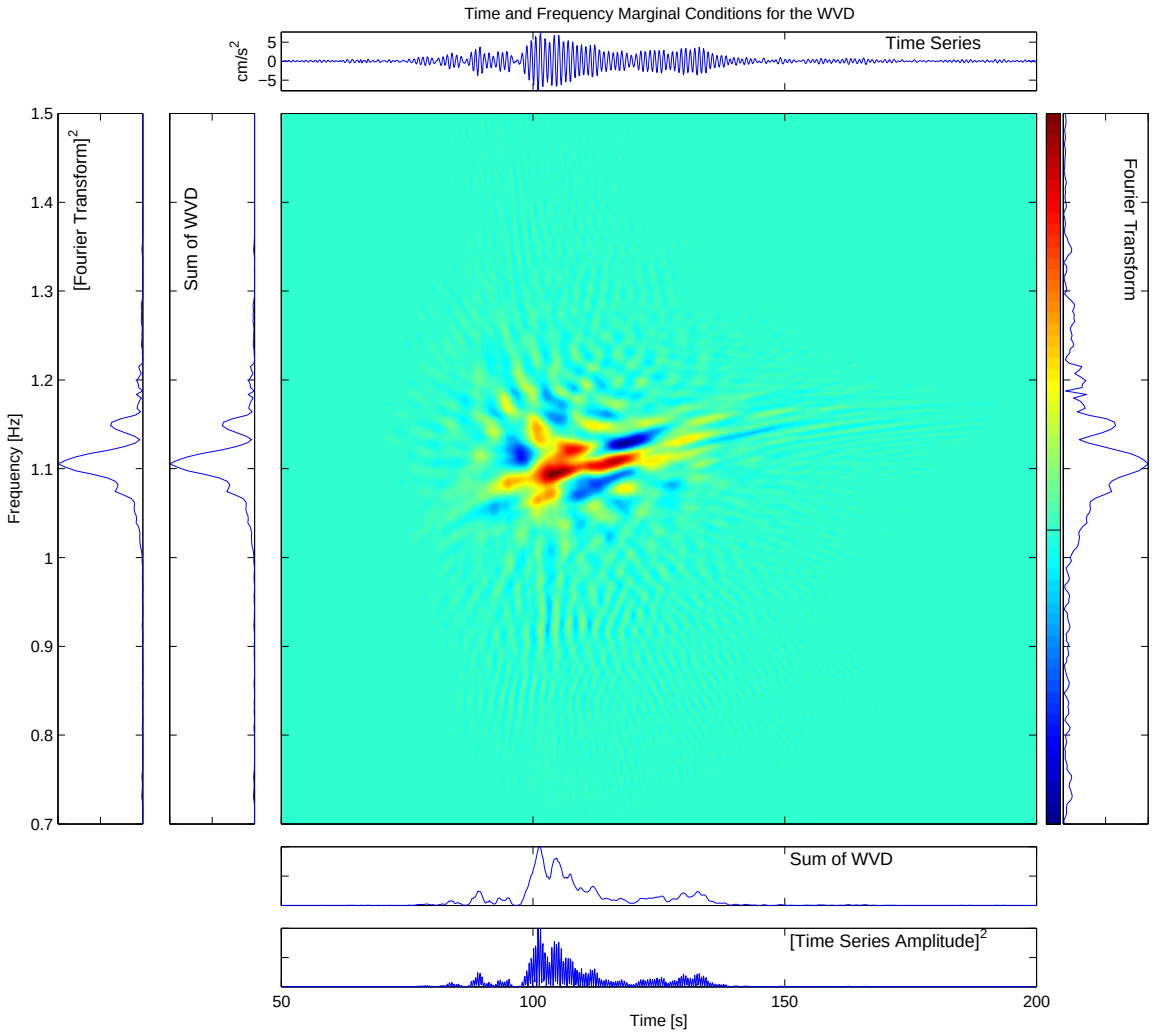

Figure 2.43: WVD Marginal Conditions Example. 2005 Parkfield Earthquake at Millikan Library. This plot illustrates the process of obtaining the time and frequency marginals for a TFR. Integrating across the time axis (horizontal sum) gives the amplitude of the squared Fourier Transform, while integrating across the frequency axis (vertical sum) gives the amplitude squared of the original signal. (Section 2.3.) The negative values in the WVD are oscillatory such that they perfectly cancel out when summed horizontally or vertically and impose no *net* negative energy on the TFR. This property helps to justify the smoothing of the WVD in the RID and other methods, as a local average will tend to remove the highly oscillatory interference terms. Figure 2.44 shows a detailed plot of the time and frequency summations.

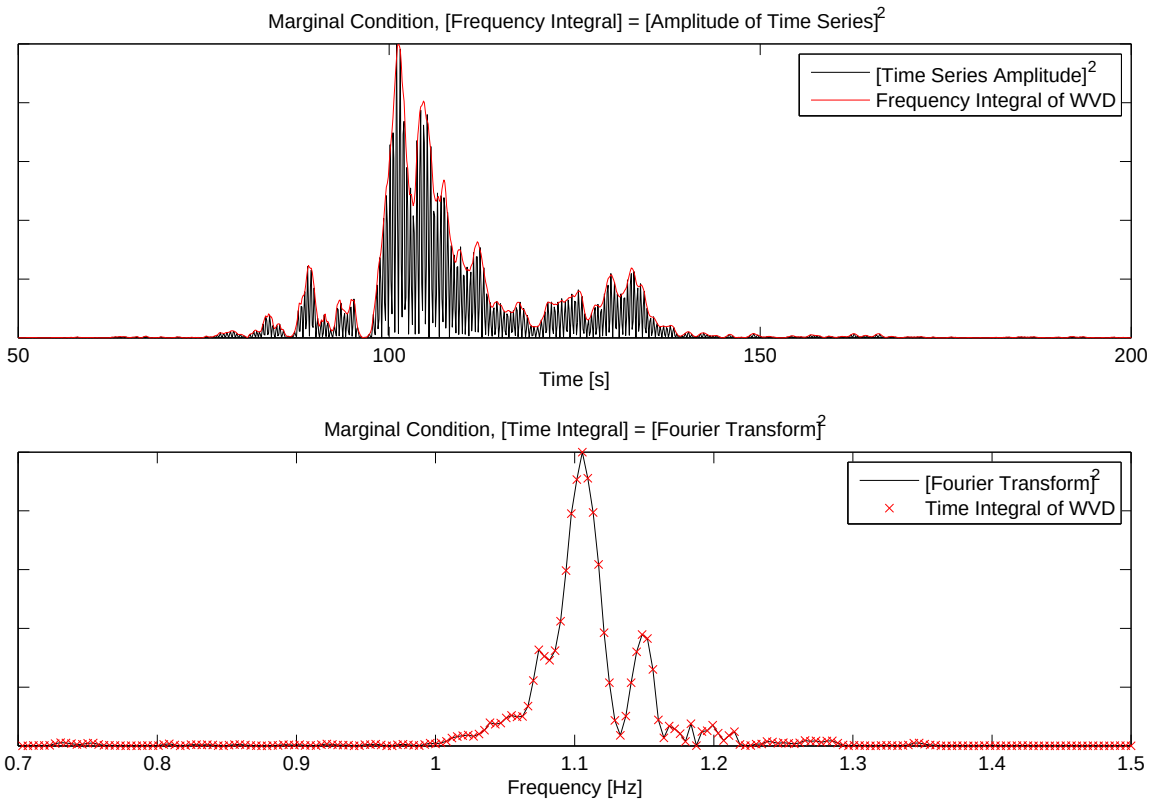

Figure 2.44: WVD Marginal Conditions, as in Figure 2.43, 2005 Parkfield Earthquake at Millikan Library: The time and frequency integrals, for the selected signal, show more detail as to the match. Matching the time and energy marginals is not an approximation, but a consequence of the definition of the Wigner-Ville Distribution.

2.14 Summary

Time-Frequency Representations such as the Reduced Interference Distribution (RID) allow for a detailed analysis of evolving signals, with excellent temporal and frequency resolution. The RID is able to create a point-for-point estimate of the frequency content in a signal, while reducing the strong interference terms which complicate the interpretation of the Wigner-Ville Distribution (WVD).

There are various properties that a Time-Frequency Representation (TFR) can satisfy, some of which (e.g., the marginal conditions) are useful for creating representations that match the physical behavior of a system. The TFR methods in this chapter represent a brief summary of existing techniques. There is no TFR which is perfectly suited for all tasks; a TFR technique must be selected for each application based on the type of signal and the information desired about the signal. The modern TFR methods presented in this thesis are a set of tools that can at times extract more useful information from a signal than other more widely used techniques such as the spectrogram and wavelet methods.

Chapter 3

Time-Frequency Representations: Response of Simulated Nonlinear Systems

To validate the use of time-frequency representations as a damage detection and system identification tool, I have applied these time-frequency analysis techniques to various synthetic nonlinear systems. By applying these techniques to a synthetic system with evolving physical properties, it becomes straightforward to correlate changes in instantaneous frequency with changes in stiffness.

The first simulated system is a distributed element model ("Iwan Model," (Iwan, 1966; Iwan, 1967)), which is a well-studied hysteretic model for a nonlinear-elastic single degree-of-freedom (SDOF) system with evolving stiffness. Stick-slip elements fail at specified load levels, causing a loss of stiffness and, therefore, a decreased natural frequency.

This is followed by a more complicated system, a nonlinear finite element model of a 20-story building under different levels of excitation. This model includes the effects of material nonlinearity and weld fractures. As the system experiences larger motions, the damage becomes more severe, and the natural frequencies are more significantly affected – time-frequency representations allow for a point-for-point correlation between damage measures and instantaneous frequency content.

3.1 Distributed Element Model

A hysteretic system that exhibits nonlinearity with increasing amplitudes of motion was described in Iwan (1966) and Iwan (1967). This model, a Distributed Element Model (DEM), has as its basic element a "stick-slip slider" and spring in series ("Coulomb Damper"). The stick-slip/spring elements are then arranged in parallel, as shown in Figure 3.1. As the amplitude of the system increases, the stick-slip elements progressively fail, decreasing the total (secant) stiffness of the system. This SDOF model has realistic hysteretic behavior, and as such it is a useful example of a nonlinear system.

Figure 3.2 presents the response of a distributed element model to a selected input motion (gaussian noise, first of constant amplitude, then scaled by a cosine envelope). The hysteretic behavior evolves with time: as the amplitude of motion crosses the element slip levels, the corresponding spring is lost, weakening the system. For this system there is hysteretic damping at high amplitudes; once the input function ends, the system motion is damped out, and eventually the system response returns to linear oscillations. In Figure 3.3, the same time history (input and response) is shown, with the estimated secant stiffness for each oscillation of the system. By estimating the peak-to-peak slope in the force/displacement plane, it is possible to extract an estimated stiffness for each cycle and correlate the observed natural frequency with the amplitude of the system response.

Figures 3.4, 3.5, and 3.6 show spectrogram energy estimates for the distributed element model for both linear and logarithmic scales. The spectrogram windows, of N/2, N/4, and N/8, respectively, give different levels of temporal and frequency resolution. For the longest time window (N/2), the evolving stiffness/frequency is smeared along the time axis. Variations in frequency content are elongated, but this representation matches the actual stiffness of the system. At the next windowing level, N/4, the evolving stiffness and instantaneous frequency are qualitatively closer, echoing the true behavior of the system. The finest window, N/8, has rapid os-

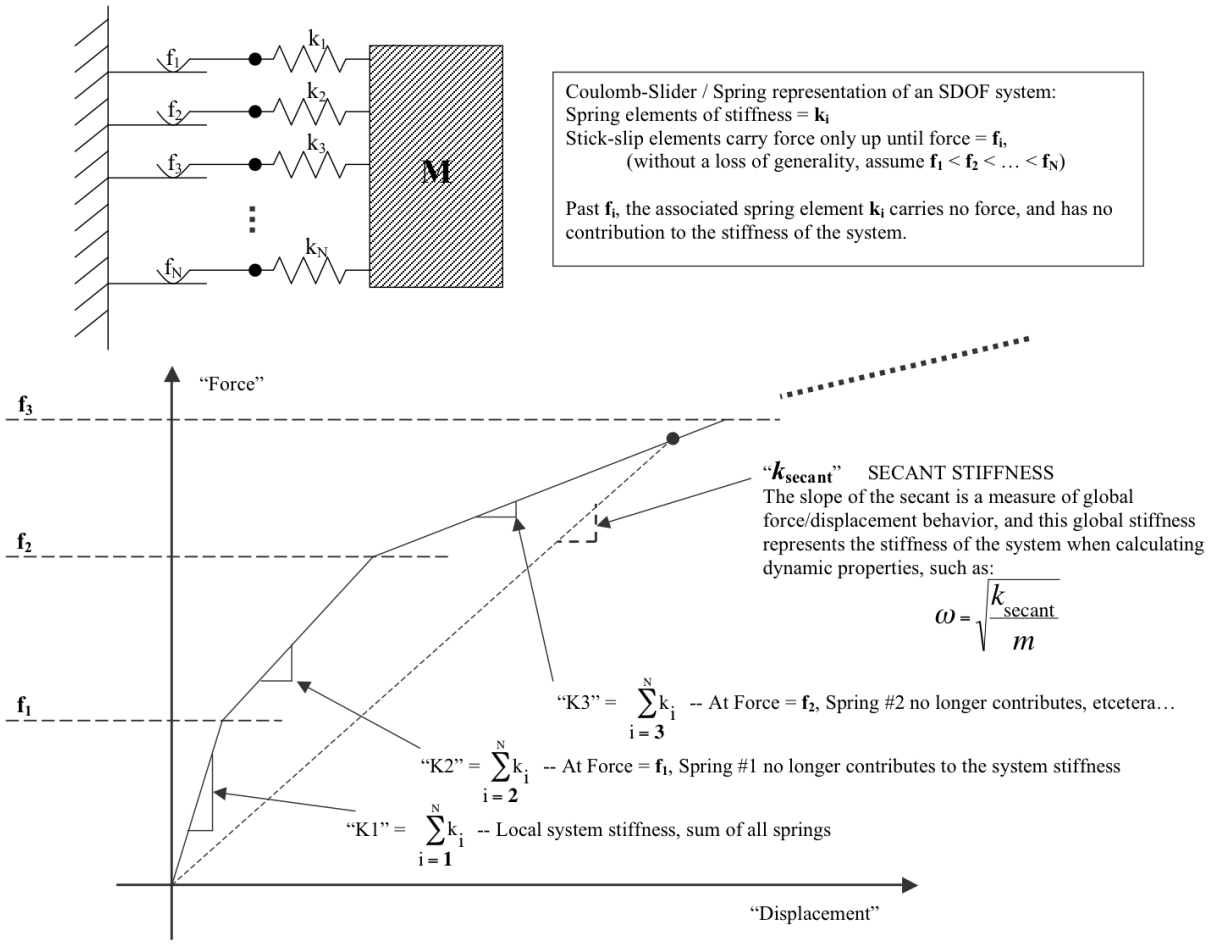

Figure 3.1: Distributed Element Model Schematic, after Iwan (1966) and Iwan (1967). Stick-slip elements ("Coulomb Sliders") are joined to linear springs – the stick-slip elements fail with increasing amplitudes of motion, at which point the attached spring contributes no stiffness to the system. This model is a useful analogy for complicated systems with evolving stiffnesses.

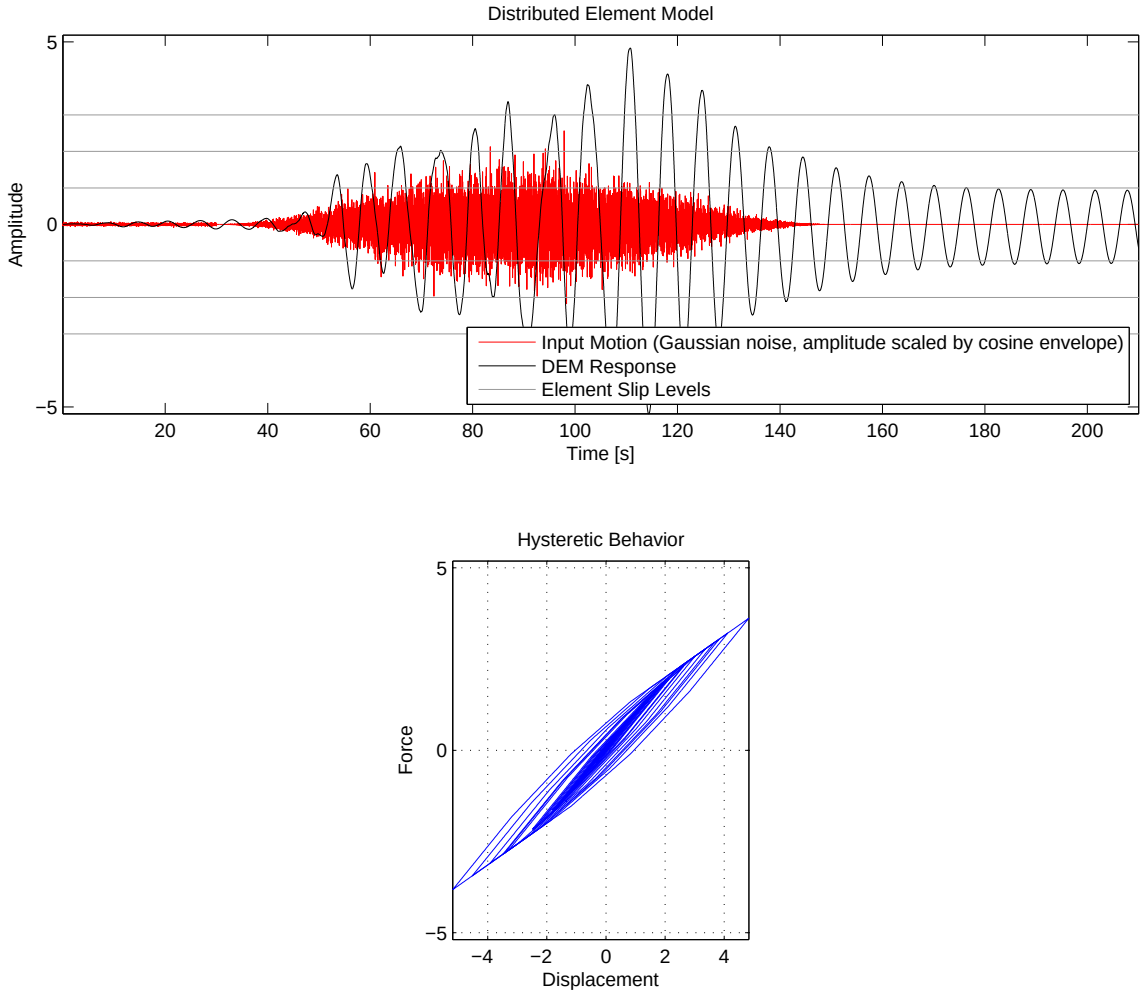

Figure 3.2: Distributed Element Model, response to enveloped gaussian noise. Input signal consists of a constant amplitude runup, cosine enveloped gaussian noise, and zero for the rest of the signal. The hysteretic behavior is defined by a backbone curve as in 3.1. For shaking in the linear range, there is no damping, and the system will oscillate perpetually between the minimum and maximum linear portion of the backbone curve. (For higher levels of input motions, hysteretic damping acts to dissipate energy until the system reaches the linear range.)

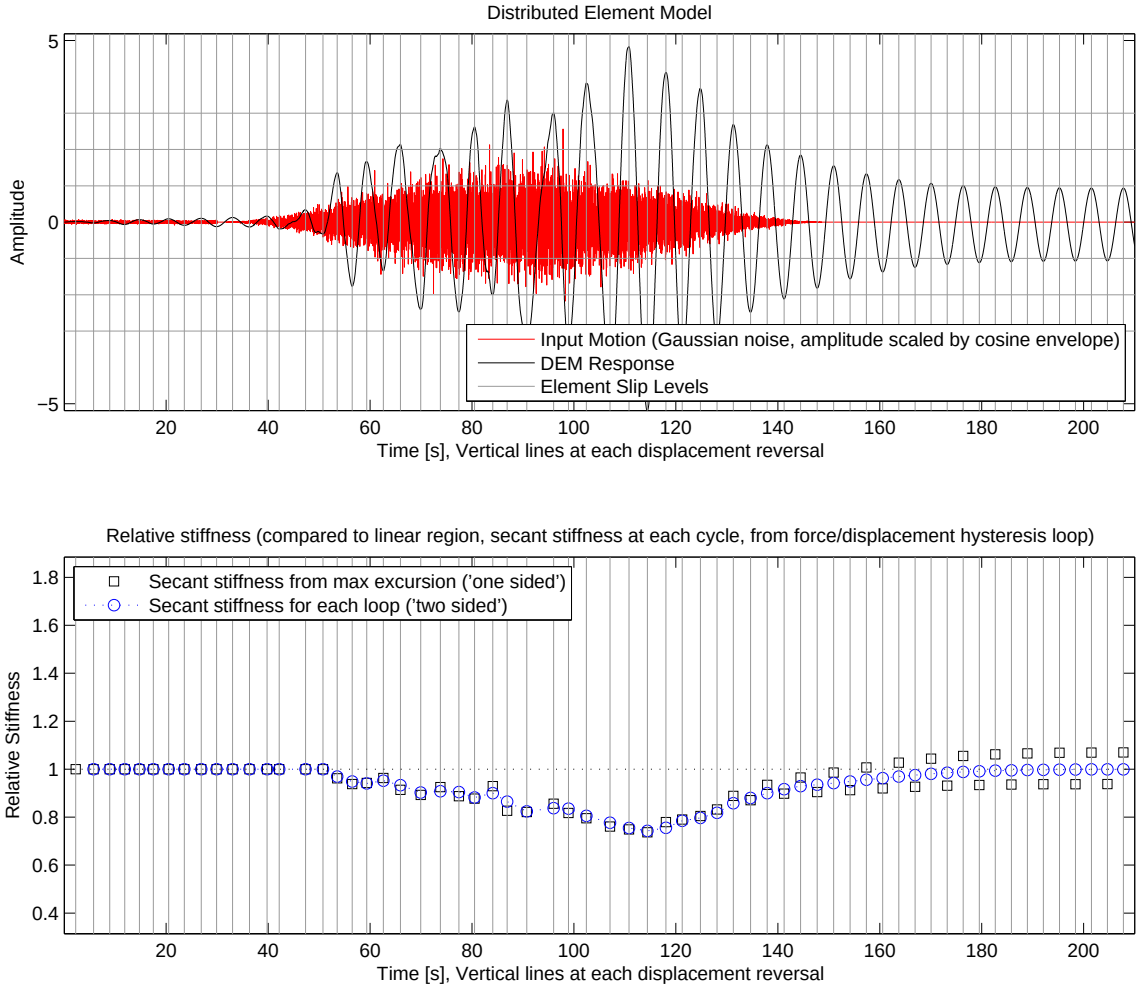

Figure 3.3: Distributed Element Model, response to enveloped gaussian noise. For each loop in the force-displacement plane, it is possible to estimate a peak-to-peak secant stiffness in the system. This is an approximation for the stiffness that shows the decrease in stiffness with increasing amplitude and in turn implies a changing instantaneous natural frequency. The "one-sided" estimate is the final stiffness estimated using the distance from the initial conditions. The "two-sided" estimate uses the slope connecting the positive excursion and the following negative excursion. These estimates differ in the case when the system does not recover to the pre-event displacement level due to permanent plastic deformations.

cillations in instantaneous frequency – this correctly represents the changing secant stiffness as the system returns to the linear regime in every cycle.

The continuous wavelet transform (Figure 3.7) shows similar behavior to the N/8 spectrogram. The changing stiffness over each cycle causes rapid changes in the estimate of instantaneous frequency. Some smearing of energy along the frequency axis follows from the scale-frequency approximation and the diffuse representation of high frequency information in the wavelet transformation.

Figure 3.8 shows the same system and the associated Reduced Interference Distribution. The instantaneous frequency estimate again tracks the changing stiffness in the system. This representation of a SDOF system illustrates the type of connection between changing stiffness and changing dynamic properties that can be created for more complicated systems.

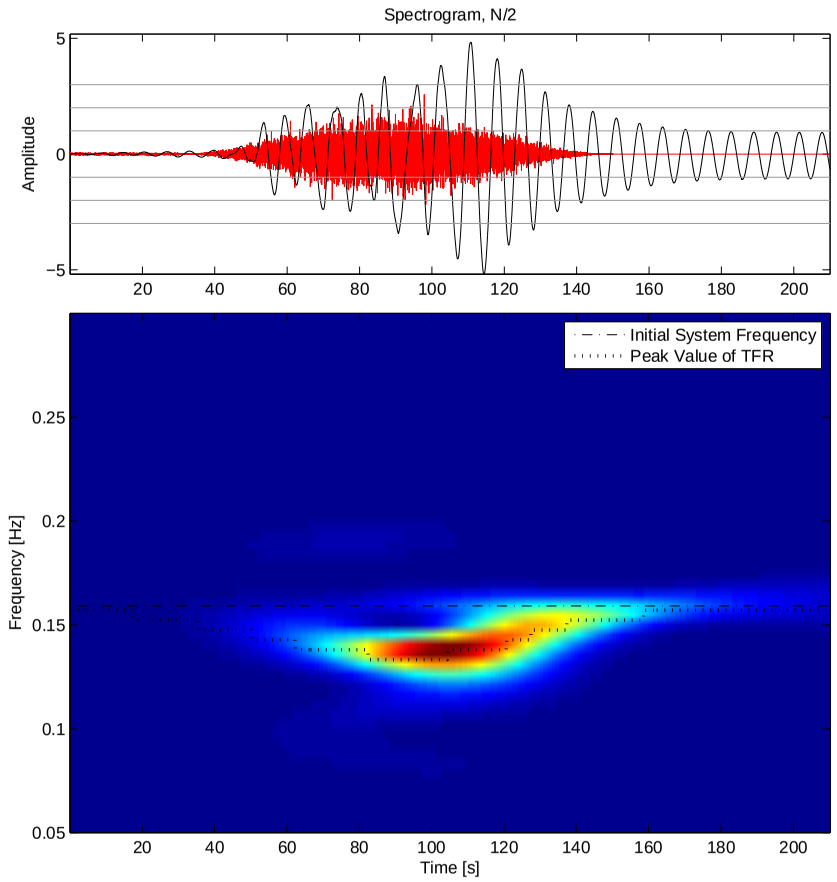

(a) Spectrogram

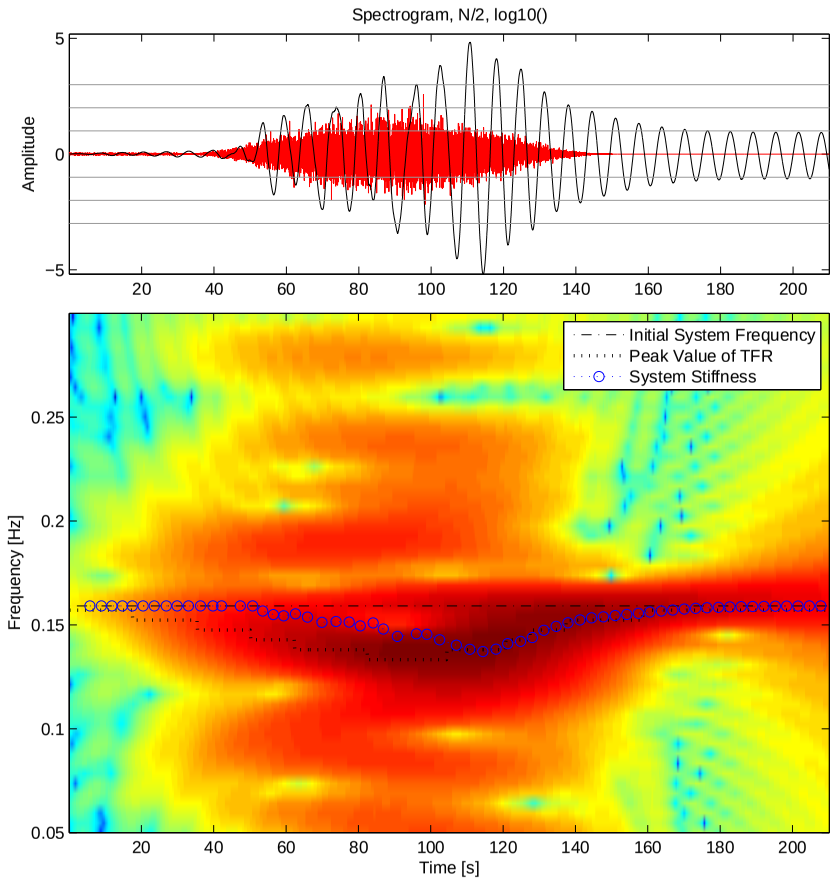

(b) Spectrogram, log10 of amplitude.

Figure 3.4: Distributed Element Model, Time Series and Spectrogram, window of N/2. Dash-dotted line is linear natural frequency, and the dark dotted line is the instantaneous frequency estimate for the system. Stiffness of the system, in blue circles, is estimated from the maximum excursion at each hysteretic loop. A Spectrogram window of N/2 gives coarser temporal resolution, smearing information along the time axis.

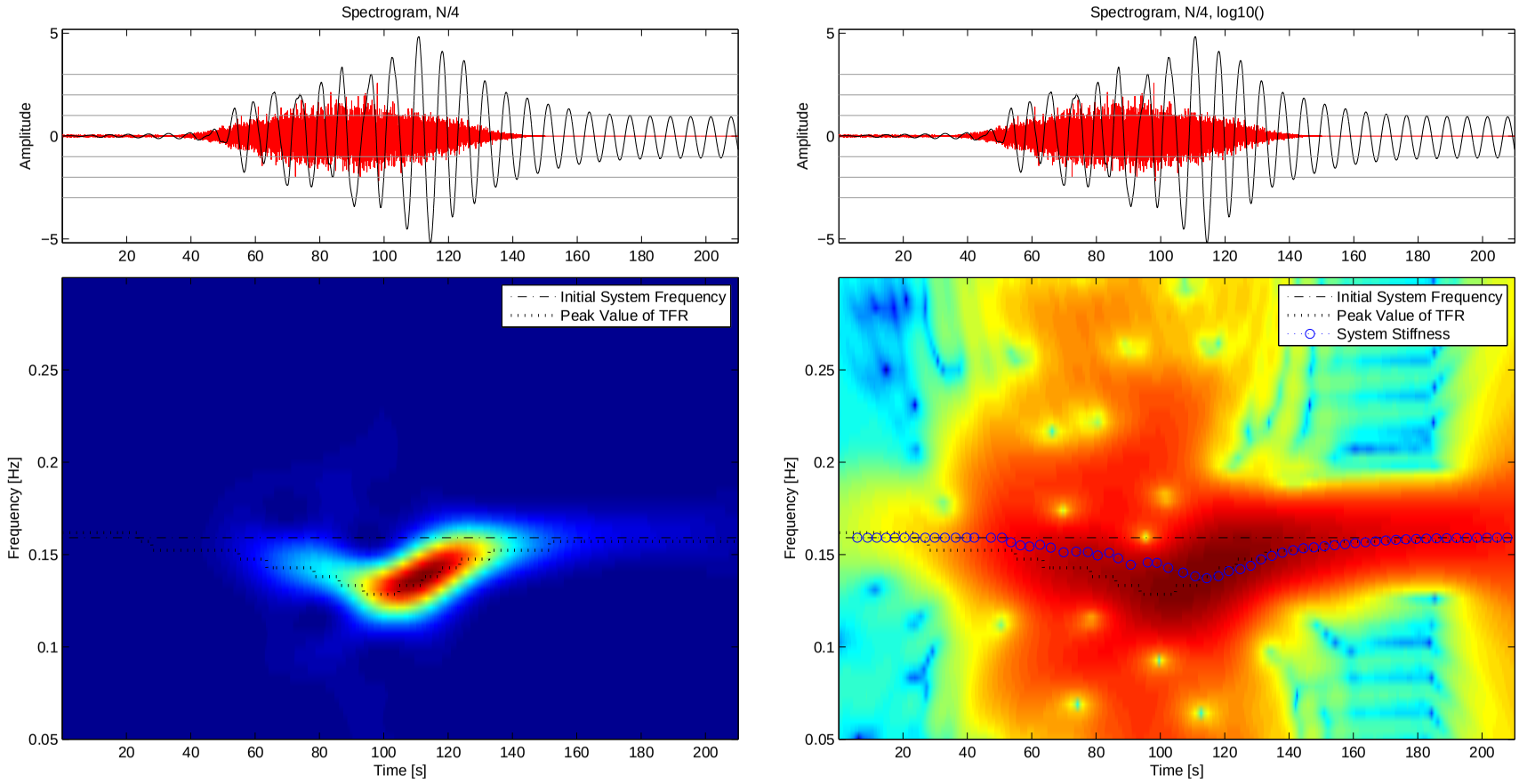

(a) Spectrogram

(b) Spectrogram, log10 of amplitude

Figure 3.5: Distributed Element Model, Time Series and Spectrogram, window of N/4. Dash-dotted line is linear natural frequency, and the dark dotted line is the instantaneous frequency estimate for the system. Stiffness of the system, in blue circles, is estimated from the maximum excursion at each hysteretic loop. A Spectrogram window of N/4 gives better temporal information than in Figure 3.4.

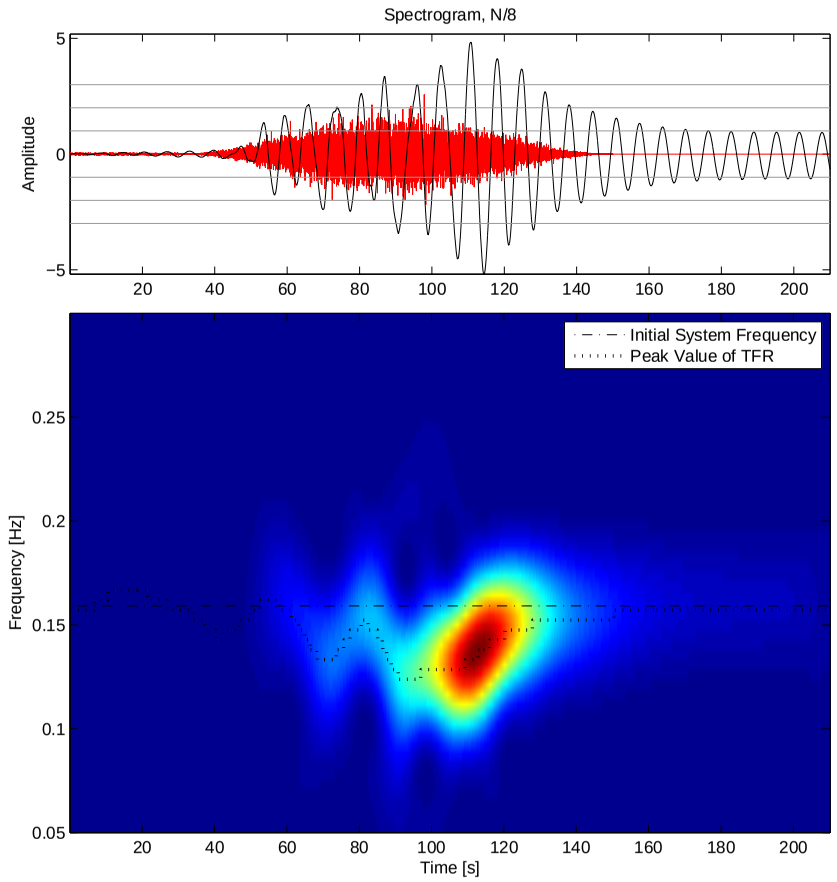

(a) Spectrogram

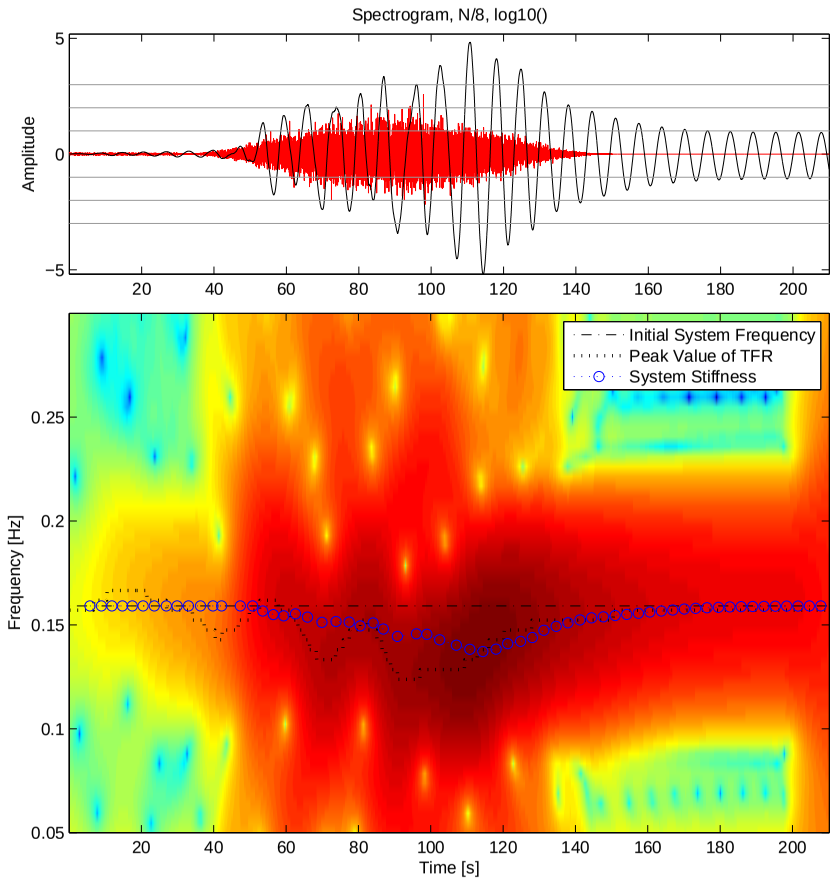

(b) Spectrogram, log10 of amplitude.

Figure 3.6: Distributed Element Model, Time Series and Spectrogram, window of N/8. Dash-dotted line is linear natural frequency, and the dark dotted line is the instantaneous frequency estimate for the system. Stiffness of the system, in blue circles, is estimated from the maximum excursion at each hysteretic loop. A Spectrogram window of N/8 gives fine temporal resolution, though the resolution in the frequency axis is coarser.

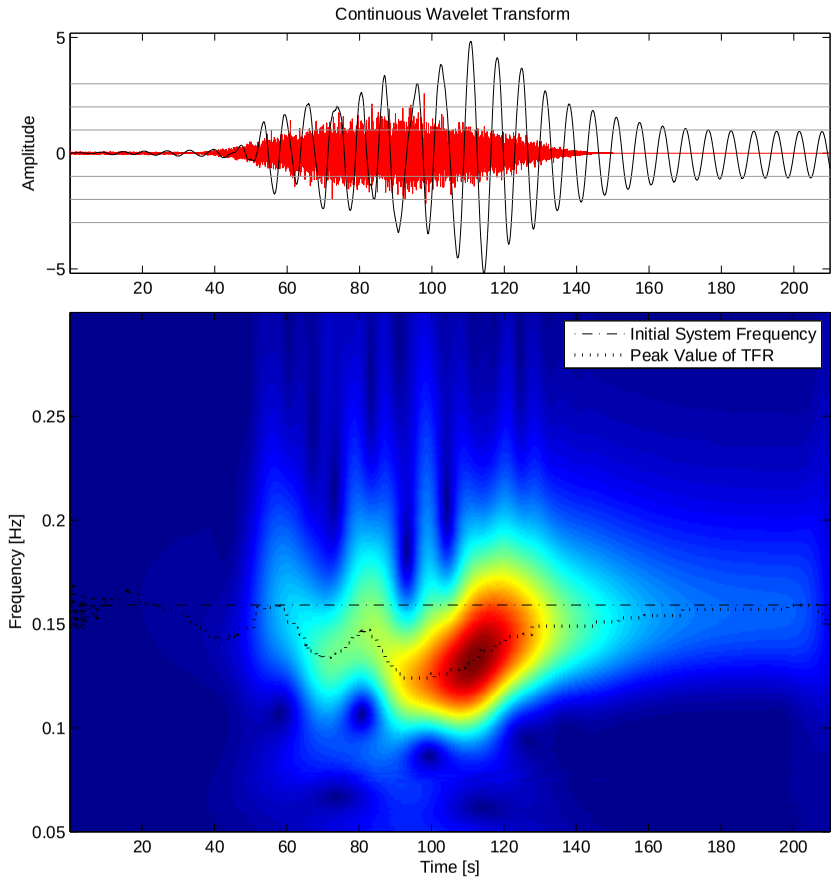

(a) Continuous Wavelet Transform

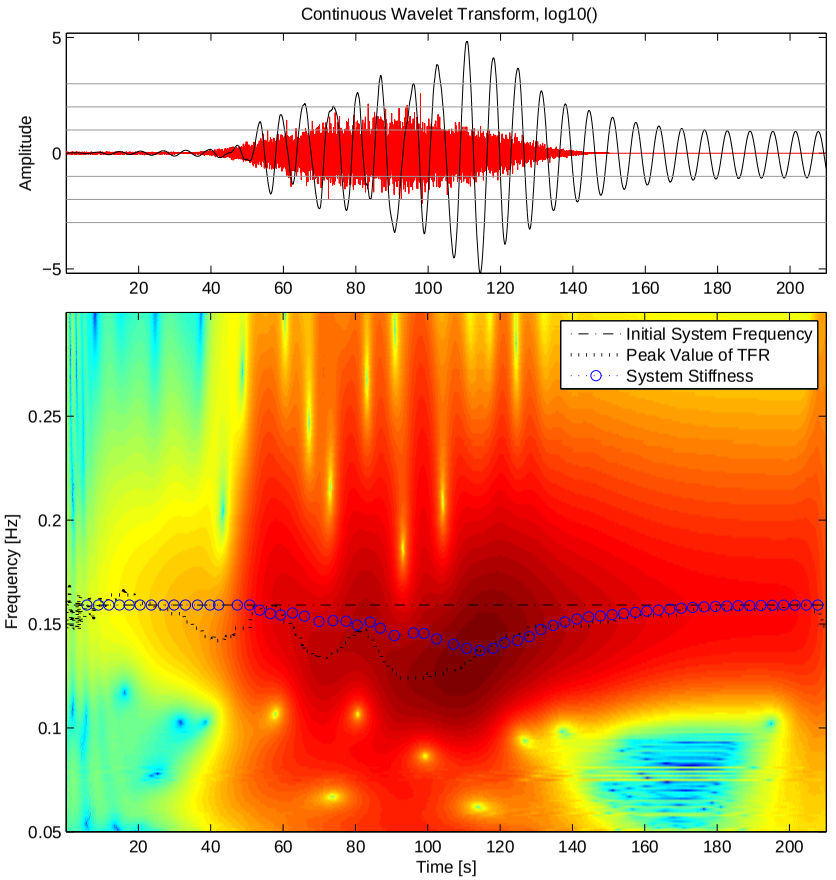

(b) Wavelet Transform, log10 of amplitude

Figure 3.7: Distributed Element Model, Time Series and Continuous Wavelet Transform (CWT). Dash-dotted line is linear natural frequency, and the dark dotted line is the instantaneous frequency estimate for the system. Stiffness of the system, in blue circles, is estimated from the maximum excursion at each hysteretic loop. The wavelet transformation gives a similar result as the spectrogram for N/8 (3.6), correctly identifying changes in stiffness.

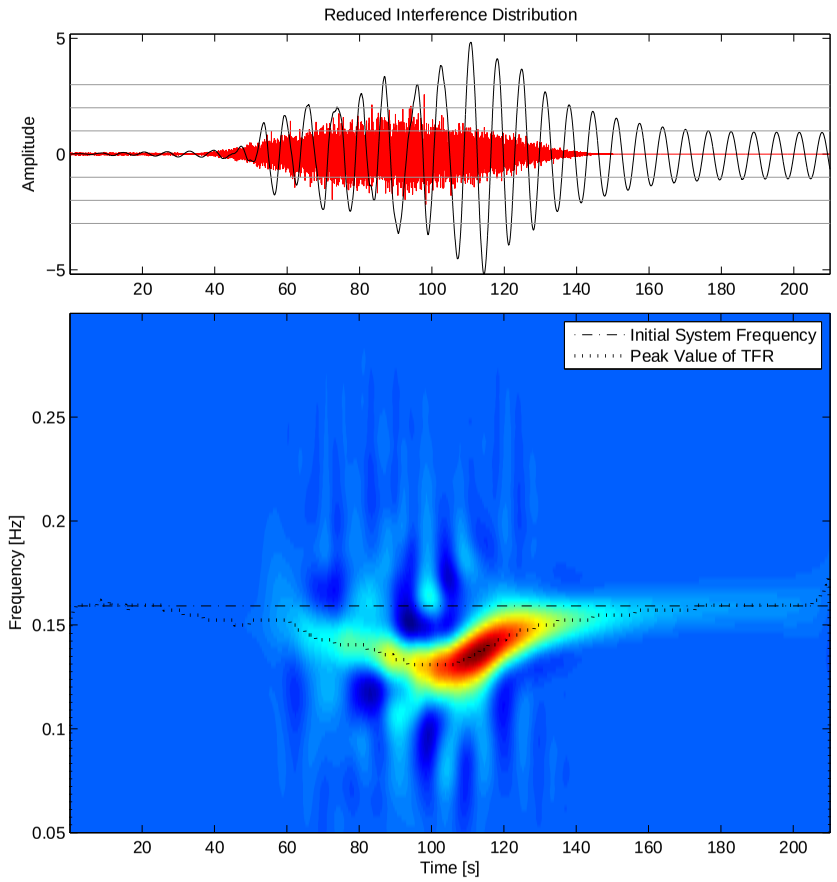

(a) Reduced Interference Distribution

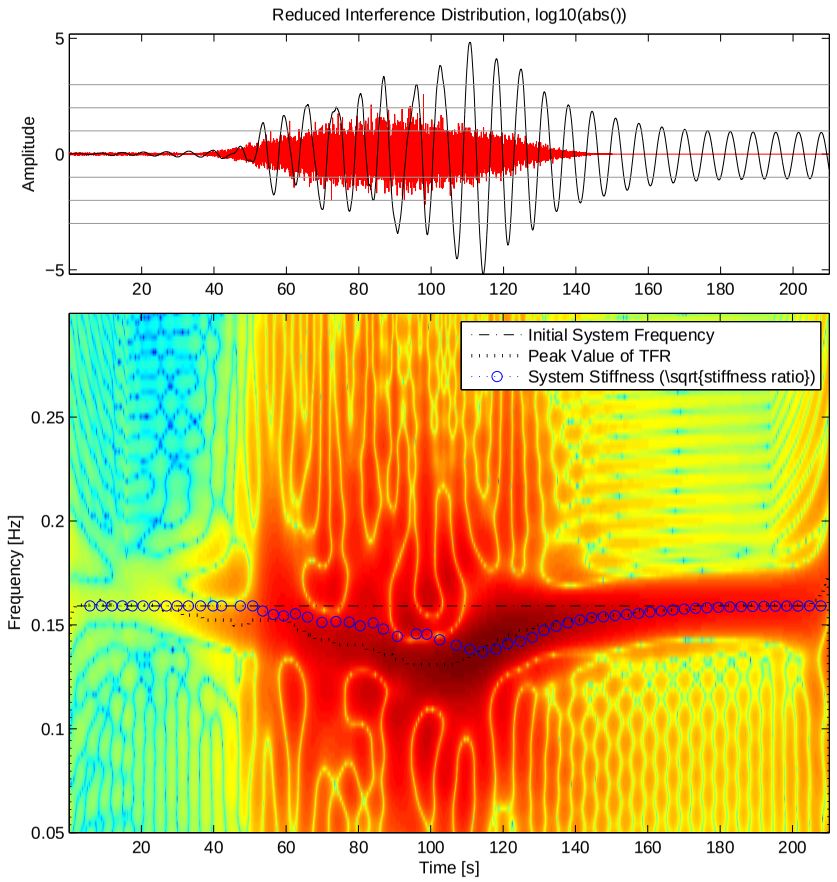

(b) Reduced Interference Distribution, log10(abs()) of amplitude

Figure 3.8: Distributed Element Model, Time Series and Reduced Interference Distribution. Dash-dotted line is linear natural frequency, and the dark dotted line is the instantaneous frequency estimate for the system. The instantaneous frequency estimate closely matches the changing stiffness in the system, though the interference terms complicate identification of the peak frequency.

3.2 Nonlinear Finite Element Building

For the signals of interest to Structural Health Monitoring, the evolution of natural frequencies becomes important for damage detection and system identification. Small to moderate earthquakes, for example, will temporarily decrease the apparent natural frequencies of structures – nonlinearity in the force-displacement relationship will cause an apparent loss of stiffness with greater excitation levels. This effect can be seen in buildings under different loading conditions, such as strong winds or forced vibration testing (e.g., Caltech's Millikan Library in Chapter B, Clinton (2004), Clinton et al. (2006), and others). Buildings can also be damaged during earthquake loading, leading to permanent changes in dynamic characteristics.

I have developed a framework in which I apply modern time-frequency analysis techniques to data from civil structures under earthquake loading. The goal in these studies is to obtain a detailed, instant-for-instant representation of the dynamic properties of a structure and use changes in these properties to infer damage patterns. The simple SDOF system of Section 3.1 demonstrated how changes in stiffness are related to changes in dynamic properties and how these changes can be tracked in the time-frequency plane. In this section, a synthetic building with many degrees of freedom is analyzed using the same techniques.

To validate these methods, I have applied time-frequency representations to data from a finite-element model that includes varying sources of nonlinearity. The finite-element program used in this study was developed by Professor John Hall, Caltech, and the models used were created by Jing Yang, Caltech (Yang et al., 2006; Bradford et al., 2006). The program is based on a planar-frame fiber model and includes material nonlinearity, geometric nonlinearity (P-Δ effects, member buckling), and weld fractures (Hall, 1997). A 20-story steel moment-frame building, with a height of 78.26m above ground, was designed according to UBC94 for use in the finite-element program. Three versions of the model: nearly elastic, nonlinear inelasticity without weld fracture ("strong weld model"), and full nonlinear behavior including weld fracture, were subjected to the strong ground motions recorded at station HKD095 during

the 2003 Tokachi-Oki earthquake (Mw 8.3). These ground motions are of sufficient amplitude to damage the building, and the resulting records from the model were then analyzed using the TFR methods described in this thesis. A description of the damage state is generated during the model analysis, and comparing this data to the time-frequency information provides a validation for our efforts to correlate damage with changes in dynamic properties of the structure.

Figures 3.9 and 3.10 give an example of the relation between information in the time-frequency plane and the evolution of damage in the structure. Figure 3.9 shows the TFR for the building in the linear elastic case without plastic hinges or weld fracture, and Figure 3.10 shows the TFR for the nonlinear case. In all of these figures, the damage and deformation measures from the models are presented along the same time axis to illustrate the connection between changes in dynamic properties and damage to the system. Figure 3.11 shows an enlargement of the time period of strongest shaking.

The resonant frequency of the building, under small excitations, is near 0.3Hz. During the event, in the "strong-weld" model, the natural frequency temporarily drops to ∼0.25Hz during the strongest shaking. Under nonlinear conditions, the frequency has a more significant decrease and reaches 0.15Hz, a drop of $\sim$ 50% in the original natural frequency, corresponding to a temporary decrease of almost 75% in the global stiffness of the structure. In the nonlinear case, the change in stiffness is matched by an increase in damage measures – plastic hinges and fractured welds. Using these joint time-frequency analysis methods, it is possible to examine the instant-for-instant correlation between damage and dynamic characteristics of a structure.

Of note in Figures 3.10 and 3.11(a) are the two dominant frequencies in the time-frequency plane, as the vibrations of the building begin to behave differently once the building is damaged. For the linear excitations of Figure 3.11(b), the time series is a smooth oscillation with varying amplitude. In the nonlinear case, the time series has "double peaks," as the roof motions are no longer in phase with the rest of the building. Interior reflections in the building begin to disperse the traveling waves

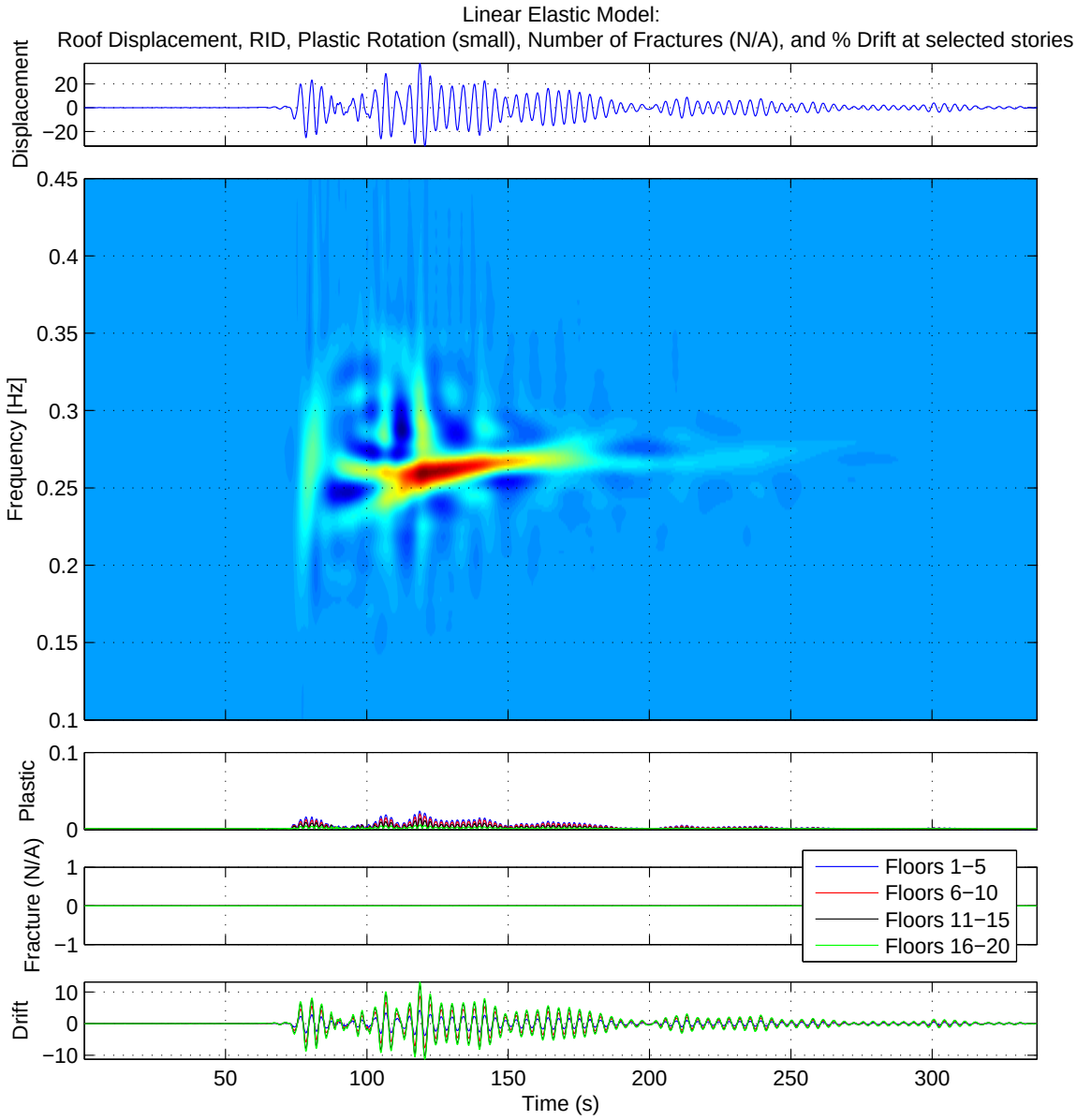

Figure 3.9: RID of synthetic data for the "strong weld" FE model. (Model is not truly linear, as there is some plastic behavior of the joints. This model was created without weld fracture, and with material properties that match linear behavior as well as possible. The small amplitude plots of Section 3.2.1 are closer to true "linear" building behavior.) Plots as in Figure 3.10.

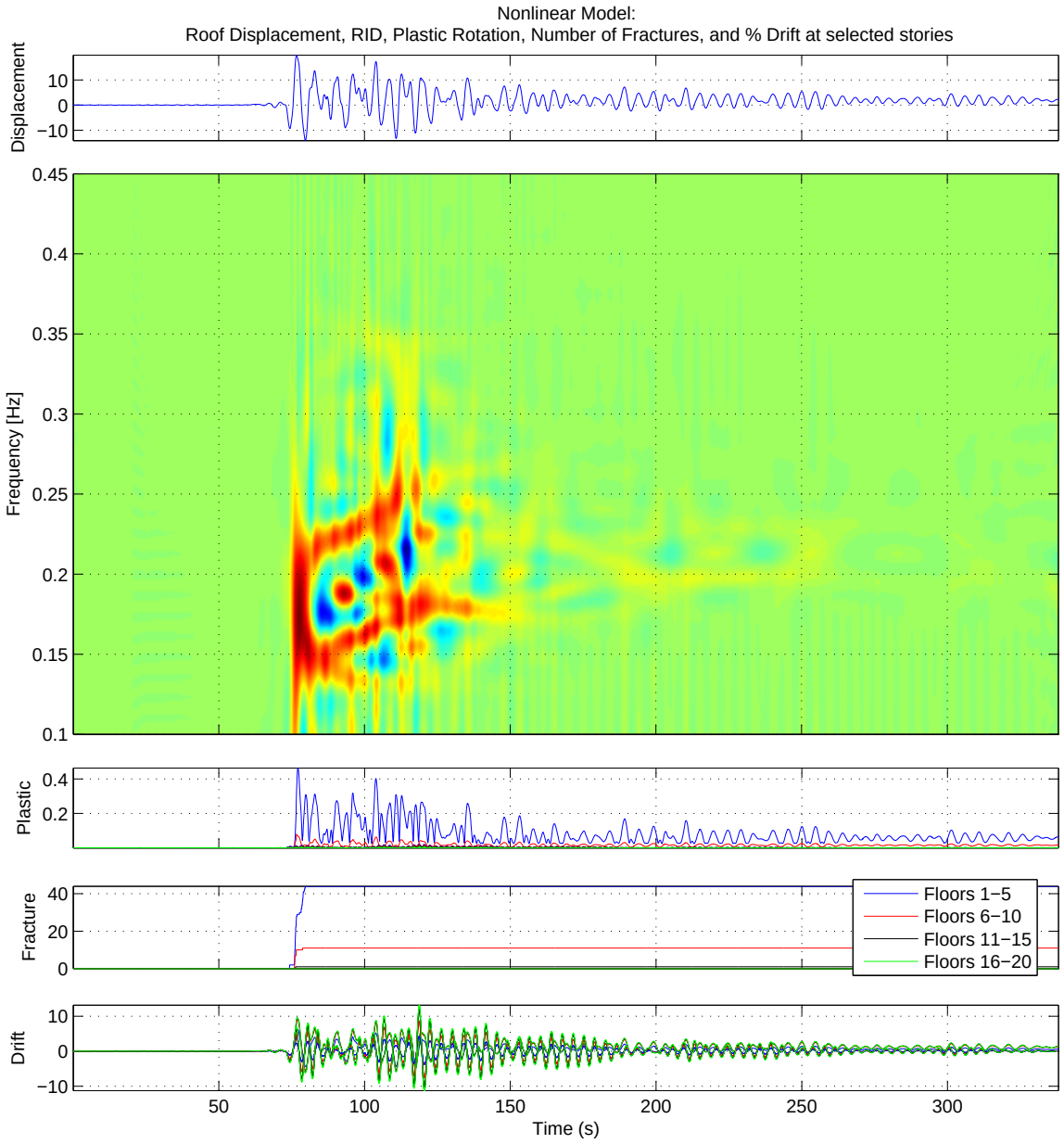

Figure 3.10: RID of synthetic data for the nonlinear FE model. The top plot is the roof displacement, the large center plot is the RID of the data, and the three bottom plots present the plastic rotation, number of fractured welds, and drift for selected stories. These damage measures are presented for selected groups of floors, as noted in the legend.

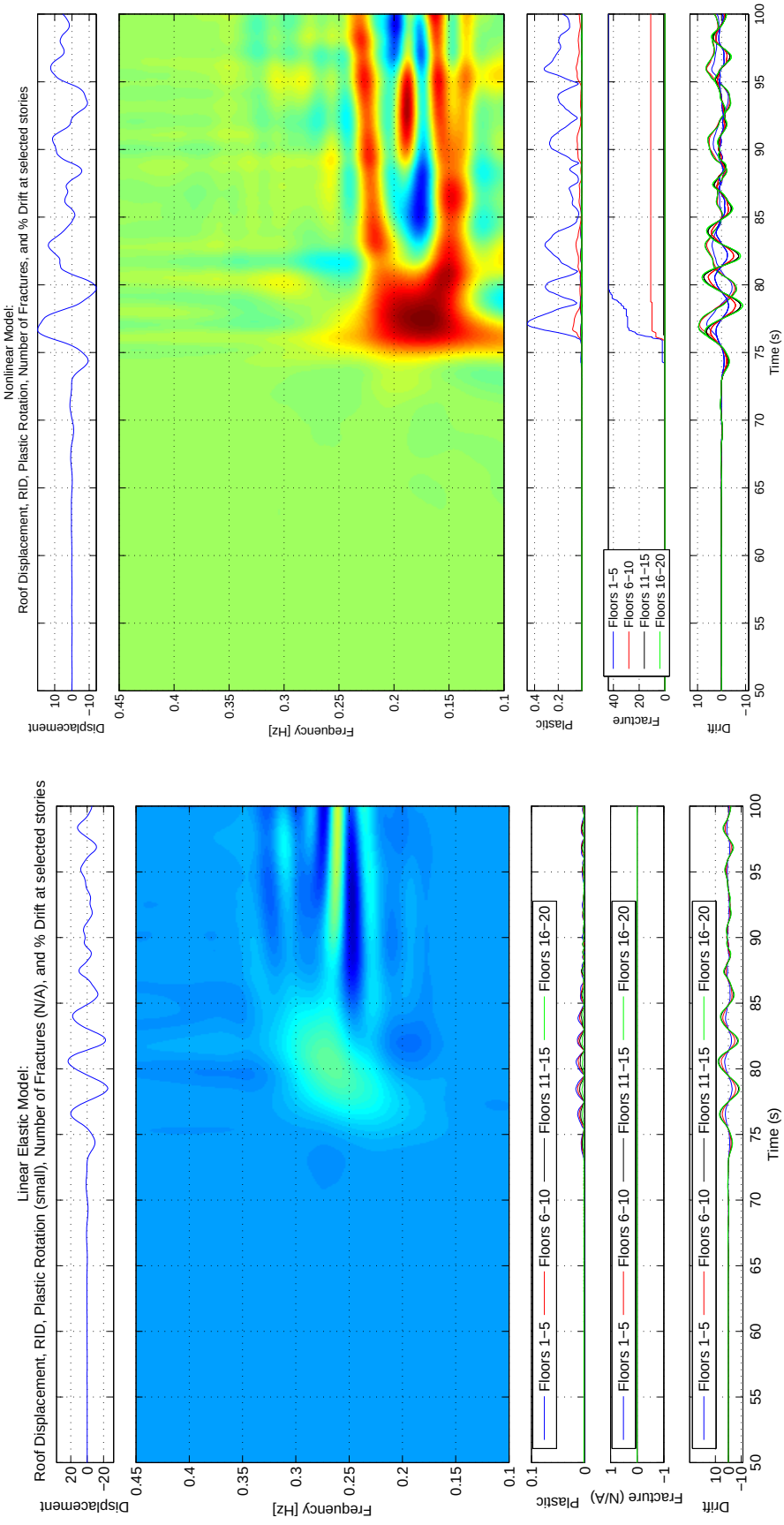

(a) Strong-Weld

(b) Nonlinear

Figure 3.11: RID of synthetic data for the "strong-weld" and nonlinear FE model. Plots as in Figure 3.10. The time period of the initial strong motion pulse is presented to more clearly show the evolution of frequencies on a time scale of seconds. The change in frequency is much less noticeable for the strong weld model than in the full nonlinear case.

of the building based on the change in stiffness in the lower floors; the kink in the lower floors represents a region of lower stiffness, and as such there are internal waves generated at the interface between the upper floors and the lower floors. The displaced shape of the building at each instant shows that the roof displacements are out of phase with the lower floors of the building during many portions of this record, particularly between $t = 70s$ and $t = 150s$. From a parametric standpoint it is not immediately obvious, a priori, that this mode-splitting would occur. This is an example of a system where exploratory time-frequency methods can be used to investigate the behavior of the system and aid in the design of a suitable parametric model of the evolving dynamic properties.

3.2.1 Response to Varying Levels of Input Motion

In order to investigate the connection between shaking levels and damage patterns, the same input motions as in the previous section were linearly scaled so as to change the damage levels experienced by the building. Damage patterns at each level of shaking (Figures 3.12 – 3.18) show the evolution of damage with stronger shaking and increased damage measures, with the level in percentage representing the scaling of the ground motions inputs used for the model (from 1% to 150% of the original shaking). The splitting of the dominant frequency into two frequencies is apparent at higher scaling levels, though at the largest level of shaking (150% in Figure 3.18), the permanent offset in the building complicates the interpretation of the results. For a signal with large offsets, the RID becomes more strongly oscillatory along the time axis (closely spaced vertical "stripes" in Figure 3.18(a) are a feature of this interference), and the normalized data is also difficult to interpret. Large amplitudes at low frequencies, the analog of a Fourier DC-offset, reduce the relative amplitudes of the RID between $0.1Hz$ and $0.3Hz$, though it is still possible to track the behavior as similar to that in Figures 3.16 and 3.17. At the strongest levels of shaking, 150% of the original ground motion amplitudes, the building is within a few percent of total collapse according to the finite element code. Gravity would likely work to topple the building in this damage state.

Figures 3.19 and 3.20 summarize the time-frequency behavior of the building under increasing amplitudes of motion. As the damage grows more severe, the final natural frequency continues to decrease, and there is a permanent change in frequency at the end of the event. The time-frequency representation of the roof records provides more information than simply looking at the Fourier Transform, though there is an obvious difference in frequency content between the different levels of excitation (the difference in frequency content can be used as a preliminary investigation tool). The RID adds further information about the onset of strong shaking, the timespan over which the frequency decreases and recovers, and identifies splitting in the time-frequency plane for the unscaled (100%) motions.

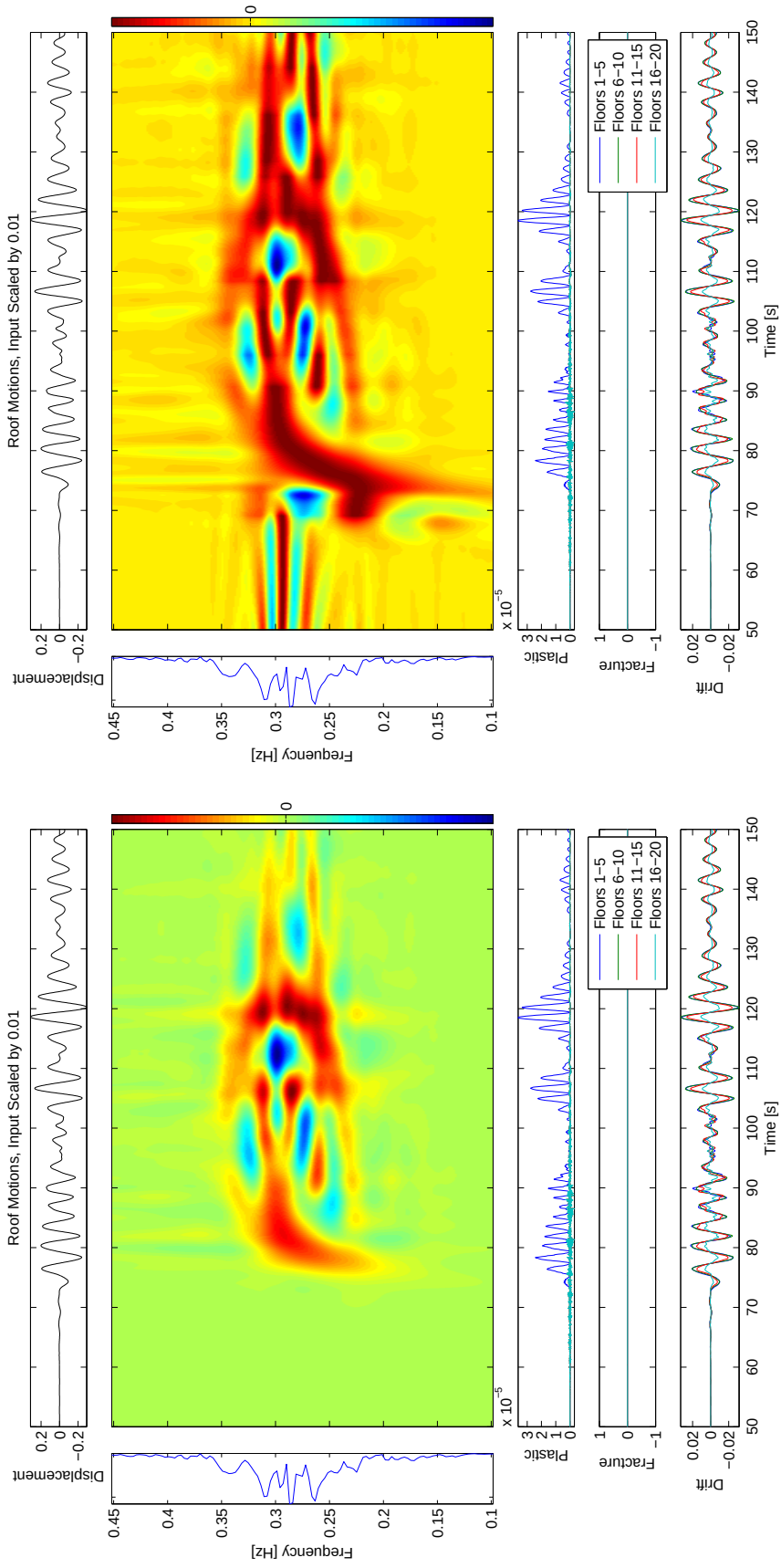

(a) Scaled by 1%

(b) Scaled by 1%, Normalized

Figure 3.12: The input motions of Figure 3.10 were scaled to show the evolution of damage patterns with increasing amplitudes. In this case, the amplitudes of 1% resulted in nearly linear behavior, with no fractured welds and and negligible plasticity.

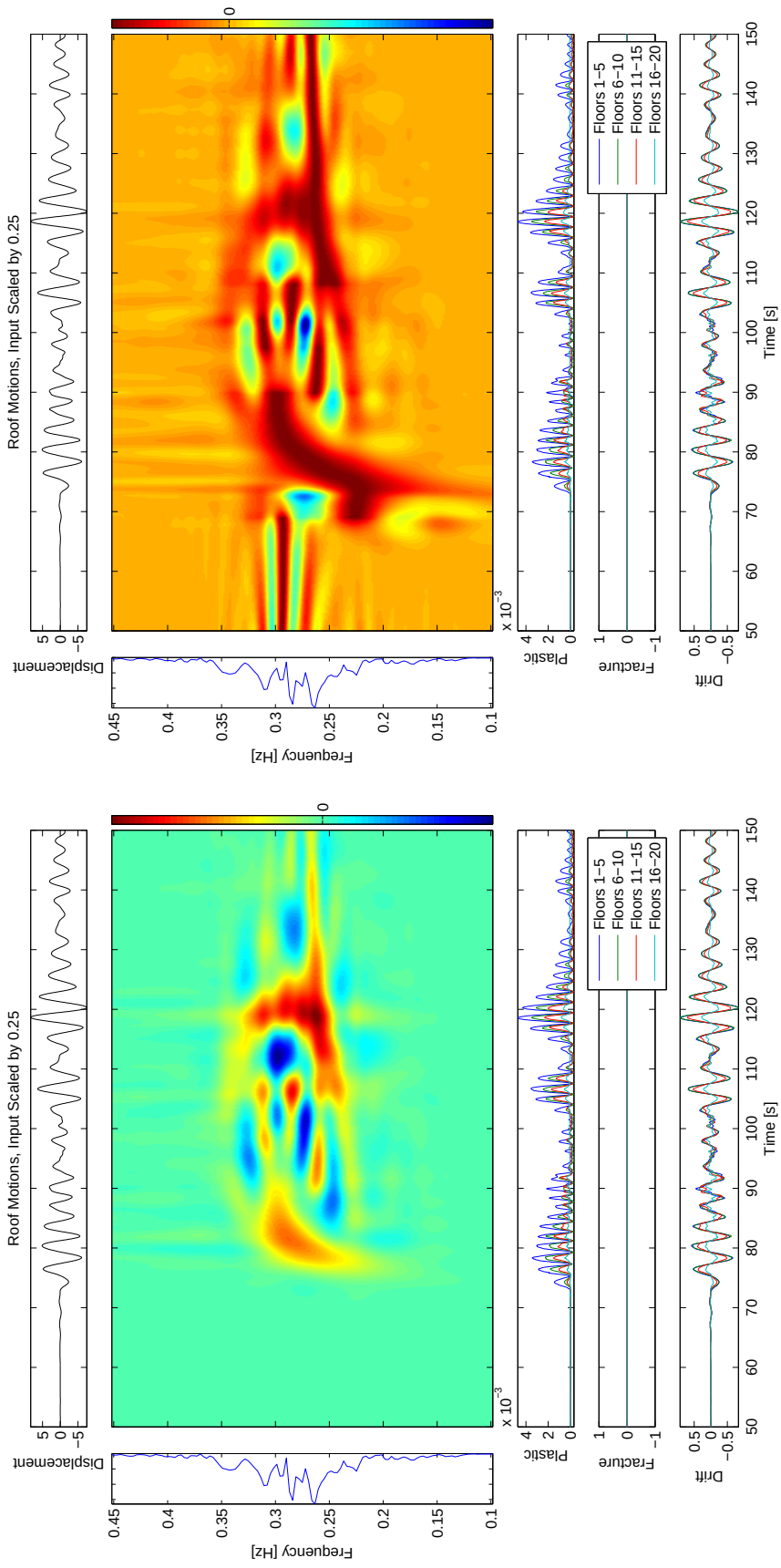

(a) Scaled by 25%

(b) Scaled by 25%, Normalized

Figure 3.13: As in Figure 3.12, for scaling of 25% of the original amplitudes. At this amplitude, the plastic behavior begins to have an effect on the system, but there is still no weld fracture, and the drifts and plasticity are small.

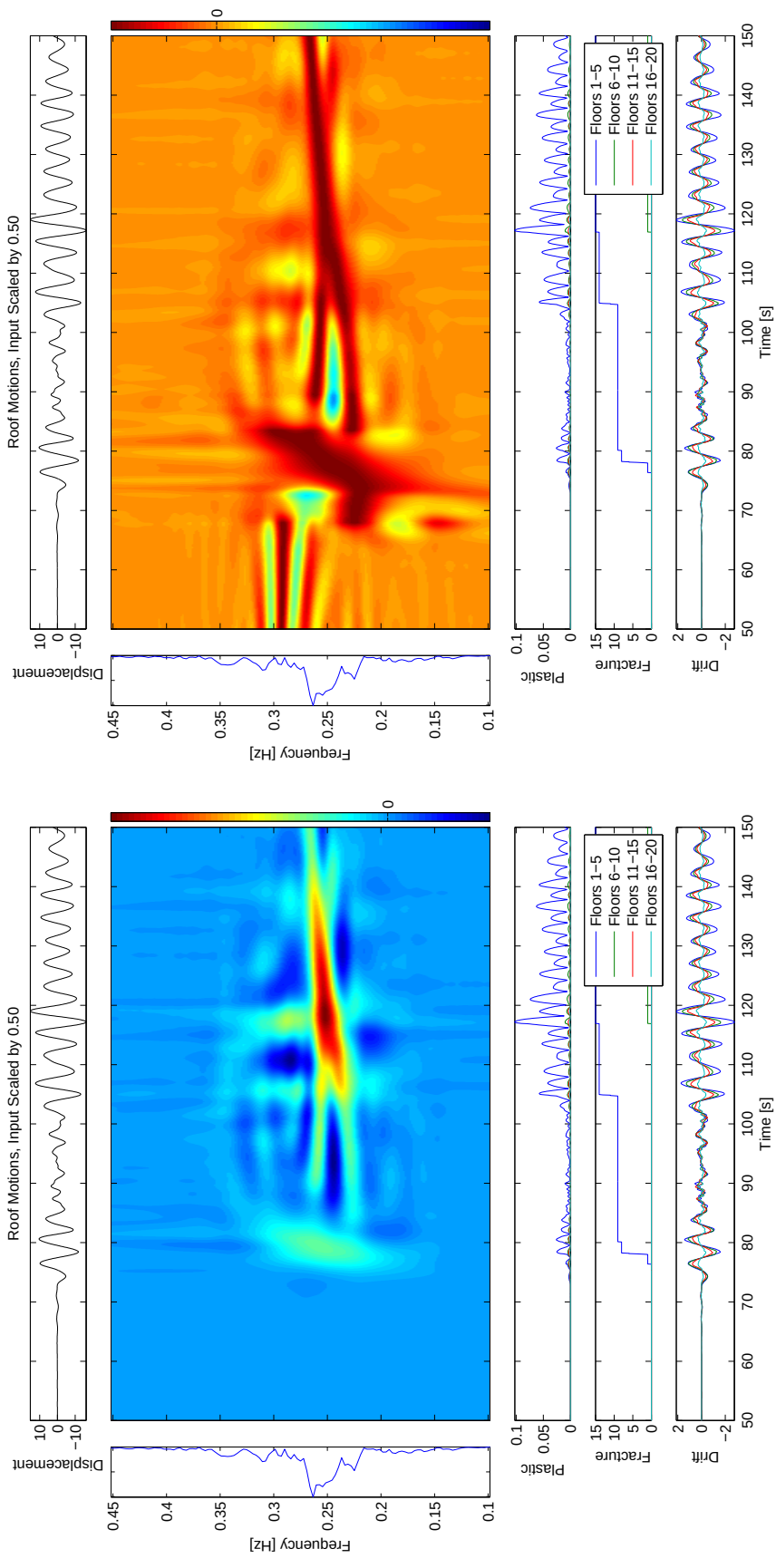

(a) Scaled by 50%

(b) Scaled by 50%, Normalized

Figure 3.14: As in Figure 3.12, for scaling of 50% of the original amplitudes. Weld fractures on the first 5 floors, some on floors 6-10, causing a change in the dynamic properties of the roof response. Natural frequency has been permanently changed by almost 10%, corresponding to a loss of $\sim 19\%$ of the total stiffness.

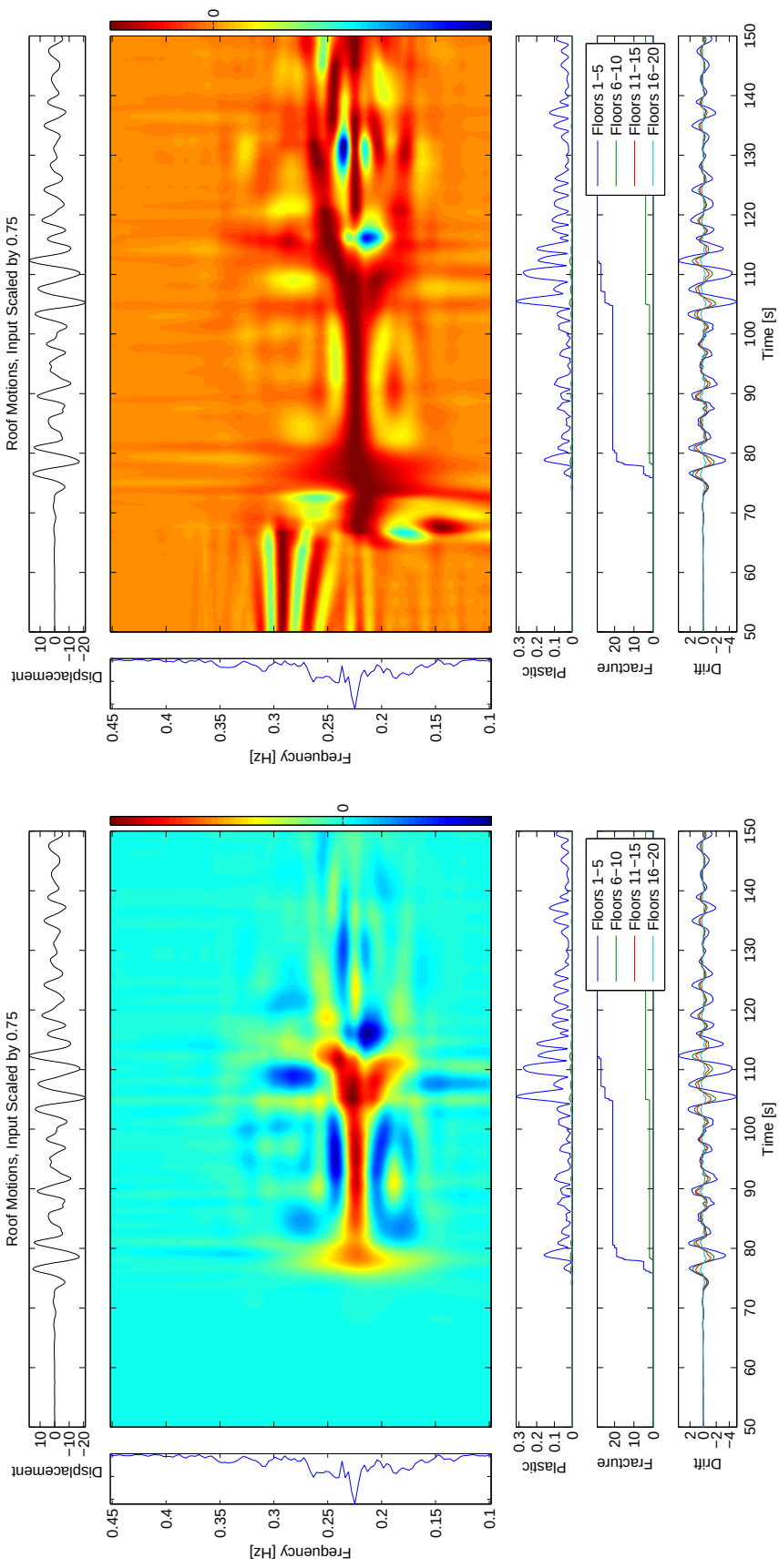

(a) Scaled by 75%

(b) Scaled by 75%, Normalized

Figure 3.15: As in Figure 3.12, for scaling of 75% of the original amplitudes. Further weld fractures on the first 5 floors, some on floors 6-10, causing a change in the dynamic properties of the roof response. Natural frequency has been permanently changed by 26%, corresponding to a loss of 45% of the total stiffness. At this level of excitation, there is a significant change to the peak of the Fourier Transform (along the Y-axis) compared with the Fourier Transform for lower levels of shaking (Figures 3.12 – 3.14).

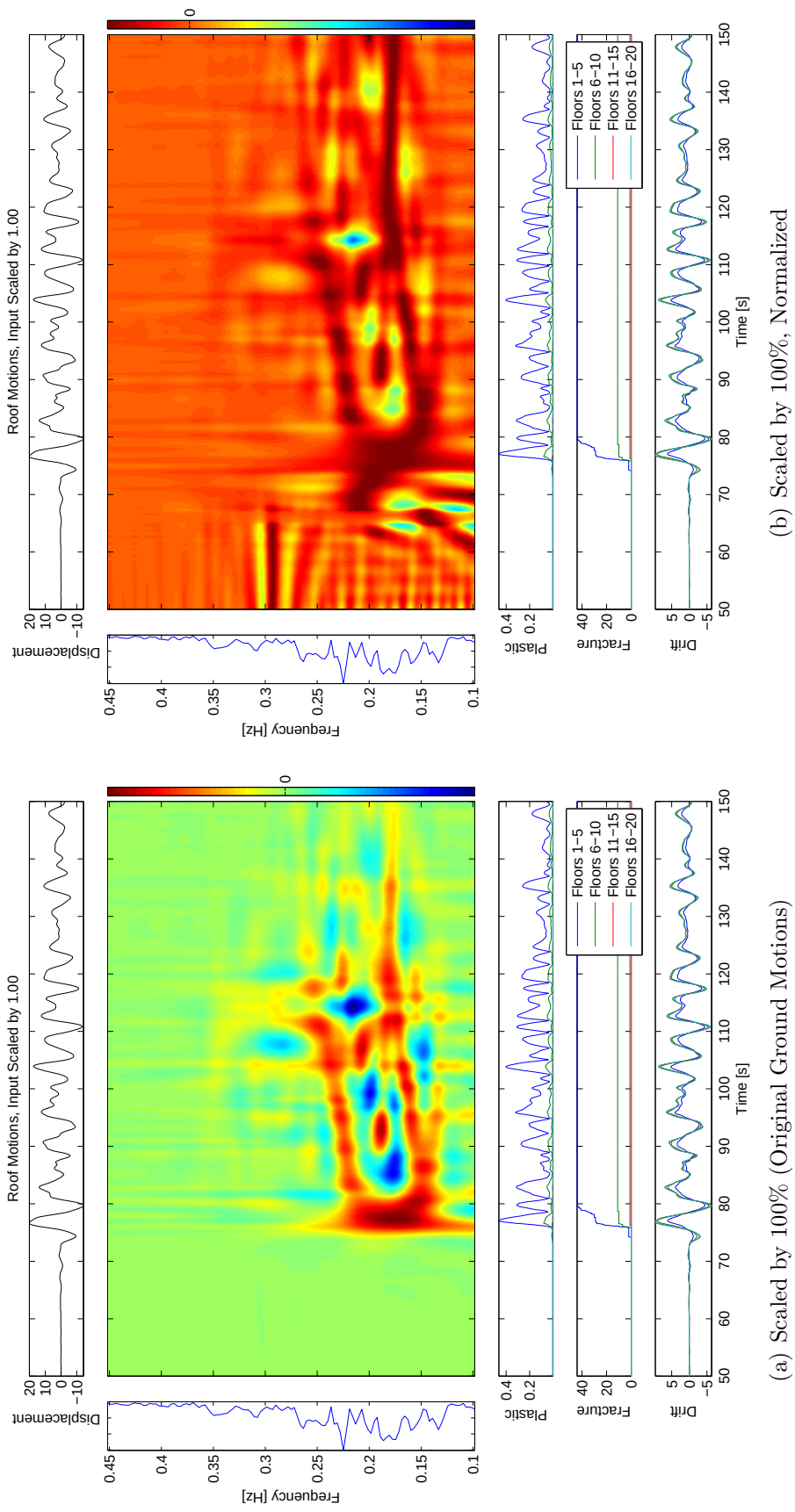

(a) Scaled by 100% (Original Ground Motions)

(b) Scaled by 100%, Normalized

Figure 3.16: As in Figure 3.12, for the original amplitudes for the synthetic ground motions. Weld fractures on the first 5 floors, some on floors 6-10 and higher, causing a change in the dynamic properties of the roof response. Natural frequency has been permanently changed by almost 40%, corresponding to a loss of 62% of the total stiffness.

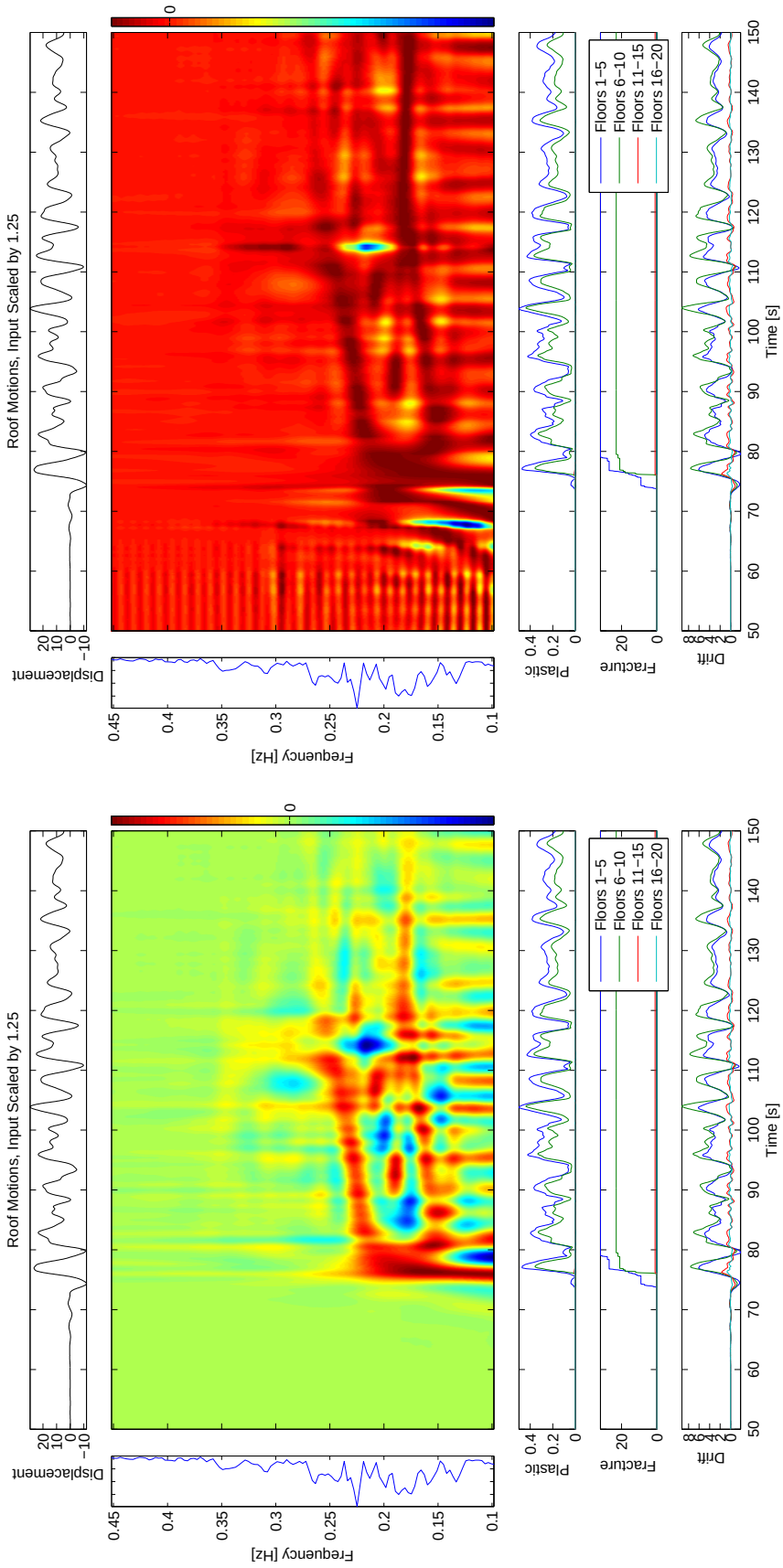

(a) Scaled by 125%

(b) Scaled by 125%, Normalized

Figure 3.17: As in Figure 3.12, for scaling of 125% of the original amplitudes. Complete weld fractures on the first 5 floors, with nearly complete weld fractures on floors 6-10. Natural frequency has been permanently changed by approximately 43%, corresponding to a loss of 67% of the total stiffness. At these amplitudes, the permanent offset in the roof (drift due to plastic deformation) results in DC-like oscillations at low frequencies, though the evolution of the frequency content is still clear in the normalized plot.

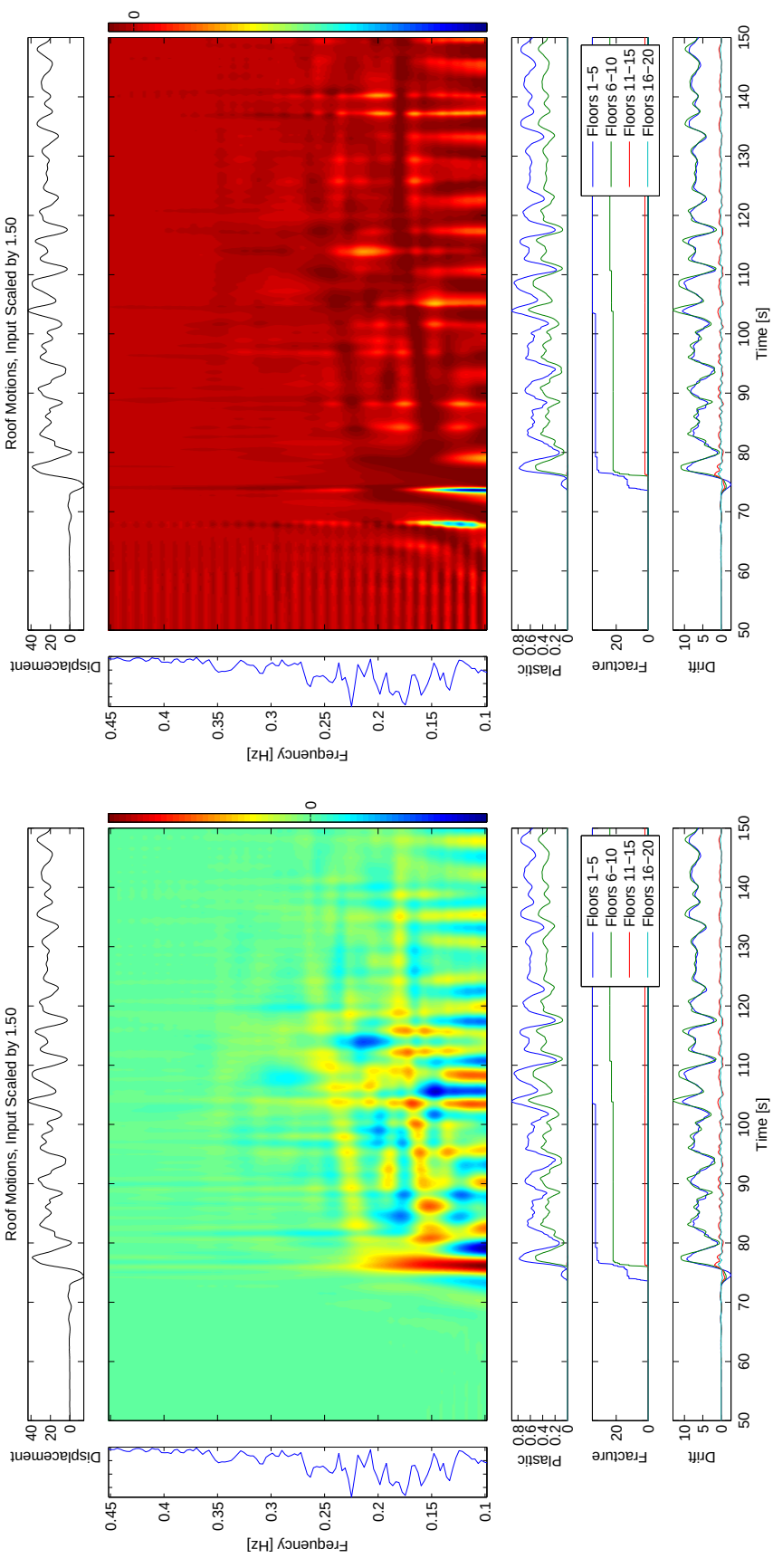

(a) Scaled by 150%

(b) Scaled by 150%, Normalized

Figure 3.18: As in Figure 3.12, for scaling of 150% of the original amplitudes. Complete weld fractures on the first 5 floors, nearly complete weld fracture on floors 6-10. Natural frequency has been permanently changed by 43%, corresponding to a loss of 67% of the total stiffness. At these amplitudes, the permanent offset in the roof (permanent drift, plastic deformation) again results in DC-like oscillations at low frequencies. Further work needs to be done in order to create a time-frequency representation that can properly handle large permanent deformations.

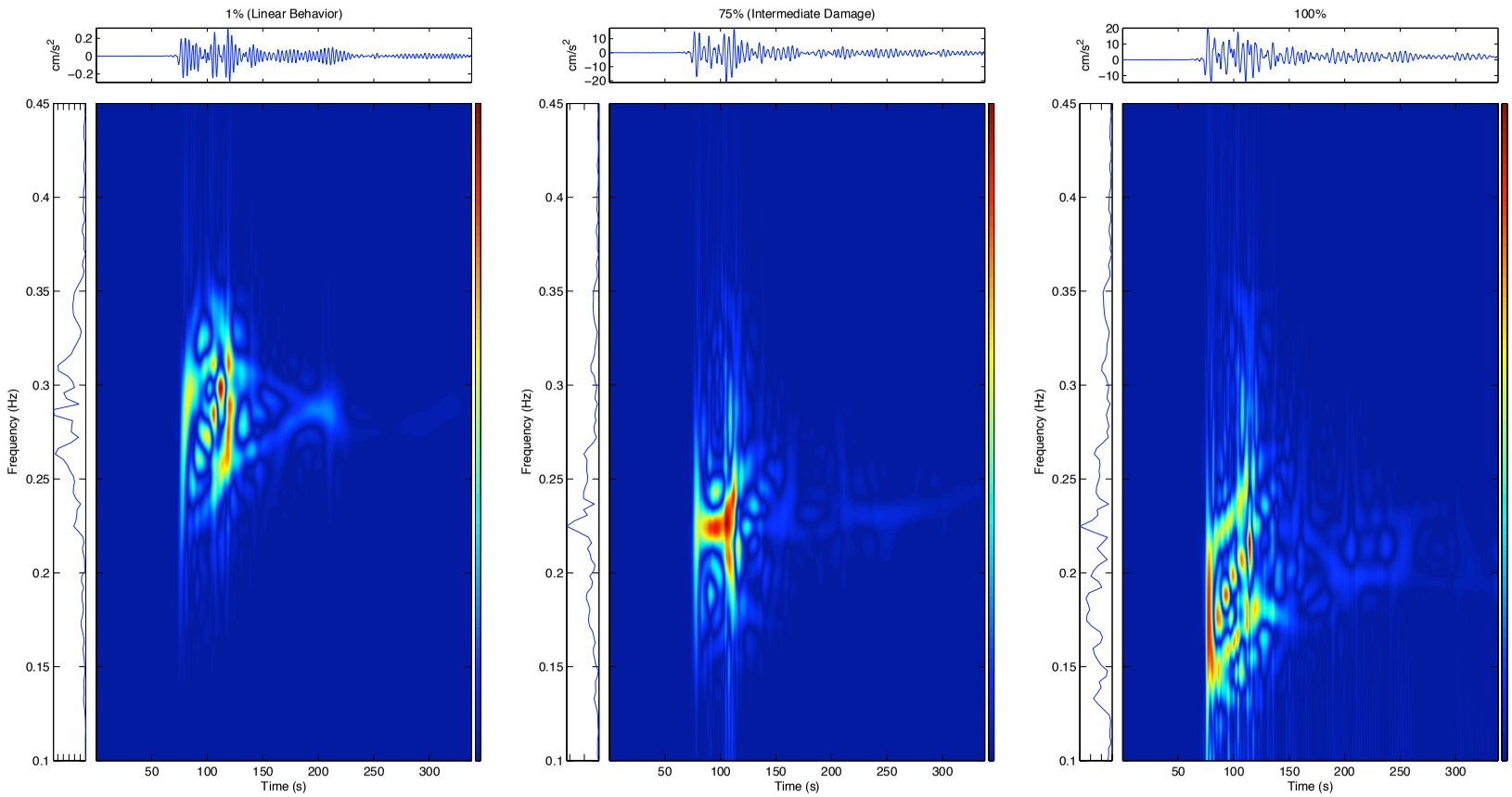

(a) Scaled by 1% (Linear)

(b) Scaled by 75%, (Intermediate)

(c) Scaled by 100%

Figure 3.19: Summary of evolving damage patterns for increasing levels of input motions and damage. (Compare with Figure 3.20.) Damage patterns as seen in Figures 3.12, 3.15, and 3.16. In addition to a change in frequency content (the Fourier Transform along the y-axis), the distribution of energy in the time-frequency plane is significantly different under these excitation levels. The splitting of the frequency content in **(c)** represents the different behavior of the roof displacements after the first few floors are severely damaged.

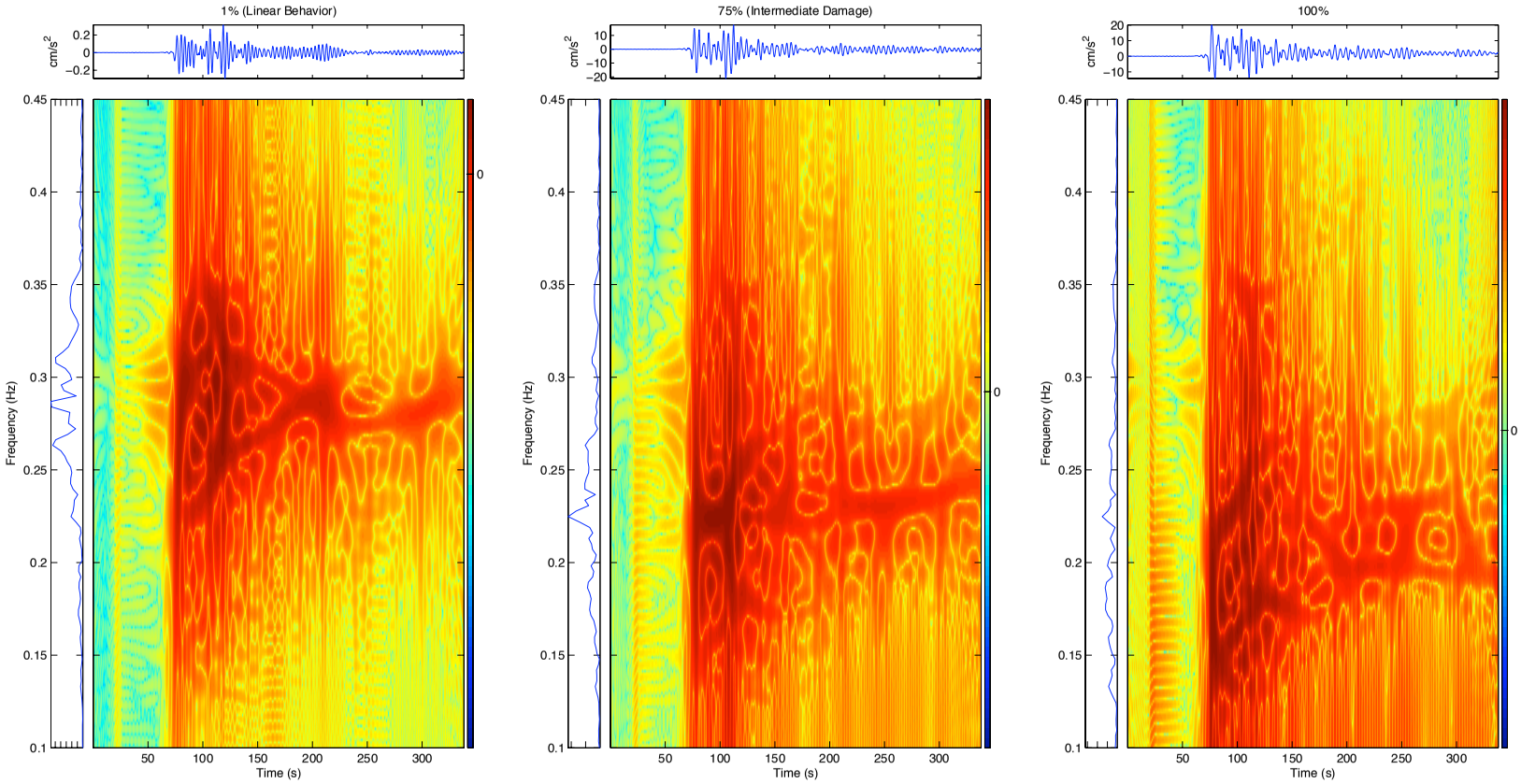

(a) Scaled by 1% (Linear) (b) Scaled by 75%, (Intermediate) (c) Scaled by 100%

Figure 3.20: Summary of evolving damage patterns for increasing levels of input motions and damage, $log10(abs())$. (Compare with Figure 3.19.) Damage patterns as seen in Figures 3.12, 3.15, and 3.16. The logarithmic scaling reveals a more complete representation of (pseudo-)energy in the time-frequency plane. At each level of excitation the roof record has a different distribution of energy in the time-frequency plane, from the nearly linear behavior in **(a)** to the nonlinear behavior in **(c)**.

3.3 Conclusions and Discussion

Physical properties of a changing system can be usefully explored through time-frequency analysis. Losses of stiffness are associated with decreases in natural frequency, and it is possible to identify nonlinear elastic behavior, plastic behavior, and damage (e.g., weld fractures) by tracking the estimated frequency at each instant. Distinguishing between nonlinear elastic behavior, plastic behavior, and damage is not straightforward. If a system's frequency decreases during strong motions and then recovers to pre-event levels, it is likely amplitude-related nonlinear elastic behavior or plastic behavior with a recovery to the original stiffness. Permanent changes in the natural frequency are more often correlated with damage.

The simple SDOF of Section 3.1 provides a useful example of using time-frequency representations to extract information about a system with changing stiffness. A 20-story finite-element building model has many more degrees of freedom than the simple system, but in Section 3.2 I show that it is possible to extract a similar relationship between the natural frequencies and the instantaneous stiffness. Increasing damage and plastic behavior decreases the observed natural frequency, though for the strongest levels of shaking the information in the time-frequency plane yields less useful information. This is not a serious shortcoming of using these methods for damage detection, as at these larger amplitudes it is already immediately obvious from the original time-domain information that large permanent deformations have occurred and, therefore, detailed time-frequency investigations are not necessary. The instantaneous behavior of the system allows for an investigation of the fragility of the building, such as correlating the instant of fracture of an element with the amplitudes of input motions. In complicated systems such as the 20-story building, time-frequency representations can also be used to explore building behavior as a first step to developing a parametric model of the system.

Chapter 4

Time-Frequency Representations: Response of Instrumented Structures

For instrumented structures, obtaining perfect information about the physical properties at each instant is impossible. The synthetic systems of Chapter 3 are useful examples of evolving systems, as the physical properties are perfectly known at each time instant. In the analysis of the behavior of real systems, physical properties are typically inferred from the building records. The natural frequencies, mode shapes, and damping parameters can be estimated from instrument records, either for an entire event of interest or evaluating the record in segments to track the evolution of the properties. An appropriate parameterization for a system is not always straightforward, particularly when analyzing a structure with changes in stiffness from damage. Exploratory methods such as time-frequency analysis are a valuable tool for investigating the behavior of a system and can be used to track evolving frequency content in an arbitrary signal. These time-frequency methods can then be expanded to provide estimates of dynamic properties of the system and provide useful insight into the physical nature of a system – which can in turn lead to a more accurate parameterization for further system identification.

There are several instrumented civil structures that have undergone strong shaking, some to failure. Applying time-frequency analysis methods to these structures reveals the instantaneous frequency content in the system, which can then be used to

create an estimated damage pattern. The numerical studies of this chapter along with the synthetic results from Chapter 3 motivate a discussion of how to associate damage with the time-frequency behavior of the system. In general, damaged structures have a distinctive "fingerprint" in the time-frequency plane, though further empirical study is required.

Sample records from several structures are presented with time-frequency analysis and discussion. I begin with an investigation of Millikan Library (California Institute of Technology campus, Pasadena, CA), which has experienced several major earthquakes since construction in the 1960s. Many of these earthquake events have had a permanent effect on the natural frequency of the building, as seen in Figure 1.1. Studies of Millikan's response to different levels of excitation (e.g., wind, earthquakes, forced vibration testing) have revealed interesting nonlinear behavior as well as sensitivity to weather conditions such as rainfall and temperature. With many potential factors influencing the observed dynamic properties of the building, time-frequency analysis methods provide a valuable exploratory tool. An introduction to frequency/amplitude studies is discussed for Millikan Library during the Northridge Earthquake in order to examine amplitude related nonlinearity during this event.

I also present a brief description of a 52-story office building in Los Angeles, CA, and the observed behavior during the 1994 Northridge Earthquake. This 52-story building is a tall, flexible building that remained nearly linear during the Northridge event and experienced no permanent change in dynamic properties.

The last section is an investigation into the Imperial County Services Building (El Centro, CA). This instrumented building was damaged (partial collapse) in the 1979 Imperial Valley Earthquake and was later demolished due to the earthquake damage.

4.1 Millikan Library (Caltech), Pasadena, CA

A well-investigated testbed building for Structural Health Monitoring is the Millikan Library on the Caltech campus – one of the world's most heavily researched and instrumented buildings. (Appendices A and B present a summary of the Millikan

Library instrumentation and the measured dynamic properties since construction in the 1960s.) This nine-story reinforced concrete building has undergone strong shaking from several earthquakes, and I present an investigation into the earthquake behavior during selected events. To place the dynamic property in context with previous studies of the Millikan Library, I begin with a summary of earlier research into the nonlinear behavior of the library. Forced vibration tests by Bradford et al. (2004) (Appendix B) demonstrated that the natural frequencies of Millikan vary based on the applied force. Analysis of continuous Millikan records also reveals sensitivity to weather conditions, such as rain, winds, and temperature, which further complicates the analysis of Millikan library.

The earthquakes investigated are: the 1971 San Fernando Earthquake, Section 4.1.2; the 1987 Whittier Narrows Earthquake, Section 4.1.3; the 1991 Sierra Madre Earthquake, Section 4.1.4; and the 1994 Northridge Earthquake and aftershock, Section 4.1.5. These earthquake records are represented in the historical summary plot of Figure 1.1 as events that have significantly affected the dynamic properties of Millikan Library. Under smaller excitations, such as the Northridge aftershock and the 2005 Parkfield Event (presented in the time-frequency example of Section 2.13.3), Millikan has a temporary change in natural frequency that recovers immediately after the shaking ends. In larger, damaging events, the natural frequency of the system never recovers to pre-event levels due to a permanent loss of stiffness.

Investigating the onset of changes in natural frequency reveals important information regarding the onset of damage. Using time-frequency techniques such as the spectrogram to derive instantaneous relationships between measures of the building (e.g., peak roof velocity/acceleration, drift) and damage (e.g., weld fracture, cracking of the foundation) provides a rough approximation for the fragility of building components to different levels of excitation. The windowing effect of the spectrogram smears information temporally such that the exact onset of changes in natural frequency are difficult to extract. Advanced time-frequency methods such as the Reduced Interference Distribution provide better temporal resolution and a more detailed exploration of the dynamic properties.

The Northridge and Sierra Madre records were digitized by the National Strong Motion Program (NSMP) through the United States Geological Survey (USGS). The Whittier Narrows event was digitized by the California Division of Mines and Geology (CDMG). Records from the San Fernando event were digitized through the Earthquake Engineering Research Laboratory (EERL) at the California Institute of Technology, and obtained with cooperation from the University of Southern California.

4.1.1 Millikan Library: Sensitivity to Weather Patterns

In Clinton et al. (2006), the authors present a description of the observed wander of the natural frequencies of Millikan Library. The natural frequencies are sensitive to the level of excitation (as seen in, e.g., Kuroiwa (1967) and Appendix B), with higher amplitudes of motions corresponding to lower observed frequencies. The nonlinear response between amplitude and observed frequency extends to the response of Millikan Library under wind and earthquake loading, where larger amplitude motions correspond to increased building response and a lower natural frequency. Millikan Library is also sensitive to other weather conditions such as rainfall and extreme temperatures, which complicates inferring changes in structural properties based on changes in apparent natural frequency.

In the historical behavior plot of Figure 1.1, the data is collected at sparse intervals throughout decades of investigation. The continuous instrumentation of station MIK (a triaxial SCEDC station on the 9th floor, see Appendices A and B) has allowed for a more detailed investigation of the wander in the natural frequencies, as in Figure 4.1. In this figure, the frequency is estimated from a spectrogram of the continuous data set, and there is considerable deviation from the mean natural frequency. Apart from weekly/monthly trends in the frequency, there are temporary changes that occur over a very short timespan, often associated with earthquakes, forced vibration tests, and weather patterns, as shown in the bottom plot. An increasing trend over the last few months of the plot (strongest in the EW mode) corresponds with construction of

non-structural partition walls and redistribution of books to repurpose several floors as office space.

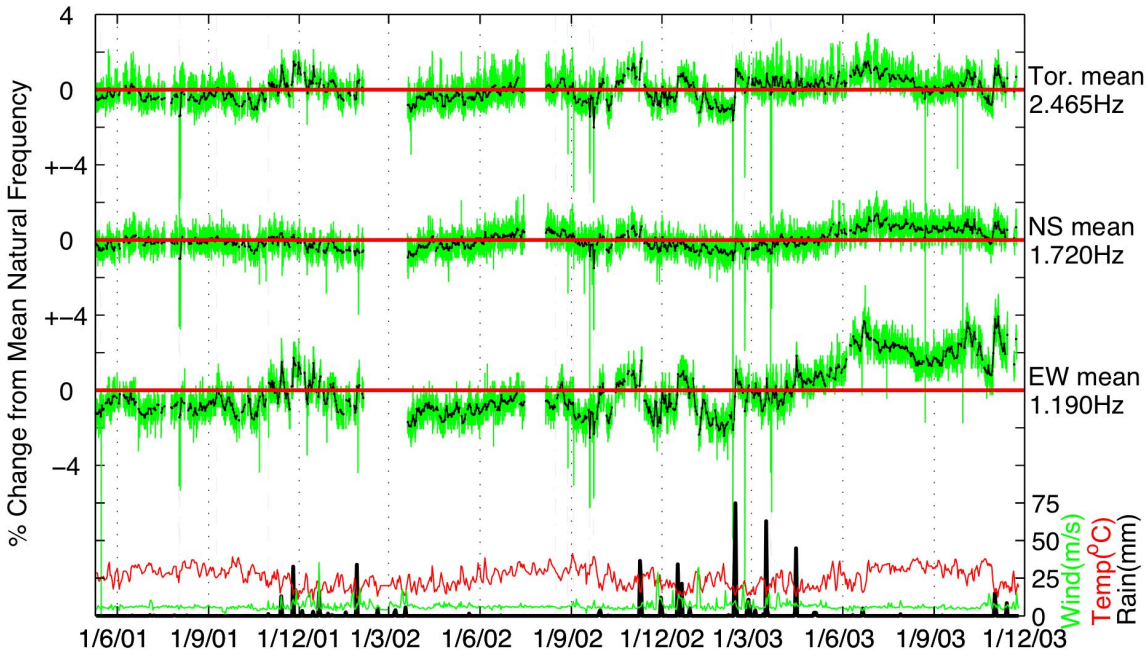

Figure 4.1: Deviation from the mean natural frequency for the 3 fundamental frequencies at Millikan Library station MIK, May 2001 – Nov 2003. Fundamental frequencies and the deviation from average are calculated at each hour. The hourly peak is shown in thin green lines, the thick black line tracks the daily average. The thick red horizontal line is the average frequency for the entire time range. Daily rainfall (black), max wind gust (green), and max temperature (red) from JPL are plotted along the bottom of the figure. Adapted from Clinton et al. (2006).

Wind storms and rainfall both influence the behavior of Millikan Library, as can be more clearly seen during a sixty day period during 2003 (Figure 4.2). This time period had both strong winds and heavy rains. In the top plot is a spectrogram of the EW component of station MIK, trimmed to show the first EW mode. (The EW component is the most sensitive to weather effects.) The middle plot is a normalized spectrogram, scaled by the peak amplitudes, which allows for a clearer investigation into the evolving natural frequency. The bottom plot shows rainfall and windspeed for this interval, as measured at the JPL weather station (`http://weatherstation.jpl.nasa.gov/`).

In the top plot of Figure 4.2, there are several interesting features of the spectrogram. Moving from left to right, the strong winds of January 5th and 6th result in high amplitudes of shaking on those days. There is also a daily cycle in amplitude, which is tied to the air conditioning equipment; the air conditioner is turned off each night from midnight to 4:00 a.m., and is responsible for a change in the ambient noise in the building. A pattern of increasing and decreasing daily amplitude, in intervals of . . . 5-2-5-2. . . , represents weekday/weekend differences in building use, though this is somewhat masked by the weather behavior during this timespan. Continuing left to right, there are noticeable glitches in the data, narrow spikes of high amplitude shaking, which represent forced vibration tests (February 10th), and a small earthquake (22 February 2003, Big Bear M5.4, $\Delta = 119km$). In the normalized plot it is easier to identify the changes in frequency correlating with the increased amplitudes during the windstorm. The overall correlation between rainfall and natural frequency from February 11th through the 13th also stands out more clearly in the normalized plot.

Figures 4.3 and 4.4, adapted from Clinton et al. (2006), quantify the observed changes during the rainfall and windstorm of Figure 4.2. For rainfall, Figure 4.3, heavy rain increased the natural frequency of the EW and Torsional modes by more than 3% within a day of the storm, leaving the NS mode largely unaffected. The second EW mode (not shown) is similarly affected (Clinton et al., 2006). At the end of the rain event, the system frequency recovers to pre-rain levels over a timespan of 7-10 days. Though this shift in natural frequency is not fully understood, one suggested mechanism involves the relation of the foundation to the surrounding soil at different levels of saturation. Applying Biot's theory of wave propagation to a shear beam embedded in a poroelastic half space gives results that qualitatively match the behavior of the Millikan Library during heavy rainfall (Todorovska and Al Rjoub, 2006a; Todorovska and Al Rjoub, 2006b).

Wind, in Figure 4.4, has the opposite effect on the natural frequency, decreasing the frequency by 3% during the period of highest windspeeds. The building recovers from the wind effects immediately, which is consistent with the known nonlinear

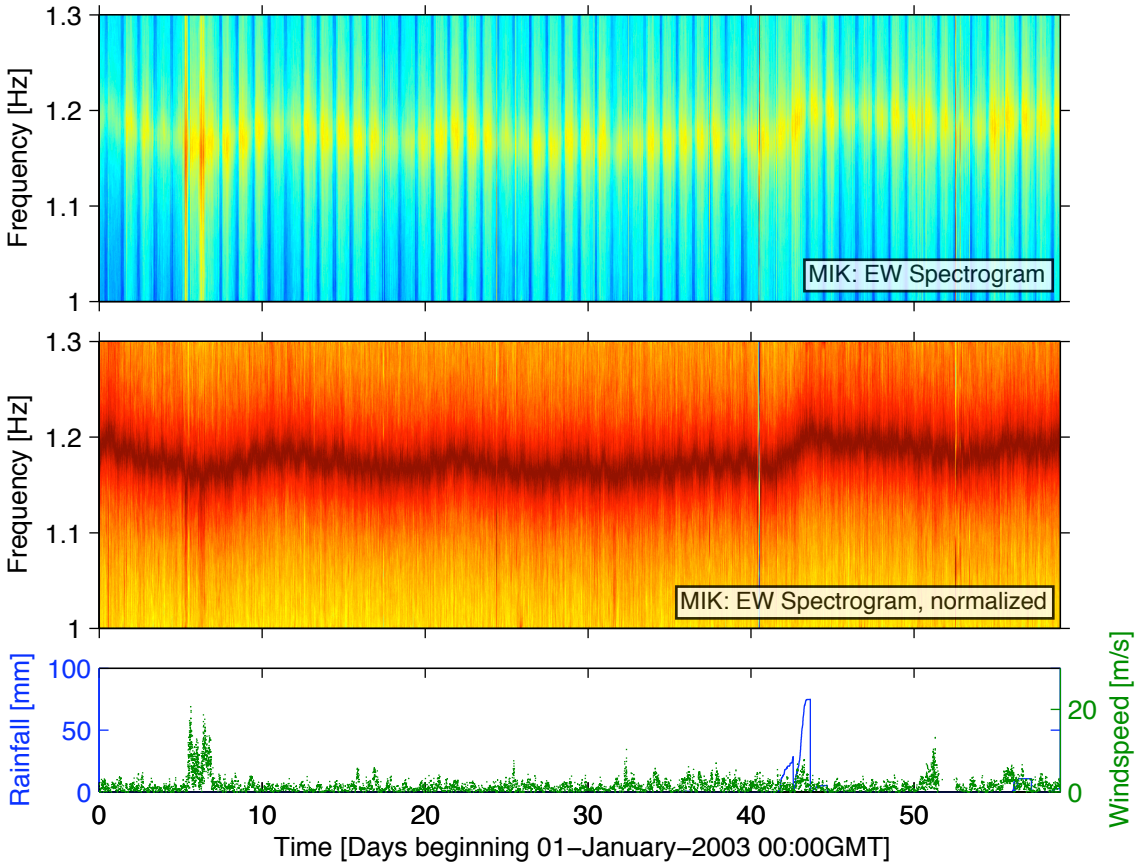

Figure 4.2: Spectrogram of 60 days of Millikan Library, from January 1st through February 28th 2003, including strong winds and heavy rainfall. EW Component of station MIK. In the top plot is the spectrogram, showing the wander of the frequency content near the first mode of the building. The second plot is a scaled spectrogram, which more clearly shows the change in observed peak frequency, particularly during the windstorms of January 5th and 6th, and the rainfall of February 11th through 13th. (Forced vibration testing, February 10th; Big Bear earthquake, M5.4, $\Delta = 119$, 22 February 2003)

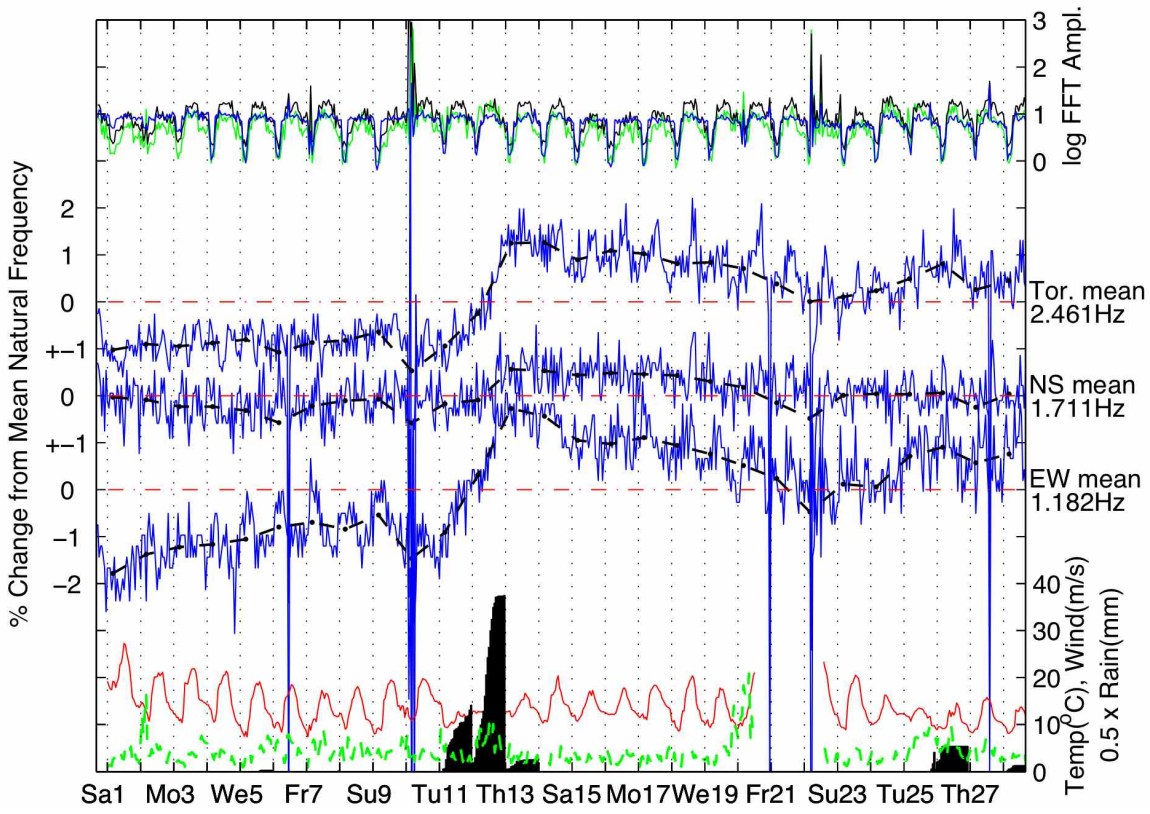

Figure 4.3: Deviation from the mean for the natural frequencies of Millikan Library during February 2003, which includes a major rainstorm. Fundamental frequencies and the deviation from average are calculated at each hour. The hourly peak is shown in thin blue lines, the thick dashed black line tracks the daily average. The dashed red horizontal line is the mean frequency for this time interval. Weather data is shown at the bottom of the figure, the black bar data is the cumulative hourly rainfall (re-zeros at midnight). The red line is the maximum hourly temperature, and the green is the wind gust. At the top of the figure are the natural frequency amplitudes for the hourly FFT peak. The rainfall coincides with a very sharp rise in natural frequencies in the EW and Torsional modes, followed by a slow return towards pre-rainfall levels. Dashed vertical lines represent the start of each new day (12:00 a.m. PST). Frequency spikes are due to instrument glitches (6th, 21st, and 27th of February), forced vibration testing (February 10th) and the Big Bear earthquake of 22 February 2003. No major increase in excitation amplitude occurs during rainfall events not associated with high winds. Adapted from Clinton et al. (2006).

behavior of the building. Again, the EW and Torsional modes are most strongly affected. As wind tends to decrease the observed natural frequency and rain tends to increase the observed frequency, the behavior of the building during a typical storm (heavy rain and strong winds at the same time) would be difficult to model. The days selected for this analysis represent windy days with no rainfall and a rainstorm with unusually low windspeeds, allowing for a separation of wind and rain effects.

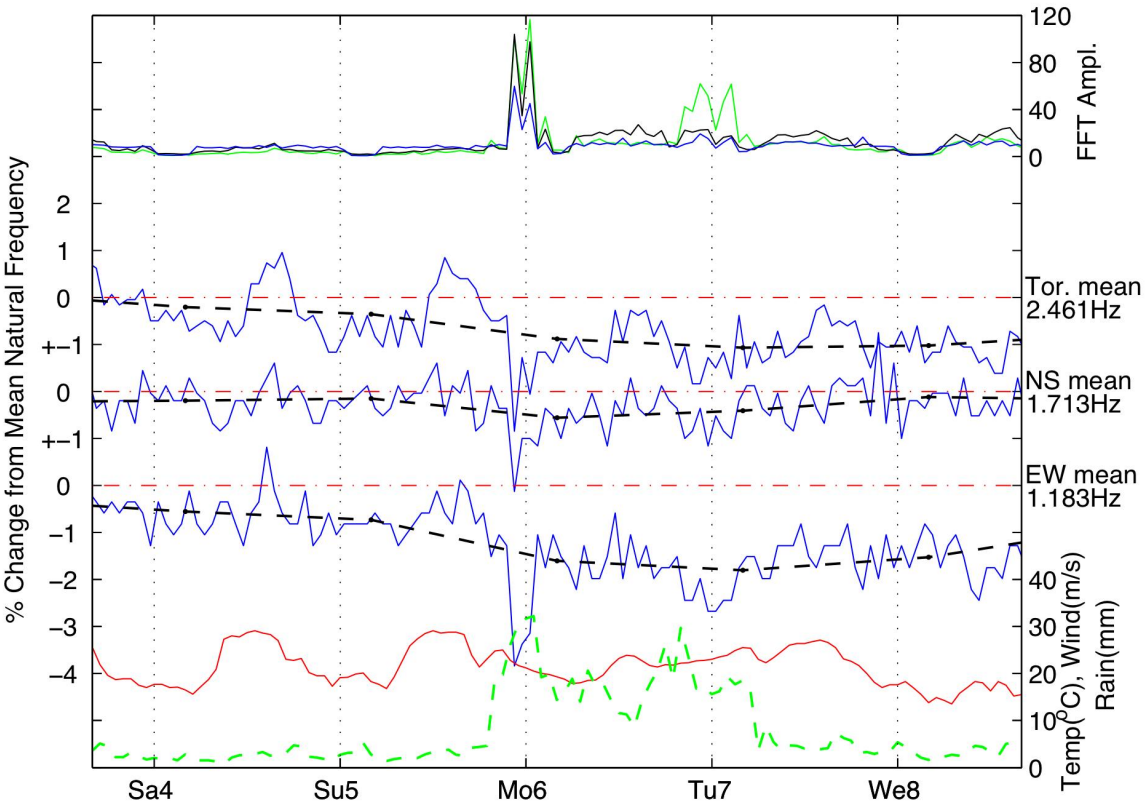

Figure 4.4: Deviation from the mean for the natural frequencies of Millikan Library in January 2003, as in Figure 4.3, for strong winds. Fundamental frequencies and the deviation from average are calculated at each hour. The hourly peak is shown in thin blue lines, the thick dashed black line tracks the daily average. The dashed red horizontal line is the mean frequency for this time interval. Weather data is plotted at the bottom of the figure. The natural frequencies of the Library dramatically decrease for the duration of the most intense windstorm, most notably in the EW direction but also significantly for the NS and torsional modes. Natural frequencies recover to pre-wind levels quickly. Adapted from Clinton et al. (2006).

One further weather-related factor is the effect of temperature on the natural frequencies (Figure 4.5). All natural frequencies can increase by more than 3% in

a daily cycle during periods of high temperatures, with the torsional mode most strongly affected.

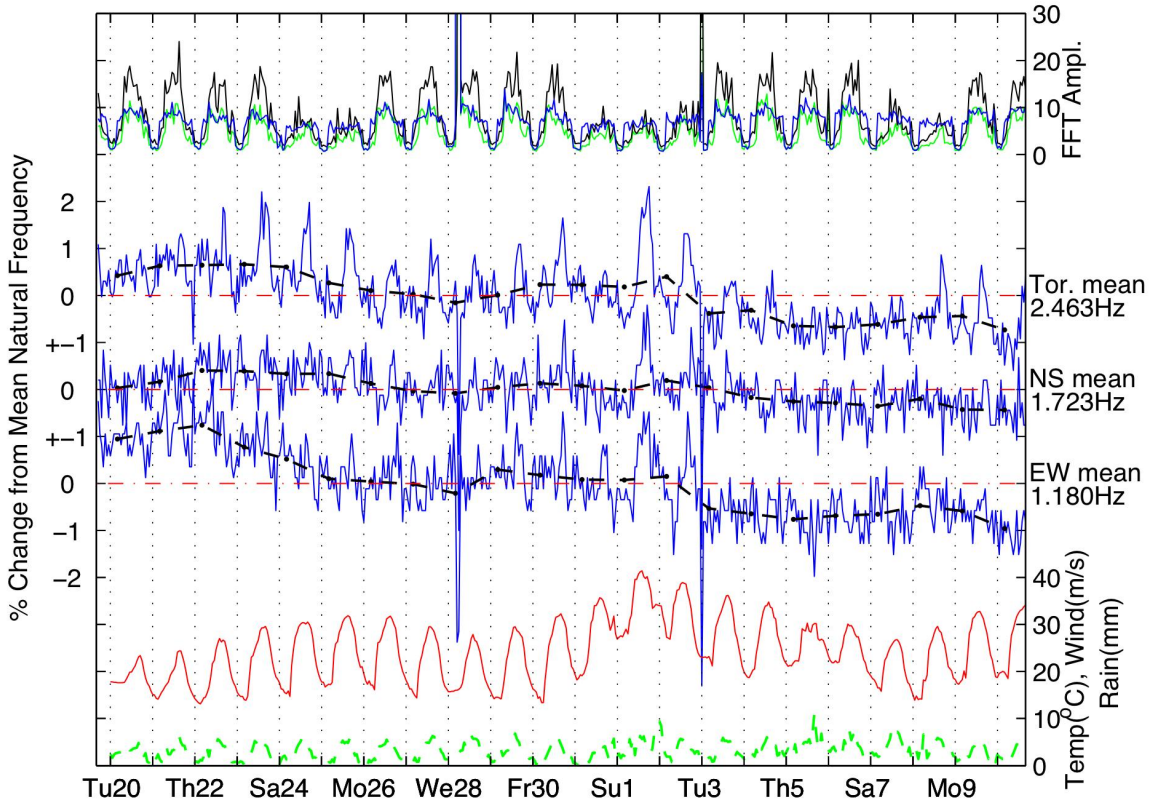

Figure 4.5: Deviation from the mean for the natural frequencies of Millikan Library in August and September of 2002, as in Figure 4.3, for high temperatures. Fundamental frequencies and the deviation from average are calculated at each hour. The hourly peak is shown in thin blue lines, the thick dashed black line tracks the daily average. The dashed red horizontal line is the mean frequency for this time interval. Weather data is plotted at the bottom of the figure. These temperatures represent typical daily variations during the summer months. All 3 natural frequencies increase during the hottest days. Adapted from Clinton et al. (2006).

4.1.2 Millikan Library: 1971 San Fernando Earthquake

In Figure 1.1, I presented the historical behavior of Millikan Library since construction, and the most striking feature in this plot was the change in natural frequency during the San Fernando event (9 February 1971, $M_w = 6.6$, $\Delta \sim 31km$), particularly in the EW component. During this event, there was a permanent loss of stiffness in the building, which has been suggested to be the result of non-structural damage to the superstructure and cracking along the foundation/basement levels. The exterior walls on the East and West side of the building are shear walls that resist NS motions, and the central elevator core provides further NS stiffness as well as resisting EW motions. (Please see Appendix B for Millikan structural diagrams.) Non-structural window panels on the North and South faces of the building provided additional stiffness in the EW direction at the time of construction (though they were not designed to carry lateral loads). After the San Fernando event there was a small amount of observed damage to these panels (Jennings, 1971). There is also evidence that some foundation elements were permanently damaged in the event, such as the concrete mat at the ground floor and the interface between underground steam tunnels and the Millikan Library basement.

As in previous sections, I present the Reduced Interference Distribution and spectrograms for the building response during this event, from a triaxial roof instrument (Figures 4.6 – 4.11) and a triaxial basement instrument (Figures 4.12 – 4.17). Comparing the spectrogram with the RID illustrates the increased resolution of the RID in the time-frequency plane. In the EW and NS roof records (Figures 4.6 – 4.9), the temporary and permanent changes in natural frequency are clearly evident. The corresponding horizontal basement records (Figures 4.12 – 4.15) show large amounts of energy at higher frequencies, and significant energy between $0.5Hz$ and $1.5Hz$ in both horizontal directions.

The pre-event NS frequency was estimated to be $\sim 1.9Hz$ based on forced and ambient vibration testing before the San Fernando event. During the event, the natural frequency decreased to near $1.6Hz$, though it recovered to $1.7Hz$ by the end

of the record (Figures 4.6 and 4.7). Subsequent testing indicated that the natural frequency after the San Fernando event recovered to near $1.75Hz$, though it remained permanently decreased from the pre-event natural frequency.

The EW component of Millikan was more strongly affected than the NS component. The pre-event NS natural frequency, estimated between $1.45Hz$ and $1.5Hz$, temporarily decreased to $\sim 1Hz$ during the event. By the end of the record the frequency had recovered to $\sim 1.2Hz$, and there was very little recovery in the following months/years. The larger change in the EW natural frequencies is suspected to be related to cracking of the non-structural window panels. These panels provided supplemental stiffness in the EW direction, and there were no corresponding panels providing stiffness in the NS direction.

In this section the RID plots of Figures 4.6 – 4.17, in general, have better resolution than the spectrogram methods, though the spectrogram methods provide a verification that the RID is locating energy in the correct regions of the time-frequency plane. The logarithmic spectrogram plots provide the best graphical estimate of the final natural frequency, while the RID plots provide the best estimate for the onset and extent of the initial decrease in natural frequency.

Earlier investigations into the response of Millikan Library to the San Fernando event (e.g., Fourier windows in Udwadia and Trifunac (1973) and parametric studies in McVerry (1980)) have revealed qualitatively the same evolution of natural frequency during the event as the time-frequency methods presented here. The parametric results of McVerry (1980) differ quantitatively from the time-frequency results in this section, showing similar evolution of properties during the event, but with increased natural frequencies compared with the spectrogram and RID methods. This is largely a result of a difference in methods, as the time-frequency tools of this chapter are being applied purely to the roof records, for a more exploratory analysis of the evolving properties. An identification of system parameters, as in McVerry (1980), is calculating equivalent properties of a system based on the input at the basement and the output at the roof level. McVerry's results, in this case, show a NS first mode response of $1.61Hz$ ($T = 0.62s$) during the event, decreased from $1.92Hz$ ($T = 0.52s$). The

frequency decreases in the first 7 seconds of the record and remains stable for $t = 7s$ to $t = 40s$, the limit of the study. From the Fourier Transform, the observed natural frequency of the roof response has peaks nearer to $1.55Hz$ ($T = 0.64s$), and the spectrogram/RID results therefore show energy at this frequency. The time-frequency results are not cross-transforms between the roof and basement response, but are simply identifying the frequency content of the roof response. Changes to the physical properties of the building (in this case, loss of stiffness from damaged non-structural elements) are represented in the time-frequency plane as decreasing natural frequencies, and the time-frequency results are qualitatively correct in estimating the onset and severity of these changes.

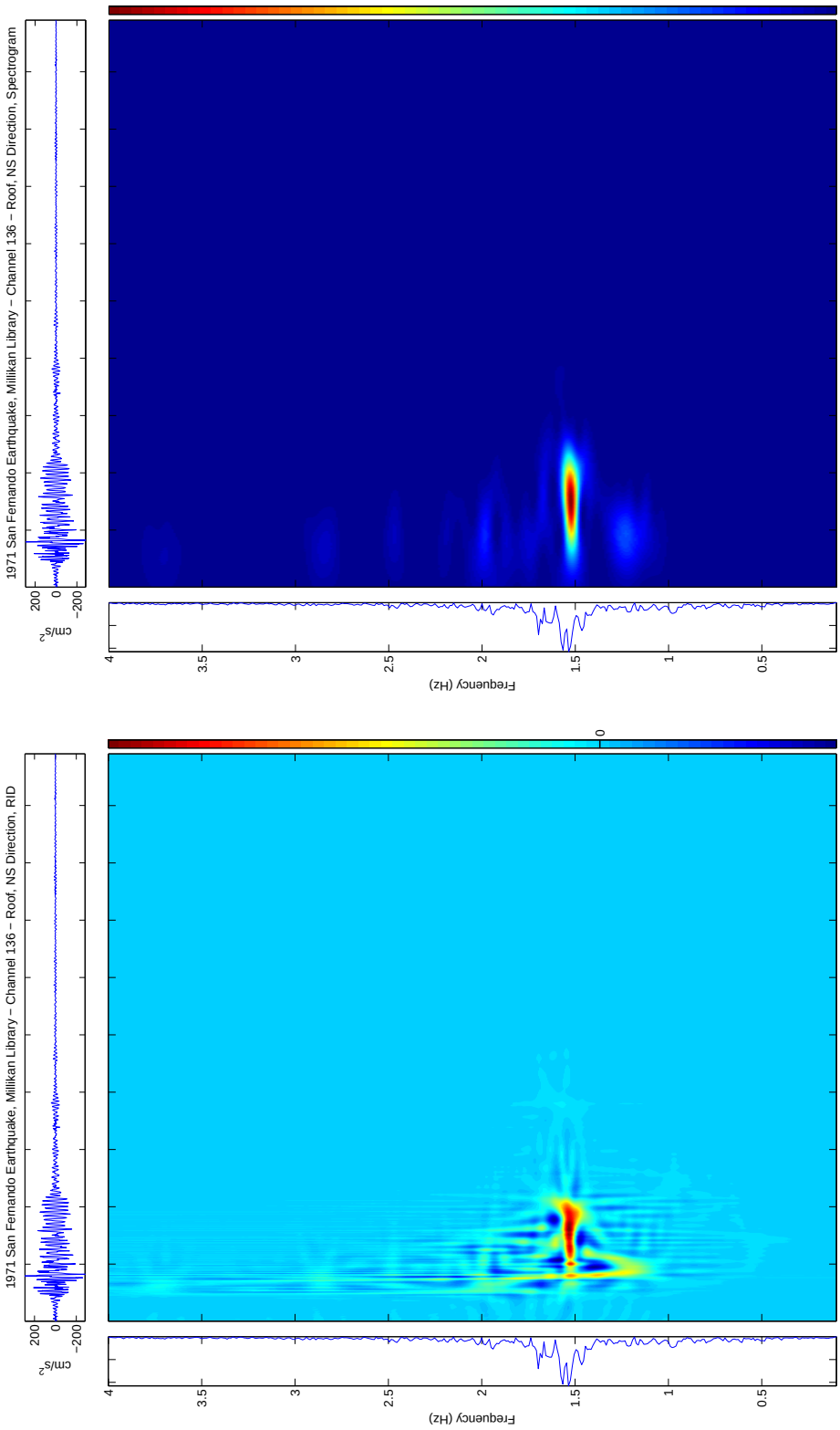

(a) RID

(b) Spectrogram

Figure 4.6: 1971 San Fernando Earthquake, Millikan Library Response. Channel 136, Roof NS. Pre-event natural frequency of $1.9Hz$ is temporarily decreased to less than $1.6Hz$, recovering to $\sim 1.7Hz$ by the end of the record. (Behavior is clearer in the logarithmic plot of Figure 4.7.)

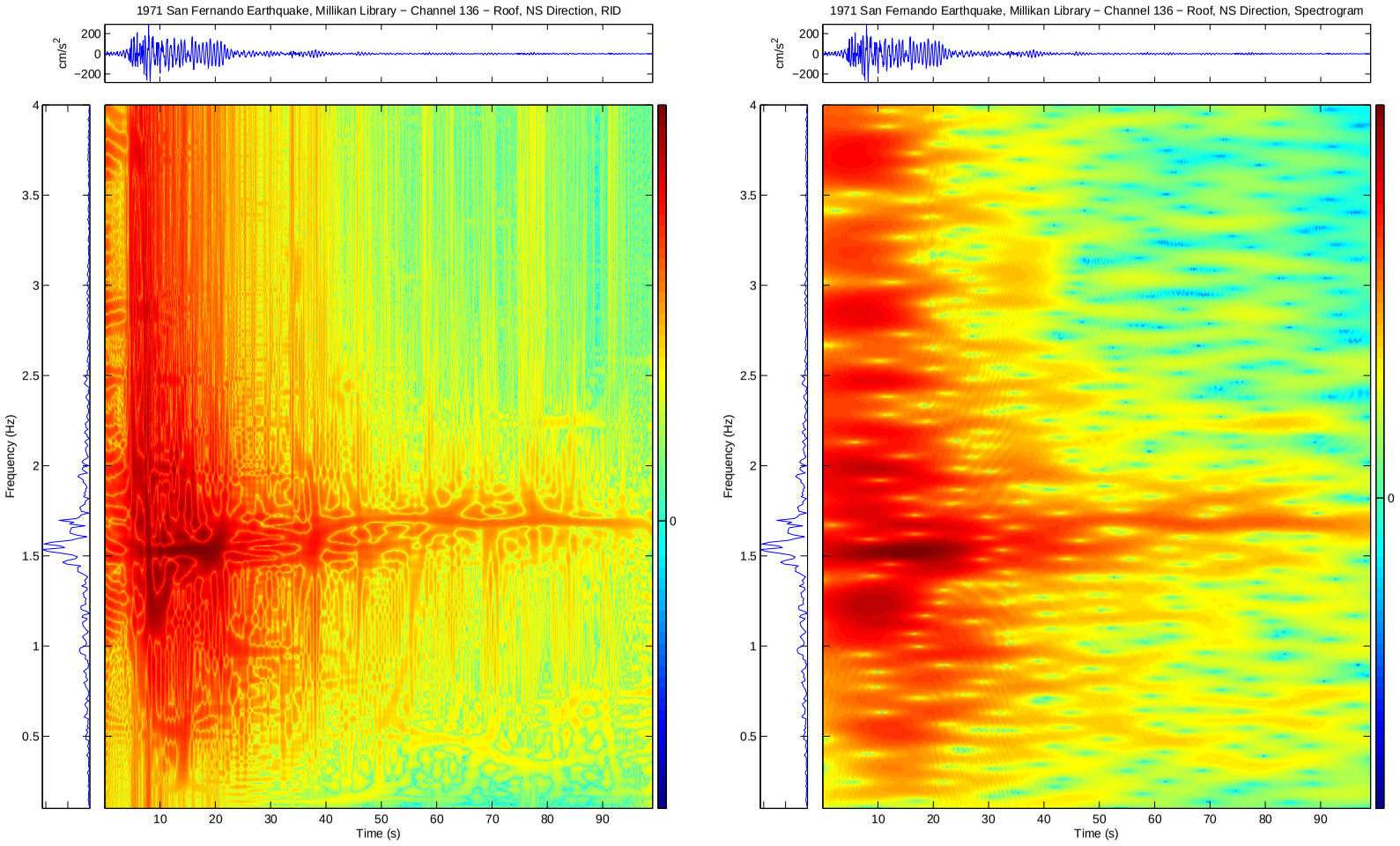

(a) RID, log10(abs())

(b) Spectrogram, log10(abs())

Figure 4.7: 1971 San Fernando Earthquake, Millikan Library Response. Channel 136, Roof NS. As in Figure 4.6, for logarithmic scaling, to more clearly show the location of (pseudo-)energy in the time-frequency plane.

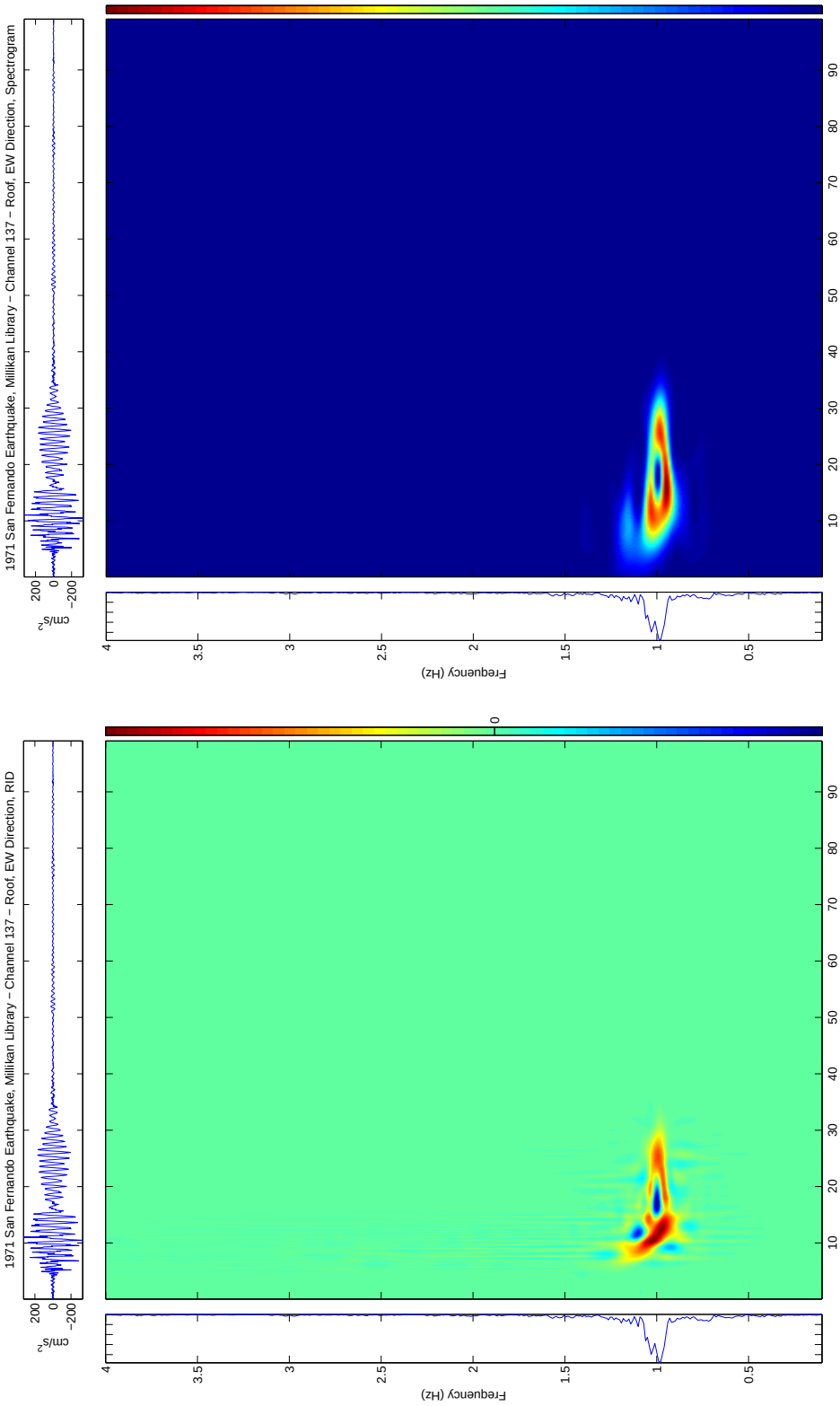

(a) RID

(b) Spectrogram

Figure 4.8: 1971 San Fernando Earthquake, Millikan Library Response. Channel 137, Roof EW. The EW component was more strongly affected than the NS component: pre-event frequency of near $1.5Hz$ was temporarily decreased to $\sim 1Hz$, recovering to $1.2Hz$ by the end of the record. Compare with the logarithmic plots of Figure 4.9.

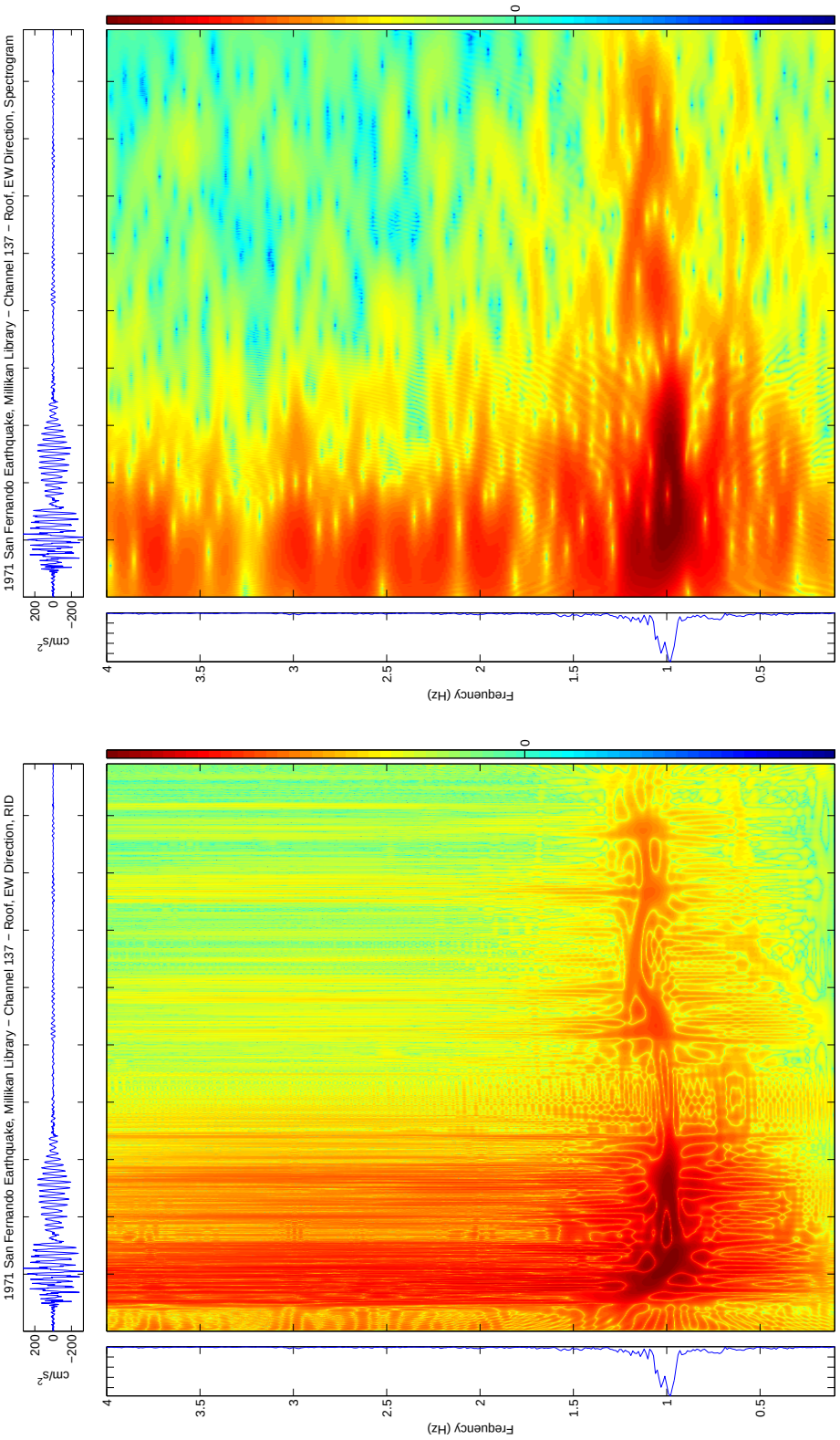

(a) RID, log10(abs())

(b) Spectrogram, log10(abs())

Figure 4.9: 1971 San Fernando Earthquake, Millikan Library Response. Channel 137, Roof EW. As in Figure 4.8, for logarithmic scaling. This allows for a better estimate of instantaneous frequency content during the record.

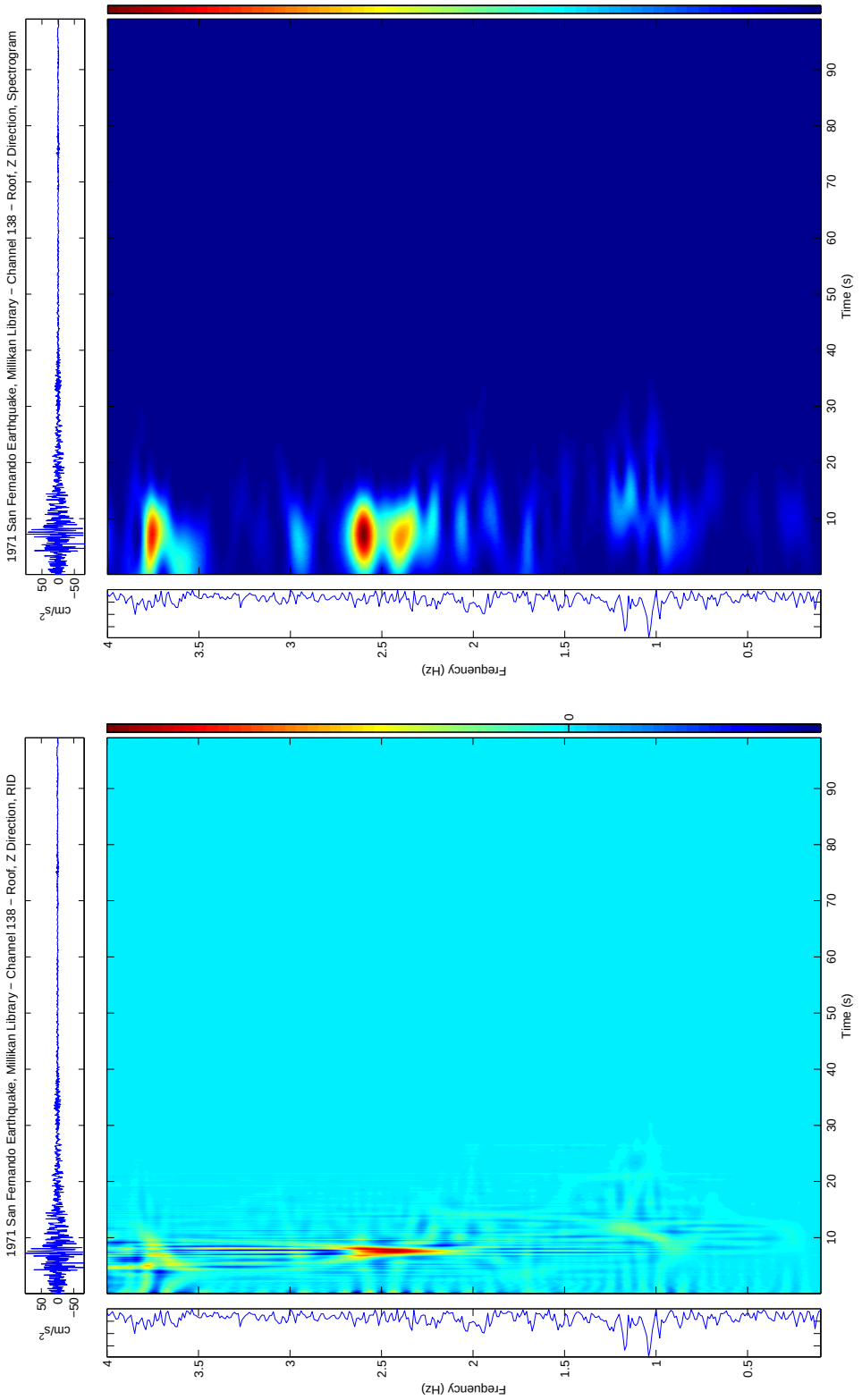

(a) RID

(b) Spectrogram

Figure 4.10: 1971 San Fernando Earthquake, Millikan Library Response. Channel 138, Roof Z.

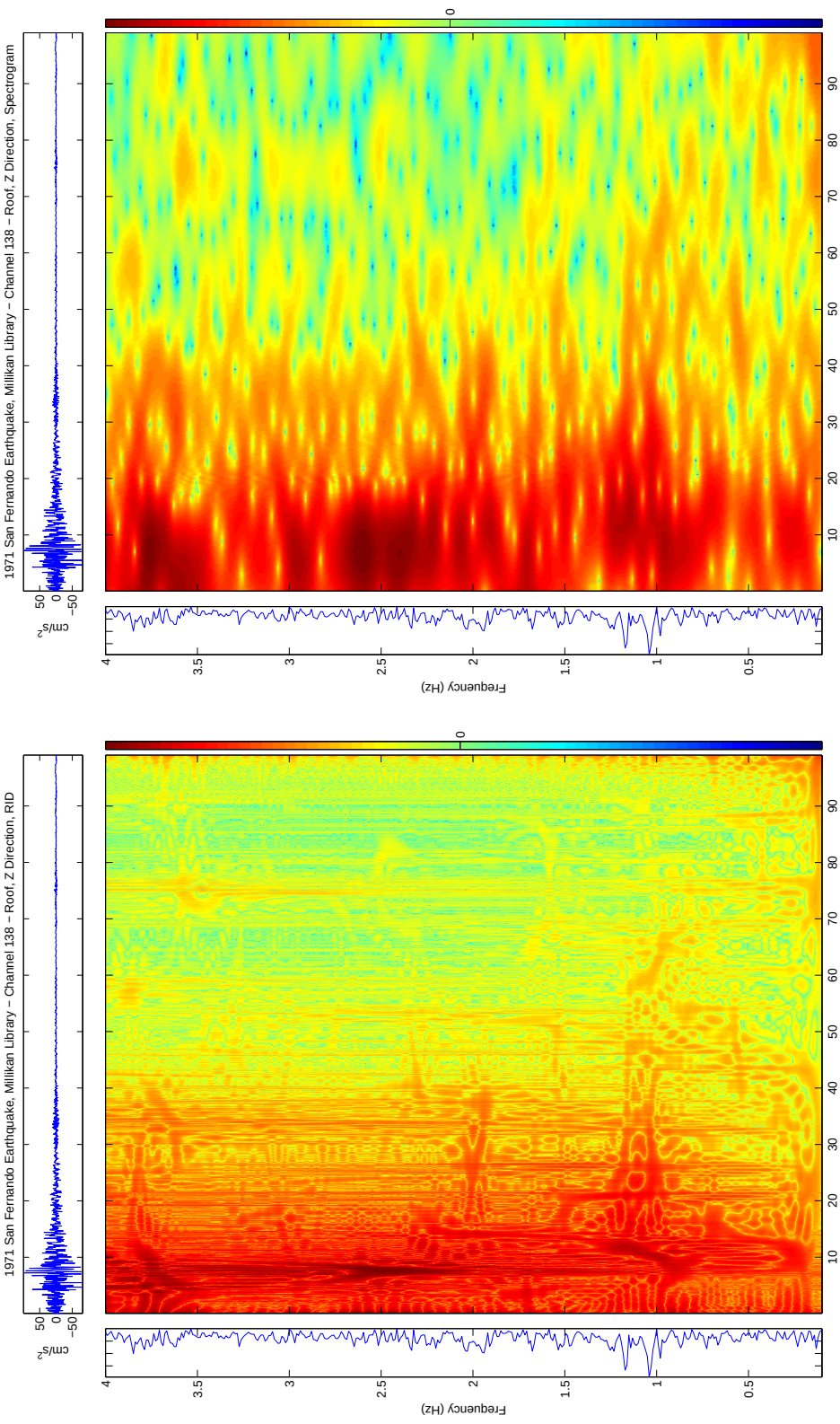

(a) RID, log10(abs())

(b) Spectrogram, log10(abs())

Figure 4.11: 1971 San Fernando Earthquake, Millikan Library Response. Channel 138, Roof Z. Logarithmic scaling.

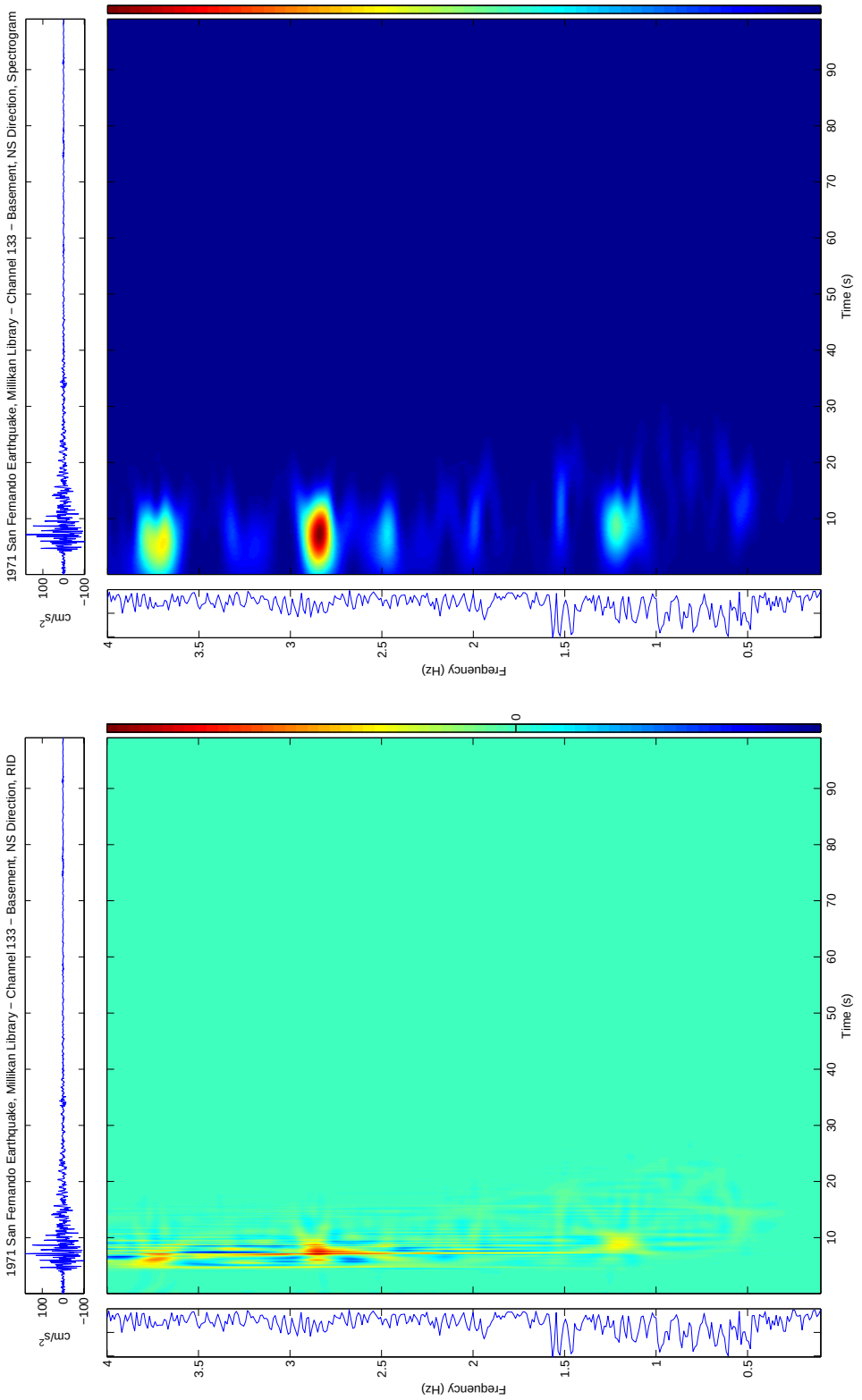

(a) RID

(b) Spectrogram

Figure 4.12: 1971 San Fernando Earthquake, Millikan Library Response. Channel 133, Basement NS.

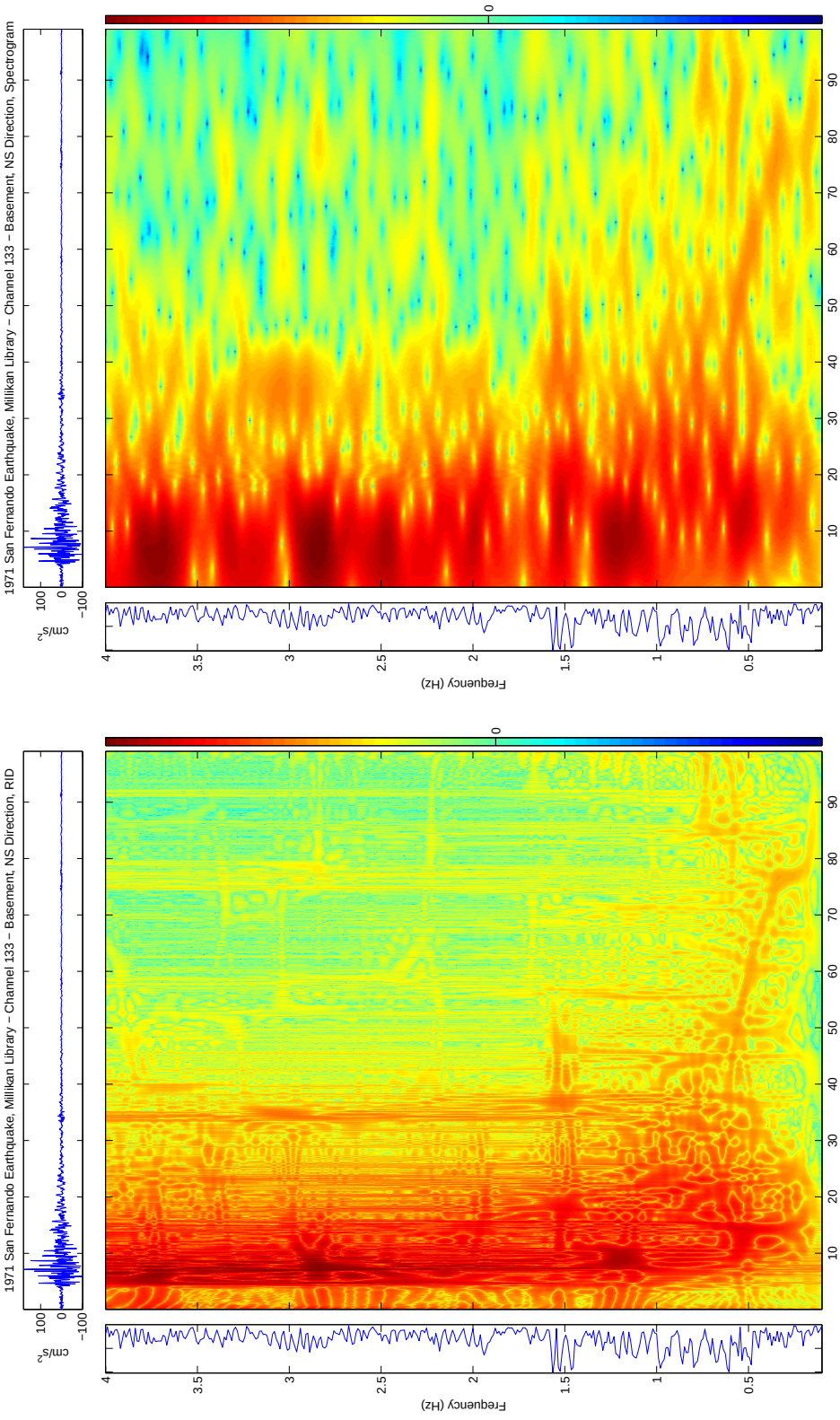

(a) RID, log10(abs())

(b) Spectrogram, log10(abs())

Figure 4.13: 1971 San Fernando Earthquake, Millikan Library Response. Channel 133, Basement NS. Logarithmic scaling.

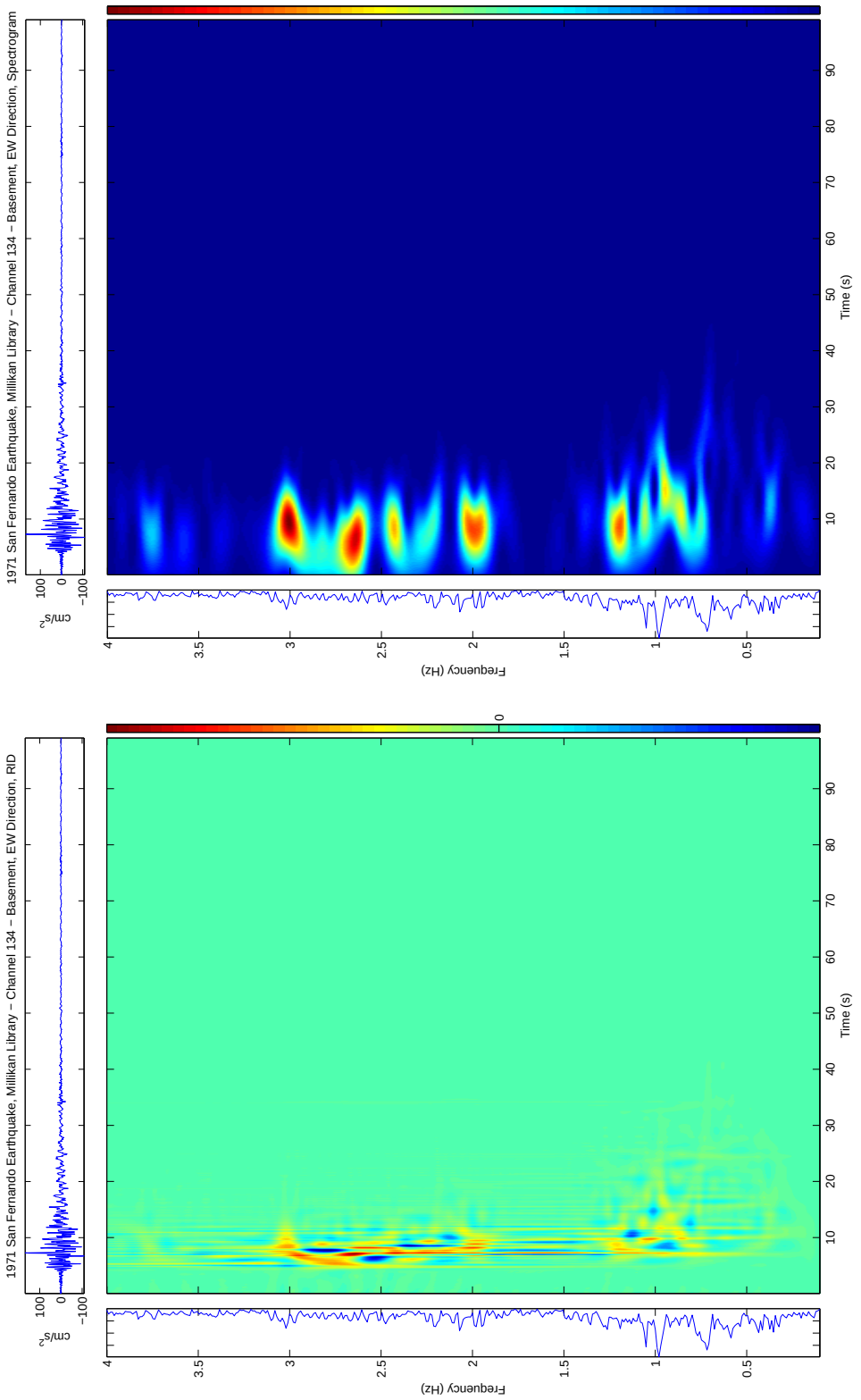

(a) RID

(b) Spectrogram

Figure 4.14: 1971 San Fernando Earthquake, Millikan Library Response. Channel 134, Basement EW.

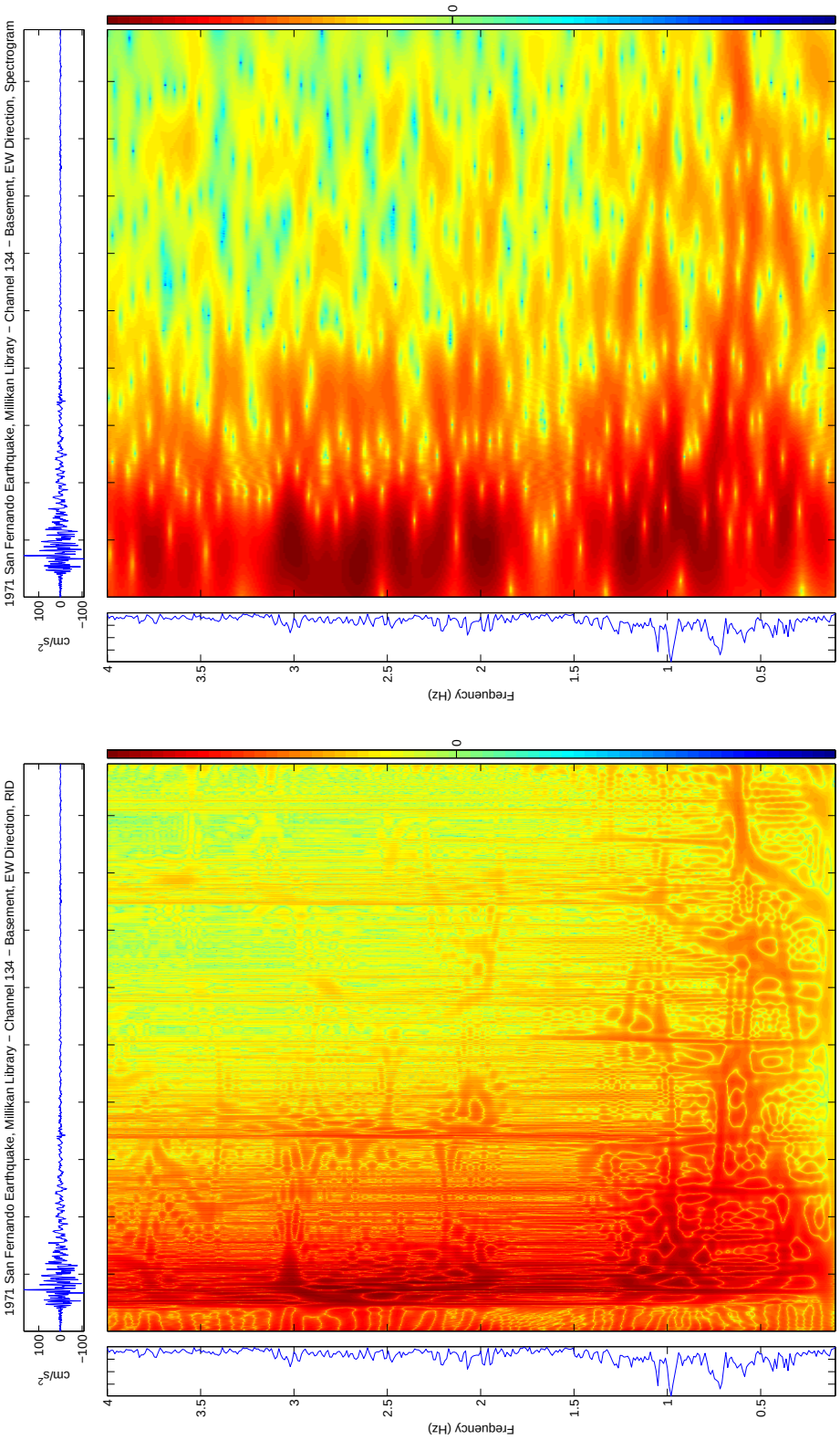

(a) RID, log10(abs())

(b) Spectrogram, log10(abs())

Figure 4.15: 1971 San Fernando Earthquake, Millikan Library Response. Channel 134, Basement EW. Logarithmic scaling.

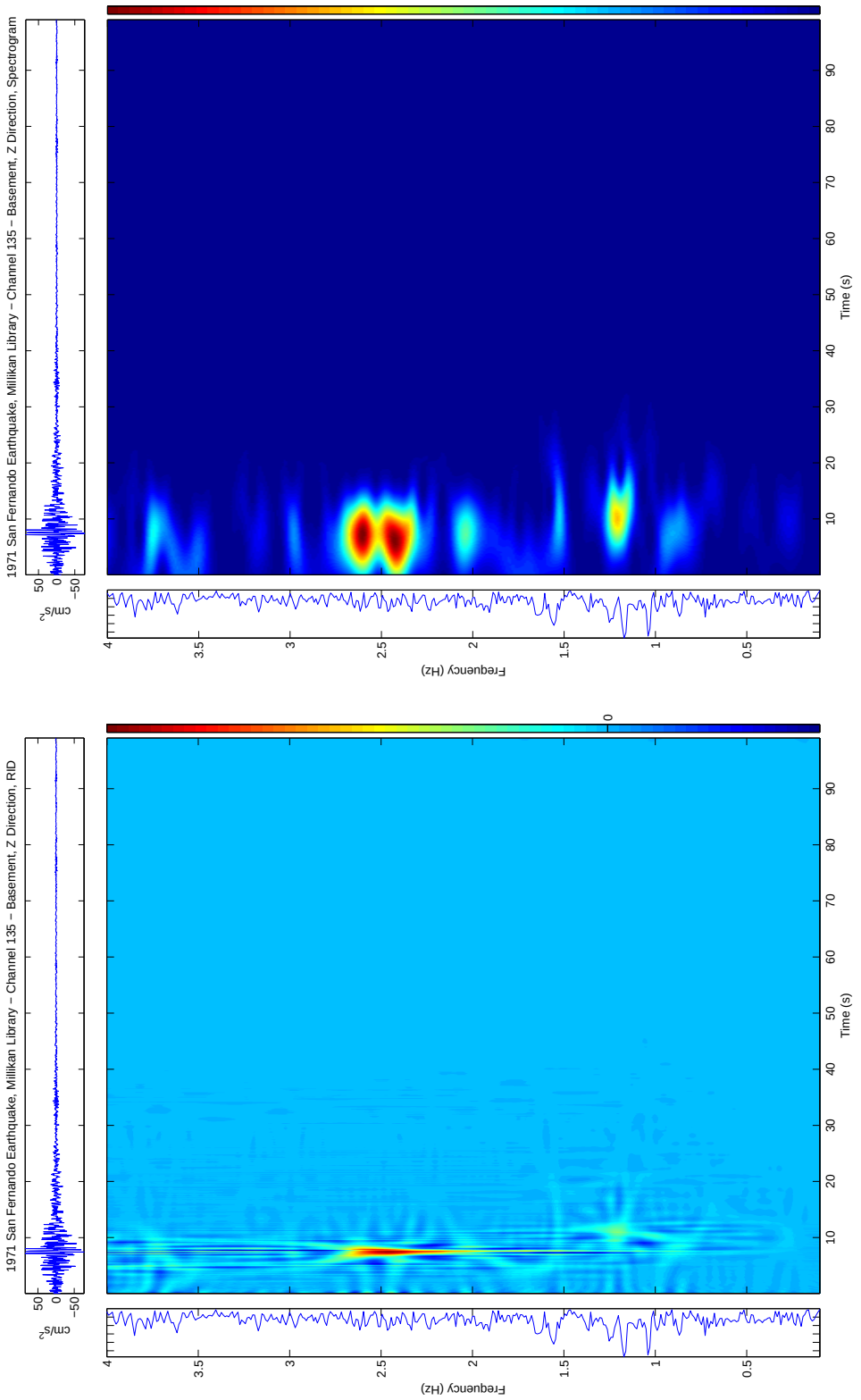

(a) RID

(b) Spectrogram

Figure 4.16: 1971 San Fernando Earthquake, Millikan Library Response. Channel 135, Basement Z.

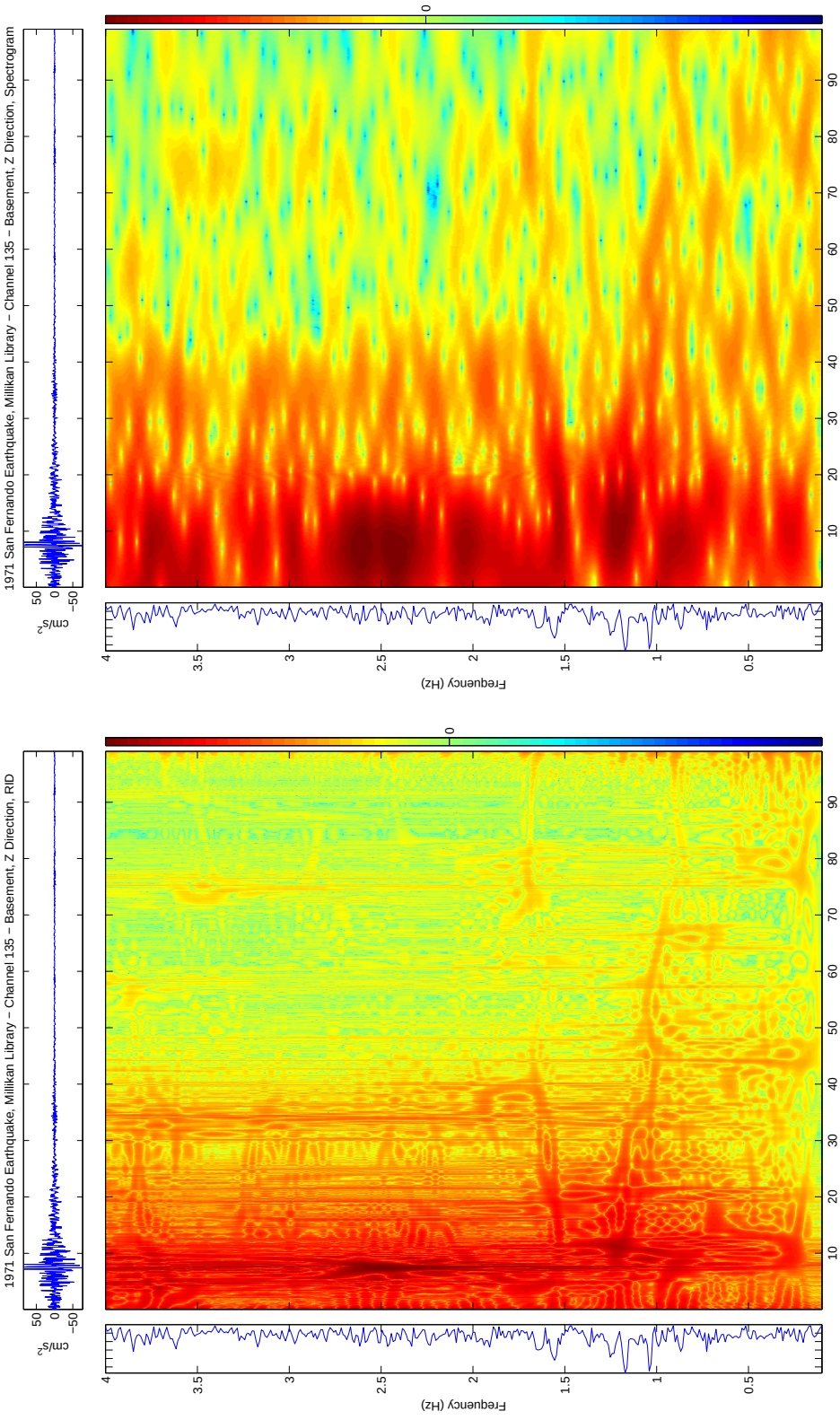

(a) RID, log10(abs())

(b) Spectrogram, log10(abs())

Figure 4.17: 1971 San Fernando Earthquake, Millikan Library Response. Channel 135, Basement Z. Logarithmic scaling.

4.1.3 Millikan Library: 1987 Whittier Narrows Earthquake

Compared with the San Fernando Earthquake, the 1987 Whittier Narrows event (01 October 1987, $M_w = 6.1$, $\Delta \sim 18km$) had slightly smaller roof accelerations in the EW direction, but a much larger response in the NS component. The Whittier event also had a smaller amount of permanent change to the dynamic properties, likely because the San Fernando event had already damaged the most vulnerable components of the building. The most fragile elements were damaged in the first significant earthquake, permanently decreasing the system frequency due to loss of stiffness. Subsequent shaking of the same amplitude will affect the structure less severely.

Figure 4.18 presents the RID and scaled RID for the EW component of the Whittier Narrows event. The natural frequency drops from a pre-event natural frequency of $\sim 1.21Hz$ to well below $1Hz$ during the strongest shaking, but recovers to above 1Hz by the end of the record. Based on subsequent tests of the building, the EW natural frequency recovered to $1.18Hz$ in the following months, for a permanent decrease of only 2.5%.

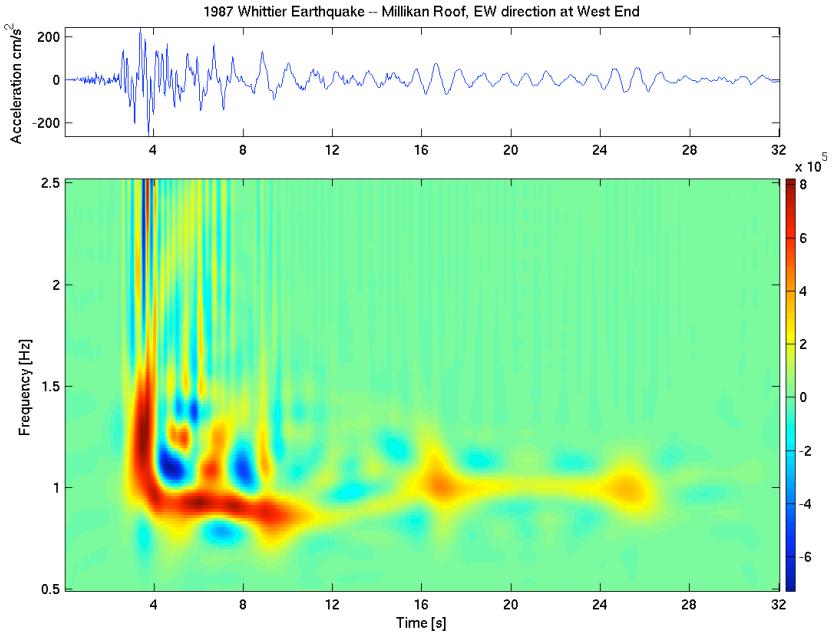

(a) RID of Millikan Library 9th floor records for 1987 Whittier Narrows event.

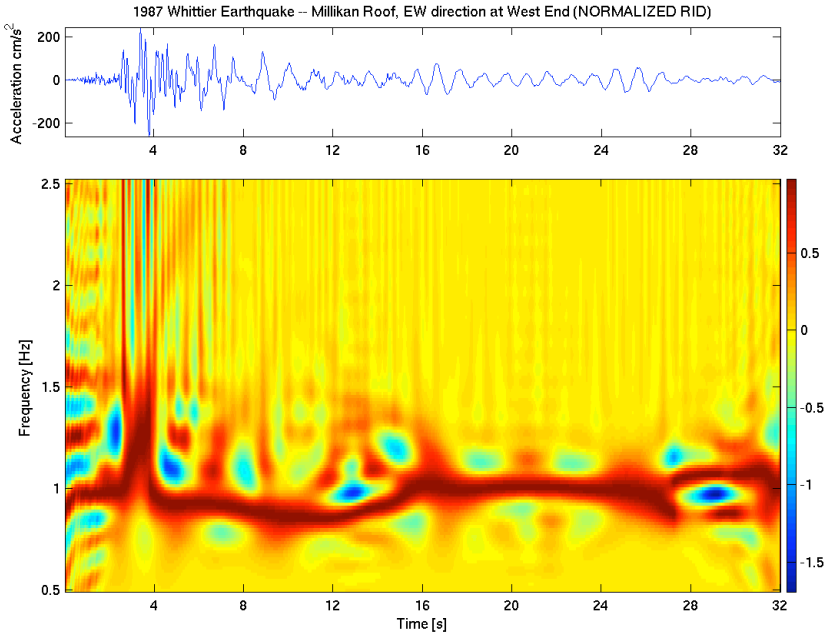

(b) RID of Millikan Library, scaled by peak amplitude at each time instant.

Figure 4.18: Millikan Library, EW Component of 9th Floor Response during 1987 Whittier Narrows event.

4.1.4 Millikan Library: 1991 Sierra Madre Earthquake

The 1991 Sierra Madre earthquake (28 June 1991, $M_w = 5.6$, $\Delta \sim 19km$) was the next strong shaking that Millikan experienced. The amplitudes were smaller than the Whittier Narrows event, and there was only a small change in natural frequency. This is in agreement with the explanation that the most fragile elements were damaged in the San Fernando event, and subsequent shaking has had a smaller damaging effect. Figures 4.19 – 4.29 show the RID for this event. The horizontal basement records (Figures 4.27 and 4.29) show a significant amount of energy at $0.5Hz$. This energy is also represented in the 6th floor and roof records (Figures 4.19 – 4.26). When analyzing roof records, the observed roof response is a combination of the building response, the system response (including rocking and soil structure interaction), and the input motion (which has its own spectrum). A potential weakness of applying time-frequency analysis techniques to roof records is that it is not immediately possible to distinguish between the different factors that contribute to changes in the apparent natural frequencies of the system.

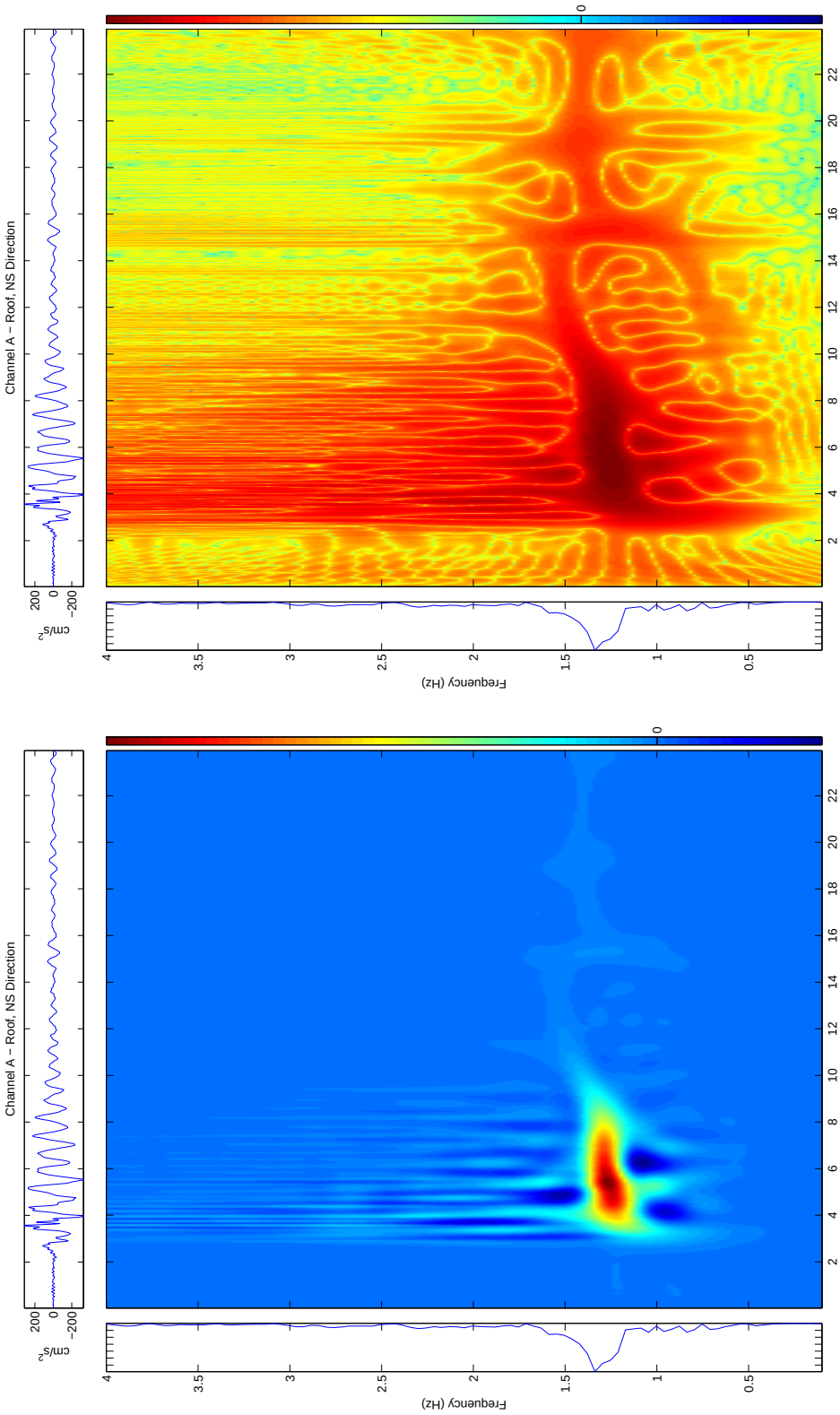

(a) RID

(b) RID, log10(abs())

Figure 4.19: Millikan Response to 1991 Sierra Madre Earthquake, Channel A – Roof, NS Direction

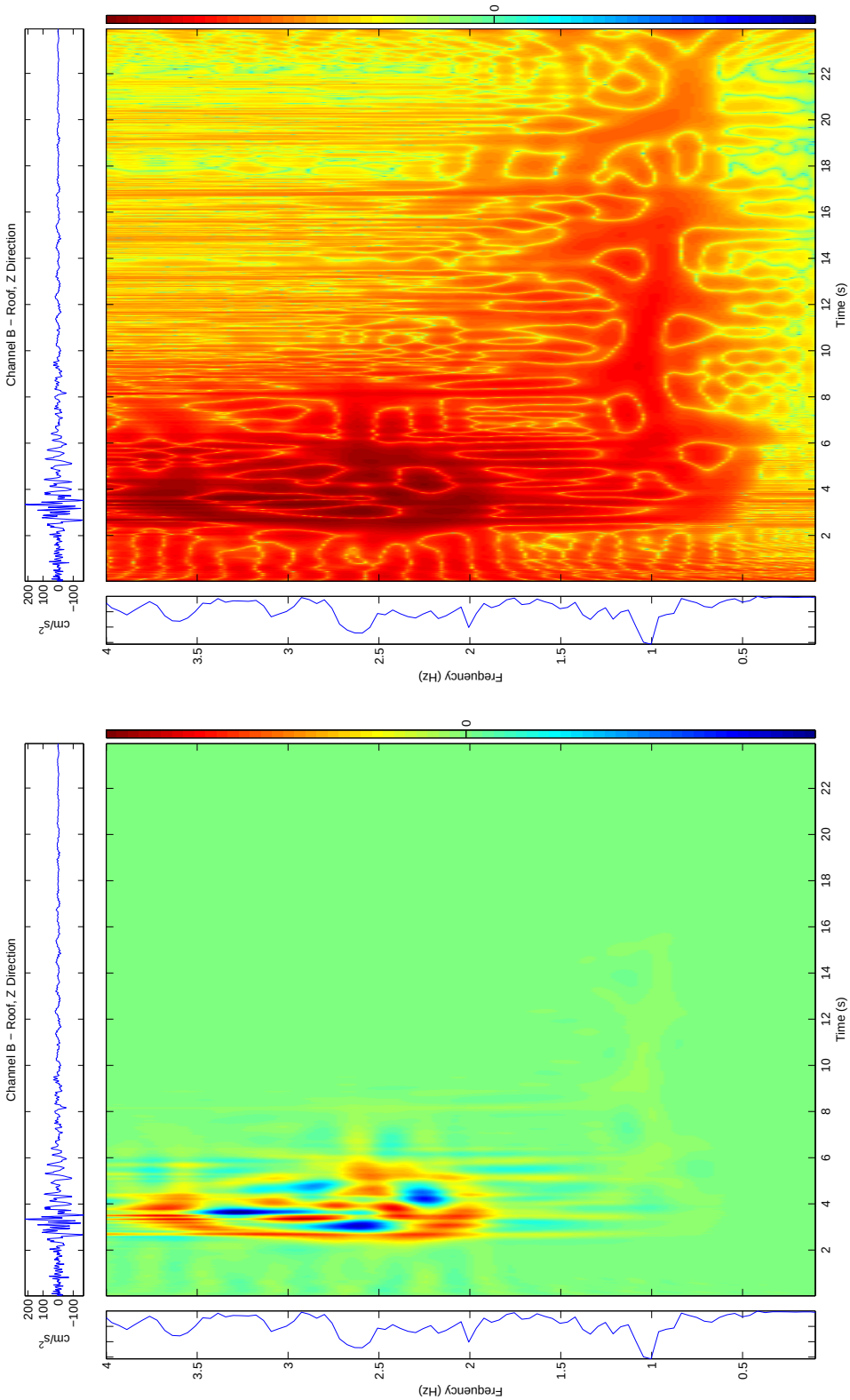

(a) RID

(b) RID, log10(abs())

Figure 4.20: Millikan Response to 1991 Sierra Madre Earthquake, Channel B – Roof, Z Direction

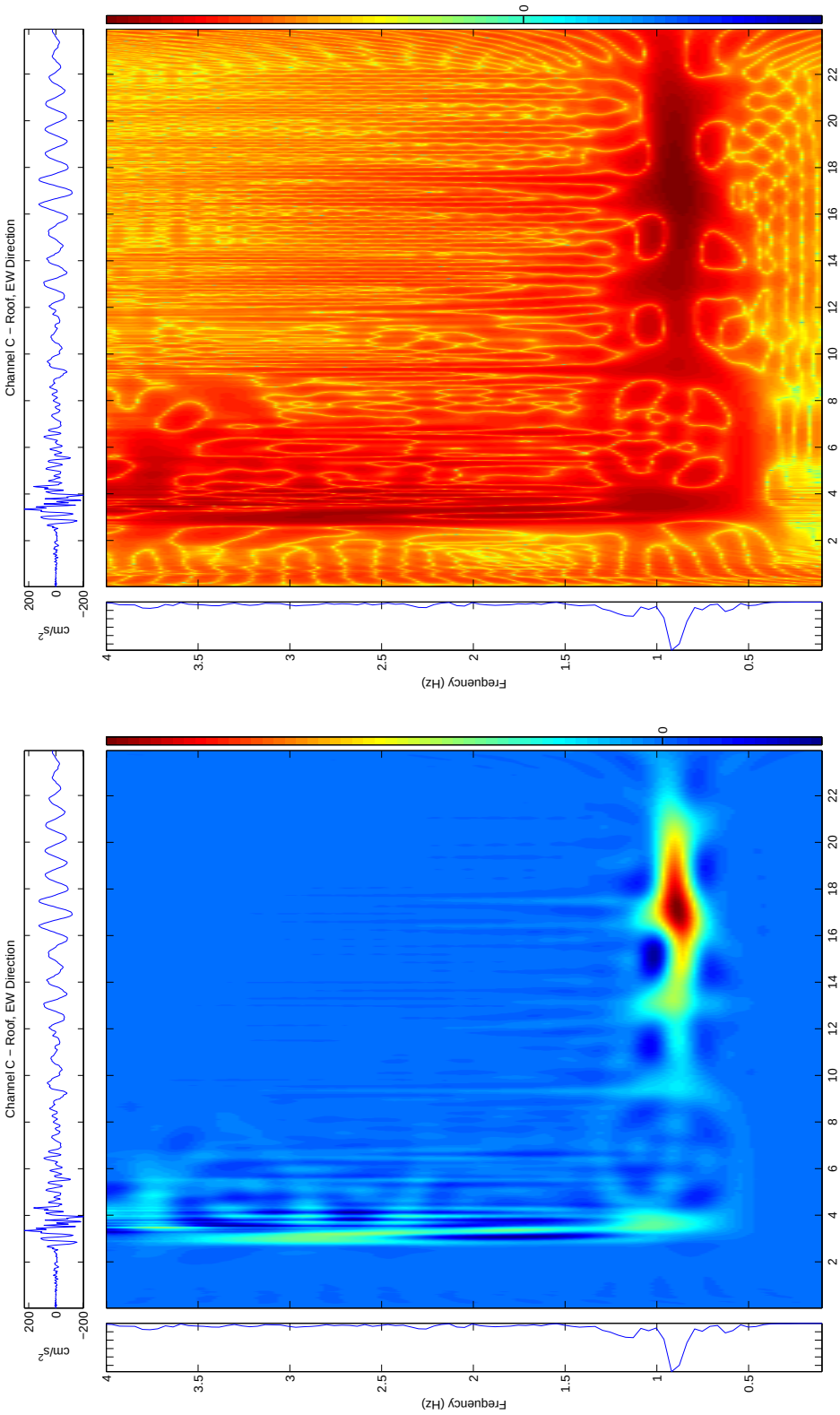

(a) RID

(b) RID, log10(abs())

Figure 4.21: Millikan Response to 1991 Sierra Madre Earthquake, Channel C – Roof, EW Direction

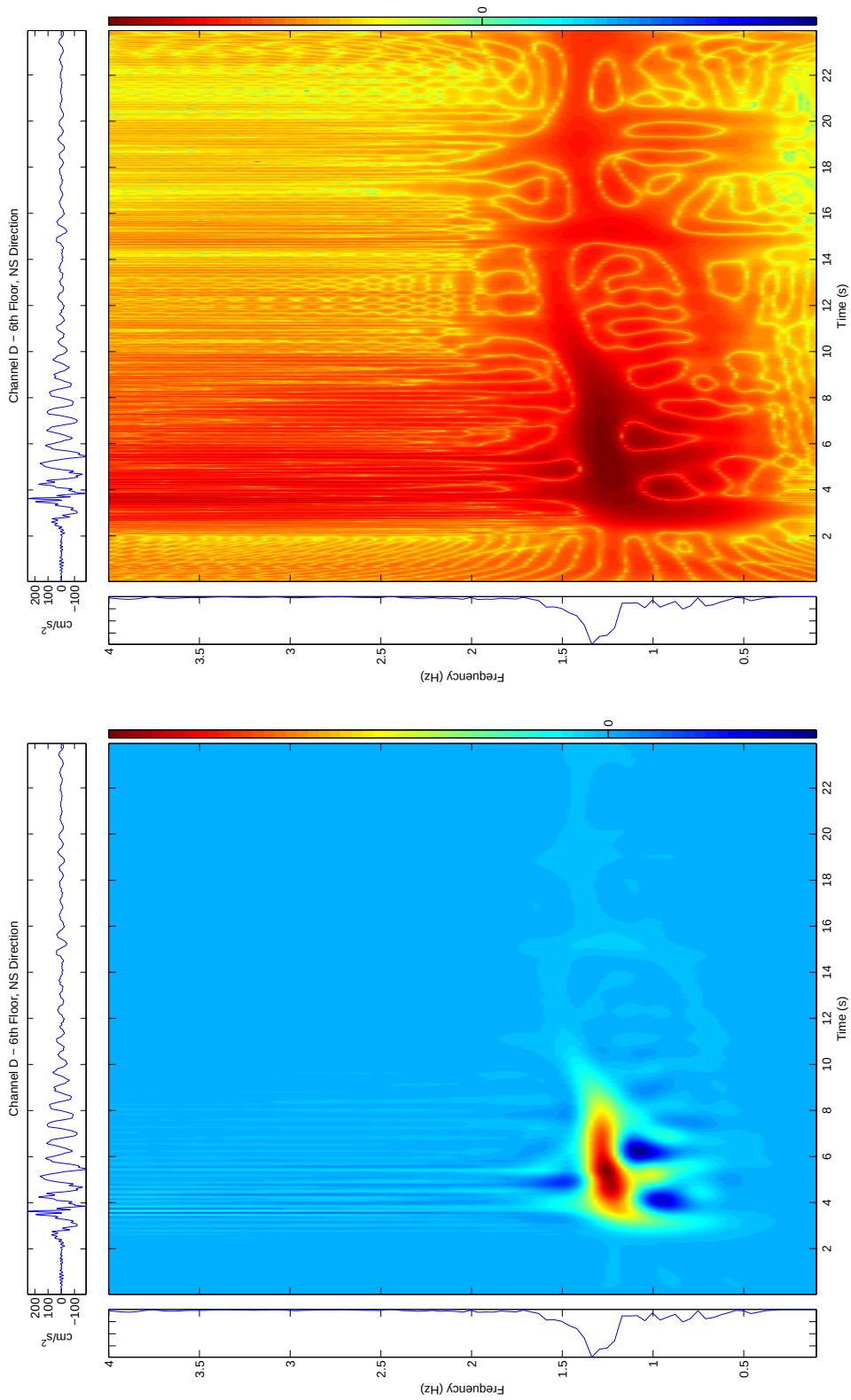

(a) RID

(b) RID, log10(abs())

Figure 4.22: Millikan Response to 1991 Sierra Madre Earthquake, Channel D – 6th Floor, NS Direction

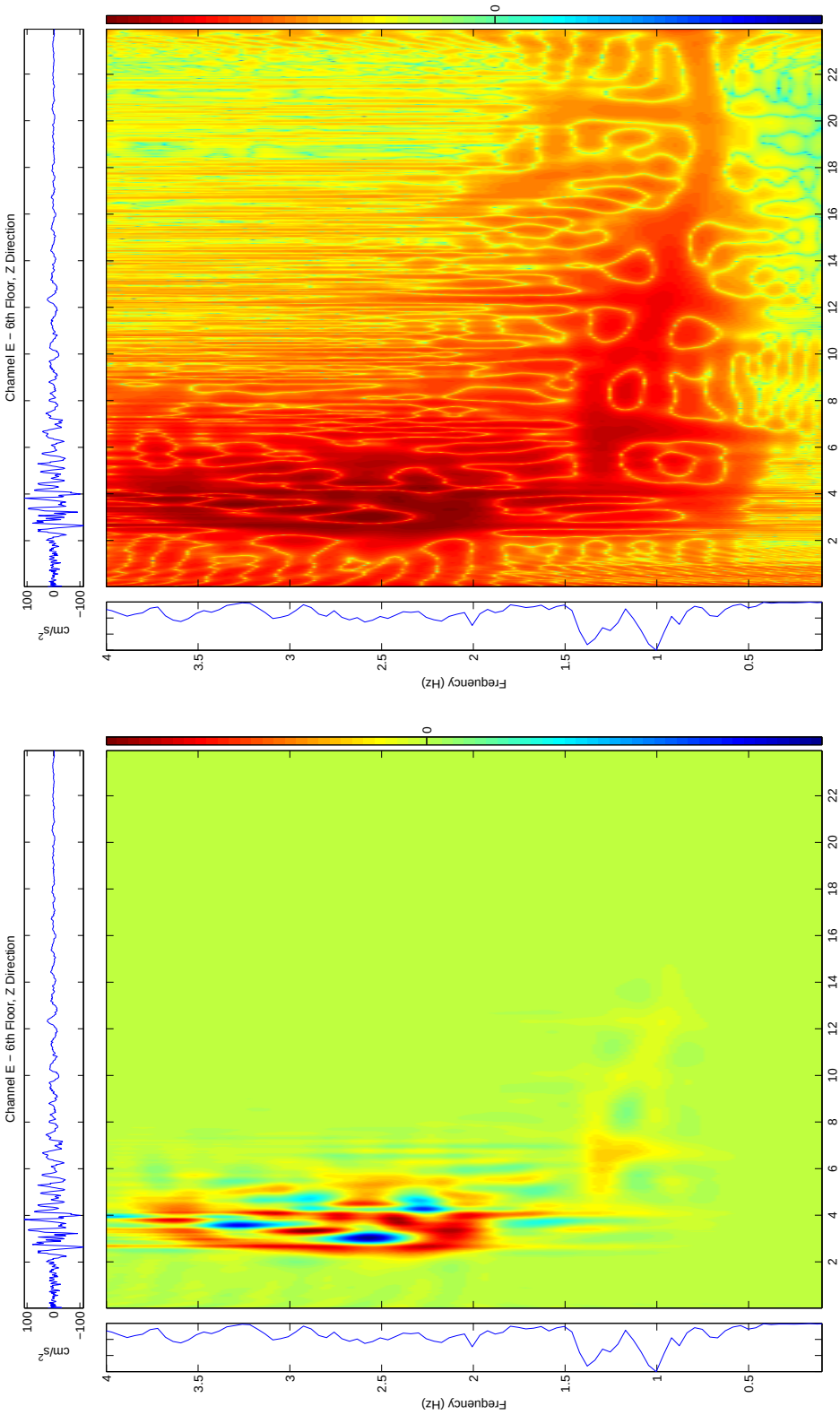

(a) RID

(b) RID, log10(abs())

Figure 4.23: Millikan Response to 1991 Sierra Madre Earthquake, Channel E – 6th Floor, Z Direction

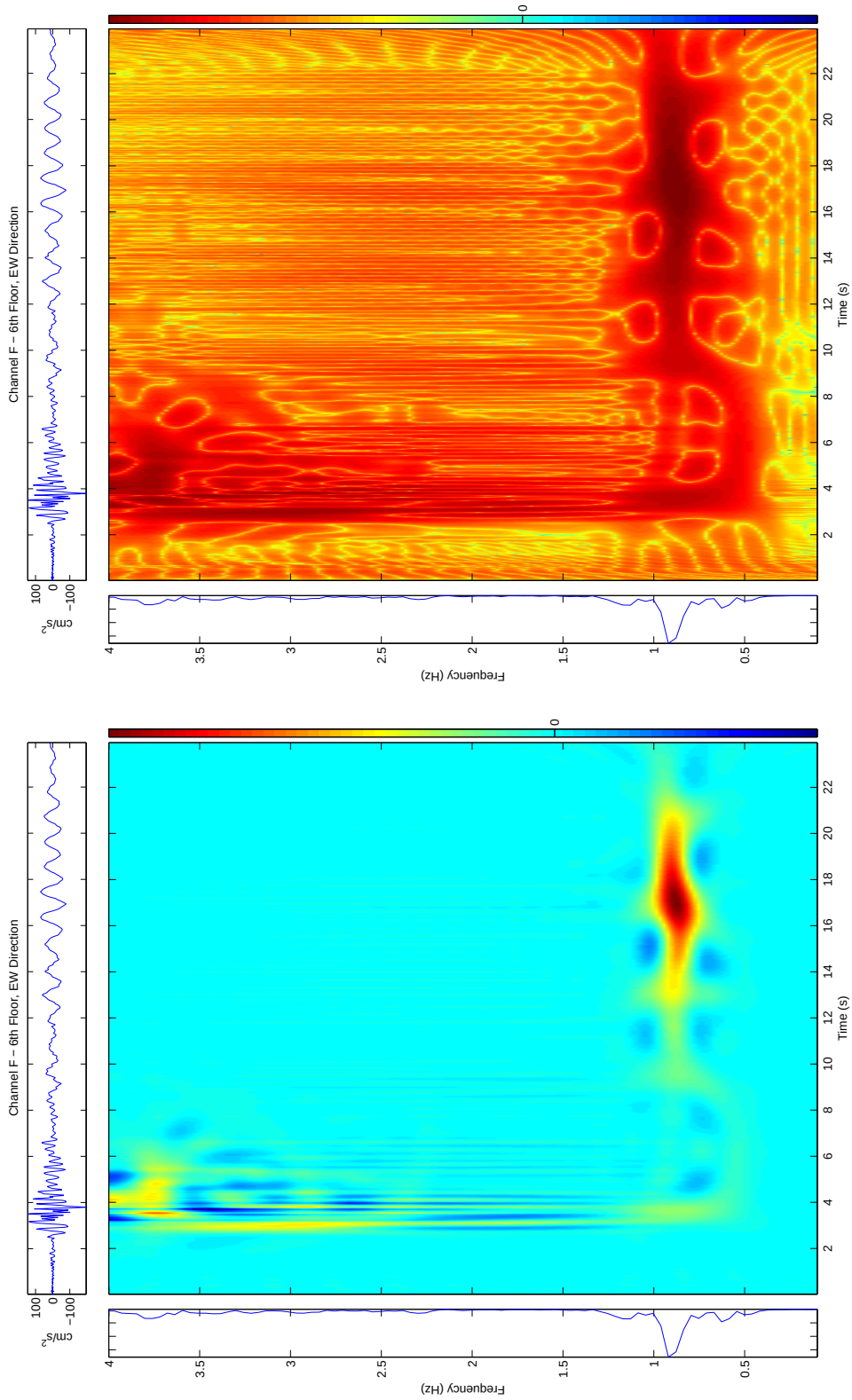

(a) RID

(b) RID, log10(abs())

Figure 4.24: Millikan Response to 1991 Sierra Madre Earthquake, Channel F – 6th Floor, EW Direction

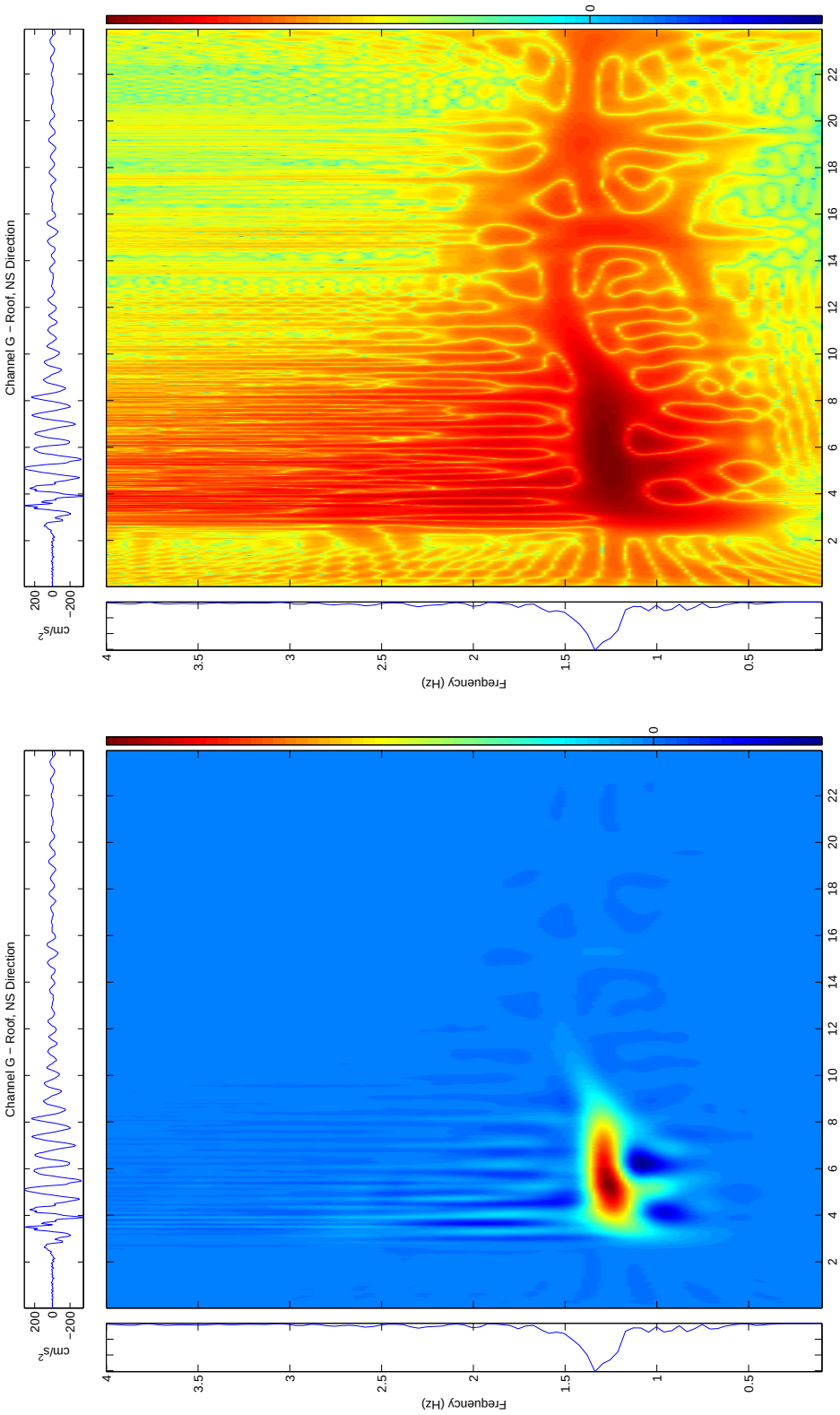

(a) RID

(b) RID, log10(abs())

Figure 4.25: Millikan Response to 1991 Sierra Madre Earthquake, Channel G – Roof, NS Direction

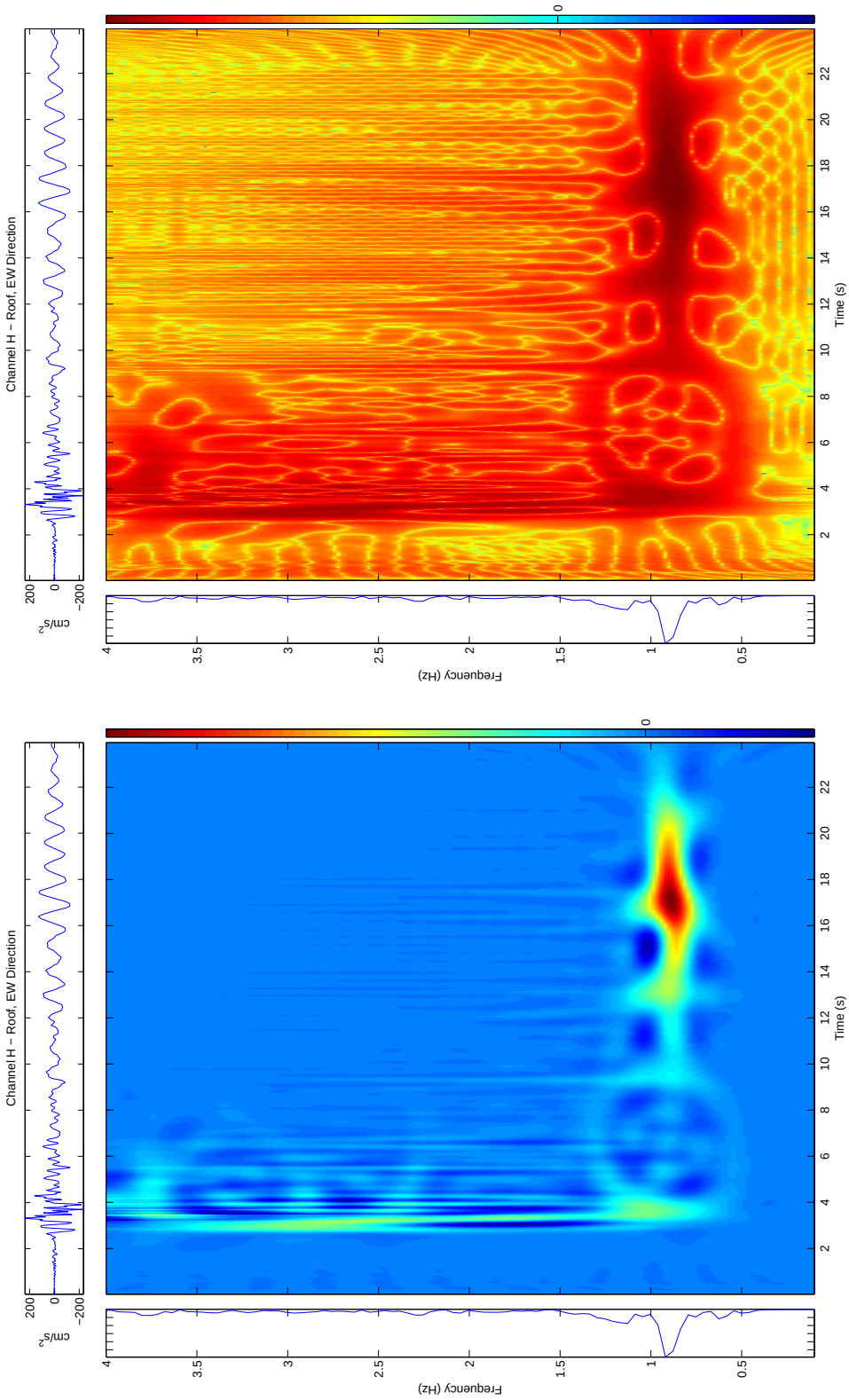

(a) RID

(b) RID, log10(abs())

Figure 4.26: Millikan Response to 1991 Sierra Madre Earthquake, Channel H – Roof, EW Direction

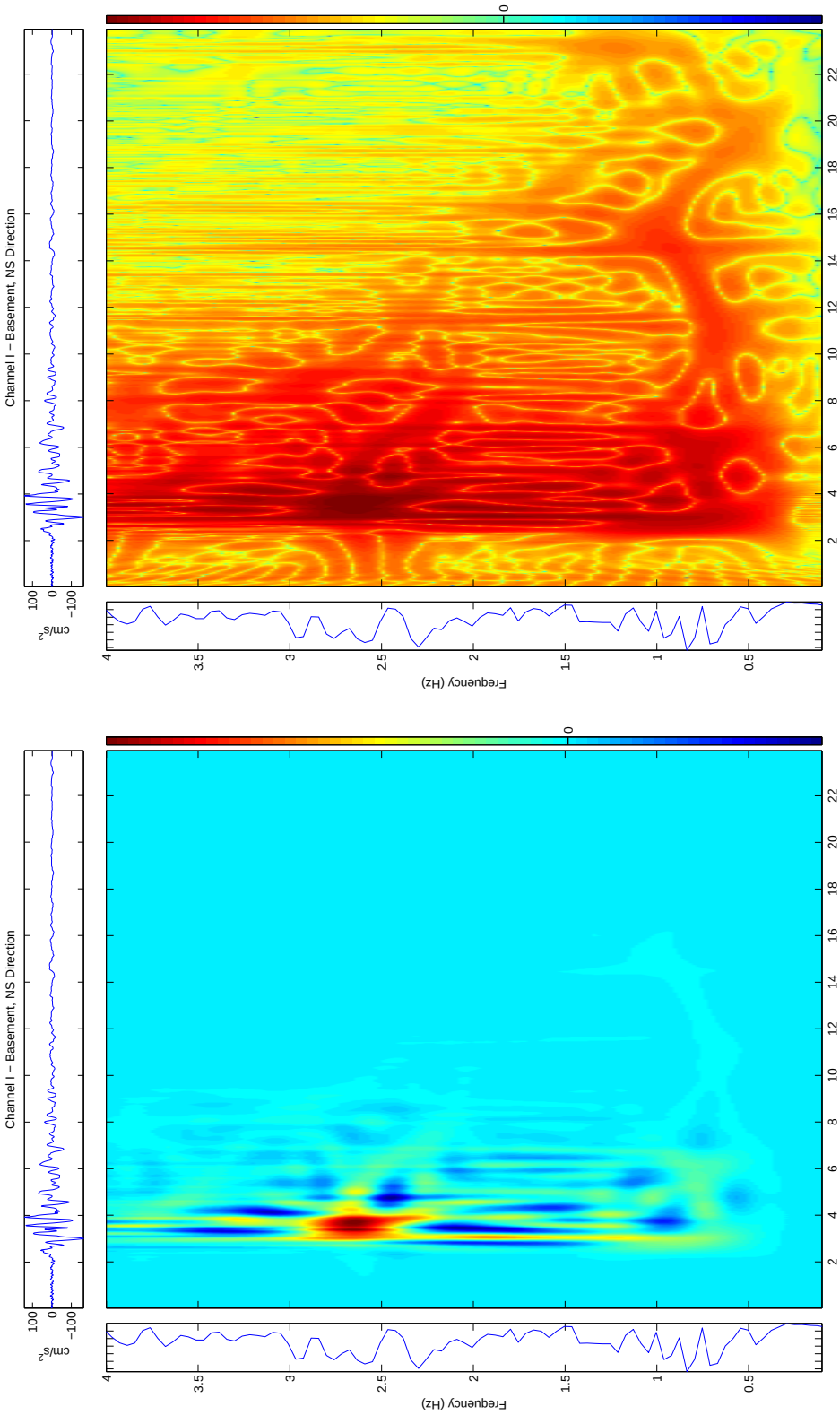

(a) RID

(b) RID, log10(abs())

Figure 4.27: Millikan Response to 1991 Sierra Madre Earthquake, Channel I - Basement, NS Direction

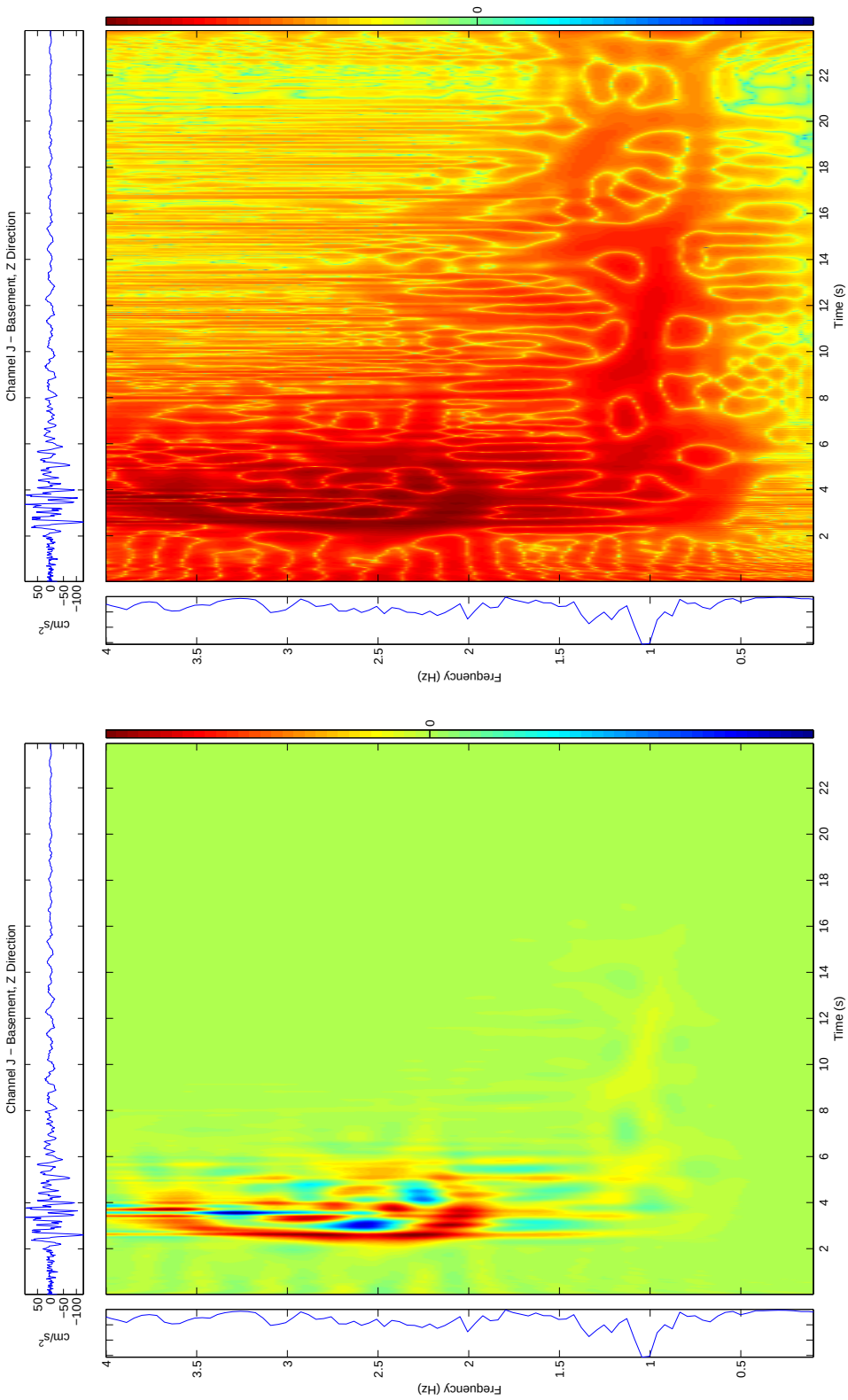

(a) RID

(b) RID, log10(abs())

Figure 4.28: Millikan Response to 1991 Sierra Madre Earthquake, Channel J - Basement, Z Direction

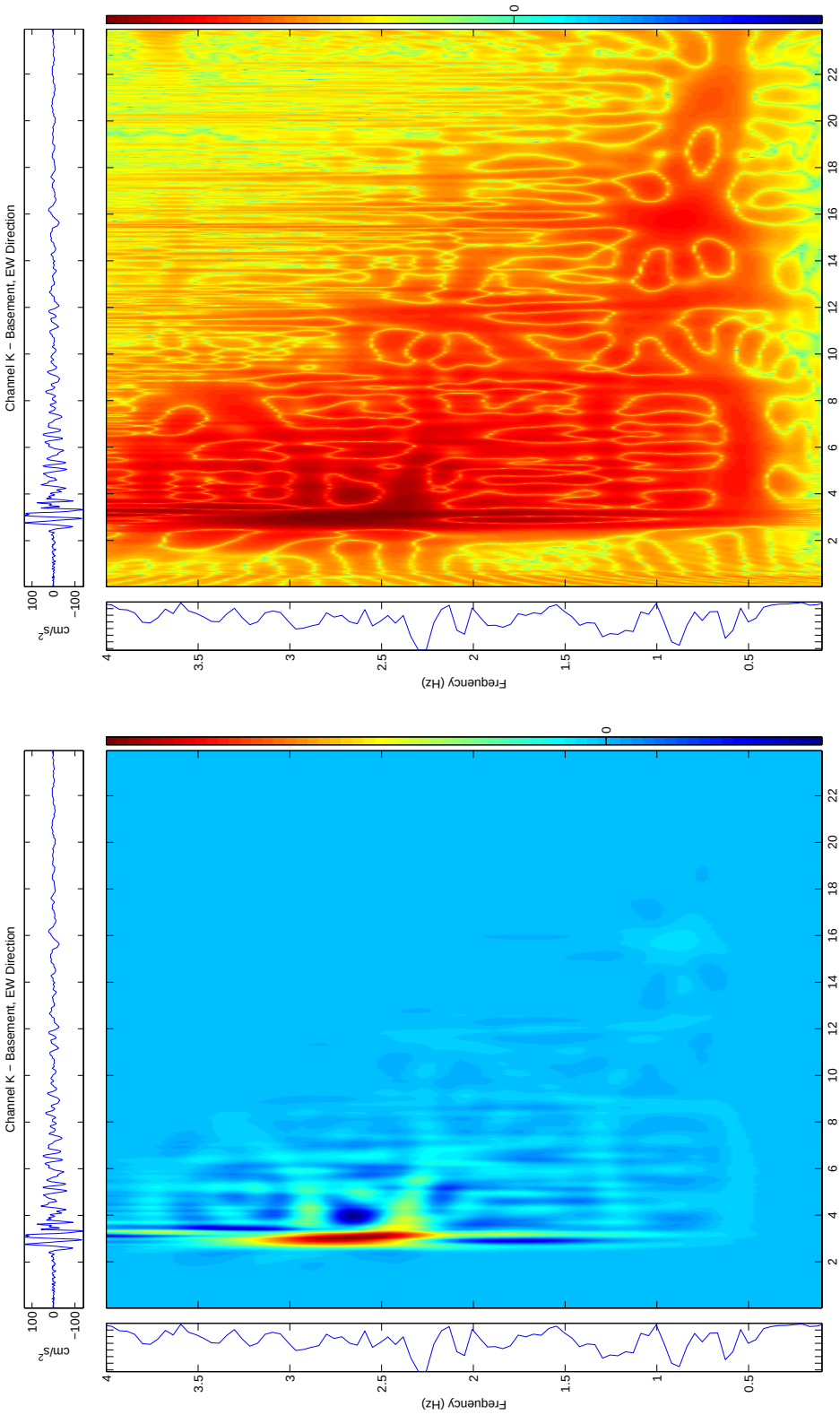

(a) RID

(b) RID, log10(abs())

Figure 4.29: Millikan Response to 1991 Sierra Madre Earthquake, Channel K - Basement, EW Direction

4.1.5 Millikan Library: 1994 Northridge Earthquake and Aftershock

The 1994 Northridge Earthquake (17 January 1994, $M_w = 6.7$, $\Delta \sim 34km$) had very large accelerations, and permanently changed the EW and NS natural frequencies by a small amount. It is interesting to compare the time-frequency plots for the Northridge event (Figures 4.30 – 4.40) with a $M_w = 5.6$ aftershock that was recorded 11 hours later (Figures 4.41 – 4.51), particularly when investigating the change in observed natural frequency.

At the end of the Northridge event, the NS roof records (Figures 4.30 and 4.36) show an estimated natural frequency of $\sim 1.4Hz$, compared with the pre-event frequency of $1.7Hz$. The NS natural frequency briefly dropped to $1.3Hz$ during the strongest shaking. The exact amount of time that it takes for Millikan to recover after an event is unknown, but a triggered aftershock of the Northridge event (Figures 4.41 and 4.47) shows that the pre-event natural frequency, 11 hours after the Northridge event, is above $1.5Hz$. (It is difficult to identify the exact initial natural frequency of the event due to interference in the RID, but it is unambiguously greater than $1.5Hz$ at the beginning of the record.)

In the EW roof components for the Northridge event (Figures 4.32 and 4.37), the pre-event frequency of $1.18Hz$ decreases to $0.9Hz$ during the strongest shaking and recovers to $\sim 1Hz$ by the end of the record. The EW aftershock records (Figures 4.43 and 4.48) do not show the same recovering behavior as the NS components; the resonant frequency during the event is $\sim 1Hz$, and it is not obvious that the natural frequency was larger than $1Hz$ at the beginning of the record.

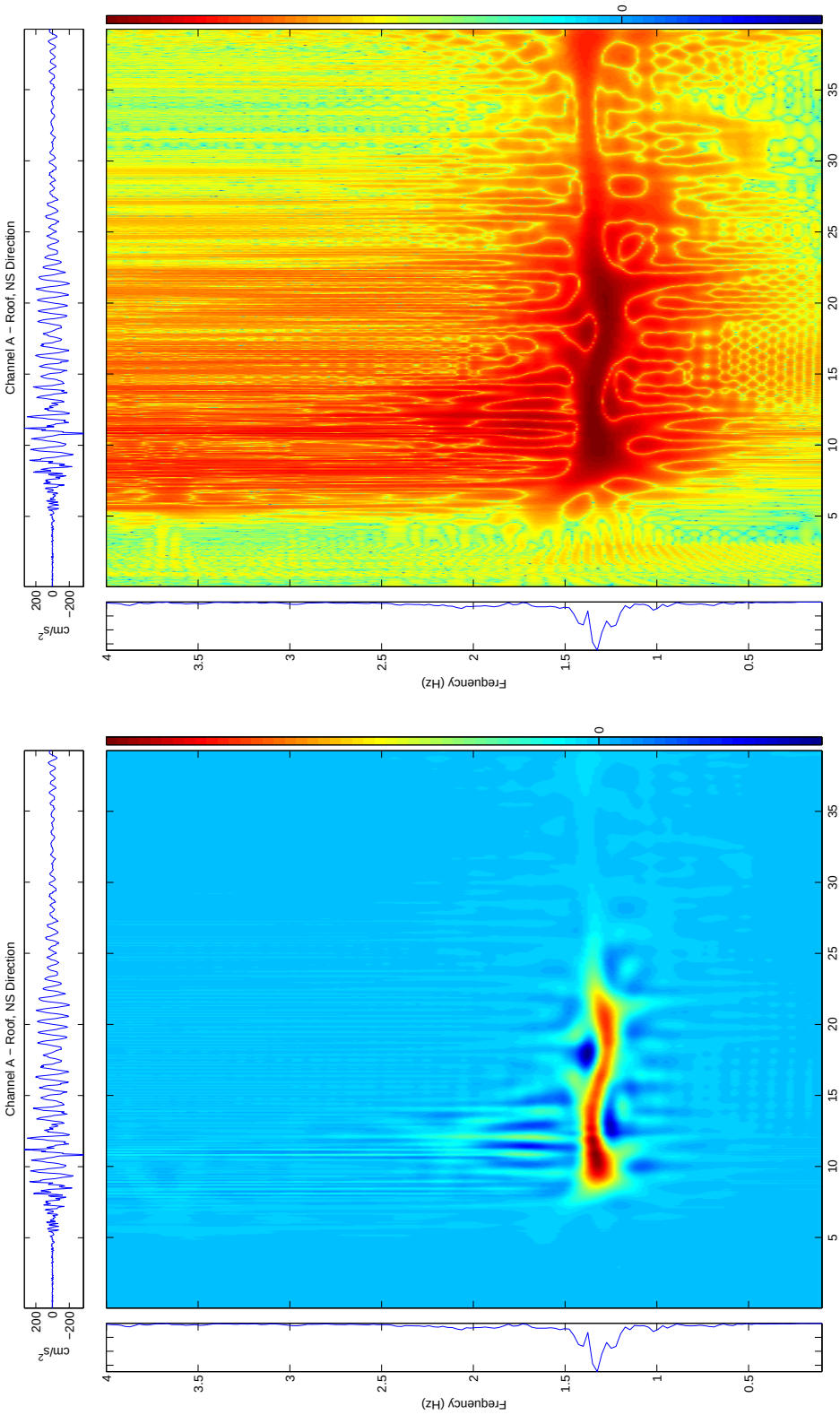

(a) RID

(b) RID, log10(abs())

Figure 4.30: Millikan Response to Northridge Earthquake, Channel A – Roof, NS Direction

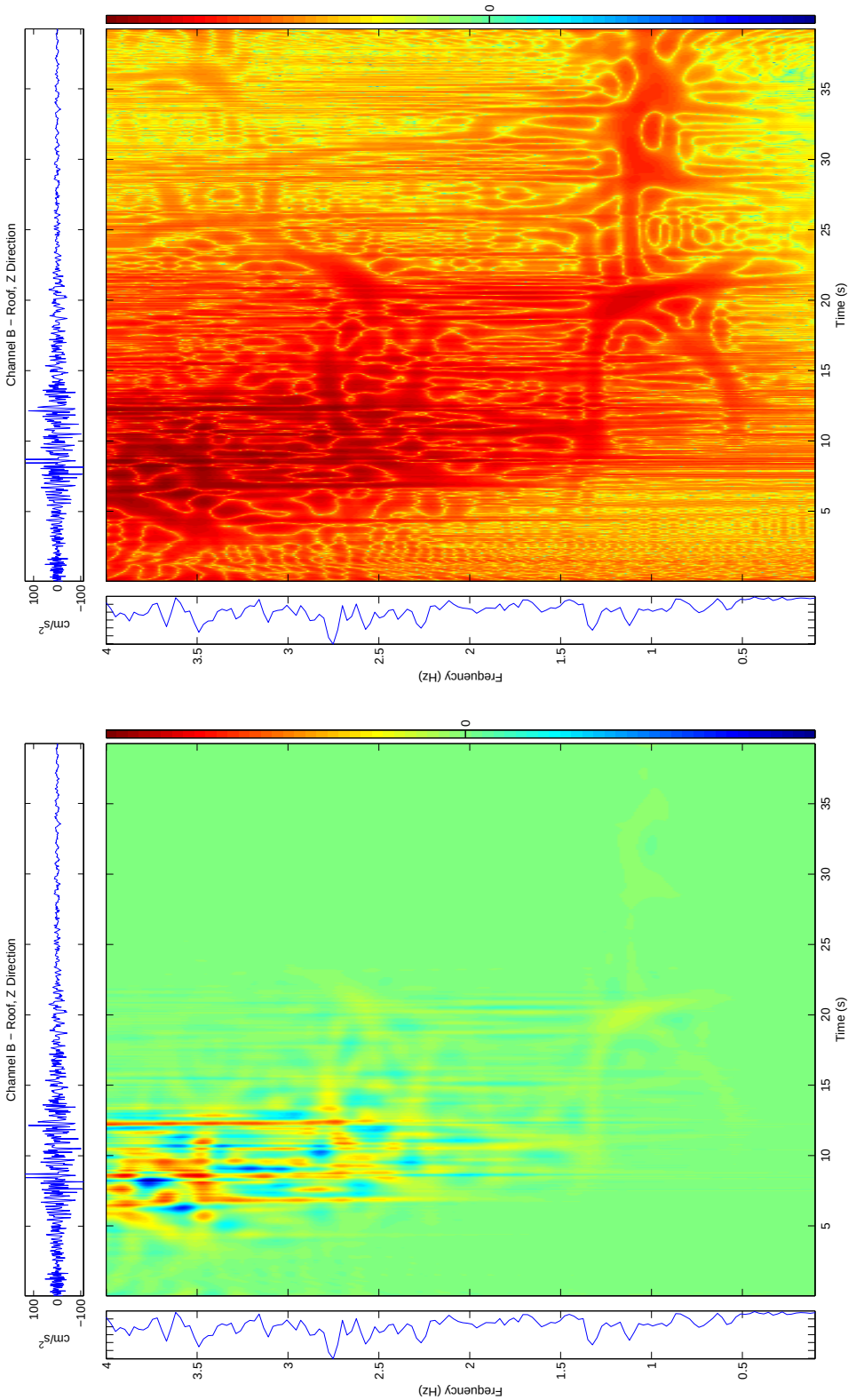

(a) RID

(b) RID, log10(abs())

Figure 4.31: Millikan Response to Northridge Earthquake, Channel B – Roof, Z Direction

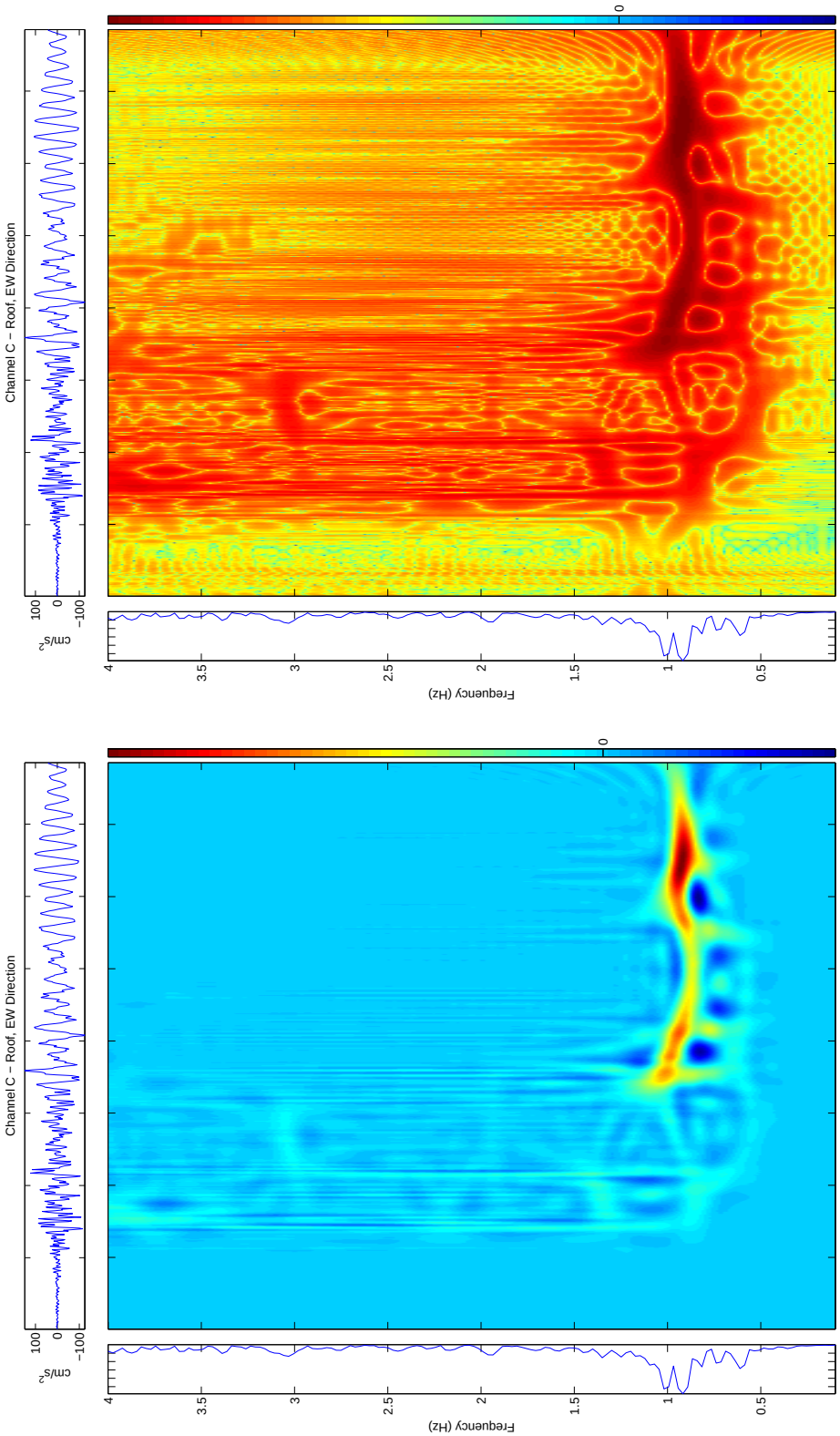

(a) RID

(b) RID, log10(abs())

Figure 4.32: Millikan Response to Northridge Earthquake, Channel C – Roof, EW Direction

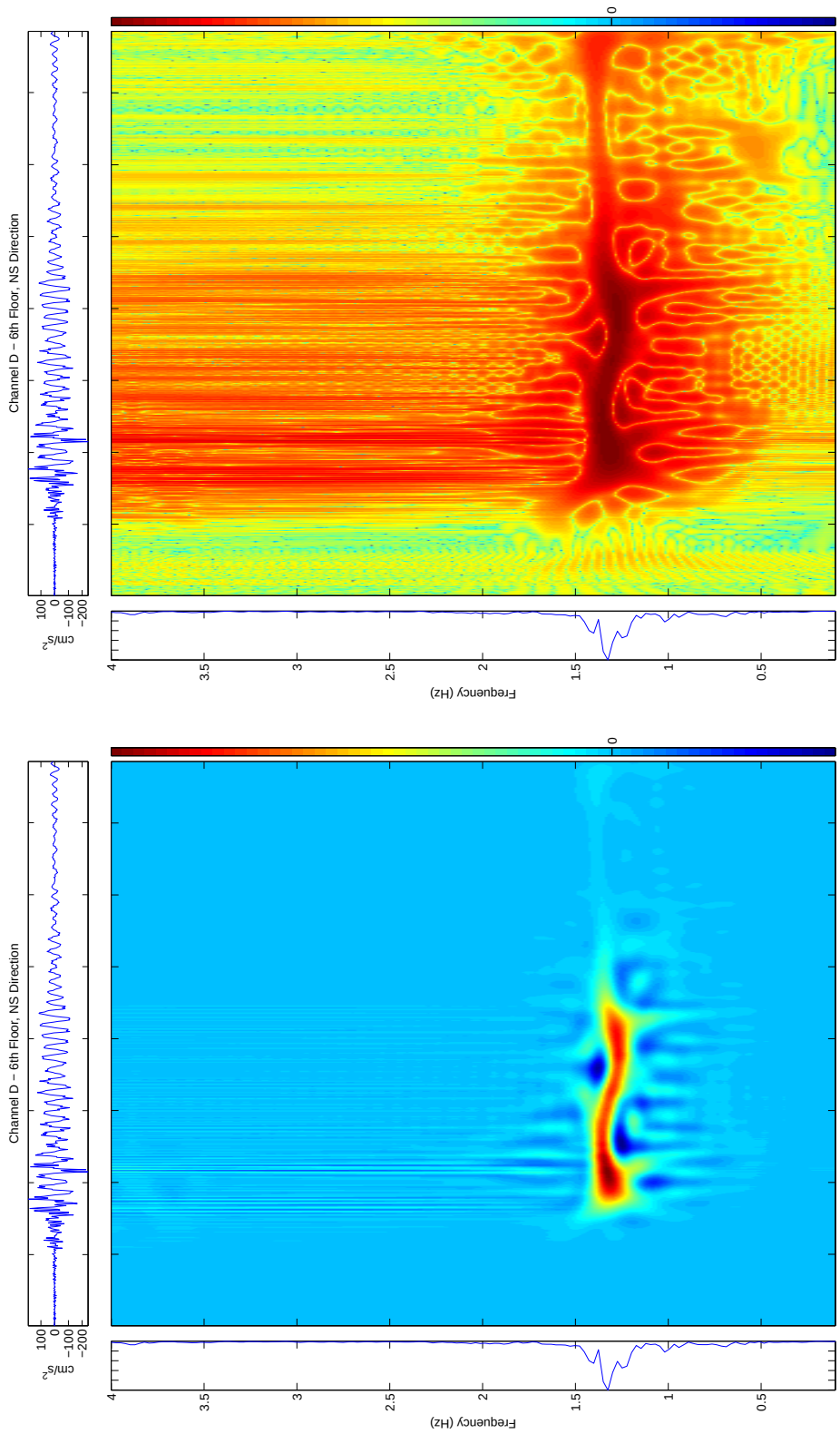

(a) RID

(b) RID, log10(abs())

Figure 4.33: Millikan Response to Northridge Earthquake, Channel D – 6th Floor, NS Direction

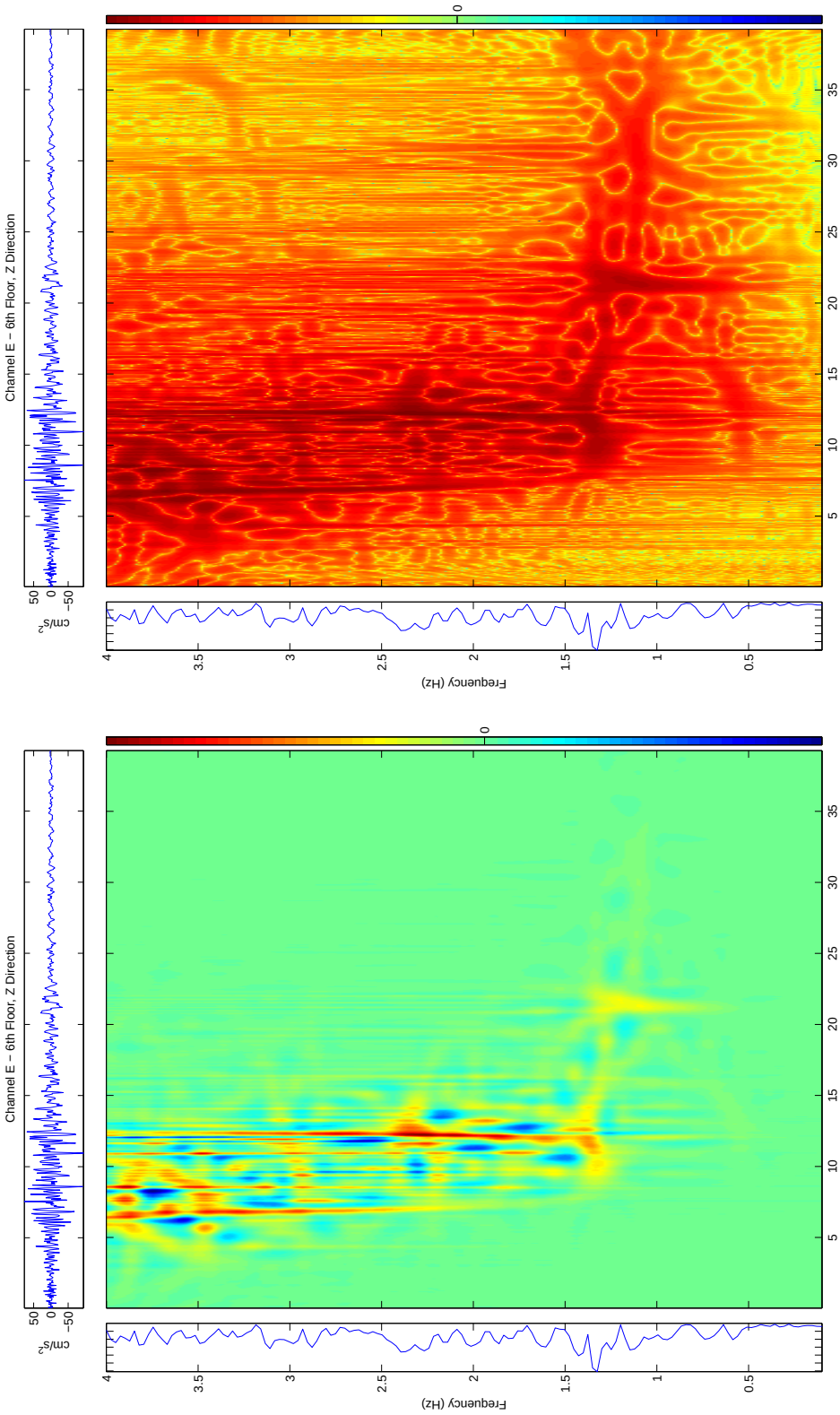

(a) RID

(b) RID, log10(abs())

Figure 4.34: Millikan Response to Northridge Earthquake, Channel E – 6th Floor, Z Direction

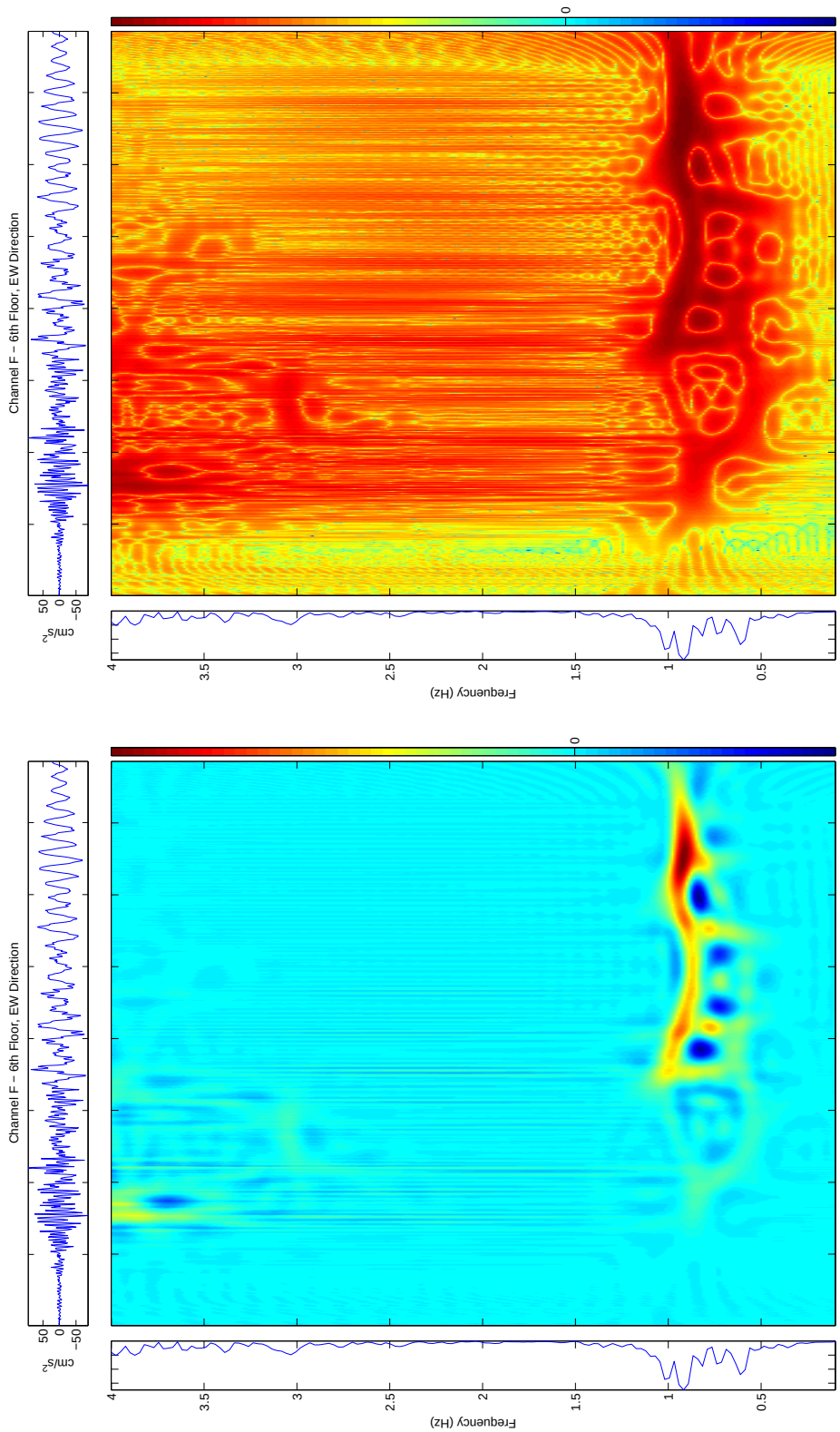

(a) RID

(b) RID, log10(abs())

Figure 4.35: Millikan Response to Northridge Earthquake, Channel F – 6th Floor, EW Direction

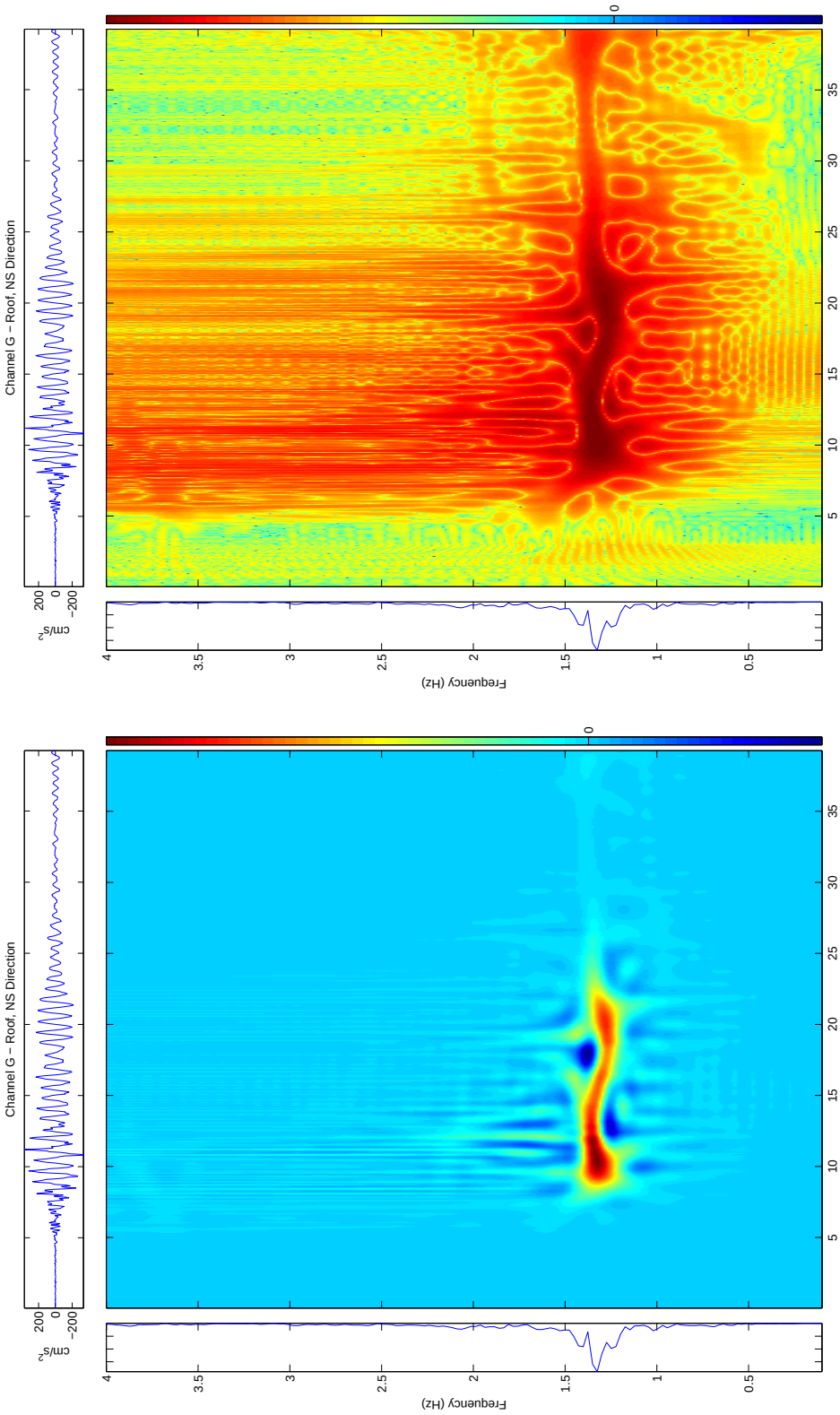

(a) RID

(b) RID, log10(abs())

Figure 4.36: Millikan Response to Northridge Earthquake, Channel G – Roof, NS Direction

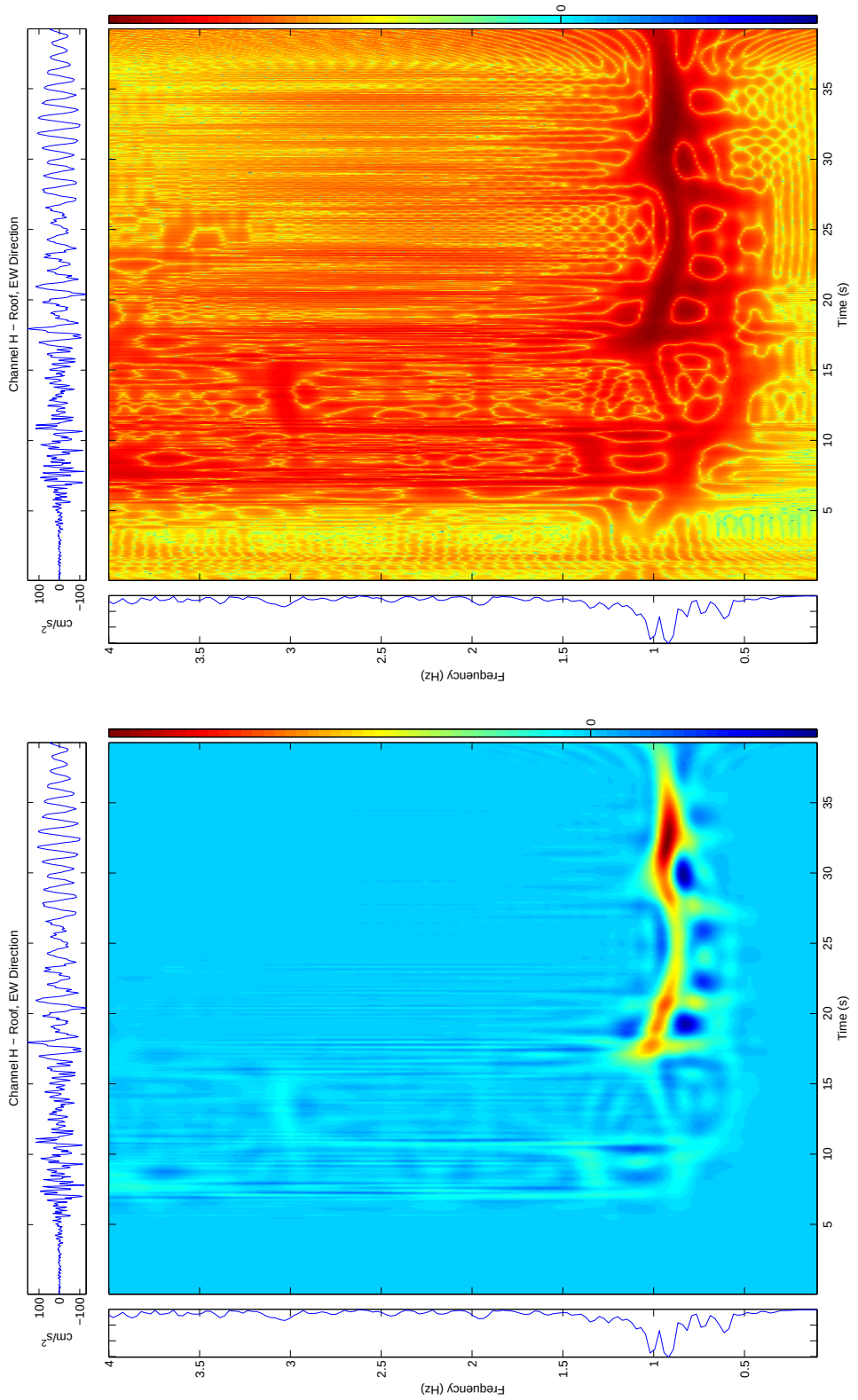

(a) RID

(b) RID, log10(abs())

Figure 4.37: Millikan Response to Northridge Earthquake, Channel H – Roof, EW Direction

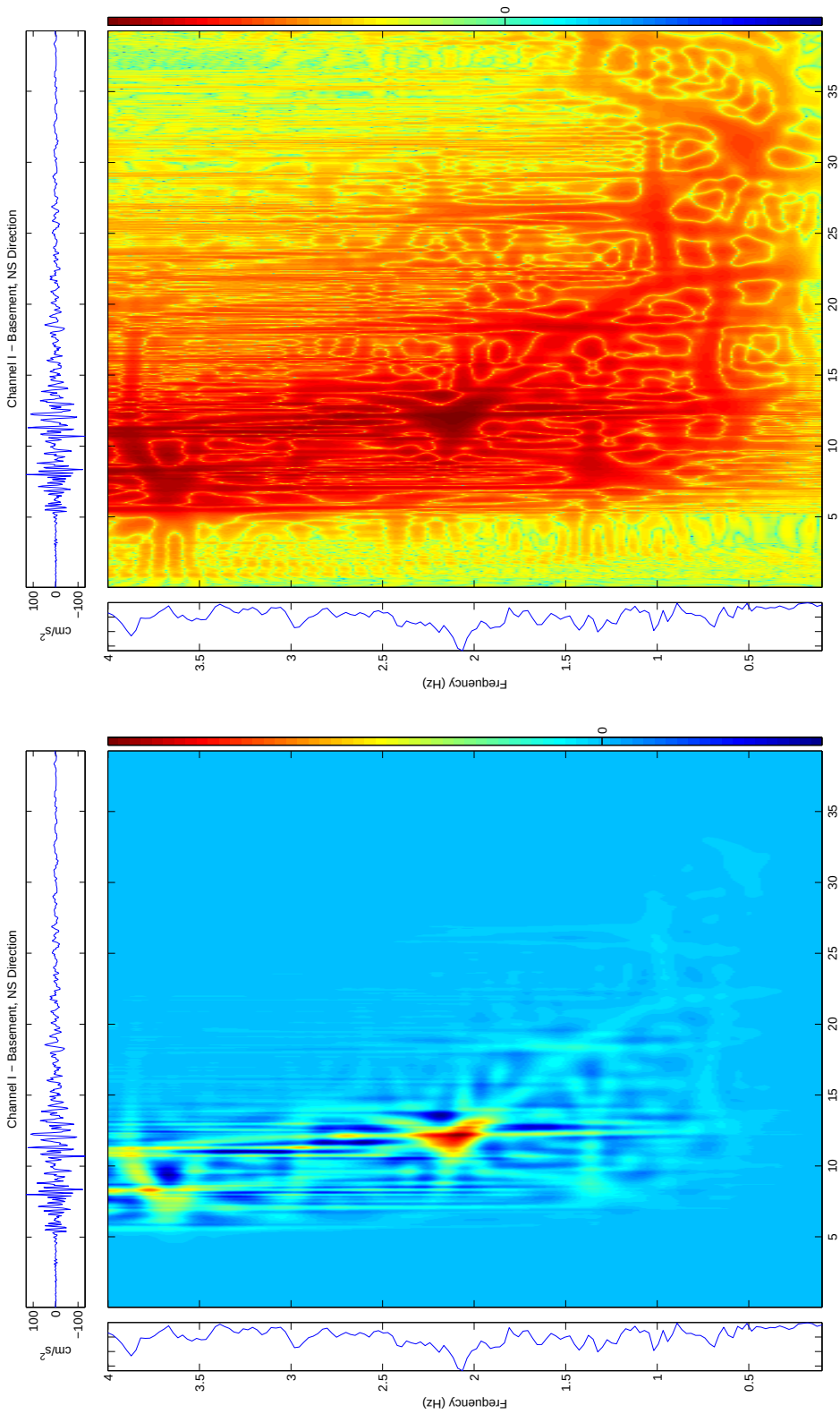

(a) RID

(b) RID, log10(abs())

Figure 4.38: Millikan Response to Northridge Earthquake, Channel I - Basement, NS Direction

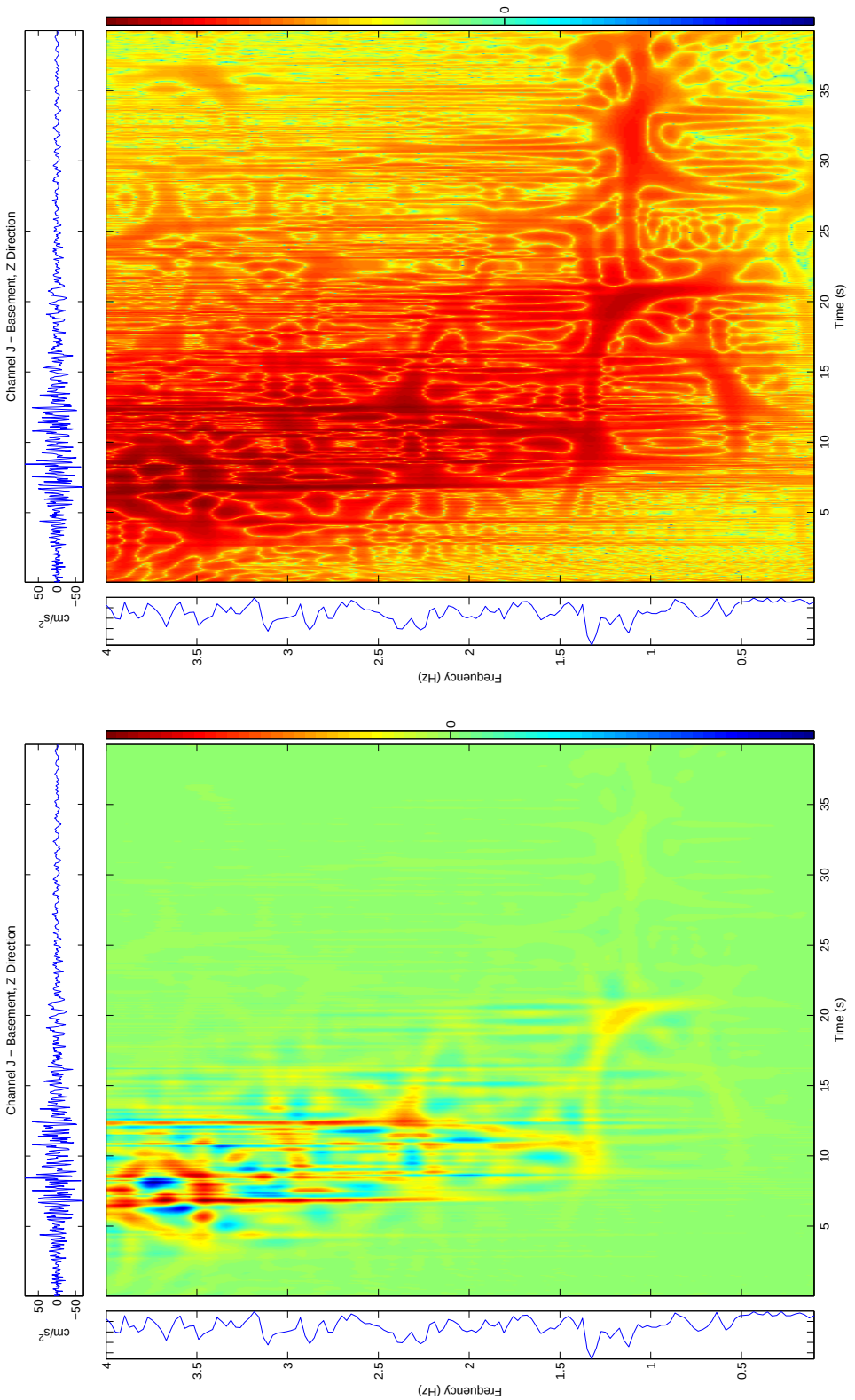

(a) RID

(b) RID, log10(abs())

Figure 4.39: Millikan Response to Northridge Earthquake, Channel J - Basement, Z Direction

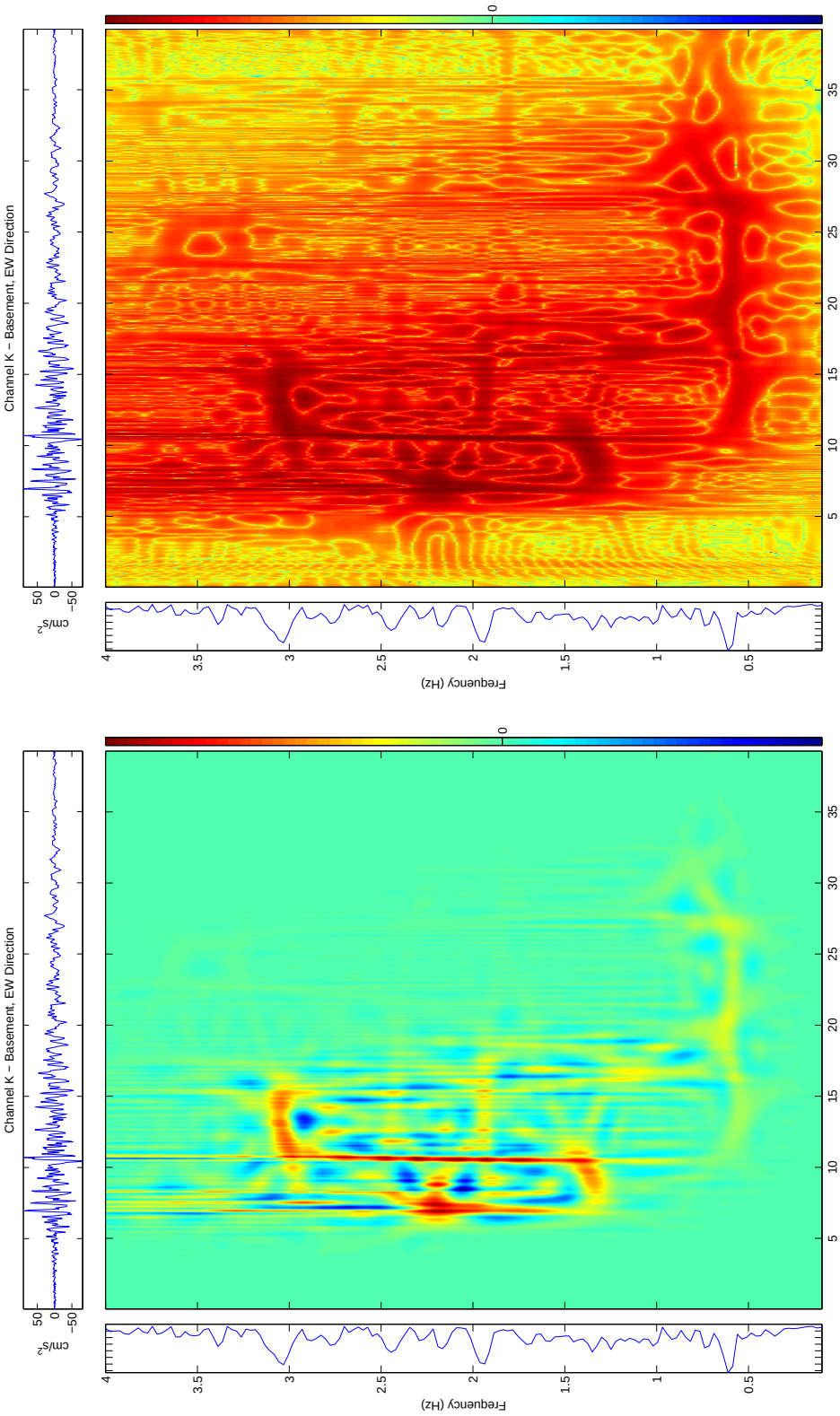

(a) RID

(b) RID, log10(abs())

Figure 4.40: Millikan Response to Northridge Earthquake, Channel K - Basement, EW Direction

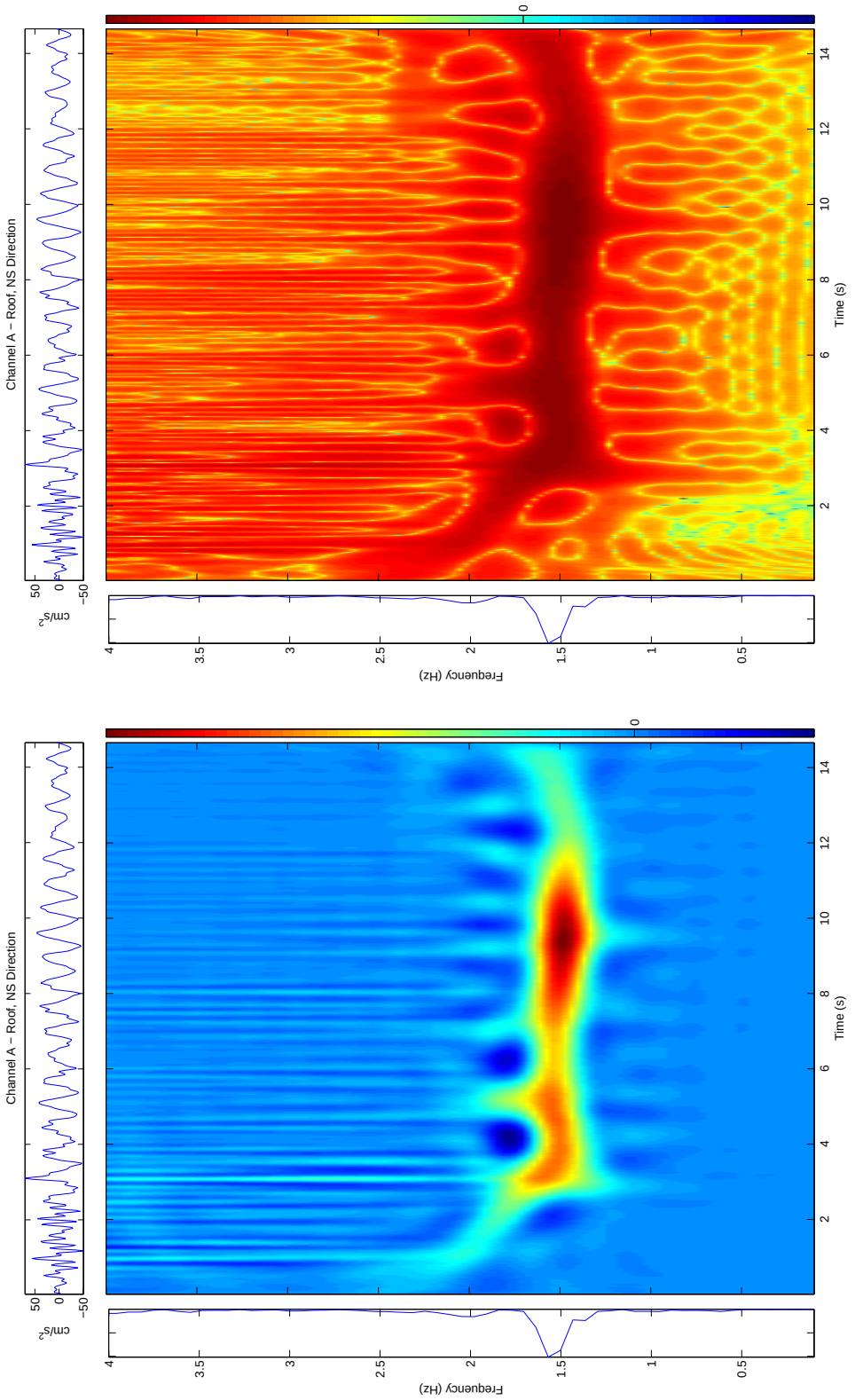

(a) RID

(b) RID, log10(abs())

Figure 4.41: Millikan Response to Northridge Aftershock, Channel A – Roof, NS Direction

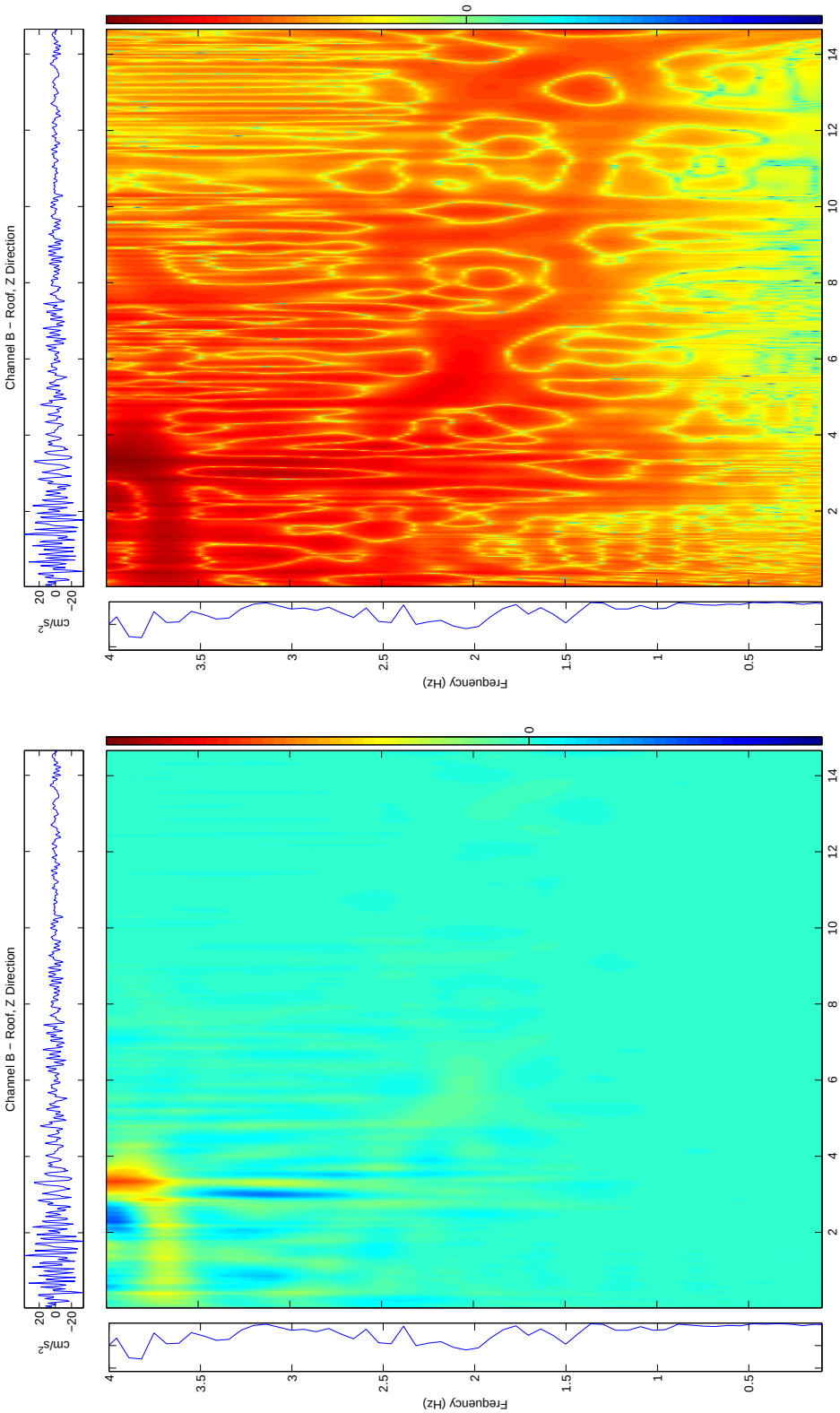

(a) RID

(b) RID, log10(abs())

Figure 4.42: Millikan Response to Northridge Aftershock, Channel B – Roof, Z Direction

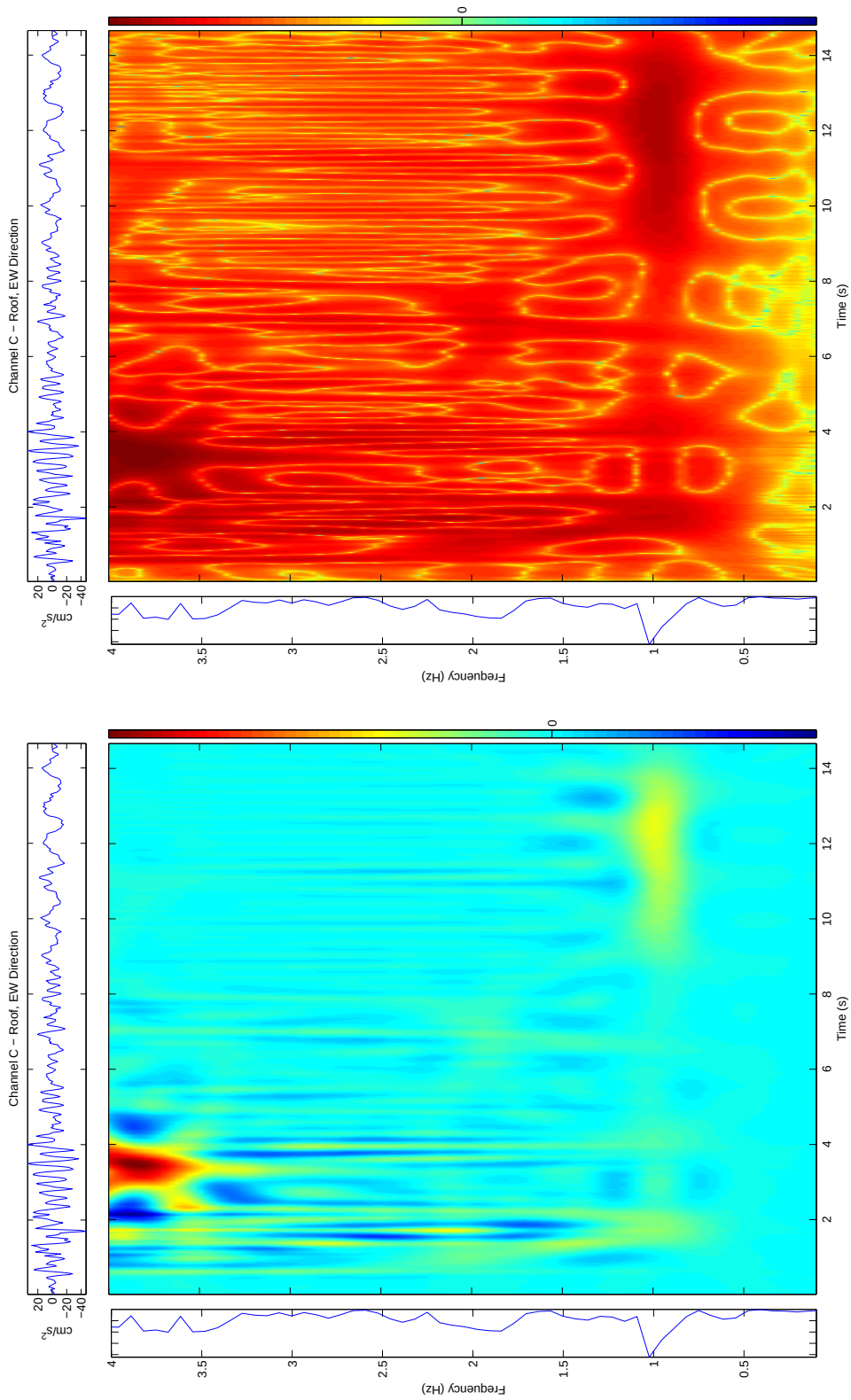

(a) RID

(b) RID, log10(abs())

Figure 4.43: Millikan Response to Northridge Aftershock, Channel C – Roof, EW Direction

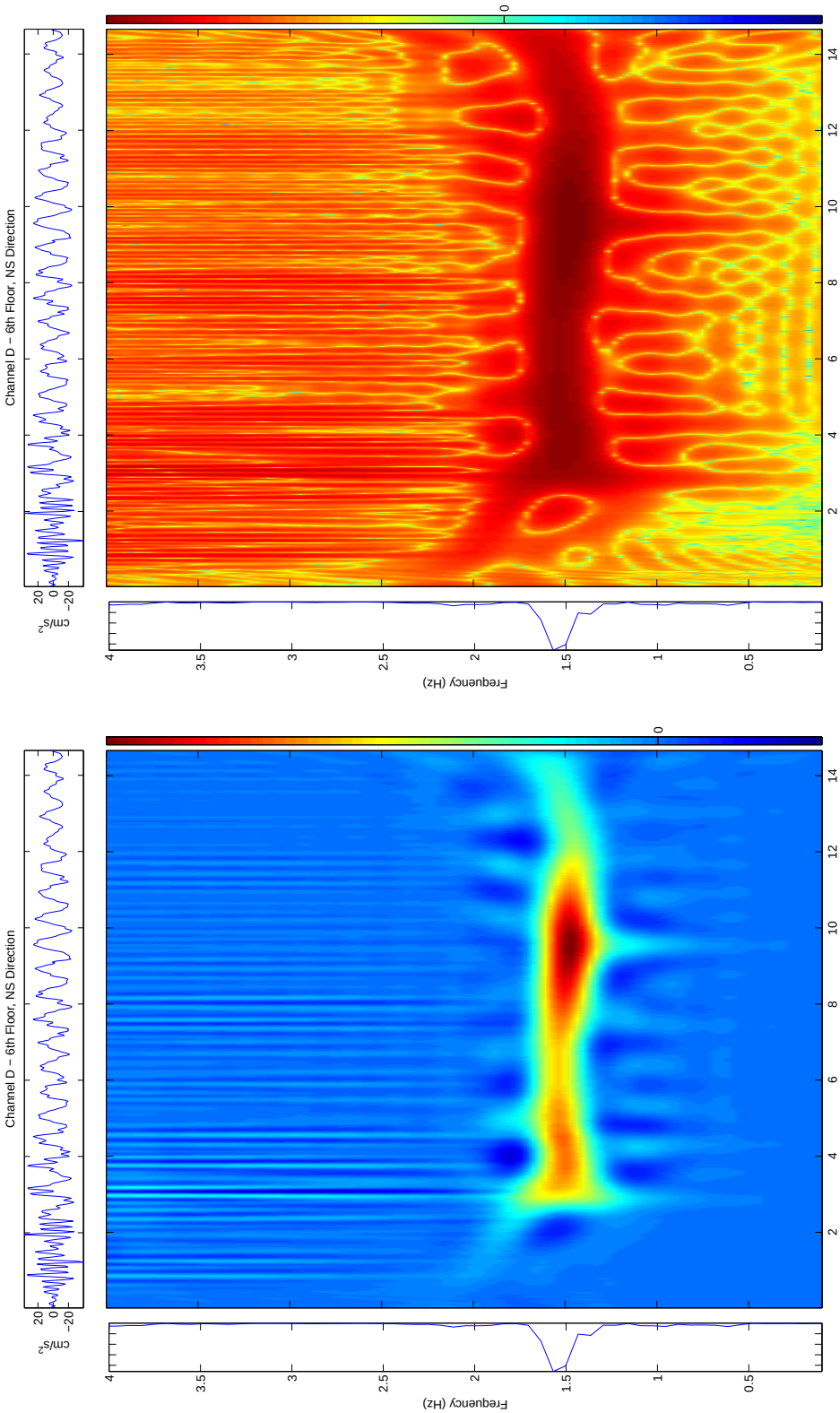

(a) RID

(b) RID, log10(abs())

Figure 4.44: Millikan Response to Northridge Aftershock, Channel D – 6th Floor, NS Direction

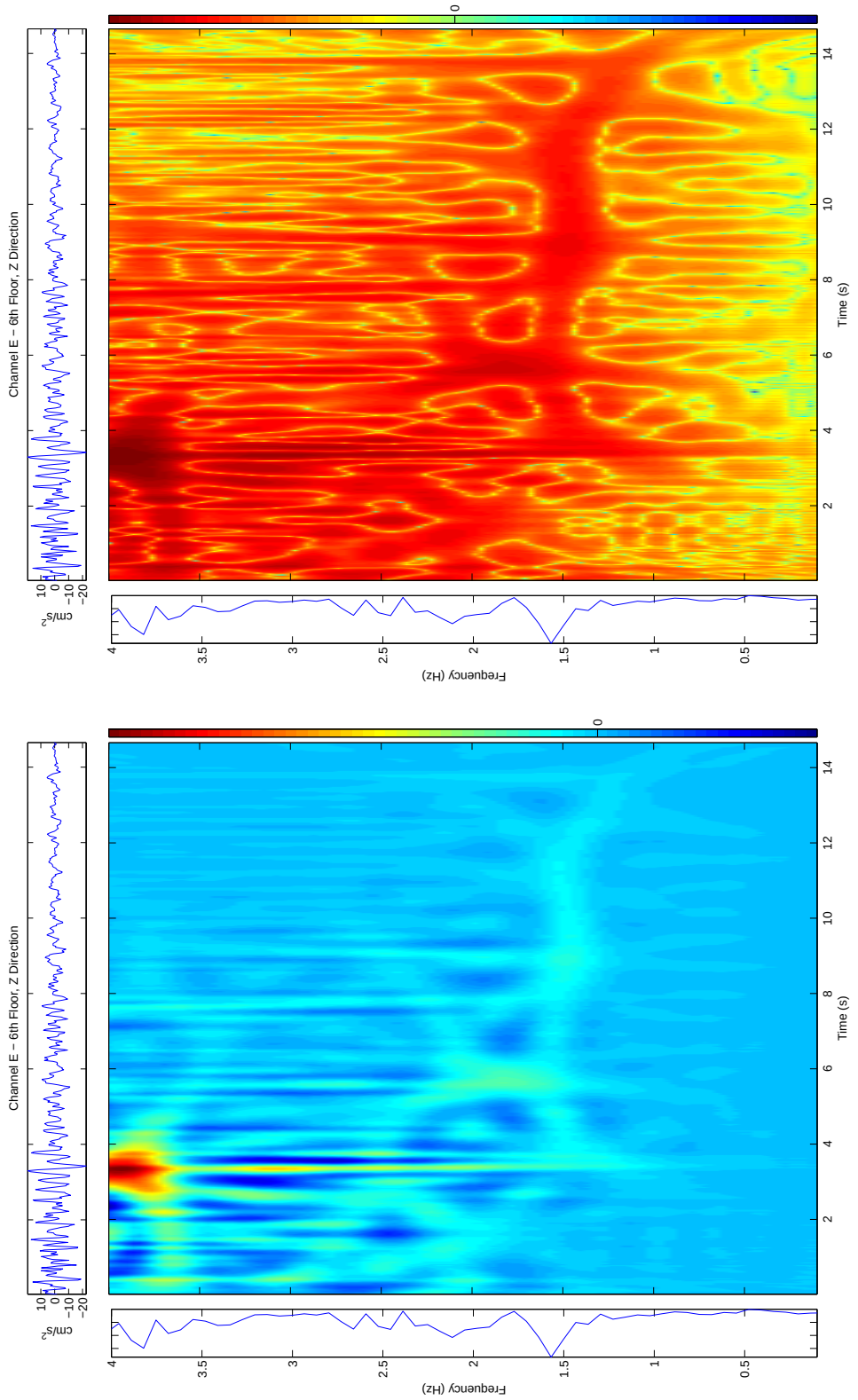

(a) RID

(b) RID, log10(abs()))

Figure 4.45: Millikan Response to Northridge Aftershock, Channel E – 6th Floor, Z Direction

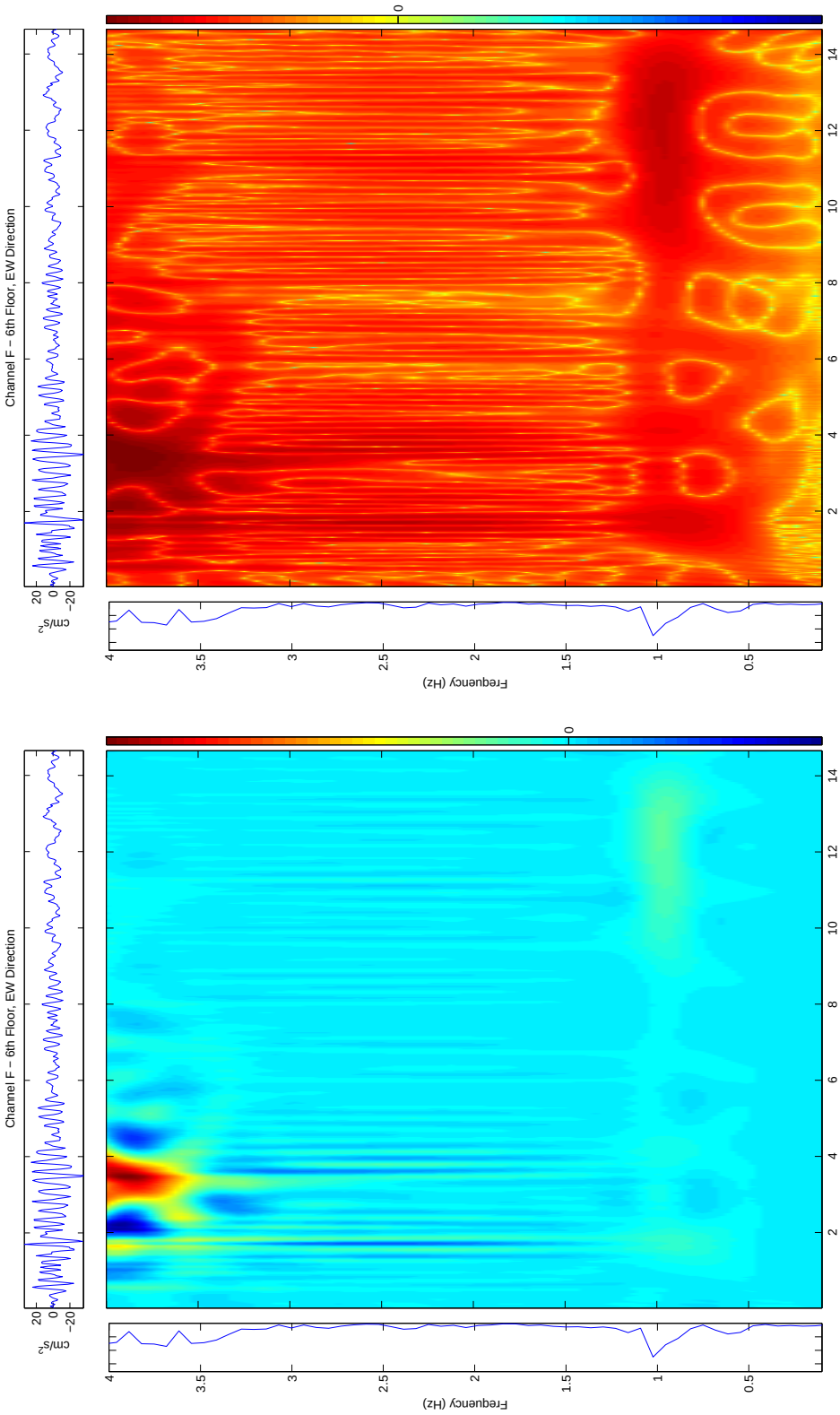

(a) RID

(b) RID, log10(abs())

Figure 4.46: Millikan Response to Northridge Aftershock, Channel F – 6th Floor, EW Direction

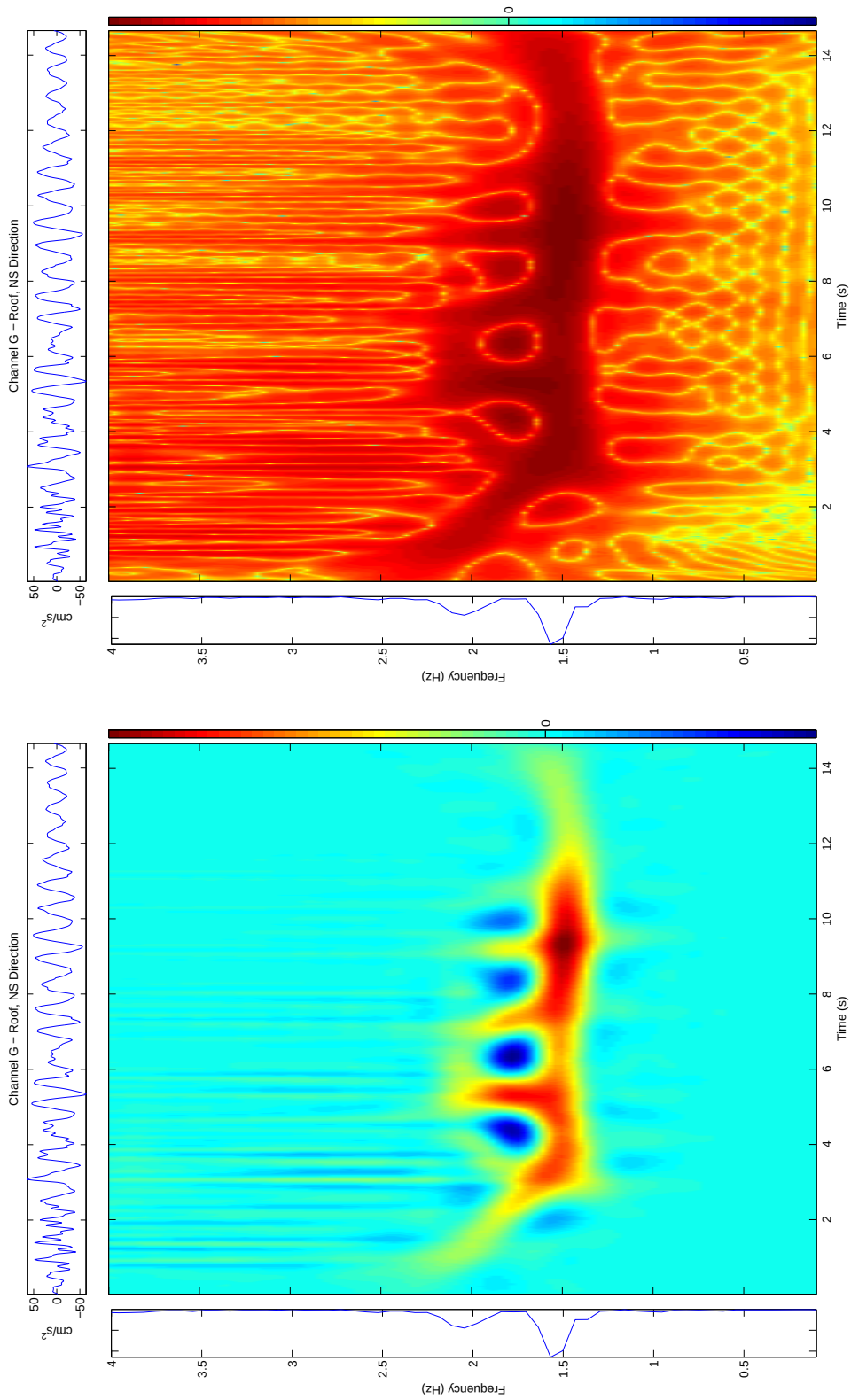

(a) RID

(b) RID, log10(abs())

Figure 4.47: Millikan Response to Northridge Aftershock, Channel G – Roof, NS Direction

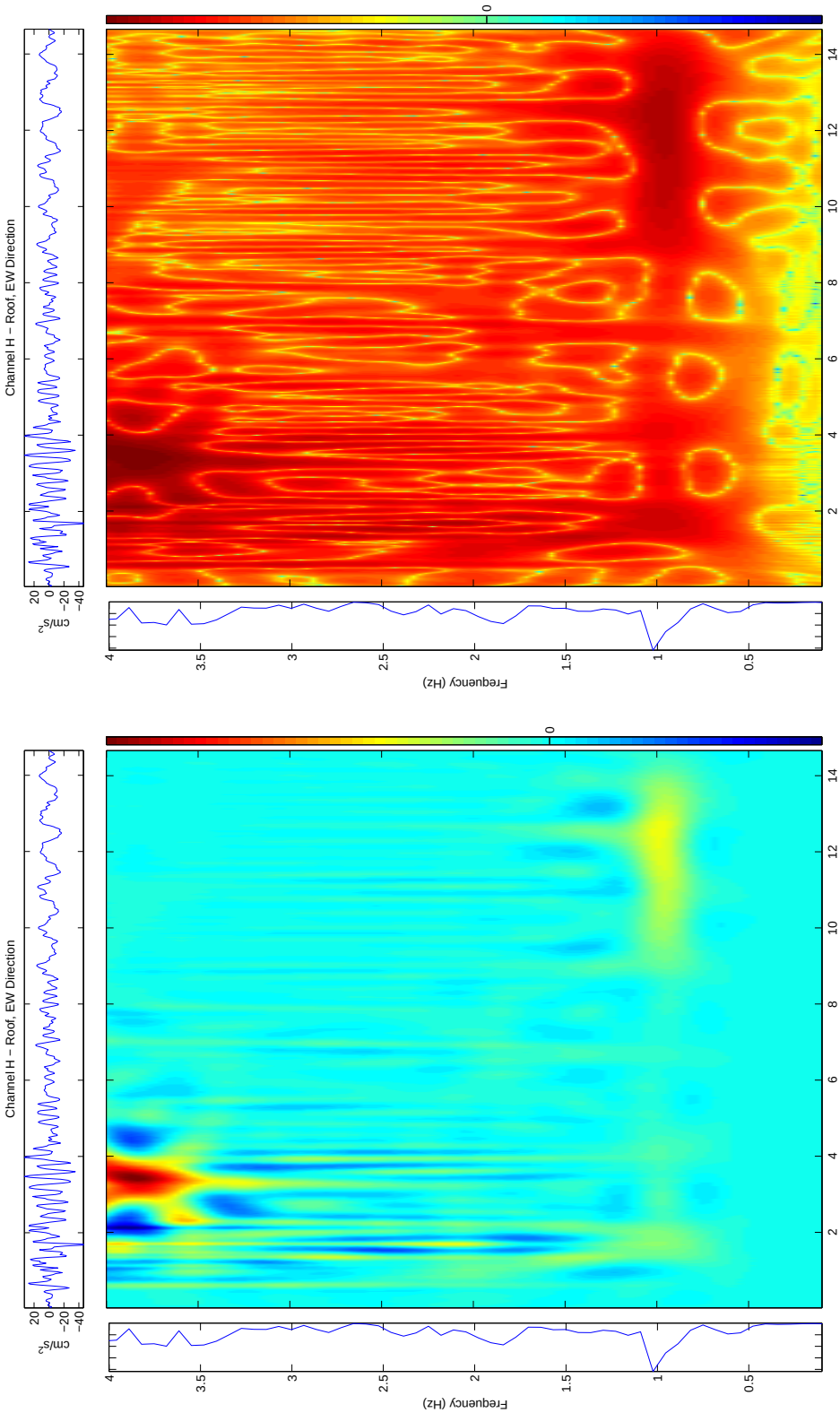

(a) RID

(b) RID, log10(abs())

Figure 4.48: Millikan Response to Northridge Aftershock, Channel H – Roof, EW Direction

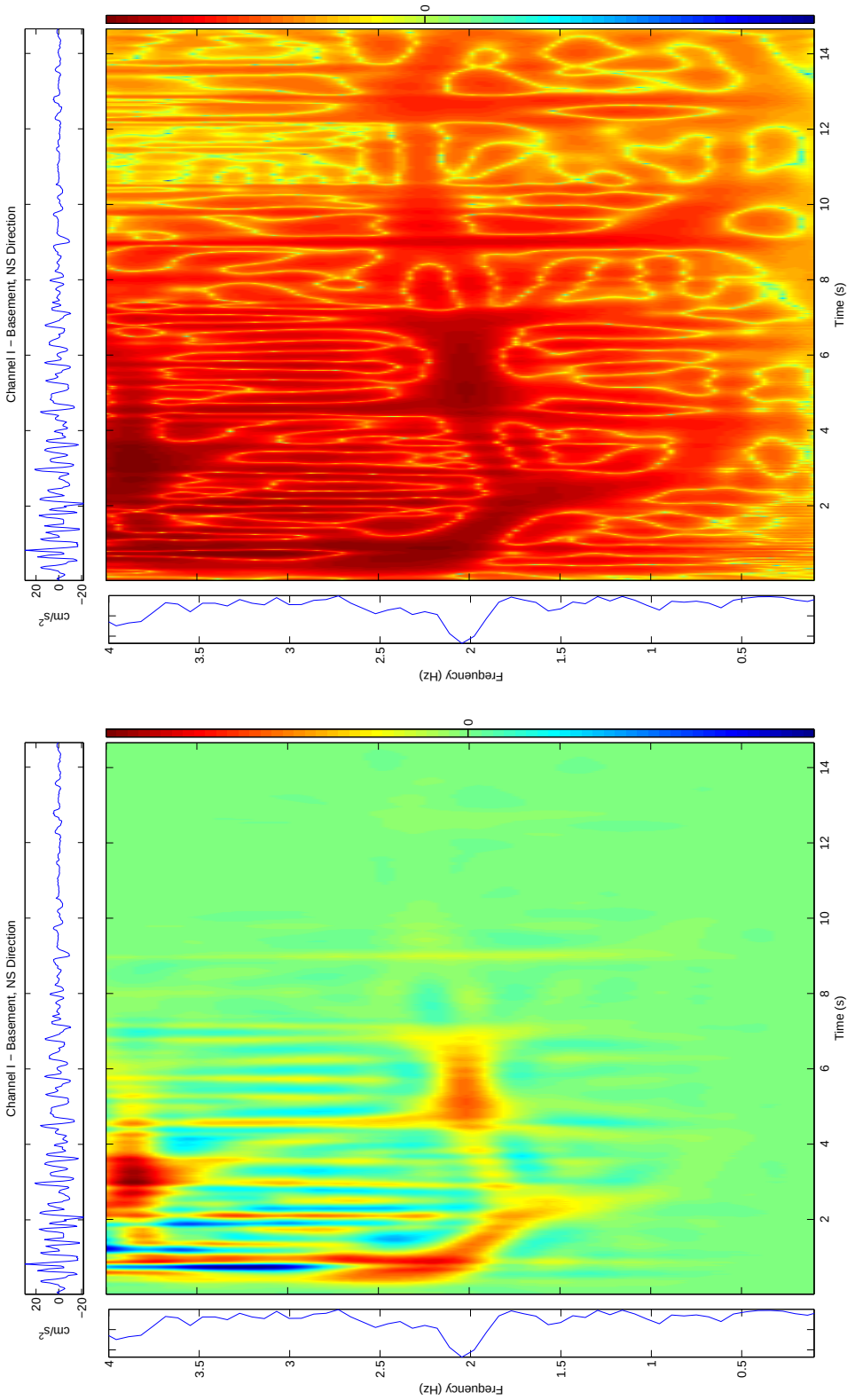

(a) RID

(b) RID, log10(abs())

Figure 4.49: Millikan Response to Northridge Aftershock, Channel I - Basement, NS Direction

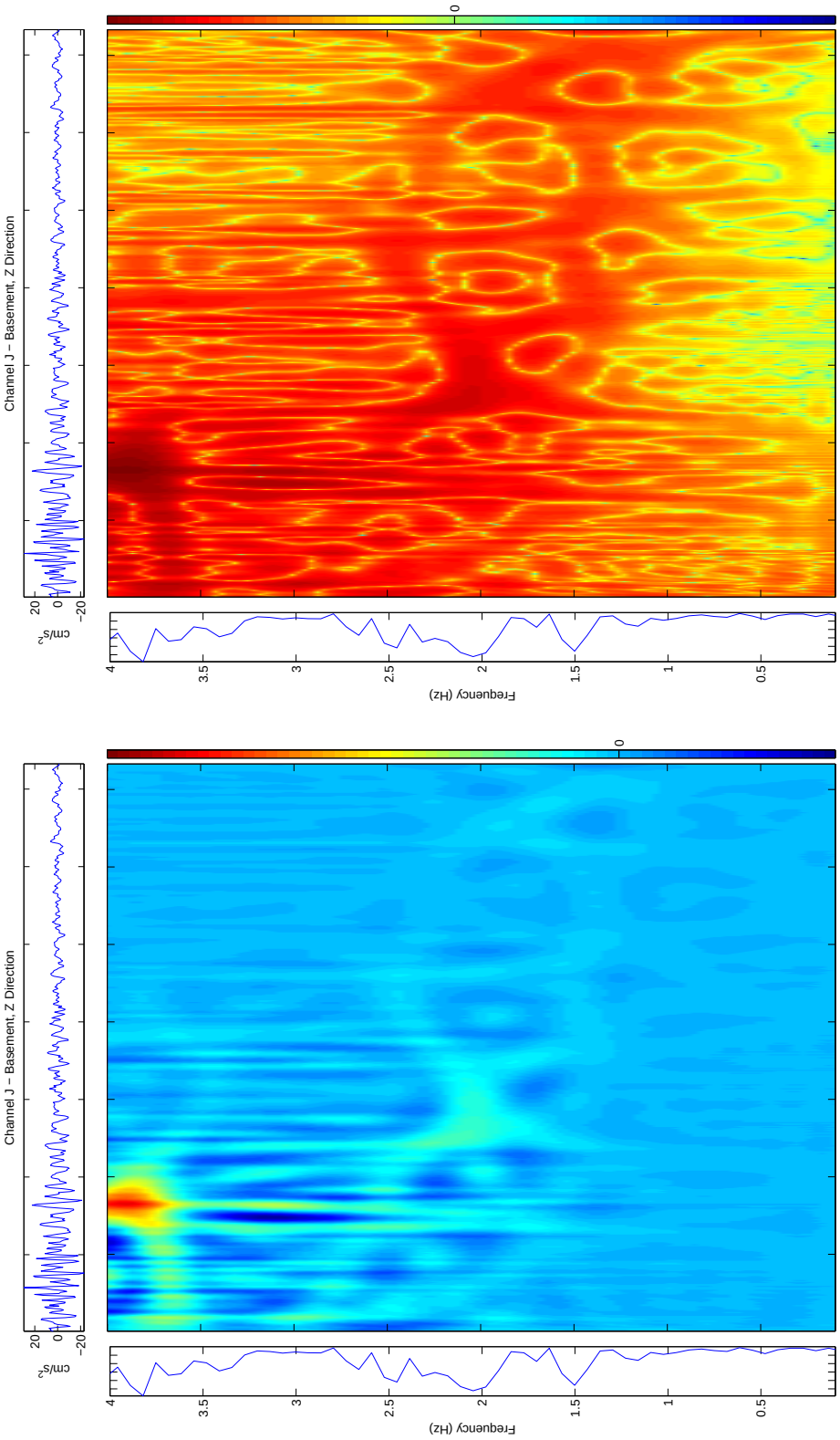

(a) RID

(b) RID, log10(abs())

Figure 4.50: Millikan Response to Northridge Aftershock, Channel J - Basement, Z Direction

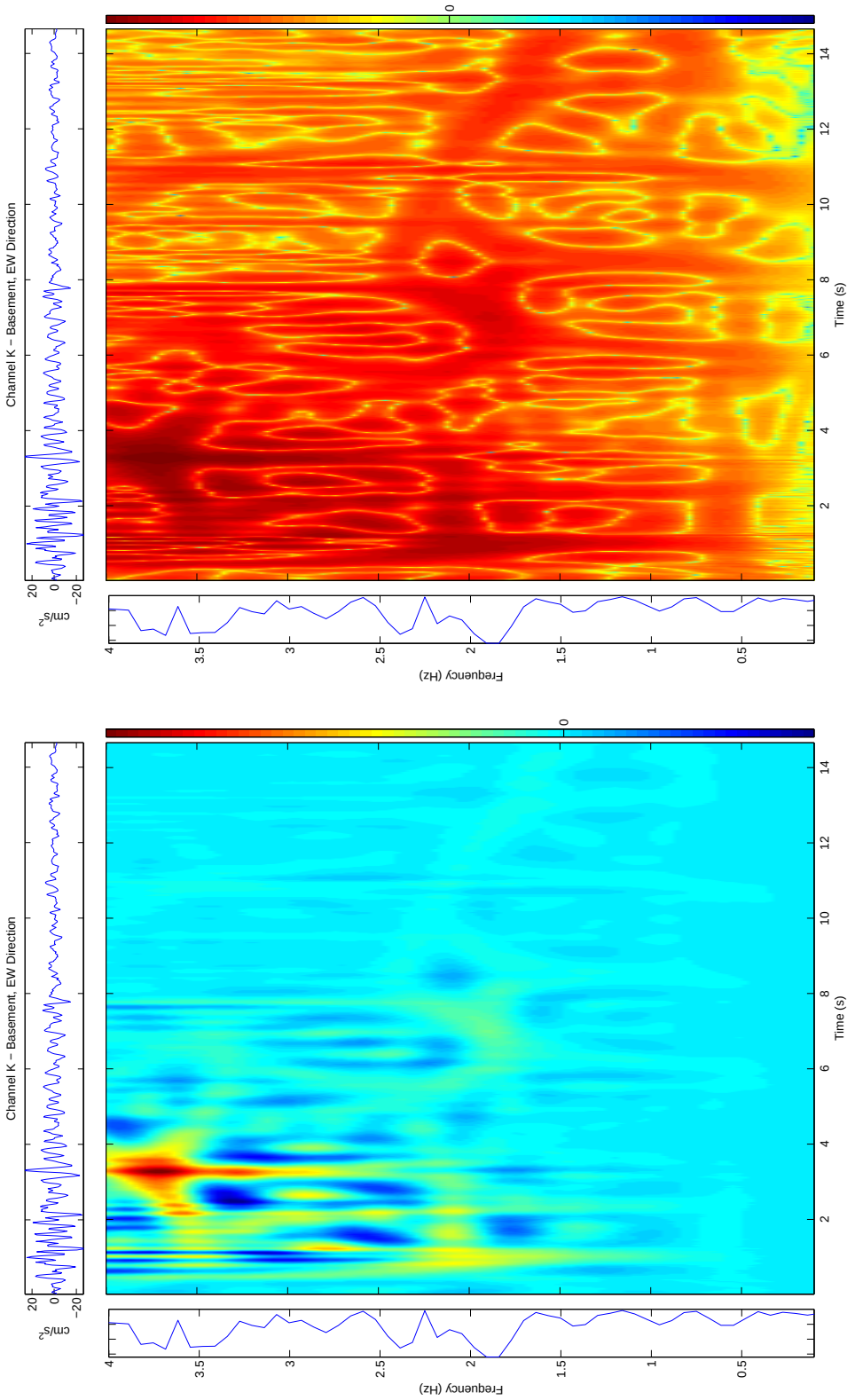

(a) RID

(b) RID, log10(abs())

Figure 4.51: Millikan Response to Northridge Aftershock, Channel K - Basement, EW Direction

4.1.6 Millikan Library: Amplitude & Frequency Nonlinearity

The Millikan Library has been instrumented since its construction in the 1960s, creating a valuable database of earthquake records. From these historical records, it is possible to extract information regarding the nonlinear relationship between the amplitude of excitation and the natural frequency of the building response. For example, in (Clinton et al., 2006), historical behavior of Millikan was compiled into a figure similar to Figure 4.52. The apparent natural frequency for each event was estimated from the free response of the building, and a best fit trendline is plotted through the data. There is a trend towards lower frequencies with higher rooftop accelerations, implying amplitude-related nonlinearity of the building system (including the foundation and soil-structure interaction). This is consistent with the known behavior of Millikan during forced vibration testing (Appendix B), where an increase in applied force results in a decreased natural frequency.

With time-frequency analysis techniques such as the spectrogram and RID, I am able to investigate amplitude and frequency at each instant during an event and compare instantaneous amplitude with estimated frequency. (This is not the same procedure as in Figure 4.52, where the peak acceleration of the record is plotted against the free response later in the same record.) By estimating the relation of instantaneous frequency to instantaneous amplitude, I am attempting a similar procedure as with the Distributed Element Model of Section 3.1, where I plotted frequency as a function of amplitude. For a clearer interpretation of building response, I use velocity instead of acceleration for calculating instantaneous frequency in the time-frequency plots of Figures 4.53 and 4.54.

As the Northridge event had large amplitudes with a small permanent offset, I selected it as a sample event to investigate the relation between instantaneous amplitude and stiffness. The results for Millikan during the Northridge event (Figures 4.55 and 4.56) show a weak trend towards lower frequencies with increasing amplitudes, though there is a large amount of scatter in the estimated response for each excursion during the event. This scatter implies that the nonlinearity of Millikan Library under

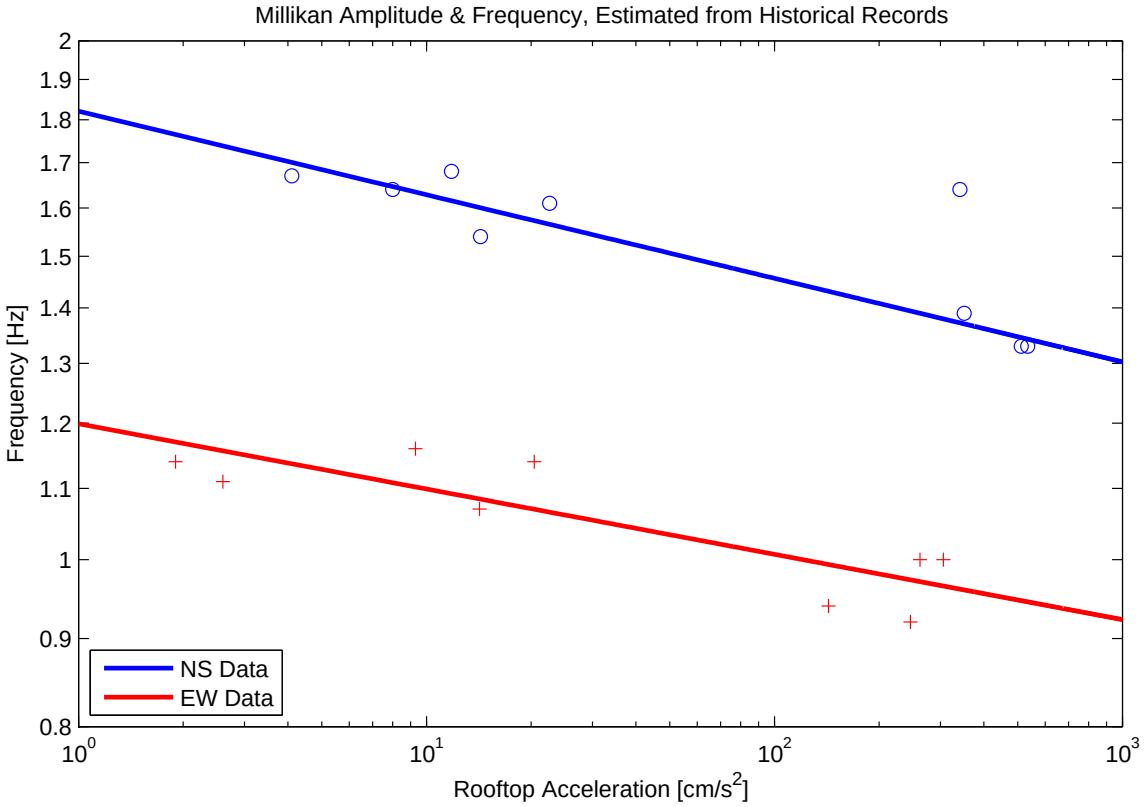

Figure 4.52: Millikan Library, historical amplitude and frequency behavior. Adapted from (Clinton et al., 2006). Peak rooftop accelerations in the EW (red, crosses) and NS (blue, circles) directions as recorded from nine historical earthquakes, and plotted against the estimated frequency (log scaling). Events are shown from 1971 San Fernando event onwards: prior to the San Fernando event the building response was significantly different (c.f. Figure 1.1), and therefore the earliest Millikan measurements are not included in calculating the best fit line. There is a clear trend for decreased frequency with increasing amplitude. This is in agreement with the known behavior of Millikan under forced vibration testing (Appendix B), where an increase in applied force results in a decreased natural frequency.

earthquake excitations is more complicated than the simple amplitude-related nonlinearity of Section 3.1. When identifying instantaneous frequency, the spectrogram (which is expressable as a smoothed WVD) loses resolution, but it also avoids the interference terms that complicate the interpretation of the RID. As an example of the difference between RID and spectrogram estimates of instantaneous frequency, I present selected measures of the roof response in Figures 4.57 and 4.58.

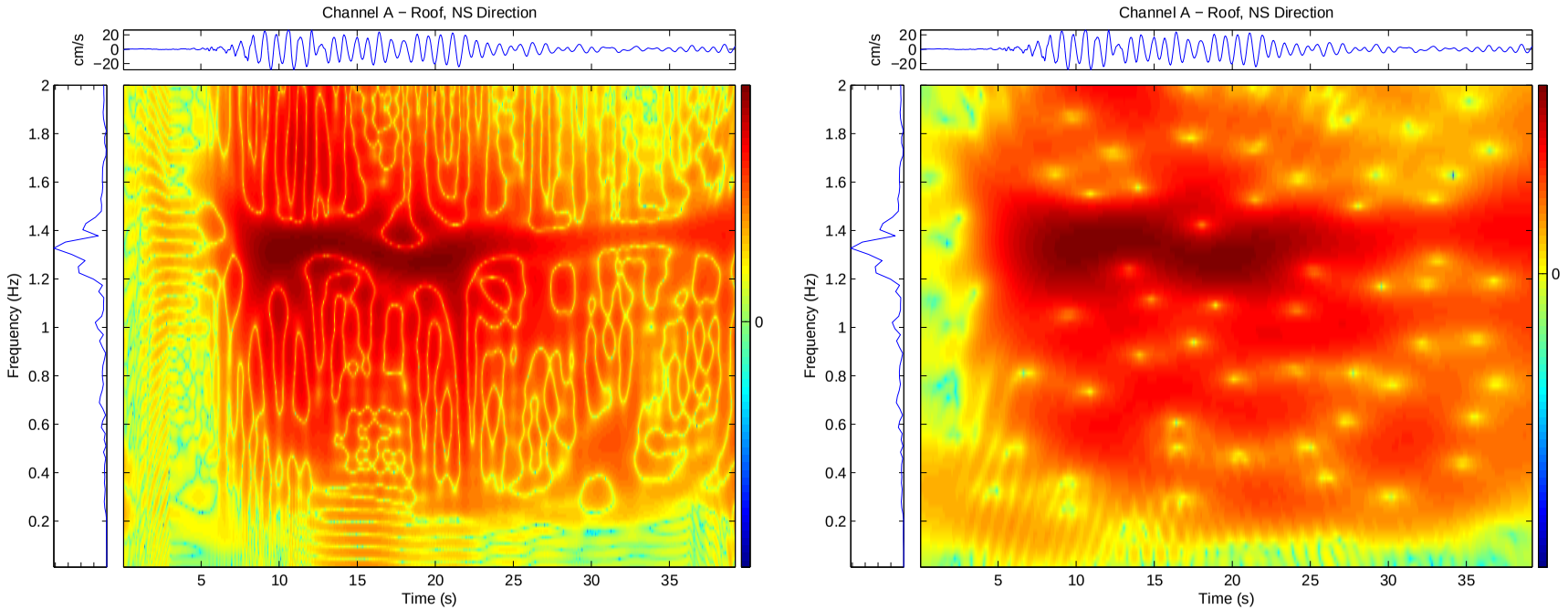

(a) RID, log10(abs())

(b) Spectrogram,log10(abs())

Figure 4.53: Northridge Earthquake, velocity records, Channel A – Roof, NS Direction. The spectrogram is a smoothed WVD, which smears information in the time-frequency plane. The RID has better resolution, but interference terms complicate analysis. Velocity records are typically used for better resolution when calculating instantaneous frequency.

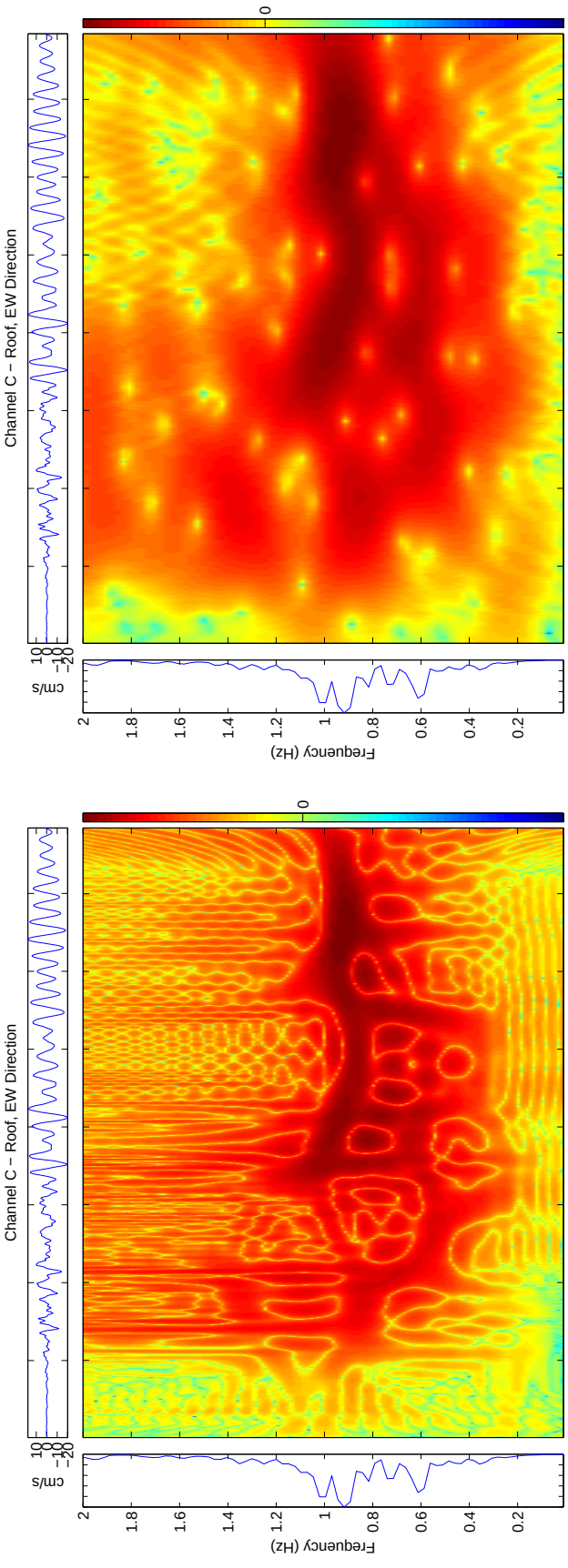

(a) RID, log10(abs())

(b) Spectrogram, log10(abs())

Figure 4.54: Northridge Earthquake, velocity records, Channel C – Roof, EW Direction. As in Figure 4.53.

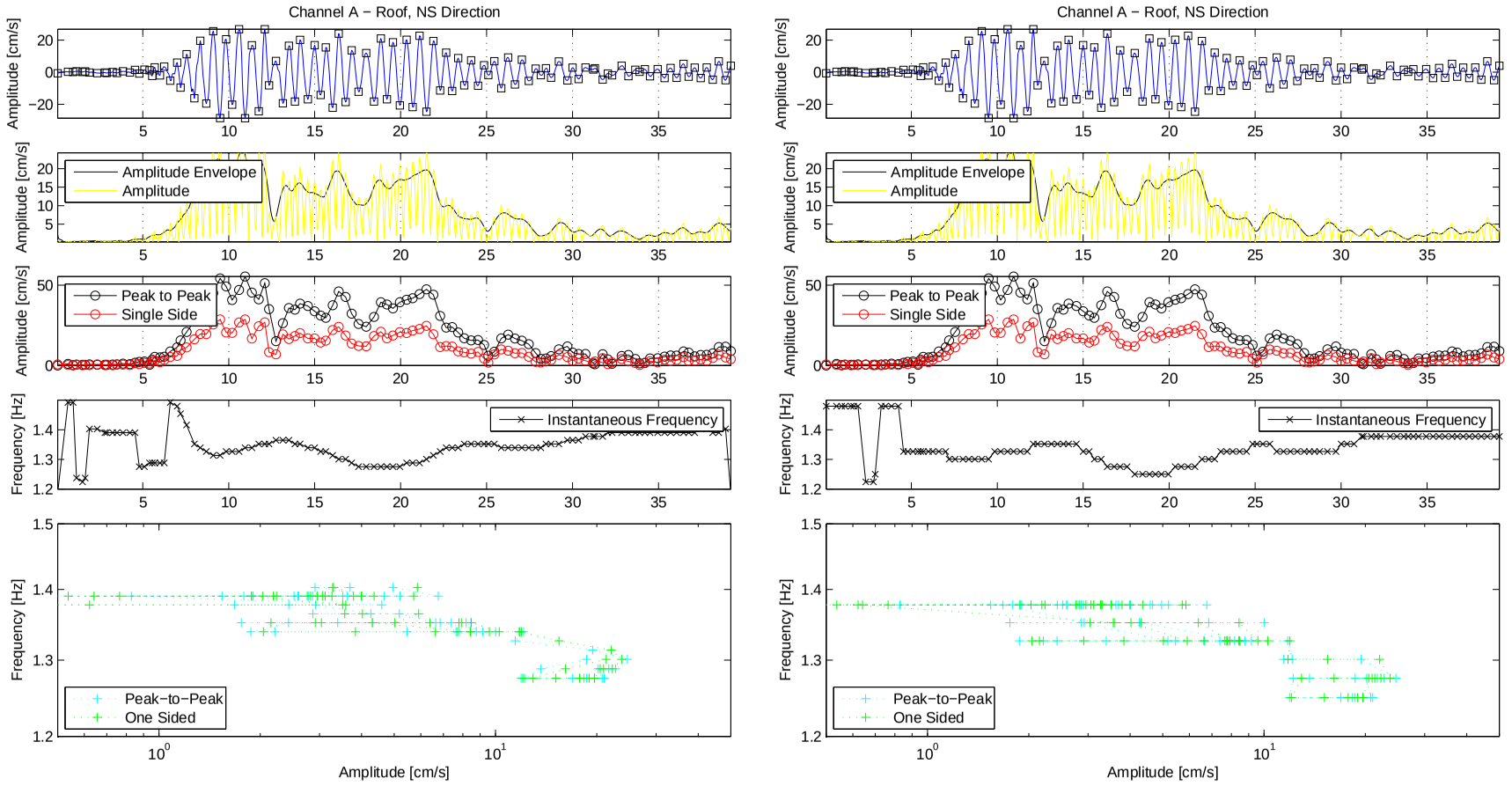

(a) RID

(b) Spectrogram

Figure 4.55: Frequency vs. amplitude relation, Millikan response to Northridge Earthquake, NS Component. The top plot is the velocity of the record, and the second plot is the amplitude envelope. In the third plot I present peak-to-peak estimates of amplitude and the single-side amplitude estimate, and the fourth plot is the frequency as estimated from the time-frequency plane. The last plot is amplitude vs. natural frequency, which reveals a linear trend.

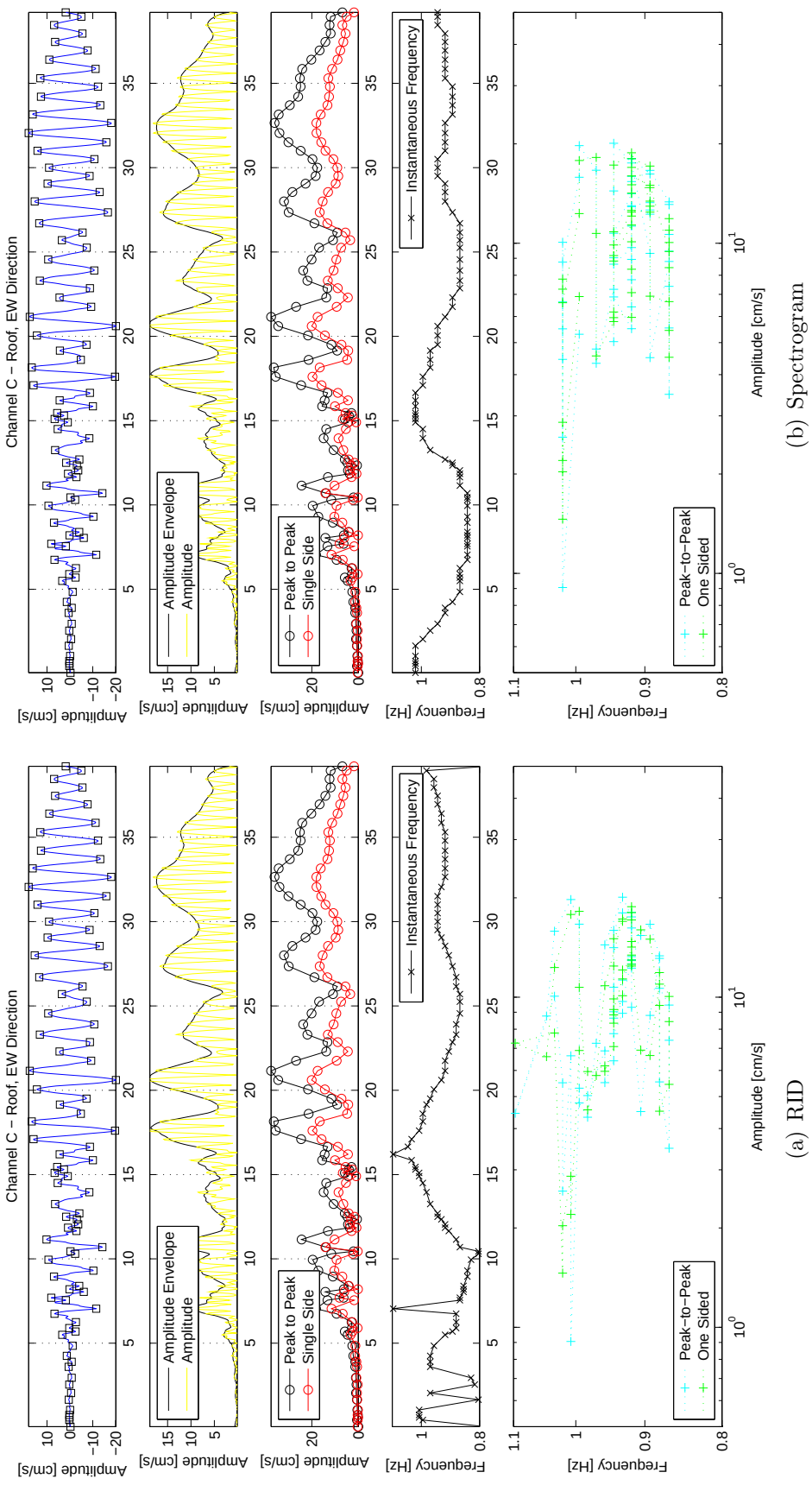

(a) RID

(b) Spectrogram

Figure 4.56: Frequency vs. amplitude, Millikan response to Northridge Earthquake, EW Component. The top plot is the velocity of the record, and the second plot is the amplitude envelope. In the third plot I present peak-to-peak estimates of amplitude and the single-side amplitude estimate, and the fourth plot is the frequency as estimated from the time-frequency plane. The last plot is amplitude vs. natural frequency, which is far more diffuse than in the NS component.

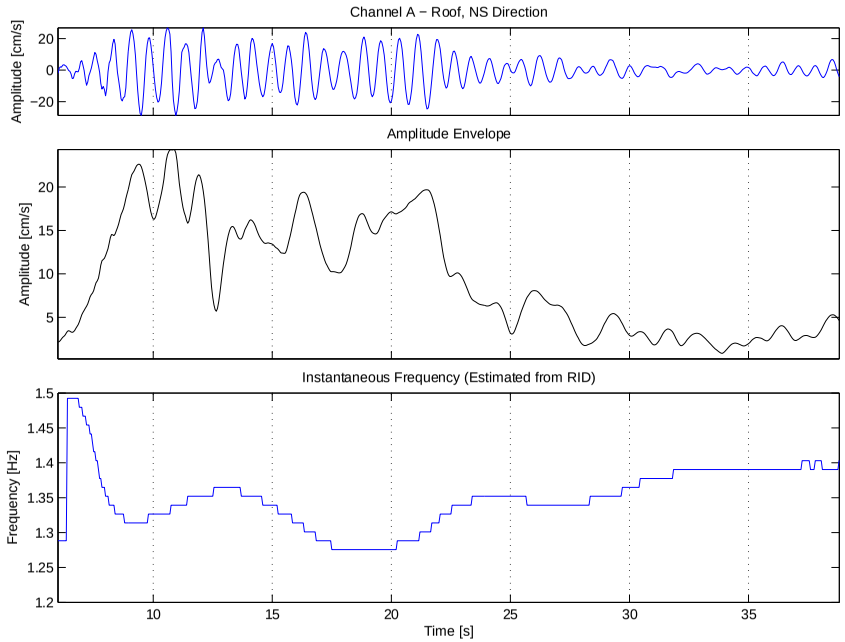

(a) RID

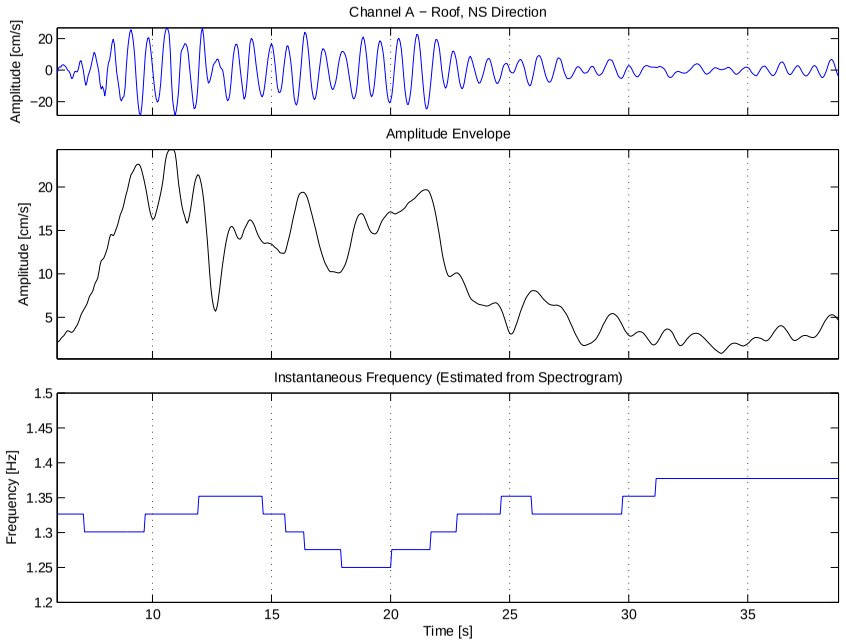

(b) Spectrogram

Figure 4.57: Frequency vs. amplitude, Millikan response to Northridge Earthquake, NS Component. These plots are selected portions of the data from Figure 4.55, focused on a shorter timespan. The spectrogram has poorer resolution, and the RID has interference terms which complicate the interpretation.

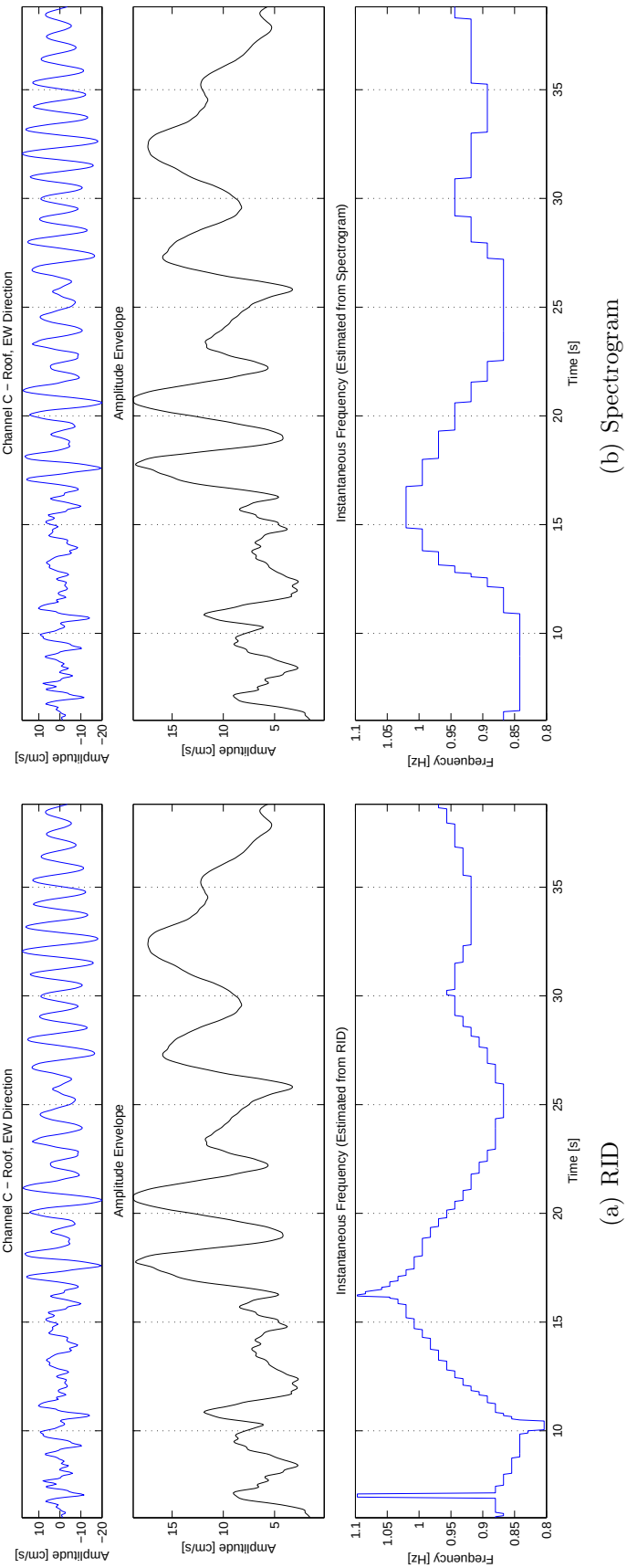

(a) RID

(b) Spectrogram

Figure 4.58: Frequency vs. amplitude, Millikan response to Northridge Earthquake, EW Component. These plots are selected portions of the data from Figure 4.56, focused on a shorter timespan. (As in Figure 4.57.)

(a) Photograph (CSMIP)

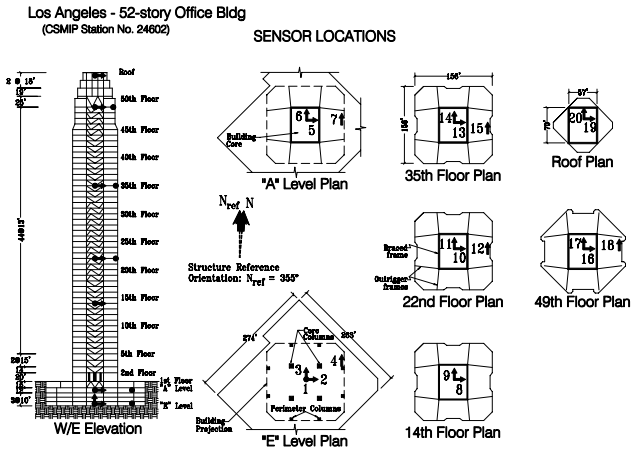

(b) Instrument Layout (CSMIP)

Figure 4.59: 52-Story Office Building, Los Angeles, CA – photograph and instrument layout. CSMIP Station 24602.

4.2 52-Story Office Building, Los Angeles, CA (1994 Northridge Earthquake)

As part of the combined California Integrated Seismic Network (CISN) Strong-Motion data set, the CISN has records from dozens of instrumented buildings. Station 24602 from the California Strong Motion Instrumentation Program (CSMIP) is a 52-story Office Building in Los Angeles (Figure 4.59).

For a tall, flexible building under moderate excitation, the dynamic behavior should be approximately linear with respect to amplitude. In the time-frequency plane (Figures 4.60 – 4.63), the fundamental modes of the building do not have a significant change over the duration of the event. The building is fairly symmetric, and the natural frequencies in the EW and NS directions are nearly identical; the NS natural frequencies are within $\sim$ 2% of the EW natural frequencies for the fundamental modes and the first two overtones. (By the third overtone, the EW and NS natural frequencies begin to differ by larger amounts.) The fundamental modes in the EW

and NS direction are near 0.16Hz, but the mode the largest response was the first overtone near 0.54Hz.

During the strongest motions between 15 and 25 seconds, the building changed from the pre-event natural frequencies to a slightly lower apparent frequency (clearest in the first overtones near 0.55Hz). This change (of less than 1%) is much smaller than the observed changes in the other systems in this thesis, as the building behaved nearly linearly for the Northridge Earthquake.

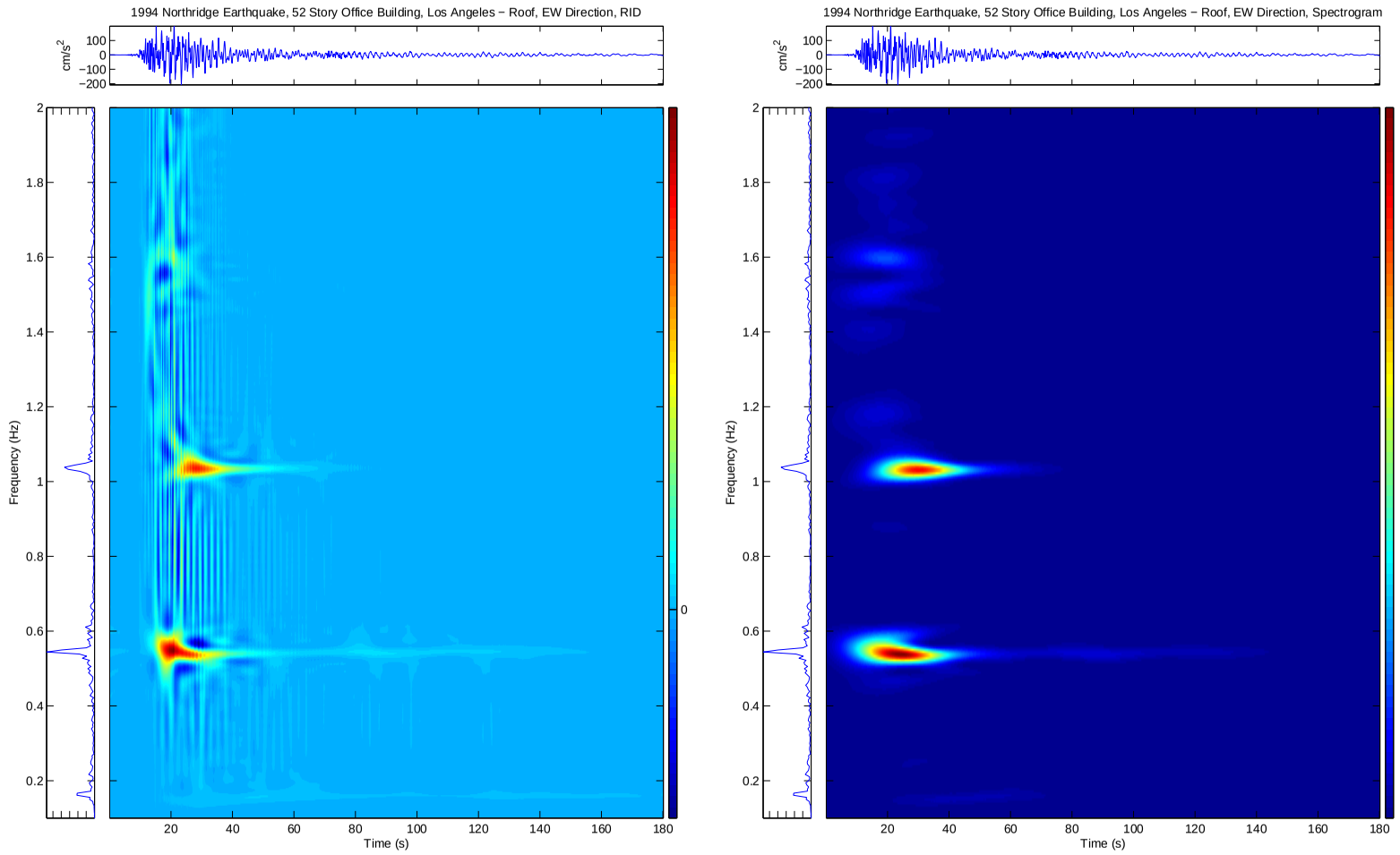

(a) RID

(b) Spectrogram

Figure 4.60: 1994 Northridge Earthquake – 52-Story Office Building, Channel 19, Roof EW. This building behaves nearly linearly for this event, though there is a small change in frequency between 15 and 25 seconds (clearest in the first overtone).

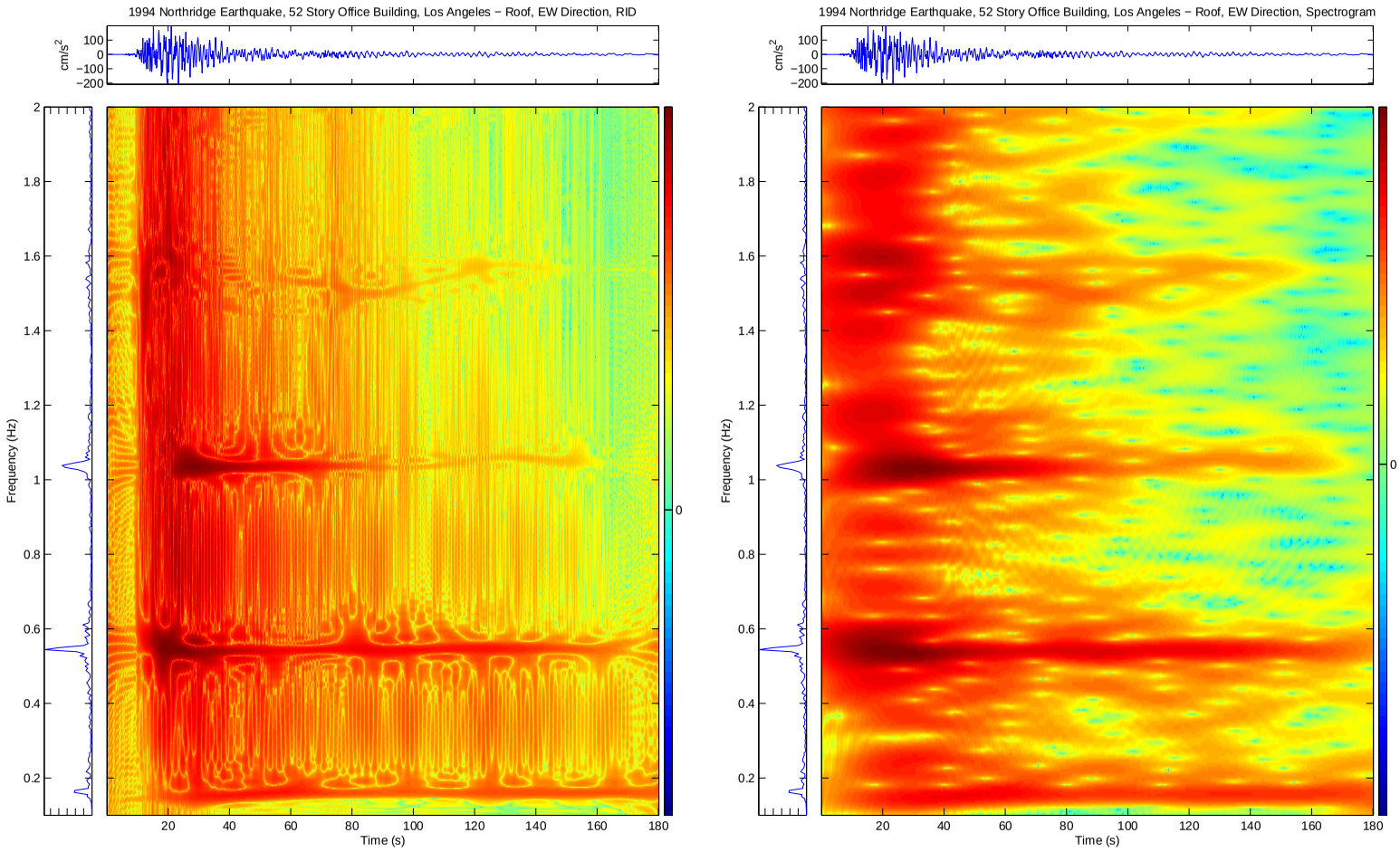

(a) RID, log10(abs())

(b) Spectrogram, log10(abs())

Figure 4.61: 1994 Northridge Earthquake – 52-Story Office Building, Channel 19, Roof EW. As in Figure 4.60, with logarithmic scaling to more clearly show the information in the time-frequency plane and compare the RID with the Spectrogram.

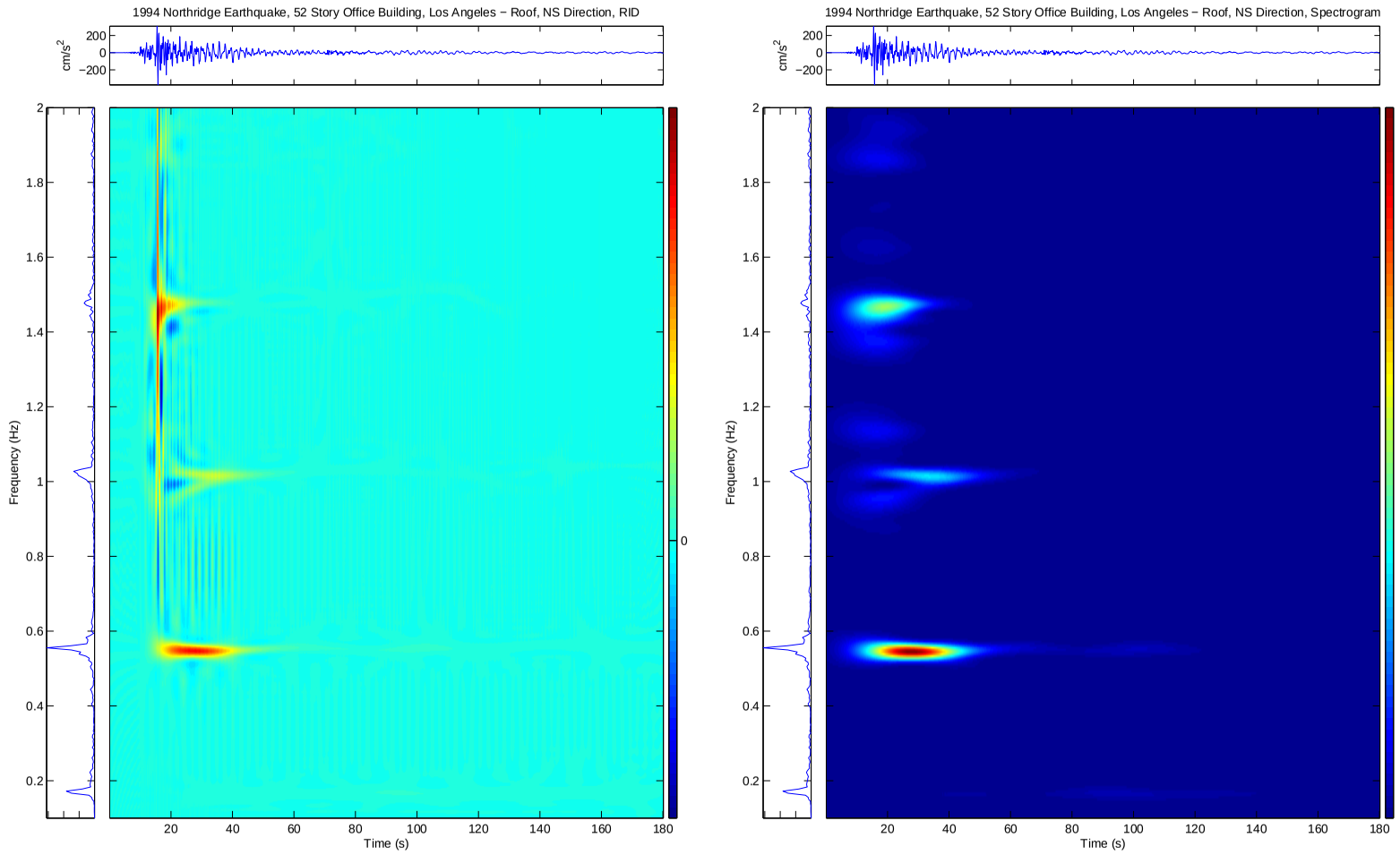

(a) RID

(b) Spectrogram

Figure 4.62: 1994 Northridge Earthquake – 52-Story Office Building, Channel 20, Roof NS. The NS natural frequencies are very similar to the EW frequencies (Figure 4.60).

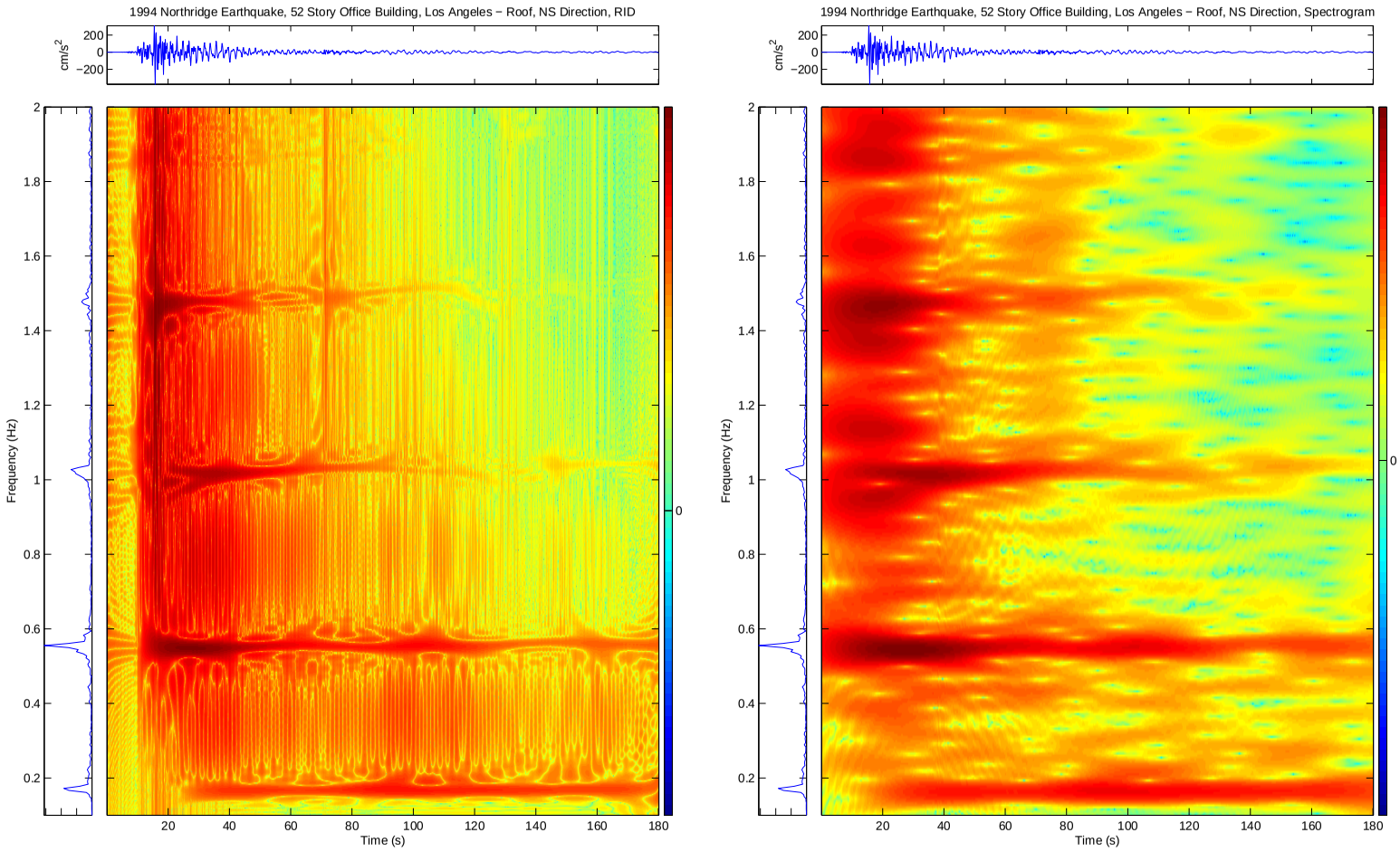

(a) RID, log10(abs())

(b) Spectrogram, log10(abs())

Figure 4.63: 1994 Northridge Earthquake – 52-Story Office Building, Channel 20, Roof NS. As in Figure 4.62, with logarithmic scaling to more clearly show the information in the time-frequency plane and compare the RID with the Spectrogram.

4.3 Imperial County Services Building, El Centro, CA – (1979 Imperial Valley Earthquake)

Time-frequency representations allow for a detailed investigation into the evolving frequency content of records from structures. As in Chapter 3, one possible use for TFR methods such as the Wigner-Ville Distribution is to correlate recorded motions with changes to the physical properties of an instrumented building.

One instrumented building that has experienced strong earthquake motions is the Imperial County Services Building in El Centro (Figure 4.64); this six-story reinforced concrete building was famously damaged during the 1979 Imperial Valley earthquake, and later was demolished due to partial collapse during the event. At the time of the event, the building was instrumented with 13 accelerometers on 4 levels in the building and 3 channels at a free-field site (`http://www.consrv.ca.gov/cgs/smip/`). In Figures 4.65(a) and 4.65(b), the building suffers a significant change in natural frequency between 6 and 12 seconds. An ambient vibration test of the building several months before the event identified the NS fundamental frequency at $2.24Hz$, and the observed natural frequency drops to $1.5Hz$ at 7 seconds into the record (a decrease of 33%). From $t = 7s$ to $t = 11s$, the natural frequency drops to less than $0.9Hz$ (a further loss of 27% for a total loss of 60% of the original frequency). The frequency recovered slightly to $1.1Hz$ by the end of the record, for a final drop of $\sim$50%. As natural frequency, ω, is proportional to $\sqrt{k/m}$ (k = stiffness and m = mass), a decrease in 50% in natural frequency corresponds to a loss of 75% of the global system stiffness. Most of the damage, and therefore most of the loss of stiffness, was due to damage in the first story, including partial collapse of a column.

Past investigations into this building have suggested that damage was initiated $\sim$ 7 seconds into the event, and columns collapsed $\sim$ 11 seconds into this record (Rojahn and Mork, 1982; Todorovska and Trifunac, 2006a; Todorovska and Trifunac, 2006b). This agrees with the information as presented in the time-frequency plane (Figure 4.65(b)), with an evolving natural frequency that agrees with the general known damage pattern of the event.

(a) Photograph (CSMIP). The column in the foreground of the photograph (the South-East corner of the building) partially collapsed during the event, shortening the entire column line.

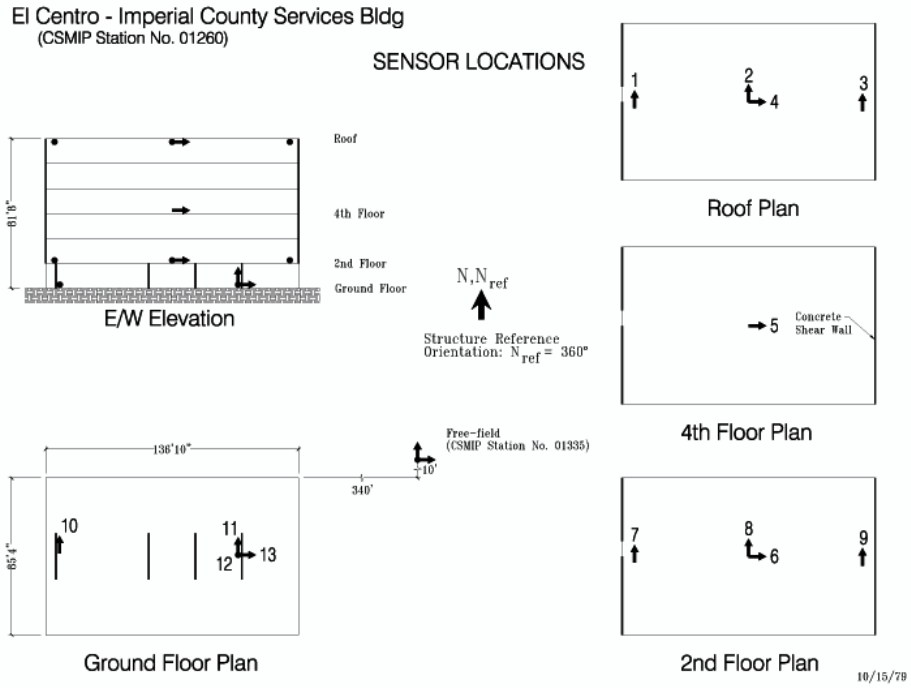

(b) Instrument Layout (CSMIP)

Figure 4.64: Imperial County Services Building, El Centro, CA – photograph and instrument layout. CSMIP Station 01260.

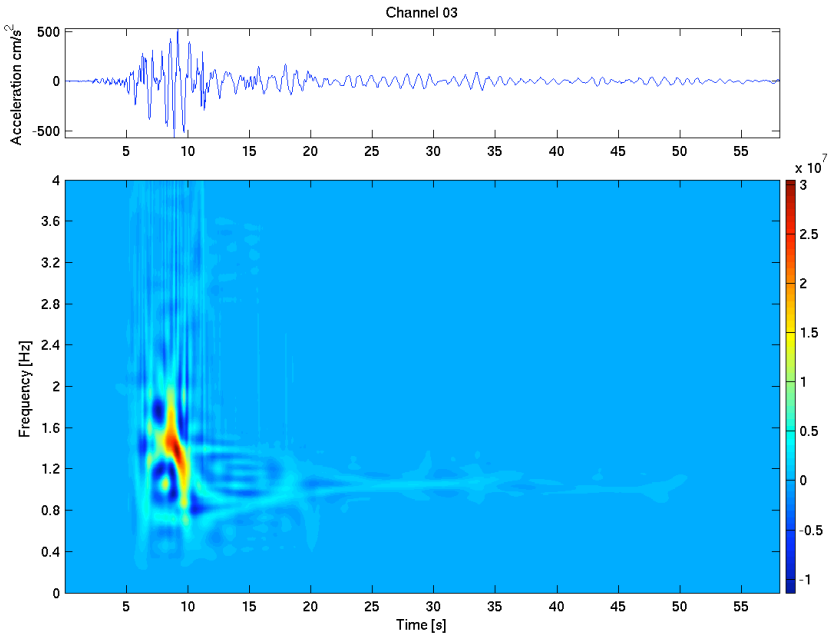

(a) RID of Imperial County Services Building roof records for 1979 Imperial Valley event.

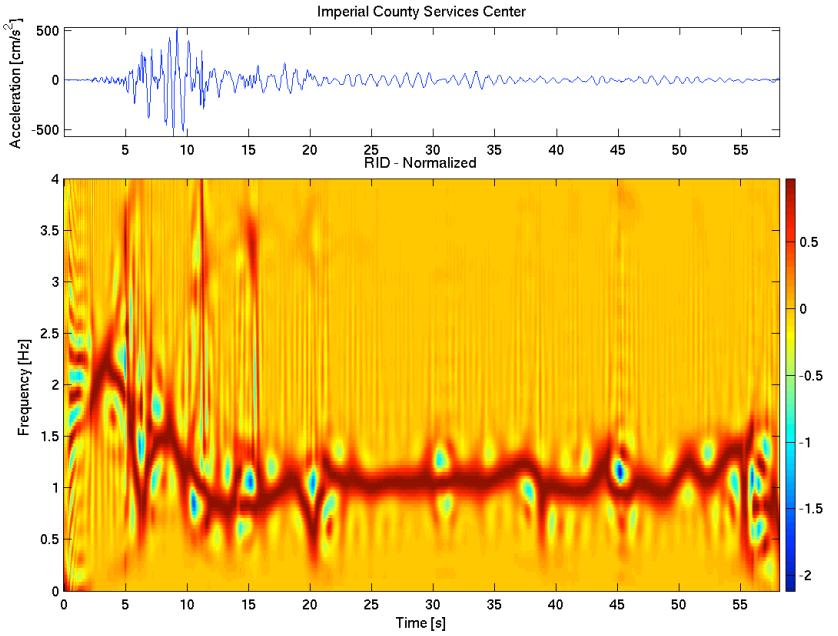

(b) RID of Imperial County Services Building records, scaled by peak amplitude at each time instant. This is an estimate for instantaneous frequency, and can be tied to the behavior of the structure, such as partial collapse between $t = 7s$ and $t = 11s$.

Figure 4.65: Imperial County Services Building (El Centro, CA). NS Component of roof response during 1979 Imperial Valley Event.

4.4 Conclusions and Discussion

Modern time-frequency representations allow for a detailed investigation into the behavior of an evolving signal. When those signals are from instrumented structures, instantaneous frequency content can be correlated with physical changes in a structure. For damaged buildings, time-frequency analysis methods such as the Reduced Interference Distribution provide increased resolution in the time-frequency plane, which allows for a detailed, instant-for-instant analysis of the building behavior.

The Millikan Library (Pasadena, CA) is one example of a well-studied building, with records from historical earthquakes as well as forced vibration tests. Analysis of continuous data has led to further discoveries regarding the wander of the natural frequencies of Millikan Library with respect to earthquake excitation, strong winds, forced vibration testing, and even weather patterns such as rainfall, winds, and temperature. Time-frequency analysis methods allow for an exploration of the evolving dynamic properties of the building, correlating them with the physical phenomena of interest such as increased rainfall, earthquake excitation, etc. Results obtained from analysis of roof records are estimates for the dynamic properties of the entire soil-structure system, combined with the frequency content of the excitation. This differs from system identification techniques where the measured response of the roof is used to create a model based on measured input at the base of the structure.

The 52-story office building (Los Angeles, CA), by contrast with Millikan Library, remains nearly linear during the moderate excitations of the 1994 Northridge Earthquake. With tall flexible buildings, time-frequency analysis methods can help to constrain the dynamic properties.

Instrumented buildings under strong earthquake excitation are rare, but one well-studied example is the Imperial County Services Building, El Centro, CA. This building was severely damaged in the 1979 Imperial Valley Earthquake and was later demolished. As the building was instrumented during the event, it is possible to use time-frequency analysis methods to investigate the changing dynamic properties of

the building response and compare the observed behavior in the time-frequency plane with previous investigations into the onset and extent of damage.

In all these cases, time-frequency analysis methods allow for an exploration of building behavior, adding another tool to the evaluation and identification of building properties. The Reduced Interference Distribution adds resolution in the time-frequency plane when compared with spectrogram and wavelet methods and provides a more exploratory tool as compared to parametric system identification techniques.

Chapter 5

Conclusions

Time-frequency analysis methods allow for the investigation of signals with evolving frequency content. The Wigner-Ville Distribution (including related techniques such as the Reduced Interference Distribution) allows for higher resolution in the time-frequency plane compared with Fourier and wavelet methods, within the constraints of the uncertainty principle. This increase in resolution makes advanced time-frequency analysis methods a useful tool for investigating the dynamic properties of instrumented systems.

Various sample signals in Chapter 2 illustrate the advantages and shortcomings of the time-frequency representations described in this thesis. The smearing of the spectrogram and the diffuse nature of the wavelet transforms complicate the interpretation of these time-frequency representations. The Reduced Interference Distribution overcomes many of these complications, though it introduces shortcoming such as interference and negative values. There is no single ideal time-frequency representation for every application; the operator needs to select a representation that most clearly reveals the information of interest for a given signal. In the case of instrumented structures under earthquake excitation, the Reduced Interference Distribution is nearly optimal for revealing information about the onset and extent of changes in observed apparent frequency. The changes in frequency content of the signal can then be correlated with physical changes to the system.

In Chapter 3 I presented synthetic systems under various types of excitation and used time-frequency representations to explore the dynamic behavior of the

system response and correlate changes in the system with changes in the observed frequency content of the signal. These synthetic systems demonstrate the value of time-frequency analysis techniques for analyzing signals that correspond to changing physical systems. Transform methods provide an essential framework for investigating the properties of these systems, particularly when the stiffness of the system changes.

Chapter 4 provides a more detailed investigation into instrumented systems of interest, including Caltech's Millikan Library. Millikan is a useful testbed for investigation of nonlinear systems, as it has been instrumented for more than 40 years and has well-established nonlinear behavior under small to moderate earthquake excitation as well as sensitivity to weather conditions such as wind, rain, and temperature. Appendix B presented a study of the nonlinear behavior of Millikan Library during a forced vibration experiment, where increasing the applied force through a different shaker configuration led to a decreased natural frequency (though the mechanism for exciting the building with a roof shaker and with earthquake excitations at the ground level are different, the general trend is consistent). This nonlinearity agrees with historical records showing a trend towards decreased natural frequency with increased amplitude of motion, both in earthquake records and in connection with strong winds. Further investigating the nonlinearity using the Reduced Interference Distribution allows for an instant-for-instant description of observed frequency with respect to changing amplitudes of excitation. A summary of digitized records, using modern time-frequency techniques, is presented in order to help build a catalog of building records under earthquake excitation. The collection of Millikan and other building records is part of an attempt to empirically derive a distinctive "fingerprint" of damage in the time-frequency plane. The character of the time-frequency representation will in turn aid in developing parametric models of the system.

Changes in the physical properties of a system (from nonlinearity, loss of stiffness, or damage) are represented in the time-frequency plane as changes in frequency content. The Wigner-Ville Distribution provides a mathematical framework to describe evolving frequencies in a signal, where the signal can be a multi-component synthetic (as in Chapter 2), a simulation of a nonlinear system (Chapter 3), or records from an

instrumented building (Chapter 4). Time-frequency analysis techniques are a valuable exploratory tool, providing guidance for the development of parametric models. Further work in connecting parametric and time-frequency analysis techniques can help build an empirical and theoretical connection between changing frequency content of a signal and changing stiffness of a system.

Appendix A

Instrumentation and Monitoring

Modern research in Structural Engineering and Structural Health Monitoring is dependent on digital instrumentation of civil structures. Buildings and bridges throughout the world have been instrumented in recent years, using the same types of instruments and digitization systems that are typically deployed in seismic networks. Of particular interest in this thesis are the instrumented buildings on the California Institute of Technology ("Caltech") campus and the University of California Los Angeles ("UCLA") campus, which are further discussed in Sections A.1 and A.2, respectively. These campus buildings, instrumented with modern digital seismic instruments, provide a research testbed for the development of building monitoring techniques.

The digitization of modern seismic stations is currently at a level of $\sim 24bits$ $(144dB)$, which allows the instruments to resolve strong earthquake motions and ambient vibrations on the same amplitude scale, with appropriate resolution to investigate changing dynamic properties on many time scales. 24-bit digitization means that the dynamic range of the instrument is divided into 2^{24} increments. For example, a $\pm 2g$ accelerometer (a total range of $4g$) would have a resolution of

$$(4g)(\frac{1}{2^{24}}) = 2.38 \times 10^{-7} g = 2.34 \times 10^{-4} cm/s^2. \tag{A.1}$$

As typical ambient vibrations in an instrumented building can range from $\pm 0.1 cm/s^2$ to $\pm 0.01 cm/s^2$, there is an effective signal-to-noise ratio of ~ 50 to 500 for the analysis of ambient building behavior.

The value of 24-bit digitization is demonstrated in Figure A.1 for sample data from Caltech's Millikan Library (station MIK). MIK is digitized at 24bits, and the data is shown for the equivalent 20-bit and 19-bit digitization. At 19-bits (32x coarser than the 24-bit data), the signal is essentially zero-crossings, as the amplitude is roughly equal to the digitization cutoffs. 20-bit data (16x coarser than the 24-bit data, 2x finer than the 19-bit data) is less blocky, though the discrete cutoffs still harm the character of the signal.

A.1 Caltech Instrumentation

There are five instrumented buildings on the Caltech campus, with various instrument types. The five buildings are the Robert A. Millikan Memorial Library ("Millikan Library"), the Broad Center for the Biological Sciences ("Broad Center"), a telescope pit beneath the Robinson Laboratory ("Robinson Pit"), the Caltech Athenæum, and the basement of the United States Geological Survey offices at 525 S. Wilson Avenue. Of these, only the Broad Center and Millikan Library have instruments throughout the structure. The other stations are located beneath the buildings. The Millikan Library and Broad Center continuously record data to the Southern California Earthquake Data Center (SCEDC), and waveforms can be freely downloaded from `http://www.data.scec.org/STP/stp.html` (data from other stations can be downloaded as described in the following sections).

A.1.1 Millikan Library

Caltech's Millikan Library (Figure A.2), one of the world's most heavily researched and instrumented buildings, has been studied extensively since its construction in the 1960s. It is a very stiff, 9-story, reinforced concrete building with one basement level.

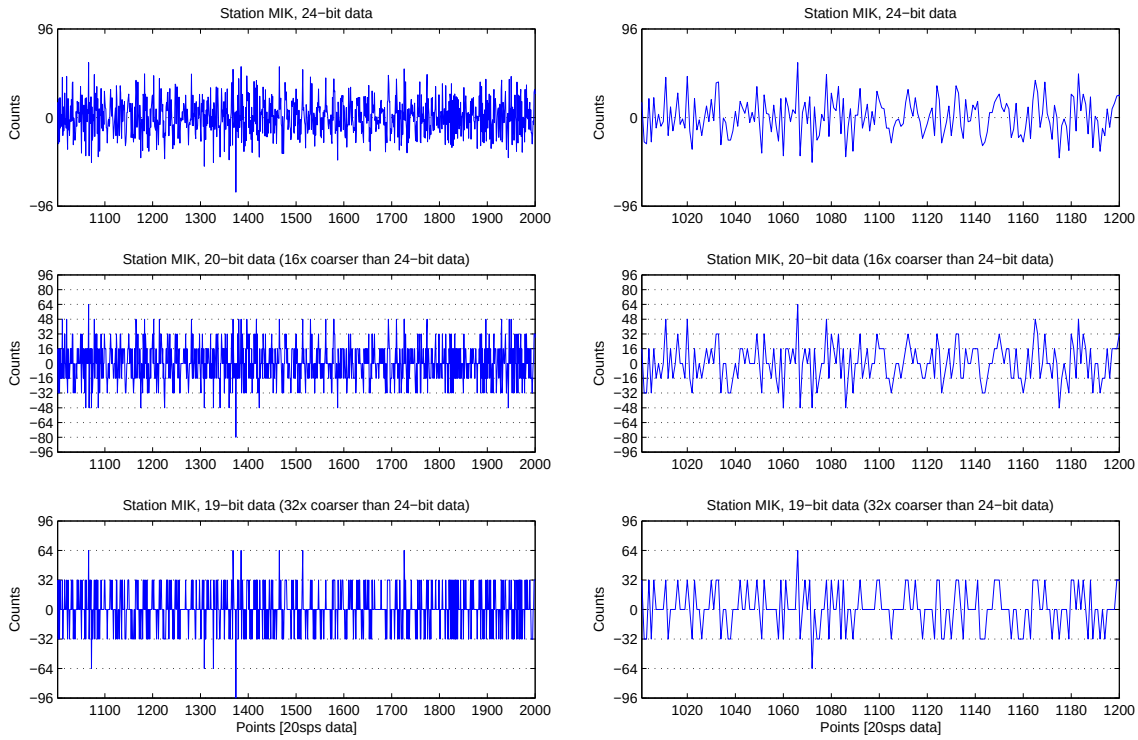

(a) Digitization example, 100s (2000 points) of MIK data

(b) Digitization example, 10s (200 points) of MIK data

Figure A.1: Digitization example. Data from MIK (02-Nov-2005), showing 24-bit data and equivalent data as would have been obtained from a 20-bit and 19-bit digitization system for the same instruments. The 20-bit data is somewhat coarser than the 24-bit data, as the bit level resolution is 16x less than the original data. The 19-bit data is 32x coarser than the 24-bit data and is essentially providing only the zero-crossing information. (Gain for station MIK is $4280 counts/(cm/s^2)$. $\pm 96 counts = \pm 0.022 cm/s^2$.)

A synchronized vibration generator ("shaker") is installed on the roof for forced vibration tests. On the 9th floor is SCEDC station MIK: a triaxial Episensor accelerometer and 24-bit Quanterra datalogger. Three channels of data from station MIK are continuously telemetered to the SCEDC archives for permanent storage of 20sps data and 80sps data for triggered events.

The USGS/Caltech Dense Instrumentation Network was installed in 1998. This dense network consists of 36 instruments: three horizontal accelerometers on each floor (from basement to roof) and three vertical accelerometers in the basement. The dense array is digitized through two parallel systems: a 19-bit Mt. Whitney system run by USGS and a 16-bit Digitexx Datalogger (a proprietary digitization and telemetry system).

A.1.2 Broad Center

The Broad Center (Figure A.3), completed in 2002, is a three story steel building with two deep basement levels. Unbonded braced frames in the North-South and East-West direction form an interior core. SCEDC station CBC was installed during construction and has been recording data since 2003. Station CBC consists of three triaxial Episensors and a 24-bit Quanterra datalogger. The instruments are located at the North-West corner of the internal braced frame core at the ground floor, the North-West corner of the core at the roof level, and the South-East corner of the core at the roof level. (The South-East roof sensor records the horizontal components and discards the vertical information, as the digitizer can only record eight channels of data.) These 8 channels are continuously telemetered to the SCEDC archives and stored at 20sps (100sps for triggered events).

A.1.3 Robinson Pit

In the basement of the Robinson Building is an unused telescope pit. This pit houses SCEDC station CRP, which is currently used as a testing station, so the instrumentation varies.

Figure A.2: Caltech Millikan Library. View from the South-East. The dark grey walls in the foreground are structural shear walls, and the white panels on the south (left) side of the building are non-structural marble cladding.

Figure A.3: Caltech Broad Center. View from the South-West. The South wing of the building has an irregular floorplan with increasing height; the main building is to the North.

A.1.4 Caltech Athenæum

SCEDC Station CAC, located in the basement of the Athenæum faculty club on the Caltech campus, is digitized through a 19-bit K-2 datalogger. Only triggered data from this station is stored in the SCEDC archives.

A.1.5 525 S. Wilson Ave

The USGS Pasadena office is located at 525 S. Wilson Ave, across the street from Caltech (200m due West of Millikan Library and 300m SSW of the Broad Center). In the basement is SCEDC station GSA (24-bit Quanterra digitizer and triaxial Episensor accelerometer), which is commonly used as a reference station for data from other Caltech stations.

A.1.6 Caltech Online Monitoring and Evaluation Testbed

The Caltech Online Monitoring and Evaluation Testbeds (COMET) site, `http://comet.caltech.edu`, was developed as an educational tool as well as a testbed for the development of structural health monitoring techniques.

The COMET site acts as an interface between the Southern California Earthquake Data Center (SCEDC) database and a web-browser, using an implementation of the

Earthworm Processing System. Real-time data from two campus buildings, Millikan Library (SCEDC station MIK) and the Broad Center (SCEDC station CBC), is archived from the SCEDC at 80sps and 100sps, respectively, and stored on a local hard drive. COMET users can log onto the site and download selected data, display these data, and perform modal analysis using Caltech's MODE-ID modal analysis software (Beck, 1996). The COMET interface was implemented by Dr. H. F. Lam, City University of Hong Kong, during a postdoctoral scholarship at Caltech.

A.2 UCLA Instrumentation: Factor Building

The Doris and Louis Factor Building ("Factor Building") is a 15-story moment-resisting steel frame building on the UCLA Campus. The Factor building has 72 channels of continuous accelerometer data, four horizontal instruments on each floor, plus two horizontal instruments and two vertical instruments on each of the two basement levels. Instruments are uniaxial FBA-11s, digitized with 24-bit Quanterras. Figure A.4 shows the distribution of instruments and their orientations. There is also a 100m borehole located approximately 25m east of the Factor Building, with triaxial Episensors at the top and the bottom of the borehole, telemetered through a Quanterra digitizer.

This dense instrumentation network makes the Factor Building one of the most heavily-instrumented buildings in the world. Data is stored in a buffer at 500sps and downsampled to 100sps for permanent storage. The 100sps Factor Building data is freely available from the IRIS Data Management Center, `http://www.iris.edu/`. For further information on the Factor Building, please see `http://factor.gps.caltech.edu` and Kohler et al. (2006).

A.3 Summary

Instrumented buildings provide a valuable testbed for structural health monitoring and system identification. Analysis of ambient vibrations in a building is highly de-

(a) UCLA Factor Building, view from the North-East

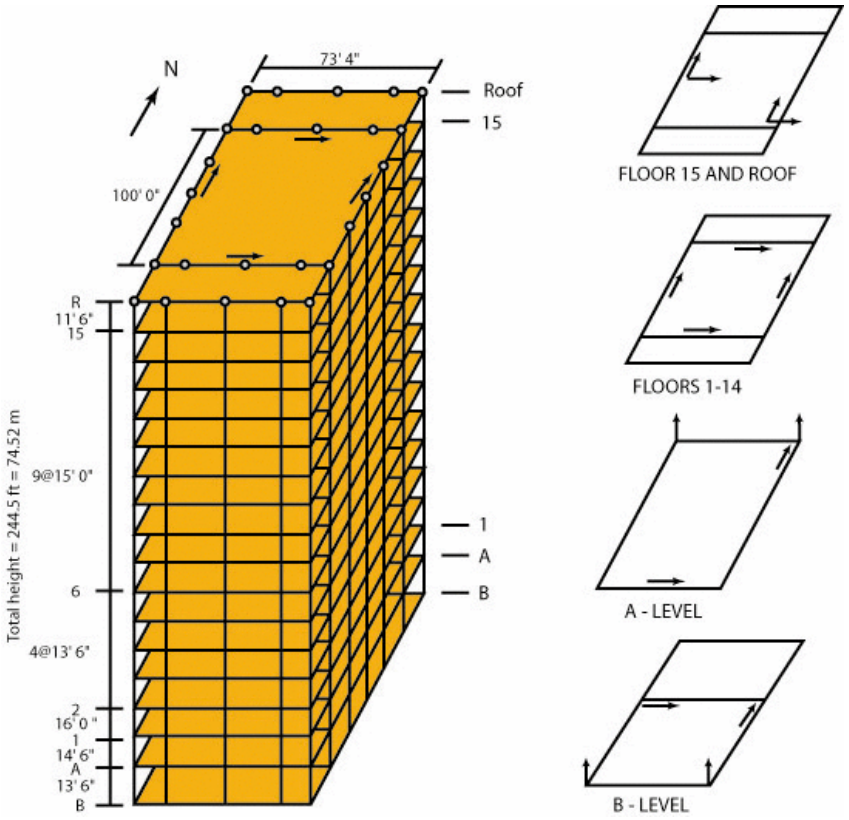

(b) Layout of instruments from the UCLA Factor Building

Figure A.4: UCLA Factor Building. (Instrument layout from `http://factor.gps.caltech.edu`.) The Factor Building is a moment frame building with an irregular floorplan that increases in area at the 10th floor. This causes an internal reflection of traveling waves.

pendent on the advances in seismic instrumentation and digitization; the 24-bit systems in common use allow for investigations of ambient vibrations as well as moderate to strong earthquake motions. Several buildings on the Caltech and UCLA campuses have been instrumented, and selected data is further analyzed in this thesis.

Appendix B

Millikan Library Forced Vibration Testing

Adapted from Bradford, Clinton, Favela, and Heaton 2004, Earthquake Engineering Research Library report on research supported by the California Institute of Technology.

ACKNOWLEDGEMENTS

The authors would like to acknowledge Arnie Acosta for data triggering and retrieval and thank him for his support. We thank Caltech's Structural Monitoring Group for their input during this project, and we also thank the Southern California Earthquake Center and the Portable Broadband Instrumentation Center at the University of California Santa Barbara for the loan of the portable instrument. We acknowledge the SCEDC for the MIK data.

ABSTRACT

This report documents an investigation into the dynamic properties of Millikan Library under forced excitation. On July 10, 2002, we performed frequency sweeps from 1 Hz to 9.7 Hz in both the East-West (E-W) and North-South (N-S) directions using a roof level vibration generator. Natural frequencies were identified at 1.14 Hz (E-W fundamental mode), 1.67 Hz (N-S fundamental mode), 2.38 Hz (Torsional fundamental mode), 4.93 Hz (1^{st} E-W overtone), 6.57 Hz (1^{st} Torsional overtone), 7.22 Hz (1^{st} N-S overtone), and at 7.83 Hz (2^{nd} E-W overtone). The damping was estimated at 2.28% for the fundamental E-W mode and 2.39% for the N-S fundamental mode. On August 28, 2002, a modal analysis of each natural frequency was performed using the dense instrumentation network located in the building. For both the E-W and N-S fundamental modes, we observe a nearly linear increase in displacement with height, except at the ground floor, which appears to act as a hinge. We observed little basement movement for the E-W mode, while in the N-S mode 30% of the roof displacement was due to basement rocking and translation. Both the E-W and N-S fundamental modes are best modeled by the first mode of a theoretical bending beam. The higher modes are more complex and not well represented by a simple structural system.

B.1 Introduction

This report documents the forced vibration testing of the Robert A. Millikan Memorial Library ("Millikan Library") located on the California Institute of Technology campus. It also provides a historical backdrop to put our results in perspective.

During and immediately after the construction of the library in the late 1960s, numerous dynamic analyses were performed (Kuroiwa, 1967; Foutch et al., 1975; Trifunac, 1972; Teledyne-Geotech-West, 1972). In these analyses, fundamental modes and damping parameters were identified for the library, and higher order modes were suggested, but not investigated. It has been established that the fundamental frequencies of the library vary during strong motion (Luco et al., 1986; Clinton et al., 2006). Some drift in the long-term behavior of the building has also been observed in compiled reports of modal analysis from the CE180 class offered every year at Caltech (Clinton, 2004).

The temporal evolution of the building's dynamic behavior, as well as the much improved density and quality of instrumentation, led to an interest in a complete dynamic investigation into the properties of the system. Our experiments were designed to provide an updated account of the fundamental modes and to identify and explore the higher order modes and modeshapes. A better understanding of the dynamic behavior of the Millikan Library will aid in the increased research being performed on the building and provide a better understanding of the data currently being recorded by the instruments in the library.

An initial test was performed on July 10, 2002, for which we performed a full frequency sweep of the building (from 9.7Hz, the limit of the shaker, to 1Hz), in both the E-W and N-S directions. Frequencies of interest were explored in more detail, with a finer frequency spacing and different weight configurations, during a second test on August 28, 2002.

B.2 Millikan Library

The Millikan Library (Figure B.1) is a nine-story reinforced concrete building, approximately 44m tall and 21m by 23m in plan. Figure B.2 shows plan views of the foundation and a typical floor as well as cross-section views of the foundation and a N-S cross-section.

The building has concrete moment frames in both the E-W and N-S directions. In addition, there are shear walls on the East and West sides of the building that provide most of the stiffness in the N-S direction. Shear walls in the central core provide added stiffness in both directions. More detailed descriptions of the structural system may be found in Kuroiwa (1967), Foutch (1976), Luco et al. (1986), Favela (2004), and Clinton (2004).

Figure B.1: Robert A. Millikan Memorial Library: View from the northeast. The dark colored walls in the foreground comprise the East shear wall.

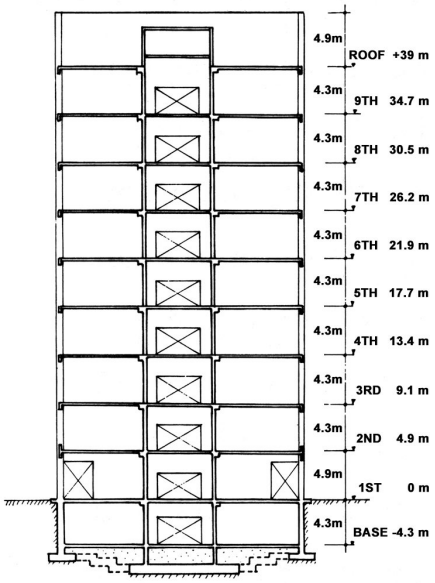

(a) North-South Cross Section

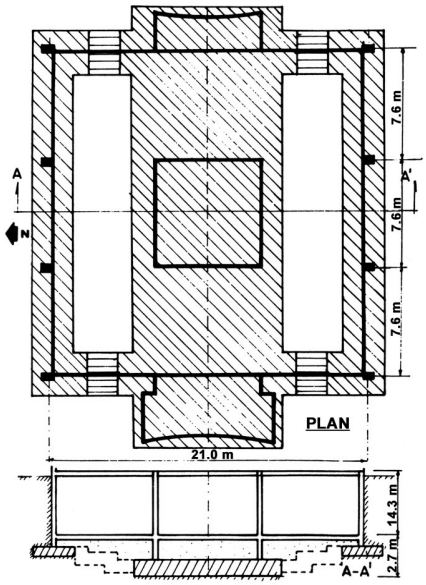

(b) Foundation Plan View and North-South Cross Section

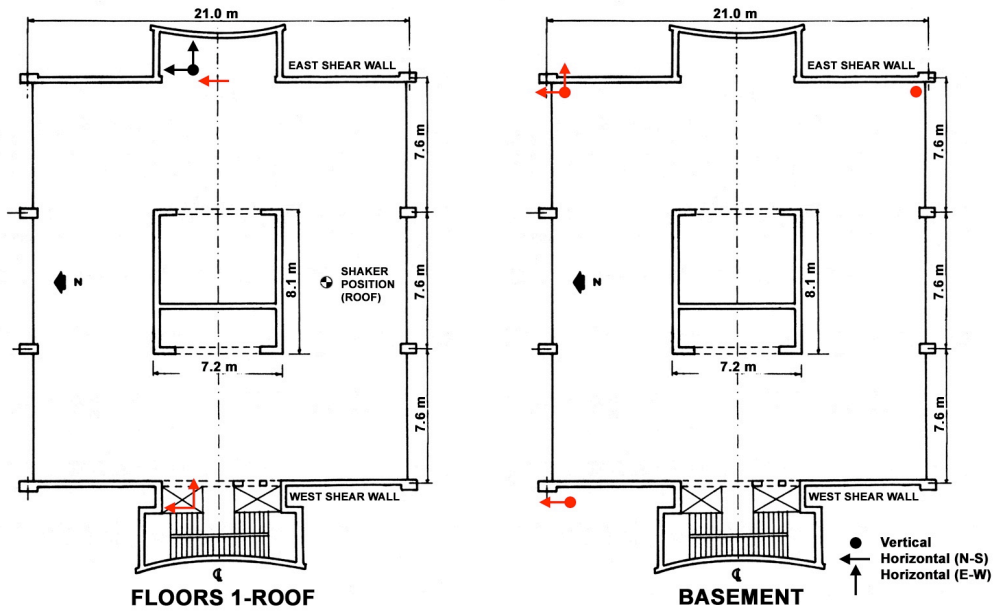

(c) Floor Plan and Instrumentation of Millikan Library, dense instrument array shown in red, station MIK (on 9th floor) shown in black. Shaker position (roof level) also shown.

Figure B.2: Millikan Library structural diagrams.

B.2.1 Historical Information

The Millikan Library has been extensively monitored and instrumented since its completion in 1966 (Kuroiwa, 1967; Trifunac, 1972; Foutch, 1976; Luco et al., 1986; Chopra, 1995). Clinton (2004) has summarized some of the previous data on Millikan Library's behavior under forced and ambient vibrations in Appendix B.6. The evolution of the building behavior, including some dramatic shifts in the fundamental modes, is documented in Clinton (2004) and is reproduced here in Table B.1 and Figure B.3. A drop of 21% and 12% for the E-W and N-S fundamental modes since construction is noted. The primary cause for these shifts appears to be a permanent loss of structural stiffness which occurs during strong ground motions, most noticeably the San Fernando (1979) and Whittier Narrows (1987) events. Small fluctuations in natural frequencies have also been noted which can depend on weather conditions at the time of testing (Clinton et al., 2006). In particular, the E-W and torsional fundamental frequencies have increased by ∼3% in the days following large rainfalls. The frequencies observed during ambient studies also differ from the frequencies observed during forced vibration tests (Clinton, 2004).

B.2.2 Millikan Library Shaker

A Kinemetrics model VG-1 synchronized vibration generator ("shaker") was installed on the roof of Millikan Library in 1972 (Figure B.4). The shaker has two buckets that counter-rotate around a center spindle. These buckets can be loaded with different configurations of lead weights, and depending on the alignment of the buckets, the shaker can apply a sinusoidal force in any horizontal direction. The force (F_i) applied by the shaker in each of its configurations can be expressed as:

$$F_i = A_i f^2 \sin(2\pi f t) \qquad \begin{aligned} A_1 &= 235.73\ N \cdot sec^2 \\ A_2 &= 1518.67\ N \cdot sec^2 \\ A_3 &= 3575.89\ N \cdot sec^2. \end{aligned} \tag{B.1}$$

Event/Test	**East - West**				**North - South**			
	Nat Freq. $[Hz]$	%**diff1** [%]	%**diff2** [%]	**max accn** $[\frac{cm}{s^2}]$	**Nat Freq.** $[Hz]$	%**diff1** [%]	%**diff2** [%]	**max accn** $[\frac{cm}{s^2}]$
forced vibrations, 1967	1.45	-	-	-	1.90	-	-	-
Lytle Creek, 1970 M5.3, Δ=57km	1.30	10.3	10.3	49	1.88	1.1	1.1	34
San Fernando, 1971 M6.6, Δ=31km	1.0	31.0	31.0	306	1.64	13.7	13.7	341
forced vibrations, 1974	1.21	16.6	16.6	-	1.77	6.8	6.8	-
Whittier Narrows, 1987 M6.1, Δ=19km	1.00	31.0	17.4	262	1.33	30.0	24.9	534
forced vibrations, 1988	1.18	18.6	2.5	-	1.70	10.5	4.0	-
Sierra Madre, 1991 M5.8, Δ=18km	0.92	36.6	22.0	246	1.39	26.8	18.2	351
forced vibrations, 1993	1.17	19.3	0.8	-	1.69	11.1	0.6	-
Northridge, 1994 M6.7, Δ=34km	0.94	35.2	19.7	143	1.33	30.0	21.3	512
forced vibrations, 1994	1.15	20.6	1.7	-	1.67	12.1	1.2	-
forced vibrations, 1995	1.15	20.6	0.0	-	1.68	11.6	-0.6	-
Beverly Hills, 2001 M4.2, Δ=26km	1.16	20.0	-0.9	9.3	1.68	11.6	0.0	11.8
forced vibrations, 2002								
- Full Weights	1.11	23.4	3.5	3.6	1.64	13.7	2.4	8.0
- 1/2 Weights	1.14	21.4	0.9	1.9	1.67	12.1	0.6	4.1
Big Bear, 2003 M5.4, Δ=119km	1.07	26.2	6.1	14.2	1.61	15.3	3.6	22.6

Table B.1: History of Millikan Library strong motion behavior. Fundamental Modes. "**%diff1**" is the difference between the recorded frequency and that obtained in the first forced vibration tests (from (Kuroiwa, 1967)). "**%diff2**" is the difference between the recorded frequency and that obtained in the most recent forced vibration test prior to the event. (Adapted from Clinton (2004).)

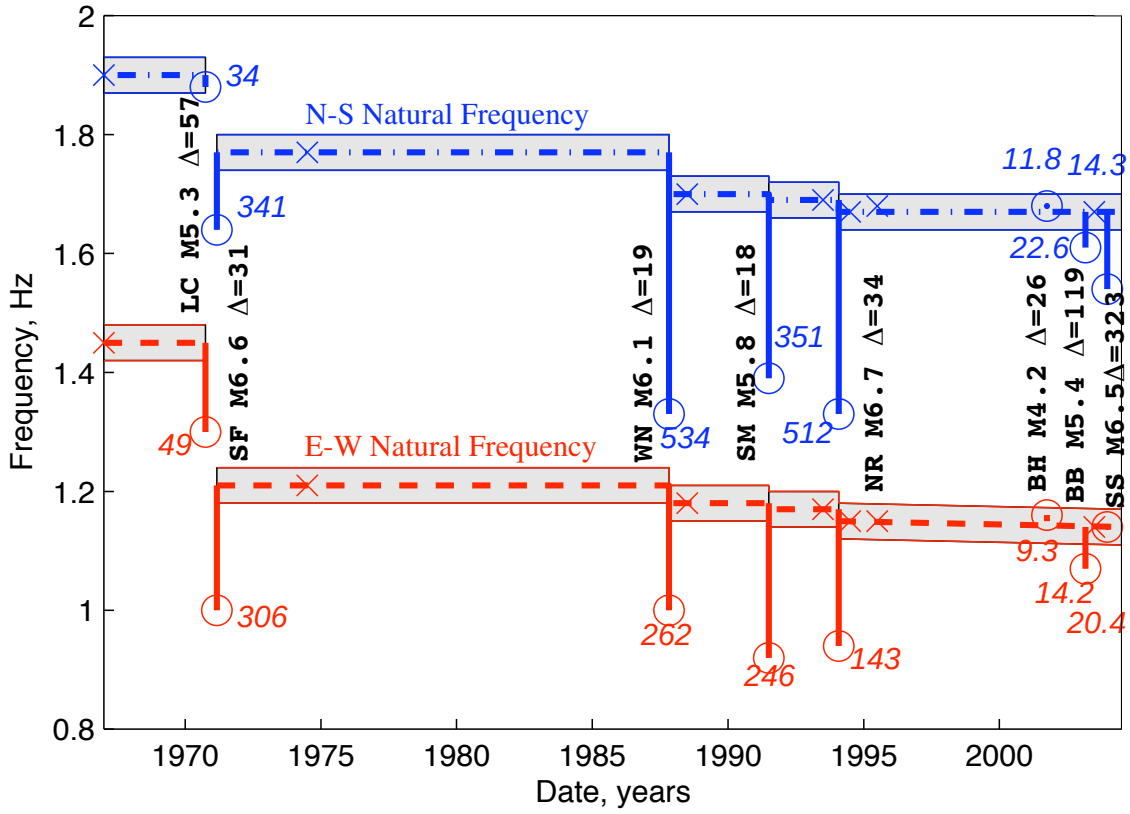

Figure B.3: Graphical depiction of Table B.1, the historical behavior of Millikan Library. Dashed lines represent the E-W natural frequencies, and the dashed-dotted lines represent the N-S natural frequencies. Shaded area is the likely range of natural frequencies taking into consideration errors in measurement due to various factors - weight configuration in the shaker, weather conditions at the time of the test, and experimental error. Crosses indicate actual time forced test was made. Circles indicate natural frequency estimates from the strong motion record during earthquake events, and numbers in italics are peak acceleration recorded for the event (cm/s^2). [Earthquake Abbreviations: LC: Lytle Creek, SF: San Fernando, WN: Whittier Narrows, SM: Santa Monica, NR: Northridge, BH: Beverly Hills, BB: Big Bear, SS: San Simeon.] (Adapted from Clinton (2004).)

Frequency, f, is in Hz; A_i (a shaker constant) is in N·sec^2; and the resulting force, F_i, is in units of N. Table B.2 lists the values of A_i and the limiting frequency for each weight configuration. For our test we used three shaker levels: A_3, full weights with the buckets loaded at 100% of capacity; A_2, an intermediate configuration with two large weights in each of the large weight sections of each bucket, corresponding to 42.5% of the mass of the full buckets; and A_1, empty buckets, which corresponds to a shake factor of 6.6% of the full weight configuration.

We can strongly excite the torsional modes through E-W shaking, as the shaker is located ∼6.1 meters to the South of the building's N-S line of symmetry (Figure B.2(c)). The shaker is located ∼0.3 meters to the East of the building's E-W centerline, and therefore we do not expect shaking in the N-S direction to effectively excite the building in torsion.

Figure B.4: Kinemetrics VG-1 Synchronized Vibration Generator (Shaker). The counter-rotating buckets, shown empty, can be loaded with different configurations of lead weights. The shaker is located on the roof of Millikan Library, as shown in Figure B.2.

Large Weights \ Small Weights	0	1	2	3	4
0	**235.73 [9.7]**	429.31 [7.2]	622.88 [6.0]	816.45 [5.2]	1010.03 [4.7]
1	877.20 [5.0]	1070.77 [4.6]	1264.35 [4.2]	1457.92 [3.9]	1651.49 [3.7]
2	**1518.67 [3.8]**	1712.24 [3.6]	1905.81 [3.4]	2099.39 [3.3]	2292.96 [3.1]
3	2160.13 [3.2]	2353.71 [3.1]	2547.28 [3.0]	2740.85 [2.8]	2934.43 [2.8]
4	2801.60 [2.8]	2995.17 [2.7]	3188.75 [2.6]	3382.32 [2.6]	**3575.89 [2.5]**

Table B.2: Shaker constant, A_i ($N \cdot sec^2$), and limiting frequencies (Hz) for different configurations of lead weights in the shaker. Bold type indicates the configurations used in these experiments.

B.2.3 Millikan Library Instrumentation

In 1996 the United States Geological Survey (USGS) and the Caltech Department of Civil Engineering installed a permanent dense array of uni-axial strong-motion instruments (1g and 2g Kinemetrics FBA-11s) in the Millikan Library, with 36 channels recording on two 19-bit 18-channel Mt. Whitney digitizers. The instruments are distributed throughout the building, with three horizontal accelerometers located on each floor and three vertical instruments in the basement. This dense array is recorded by the Mt. Whitney digitizer system, providing local hard-drive storage of triggered events. In 2001 a 3-component Episensor together with a 24-bit Q980 data logger was installed on the 9th floor. Data from this sensor is continuously telemetered to the Southern California Seismic Network (SCSN) as station MIK. Figure B.2(c) provides a schematic of the instrument locations.

B.3 Frequency Sweep

A frequency sweep of Millikan Library was performed on July 10, 2002. This test was designed to identify the natural frequencies and their damping; modeshapes would be determined with later detailed testing. The building response was recorded using the SCSN station MIK on the 9th floor and a Mark Products L4C3D seismometer with a 16 bit Reftek recorder on the roof (provided by the Southern California Earthquake Center (SCEC) Portable Broadband Instrument Center located at the University of

California, Santa Barbara). We also used a Ranger seismometer with an oscilloscope at the roof level to provide an estimate of roof level response during our experiment.

We began with a N-S frequency sweep and the shaker set with empty buckets, starting near the frequency limit of the shaker at 9.7Hz. We held the frequency constant for approximately 60 seconds to allow the building response to approach steady state and then lowered the shaker frequency in either .05Hz or .1Hz increments, again pausing for 60 seconds at each frequency. Once we reached 3.8Hz, we turned off the shaker and loaded it with two large weights in each of the large weight compartments in each of the buckets (the intermediate 42.5% loading configuration). We then continued the frequency sweep from 3.7Hz to 1.5Hz. This procedure was repeated for the E-W direction, driving the empty shaker from 9.7Hz to 3.8Hz, then sweeping from 3.7Hz to 1Hz using the intermediate configuration.

Figure B.5 shows normalized peak displacement curves for the frequency sweeps. For each frequency, a representative section from the steady state portion of the data was selected, bandpass filtered (0.2Hz above and below each frequency, using a 2-pass 3-pole butterworth filter), and fit to a sine wave to estimate the exact frequency, amplitude, and phase. These sinusoidal amplitudes were then normalized by the applied shaker force for the particular frequency and weight combination (Equation B.1).

Furthermore, damping was determined by applying the half-power (band-width) method (Meirovitch, 1986). We estimated the peak displacement frequency from a cubic interpolation of the normalized data, as our data sampling is somewhat sparse for a frequency/amplitude curve. As the higher modes have too much lower mode participation to determine the half-power points, damping was only determined for the fundamental modes. Damping is estimated to be 2.28%, 2.39%, and 1.43% for the E-W, N-S, and Torsional fundamental modes, respectively.

B.4 Modeshape Testing

We performed a forced excitation test of Millikan Library on August 18, 2002, recording data using the dense instrumentation network operated by the USGS and station

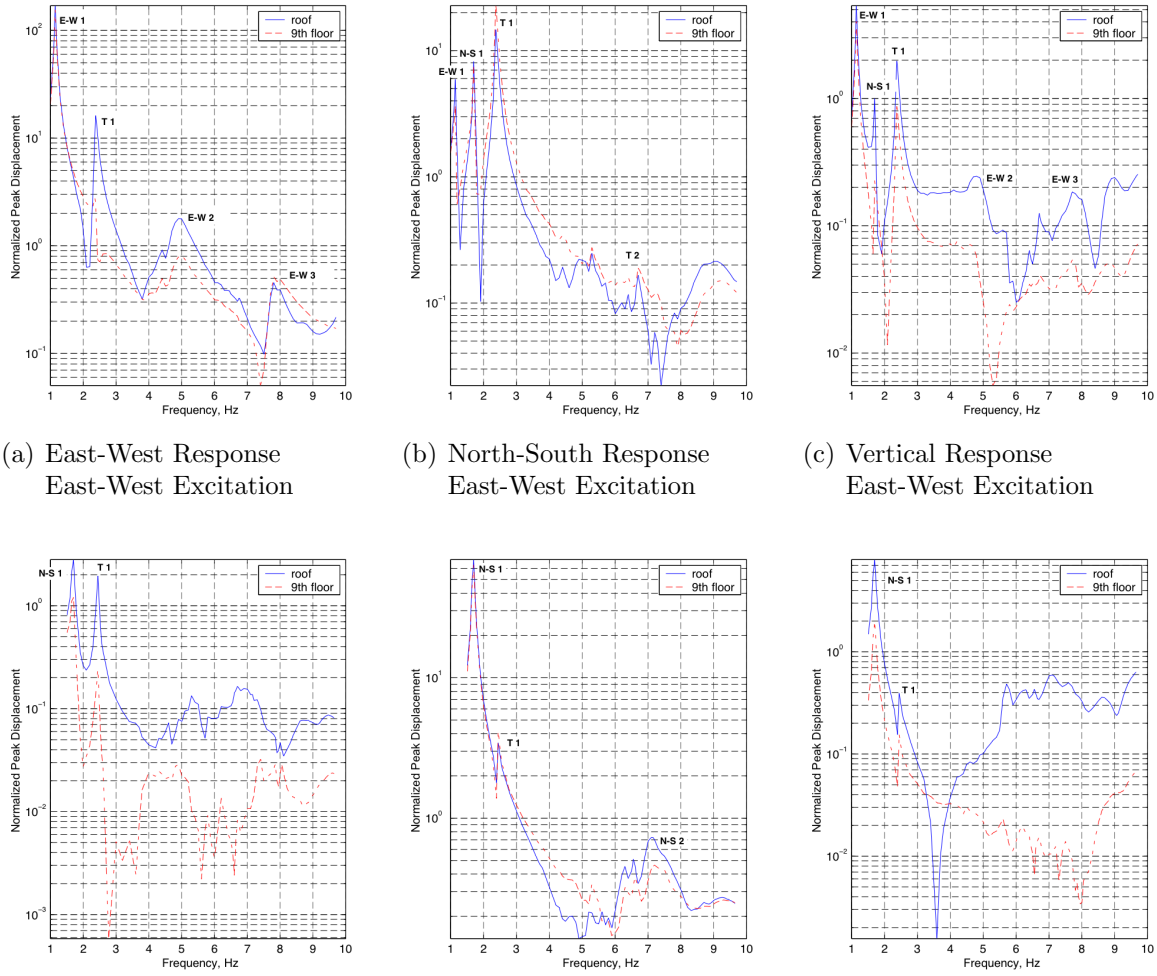

(a) East-West Response
East-West Excitation

(b) North-South Response
East-West Excitation

(c) Vertical Response
East-West Excitation

(d) East-West Response
North-South Excitation

(e) North-South Response
North-South Excitation

(f) Vertical Response
North-South Excitation

Figure B.5: Lin-Log normalized peak displacement curves for the frequency sweep performed on July 10, 2002. Amplitudes for E-W and N-S shaking are normalized by the force factor corresponding to the weight configuration and frequency, as calculated in Equation B.1. Roof response is shown in solid blue lines, and station MIK (9th floor) is shown in dashed red lines.

MIK. We compare the behavior of the library with the behavior of uniform shear and bending beams (see Appendix B.5), but it is important to note that these are simple structural approximations which do not include the behavior of the foundation or the true structural system of the library.

Mode	Shake Direction/ Weight Configuration	Resonance Peak (Hz)	Normalized Roof Displacement [cm/N] x 10^{-7}	Percent Roof Displacement due to tilt and translation
Fundamental E-W	E-W / 100%	1.11	175(E-W)	3%
	E-W / 42.5%	1.14	180(E-W)	3%
Fundamental N-S	N-S / 100%	1.64	80(N-S)	30%
	N-S / 42.5%	1.67	80(N-S)	30%
Fundamental Torsion	E-W / 42.5%	2.38	25(N-S)	2% *
	N-S / 100%	2.35	5(N-S)	2% *
	N-S / 42.5%	2.38	5(N-S)	2% *
1st E-W Overtone	E-W / 6.6%	4.93	2(E-W)	1%
1st N-S Overtone	N-S / 6.6%	7.22	0.8(E-W)	-21%
1st Torsion Overtone	E-W / 6.6%	6.57	0.4(E-W) / 0.15(N-S)	23% *
	N-S / 6.6%	6.70	0.5(N-S)	23% *
2nd E-W Overtone	E-W / 6.6%	7.83	0.6(E-W)	0%

*: For torsional modes, % of rotation recorded at roof due to basement rotation

Table B.3: Results for modeshape testing of August 28, 2002.

B.4.1 Procedure and Data Reduction

We began the experiment with the shaker buckets fully loaded and set to excite the E-W direction. We excited the building at frequencies near the fundamental E-W and torsional modes, in frequency increments of .03-.05 Hz (again holding for 60s at each frequency to allow the building to approach steady-state response). With full buckets we then set the shaker to excite in the N-S direction to examine the fundamental N-S mode. We then repeated the excitation of the fundamental E-W, N-S, and torsional modes with the intermediate 42.5% weight configuration, to examine the shift in natural frequencies with different levels of exciting force. With empty shaker

buckets, we excited the first and second E-W overtones, the first torsional overtone, and the first N-S overtone. Table B.3 summarizes our testing procedure and results.

There are two parallel arrays of instruments in the N-S direction: one set located on the east side of the library and the other on the west side of the library, as shown in Figure B.2. In the E-W orientation there is one array, located on the west side of the building. The two N-S arrays are positioned towards the East and West edges of the building, far from the E-W centerline, while the E-W array on the west side of the building is located only 1m from the N-S centerline. Therefore, we expect to observe torsional response as strong, out of phase motion from the N-S arrays, with relatively small motion observed from the E-W array.

For each frequency, we selected a representative section from the the steady-state portion of the data, bandpassed the data (1/2 octave above and below each frequency using a 2-pass 2-pole butterworth filter), and integrated twice to obtain displacement values. We created resonance curves by fitting the displacement data to a sine wave to estimate frequency and amplitude and then normalizing the response based on the applied force for each frequency and weight combination (Section B.2.2). The mode shape snapshots in Figures B.6 to B.11 depict the behavior of the building at the point of maximum roof displacement for each frequency. Using the geometry of the basement and the position of the vertical basement sensors, we were able to estimate the rigid body rocking of the building and use it to correct our mode shapes. The horizontal basement sensors were used to correct for rigid building translation. Our mode shape figures present the raw results from all three instrument arrays, and the corrected results with basement translation and rocking removed.

For the torsional modes, Figures B.8 and B.11, we present a snapshot of the displacement records and also provide a snapshot in terms of rotation angle, θ, at each floor. The rotation angle at each floor was calculated by subtracting the western N-S array displacement values (D_2) from the eastern N-S array displacement values (D_1) and dividing by the E-W length ($L_{E\text{-}W}$) between the arrays (Equation B.2). For our rotation angle figures, we present the rotation angle at each floor, the basement

rotation angle, and the rotation angle corrected for basement rotation.

$$\theta \approx \tan\theta = \frac{D_1 - D_2}{L_{E\text{-}W}}. \tag{B.2}$$

The instruments in the Eastern N-S array malfunctioned on floors 2 and 8, and as a result we show a linearly interpolated value for those floors in our mode shape diagrams.

B.4.2 Fundamental Modes

East-West Fundamental Mode

Figures B.6(a) and B.6(b) show the resonance curve obtained from forced E-W shaking with full weights and 42.5% weights, respectively. Figures B.6(c) and B.6(d) show the respective mode shapes observed at the resonant frequencies for the different weight configurations. Shapes from all three sets of channels are shown on the same plot – the E-W response clearly dominates during E-W excitation. The observed mode shapes for different weight configurations are similar, but due to the nonlinear force-response behavior of the building, the resonant frequency shifts from 1.11Hz with full weights to 1.14Hz with 42.5% weights. This shift in resonant frequency with respect to changing the applied force is small, and though obvious, is at the limit of the resolution of our survey.

Figures B.6(c) and B.6(d) show the mode shapes for both the raw displacements and the displacements corrected for translation and tilt. The mode shapes have a strong linear component and closely resemble the theoretical mode shape for a bending beam, with the inclusion of the kink at the ground floor. See Appendix B.5 for a brief summary and comparison of bending and shear beam behavior. Tilting and translation effects in this mode account for 3% of the roof displacement.

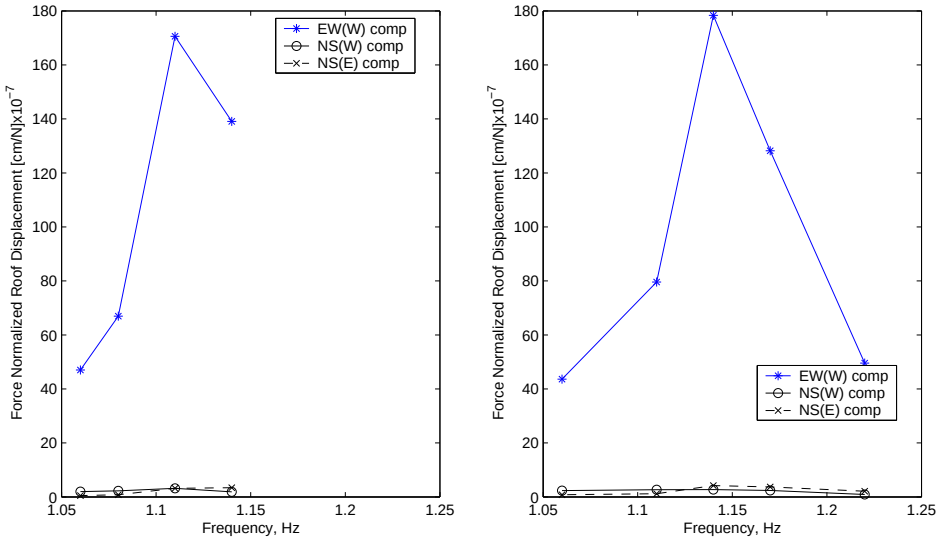

(a) Resonance curve for E-W Shaking with full weights

(b) Resonance curve for E-W Shaking with intermediate (42.5%) weights

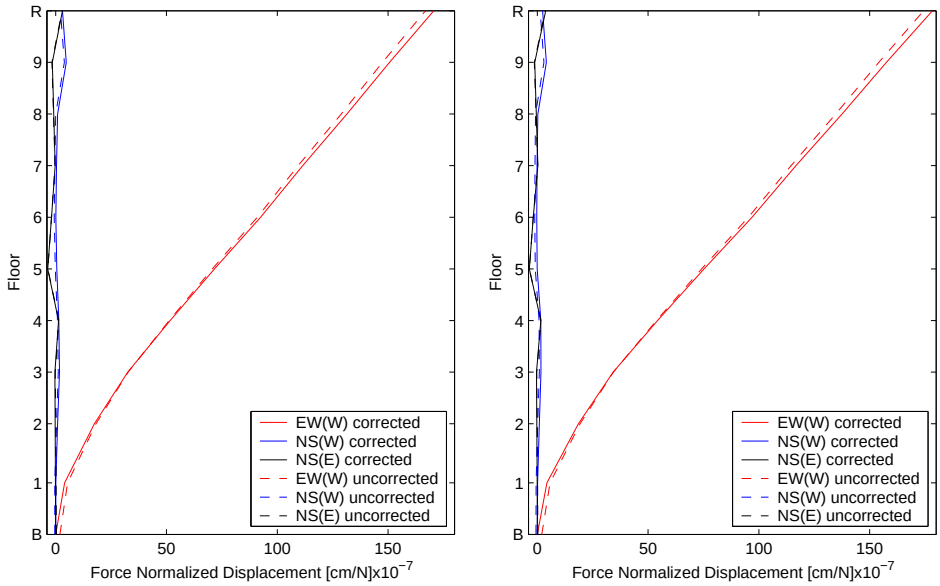

(c) Snapshot of building behavior at 1.11Hz with full weights, Force = 4,405.9N.

(d) Snapshot of building behavior at 1.14Hz with intermediate (42.5%) weights, Force = 1,973.7N.

Figure B.6: Resonance curves and mode shapes for the E-W fundamental mode under two loading conditions. Mode shapes are shown corrected (for rigid body motion) and uncorrected. The mode shapes and resonance curves are shown for the east-west array located on the west side of the building, EW(W); the western north-south array, NS(W); and the eastern north-south array, NS(E). Force is calculated as in Equation B.1 based on the frequency and loading configuration of the shaker.

North-South Fundamental Mode

Figures B.7(a) and B.7(d) contain the resonance curves for N-S shaking with full weights and 42.5% weights, respectively. The fundamental N-S mode is also non-linear with respect to applied force, and we observe a resonant frequency shift from 1.64Hz for full weights to 1.67Hz with 42.5% weights. The mode shapes, Figure B.7(c) and Figure B.7(d) are near identical, and show a more pronounced hinge behavior than the first E-W mode. When compared to the theoretical mode shapes of Appendix B.5, the observed shape most closely resembles theoretical bending beam behavior, differing near the ground floor due to the pronounced hinge behavior in this mode shape. We also observe that the two N-S arrays are exhibiting in-phase motion and that the E-W response to N-S shaking is small, as expected. Foundation compliance becomes much more important for this mode, as we observe that $\sim$25% of the roof displacement is due to tilting of the library, and $\sim$5% is due to translation of the base of the library. Similar observations for the rigid-body rotation and translation of the building were made by Foutch et al. (1975).

Torsional Fundamental Mode

The fundamental torsional mode involves the twisting of the building and therefore has more complicated three-dimensional behavior. Due to the positioning of the instruments, a small amplitude response is observed from the accelerometers in the E-W array, while the two N-S arrays recorded a large amplitude out of phase response. Figure B.8(a) shows the resonance curve for the fundamental torsional mode. Figure B.8(b) gives the displacement records for the torsional mode shapes, and Figure B.8(c) shows the torsional mode shapes in terms of twist angle, θ (as defined in Equation B.2), instead of displacement. In Figure B.8(b), the two N-S arrays display the expected out of phase displacements, although some asymmetry is observed.

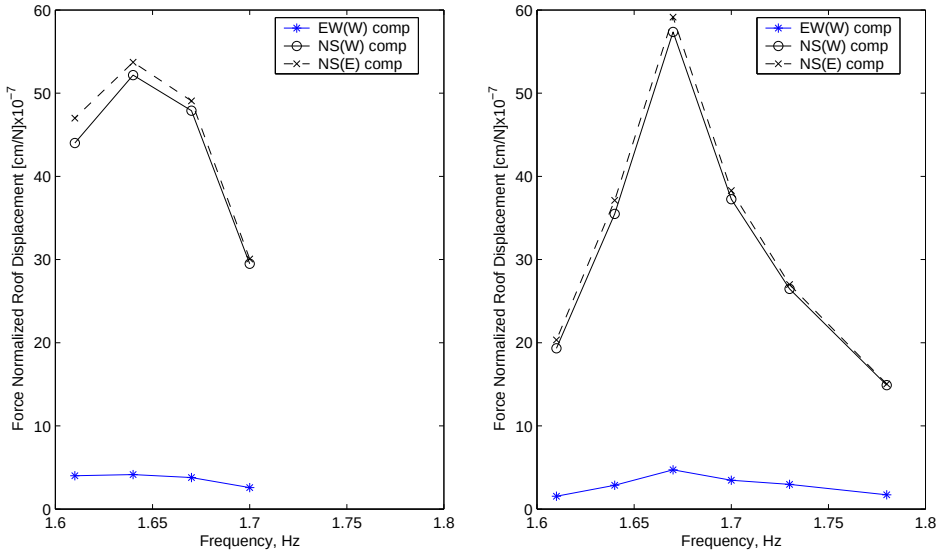

(a) Resonance curve for N-S Shaking with full weights

(b) Resonance curve for N-S Shaking with intermediate (42.5%) weights

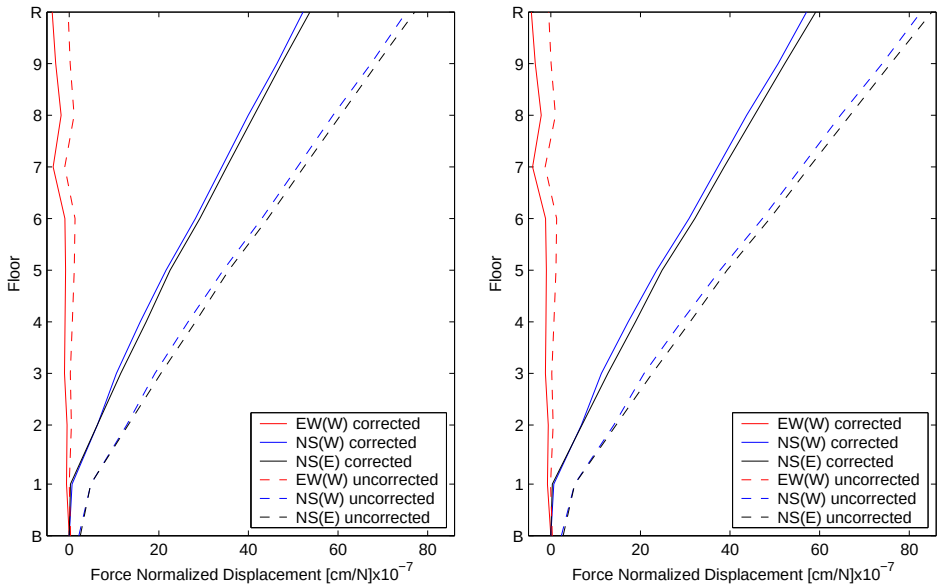

(c) Snapshot of building behavior at 1.64Hz with full weights, Force = 9,617.7N.

(d) Snapshot of building behavior at 1.67Hz with intermediate (42.5%) weights, Force = 4,235.4N.

Figure B.7: Resonance curves and mode shapes for the N-S fundamental mode under two loading conditions. Mode shapes are shown corrected (for rigid body motion) and uncorrected. The mode shapes and resonance curves are shown for the east-west array, located on the west side of the building, EW(W); the western north-south array, NS(W); and the eastern north-south array, NS(E). Force is calculated as in Equation B.1 based on the frequency and loading configuration of the shaker.

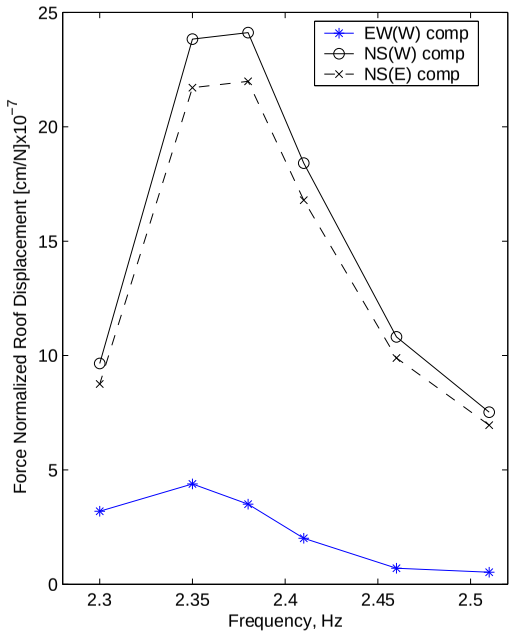

(a) Resonance curve for E-W Shaking with 42.5% weights

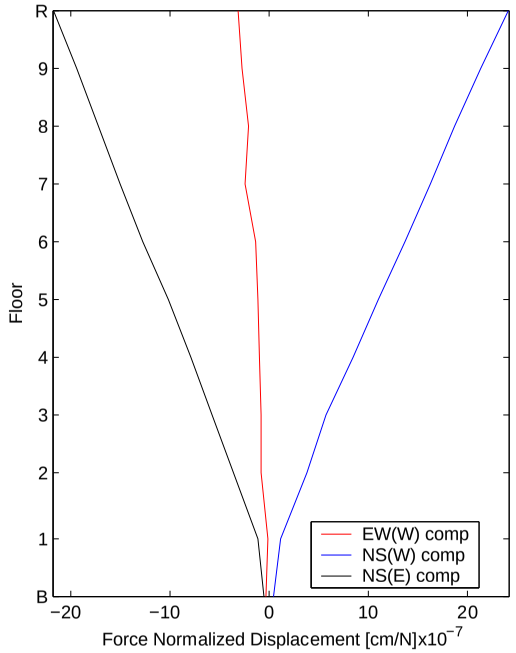

(b) Snapshot of building behavior at 2.38Hz with 42.5% weights, Force = 8,602.3N.

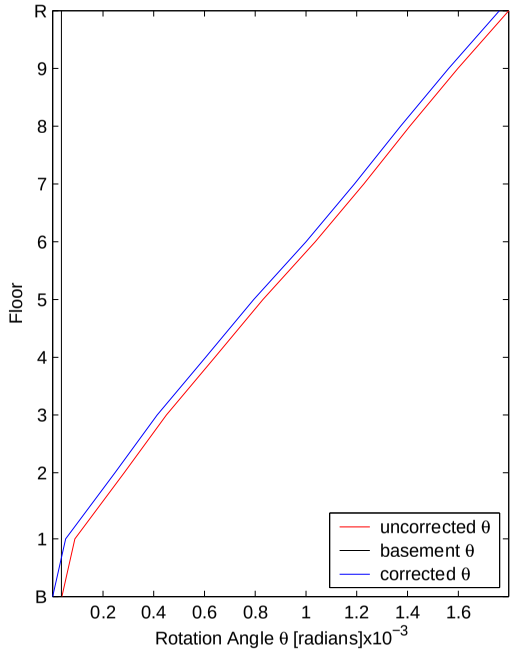

(c) Snapshot of building behavior in terms of rotation angle θ. Same configuration as in subfigure B.8(b). The uncorrected snapshot is the rotation angle at each floor, calculated as in Equation B.2. The corrected snapshot is the basement rotation angle subtracted from the rotation angle at each floor.

Figure B.8: Resonance curves and mode shapes for the Torsional fundamental mode. Force is calculated as in Equation B.1 based on the frequency and loading configuration of the shaker.

B.4.3 Higher Order Modes

Prior to the installation of the dense instrument array, the higher order mode shapes were difficult to observe; determining the modeshapes and frequencies for these higher order modes was one of the primary goals of our suite of experiments.

Second and Third East-West Modes

The first E-W overtone (second E-W mode) has a broad resonance peak, with a maximum response at 4.93Hz (Figure B.9(a)). The mode shape, seen in Figure B.9(c), is typical of the second mode shape of a beam in bending (Appendix B.5). The ratio of the frequency of the second mode to the first mode is 4.32, much lower than the theoretical ratio for a bending beam of 6.26. For comparison, the theoretical ratio for a shear beam is 3.

Also observed during our testing was the second E-W overtone (third E-W mode). Figure B.9(b) shows a resonance peak with a maximum response at 7.83Hz. The mode shape for this frequency is presented in Figure B.9(d) and is typical of the second mode of a theoretical shear beam (Appendix B.5). The ratio of the frequency of the third mode to the second mode is 1.59, lower than the theoretical ratio for a bending beam of 2.80 and closer to the theoretical ratio for a shear beam of 1.67. The ratio of third mode to first mode frequencies for a bending beam is 17.55, the ratio for a shear beam is 5, and for our observed building behavior the ratio is 6.87.

Second North-South Mode

As can be seen in Figure B.10(a), the first N-S overtone (second N-S mode) also has a broad resonance peak. The resonance curves for the two N-S arrays did not have their peaks at the same frequency, so this test did not provide a single resonance peak. However, based on the frequency sweep of Section B.3, and the shapes of the two resonance curves, we selected 7.22Hz as the modal frequency. The mode shape at this frequency, shown in Figure B.10(b), is qualitatively typical of a bending beam's second mode, but we see that the two N-S arrays have very different amplitudes

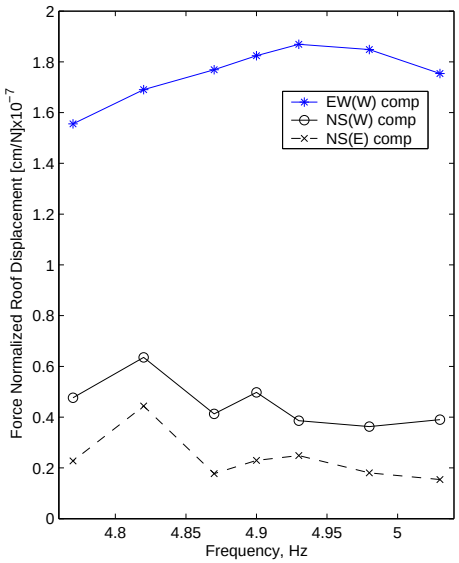

(a) Second E-W mode. Resonance curve for E-W shaking with empty buckets

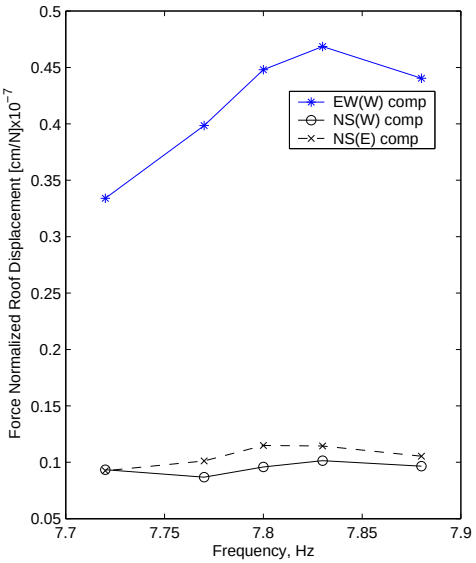

(b) Third E-W mode. Resonance curve for E-W shaking with empty buckets

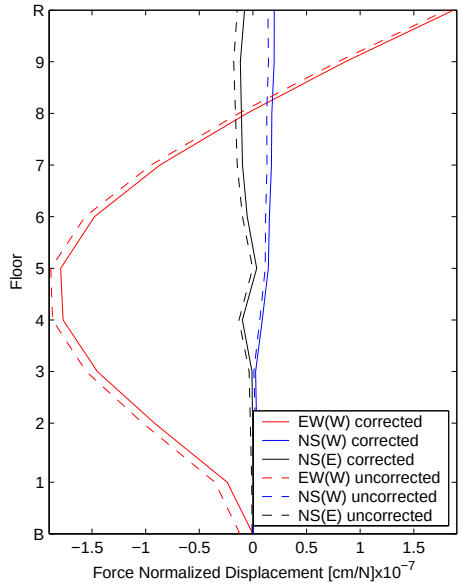

(c) Second E-W mode. Snapshot of building behavior at 4.93Hz with empty buckets, Force = 6,166.9N.

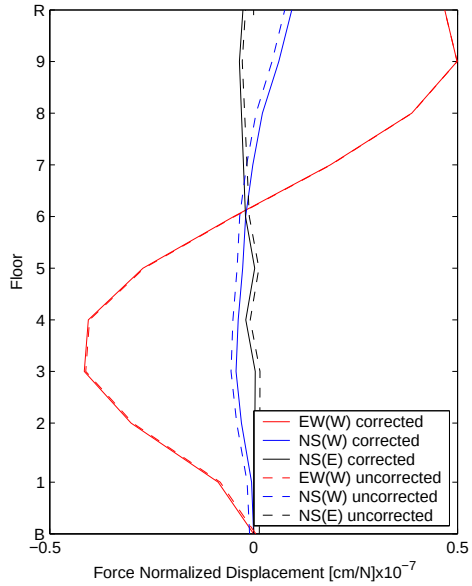

(d) Third E-W mode. Snapshot of building behavior at 7.83Hz with empty buckets, Force = 14,452.3N.

Figure B.9: Second and third E-W modes (first and second E-W overtones), with resonance curves and mode shapes. Mode shapes are shown corrected (for rigid body motion) and uncorrected. The mode shapes and resonance curves are shown for the east-west array, located on the west side of the building, EW(W); the western north-south array, NS(W); and the eastern north-south array, NS(E). Force is calculated as in Equation B.1 based on the frequency and loading configuration of the shaker.

with zero crossings at different heights. For the N-S second mode, the eastern and western arrays should have similar shapes and amplitudes (cf. the first N-S mode in Figure B.7), as the building is approximately symmetric. This implies that we did not excite the exact modal frequency or that this mode has a more complicated three-dimensional response than the first N-S mode. The ratio of the frequency for the second mode (approximate) to the first mode is 4.32, which is close to the ratio of frequencies observed in E-W bending and is also lower than the theoretical ratio for the first two modes of a bending beam.

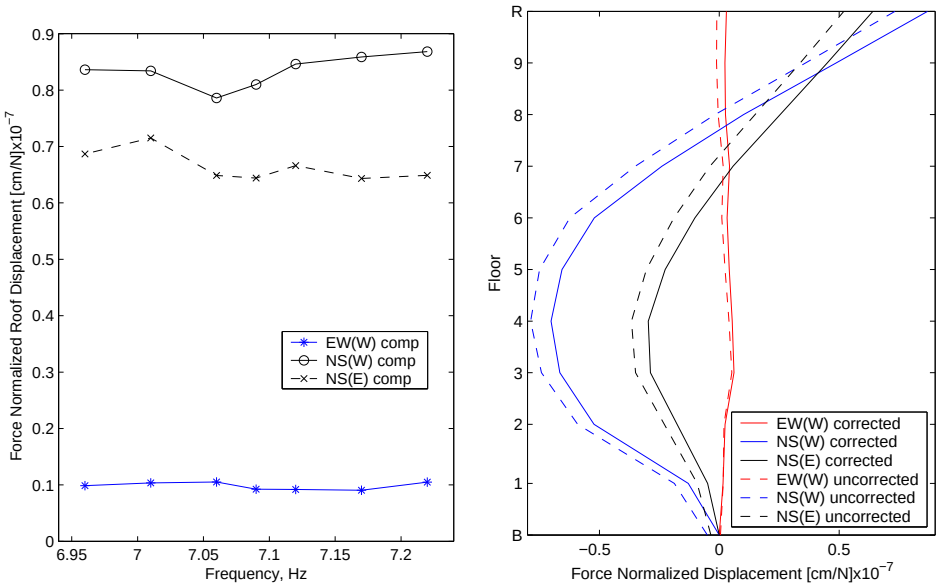

(a) Resonance curve for N-S shaking with empty buckets

(b) Snapshot of building behavior at 7.22Hz with empty buckets, Force = 12,288.2N.

Figure B.10: Resonance curves and mode shapes for the second NS mode (first NS overtone). Mode shapes are shown corrected (for rigid body motion) and uncorrected. The mode shapes and resonance curves are shown for the east-west array, located on the west side of the building, EW(W); the western north-south array, NS(W); and the eastern north-south array, NS(E). Force is calculated as in Equation B.1 based on the frequency and loading configuration of the shaker.

Second Torsional Mode

The first torsional overtone was difficult to excite in the building and difficult to observe. We excited the torsional mode using E-W excitation and expected small

torsional response on the E-W channels and large out of phase response from the two N-S arrays. However, the observed response was dominated by E-W motion from the E-W shaking used to excite the system, which drove the building in a mode shape similar to that of the second E-W mode. We observed out of phase motion in the two N-S arrays, but the response of the N-S arrays was much smaller than the E-W response. Figure B.11(a) shows the response curve for this mode, which is dominated by the E-W motion. Figure B.11(b) shows the mode shapes, and Figure B.11(c) shows the response in terms of twist angle, θ, as defined in Section B.4.1. As with the N-S overtone, the resonance curve did not clearly identify a modal frequency, but we chose 6.57Hz as the frequency of interest based on the shapes of the resonance curves and the results of the frequency sweep of Section B.3.

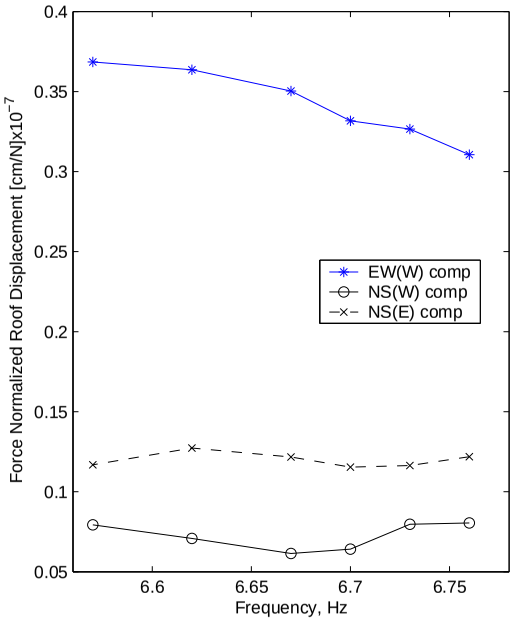

(a) Resonance curve for E-W shaking with empty buckets

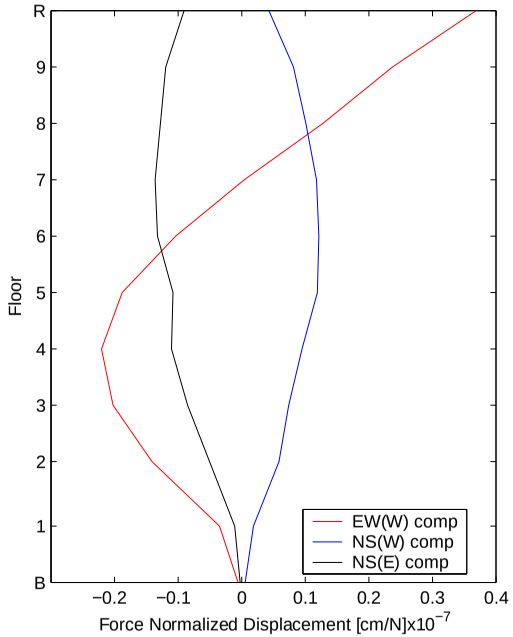

(b) Snapshot of building behavior at 6.57Hz with empty buckets, Force = 10,175.3N.

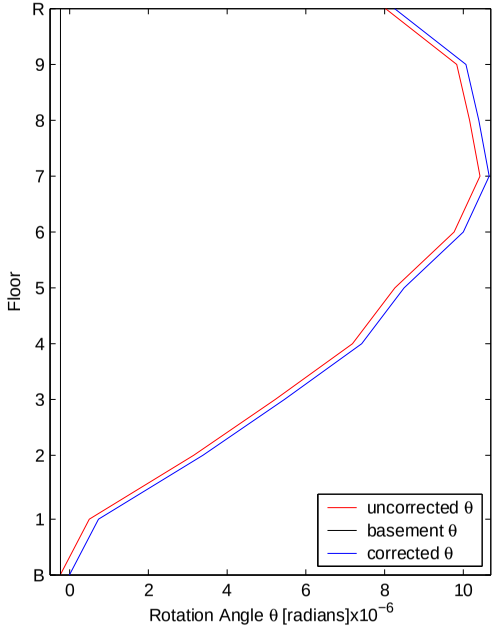

(c) Snapshot of building behavior in terms of rotation angle θ. Same configuration as in subfigure B.11(b). The uncorrected snapshot is the rotation angle at each floor, calculated as in Equation B.2. The corrected snapshot is the basement rotation angle subtracted from the rotation angle at each floor.

Figure B.11: Resonance curves and mode shapes for the second Torsional mode (first Torsional overtone). Force is calculated as in Equation B.1 based on the frequency and loading configuration of the shaker.

B.4.4 Modeshapes Summary

Table B.4 contains a summary of the ratios of frequencies found for Millikan Library, along with theoretical results for bending and shear beams. Appendix B.5 presents a summary of theoretical bending and shear beam behavior. To further analyze the data, the mode shapes were fit using theoretical bending and shear beam behavior by a modified least squares method. Figure B.12 shows the results of the least squares curve-fitting for the E-W and N-S modes. The experimental data and best fit are shown, along with the theoretical mode shapes which are scaled according to their participation in the best fit curve. Both the fundamental E-W and N-S modes, Figures B.12(a) and B.12(d), are dominated by the bending component, as are the second E-W and N-S modes, Figures B.12(b) and B.12(e). The third E-W mode was not matched well using the third theoretical bending and shear modes; a fit including the second theoretical bending and shear modes is presented in Figure B.12(c), implying that the mode shape is best approximated by the second mode of a theoretical shear beam.

	Bending	Shear	Millikan E-W	Millikan N-S
ω_2/ω_1	6.26	3	4.32	4.32
ω_3/ω_1	17.55	5	6.87	N/A
ω_3/ω_2	2.8	1.67	1.57	N/A

Table B.4: Ratio of frequencies for bending beam behavior, shear beam behavior, and the observed behavior of Millikan Library.

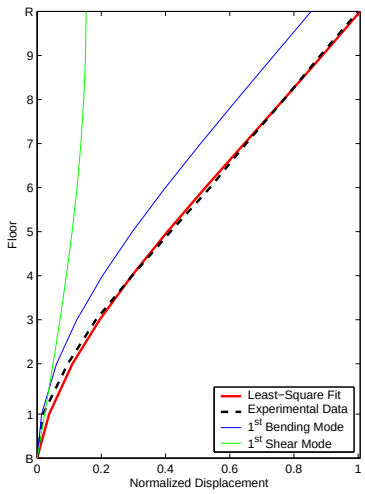

(a) Least square fit for fundamental E-W mode.

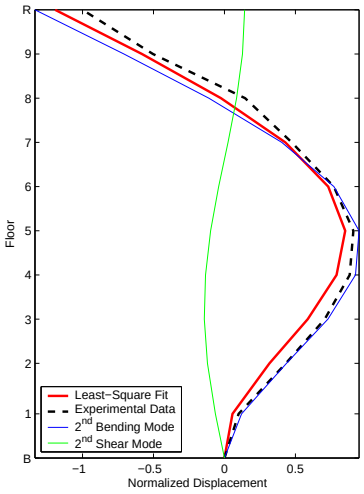

(b) Least square fit for second E-W mode (first E-W overtone).

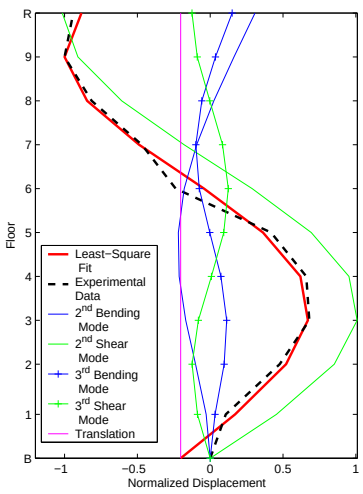

(c) Least square fit for third E-W mode (second E-W overtone). Translational term included in curve-fitting to accommodate large kink at ground level.

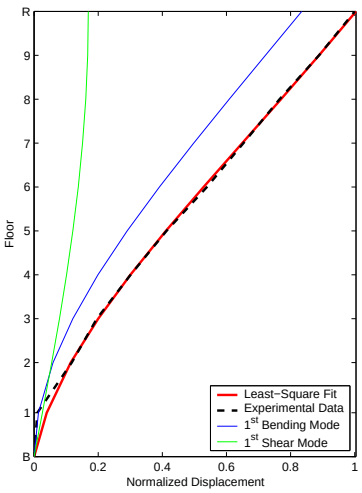

(d) Least square fit for fundamental N-S mode.

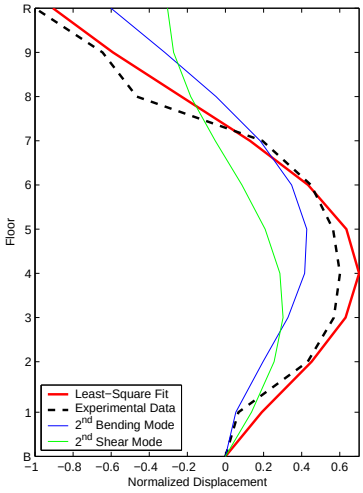

(e) Least square fit for second N-S mode (first N-S overtone).

Figure B.12: Least squares curve fitting for E-W and N-S modes. Linear tilt and translation removed when calculating the best fit.

B.5 Theoretical Beam Behavior

Adapted from Meirovitch, (1986).

The mode shapes ($X_n(z)$) and associated natural frequencies (ω_i) for a cantilevered fixed-free bending beam are found by solving the differential equation:

$$\frac{\partial^4 X(z)}{\partial z^4} - \beta^4 X(z) = 0 \qquad \beta^4 = \frac{\omega^2 m}{EI}, \tag{B.3}$$

where m is mass per unit length, E is Young's Modulus and I is the moment of inertia.

The following boundary conditions apply:

$$X(0) = 0 \qquad \frac{\partial X(z)}{\partial z}|_{x=0} = 0 \qquad \text{at the fixed end,} \tag{B.4}$$

$$\tag{B.5}$$

$$\frac{\partial^2 X(z)}{\partial z^2}|_{x=L} = 0 \qquad \frac{\partial^3 X(z)}{\partial z^3}|_{x=L} = 0 \qquad \text{at the free end.} \tag{B.6}$$

This leads to the characteristic equation

$$\cos(\beta L)\cosh(\beta L) = -1, \tag{B.7}$$

which can be solved analytically to give the following values for the first three modes:

$$\text{Mode 1} : \beta_1 L = 1.875, \tag{B.8}$$

$$\text{Mode 2} : \beta_2 L = 4.694, \tag{B.9}$$

$$\text{Mode 3} : \beta_3 L = 7.855, \tag{B.10}$$

$$\text{with } \omega_i = \beta_i^2 \sqrt{\frac{EI}{mL^4}}. \tag{B.11}$$

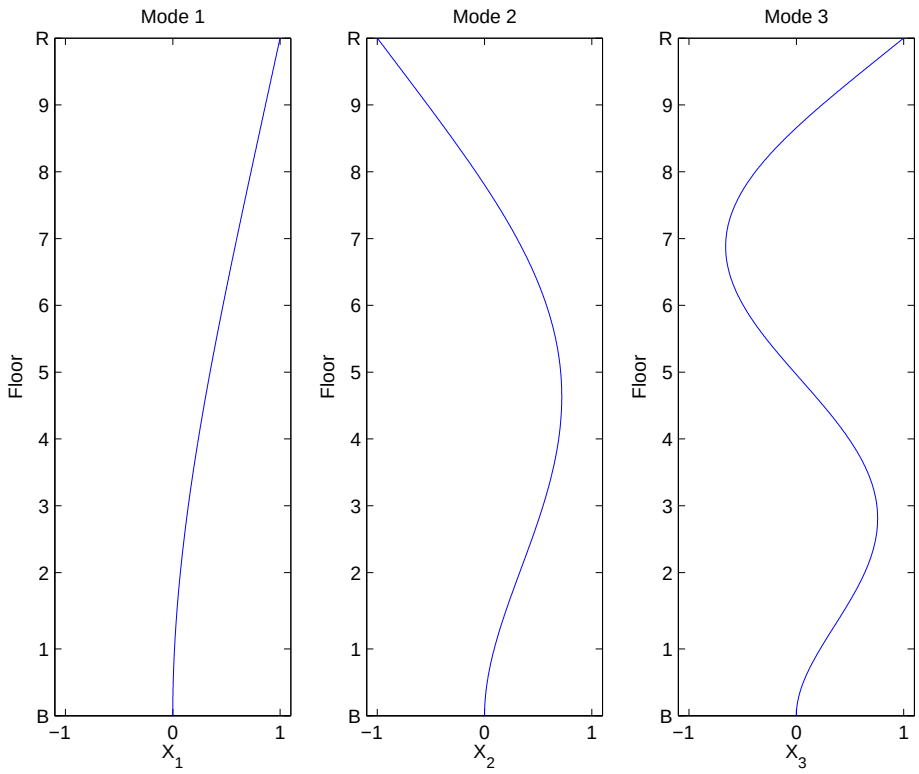

Figure B.13: From left to right, theoretical mode shapes for the fundamental mode (1st mode) and the first two overtones (2nd and 3rd modes) for a cantilevered bending beam. Mode shapes X_n are normalized such that the maximum displacement is equal to 1.

The mode shapes of a bending beam are given by:

$$X_n(z) = C_1 \left[(\sin \beta_n z - \sinh \beta_n z) + \frac{(\cos \beta_n L + \cosh \beta_n L)}{(\sin \beta_n L - \sinh \beta_n L)} (\cos \beta_n z - \cosh \beta_n z) \right]. \tag{B.12}$$

The first three modes are plotted in Figure B.13.

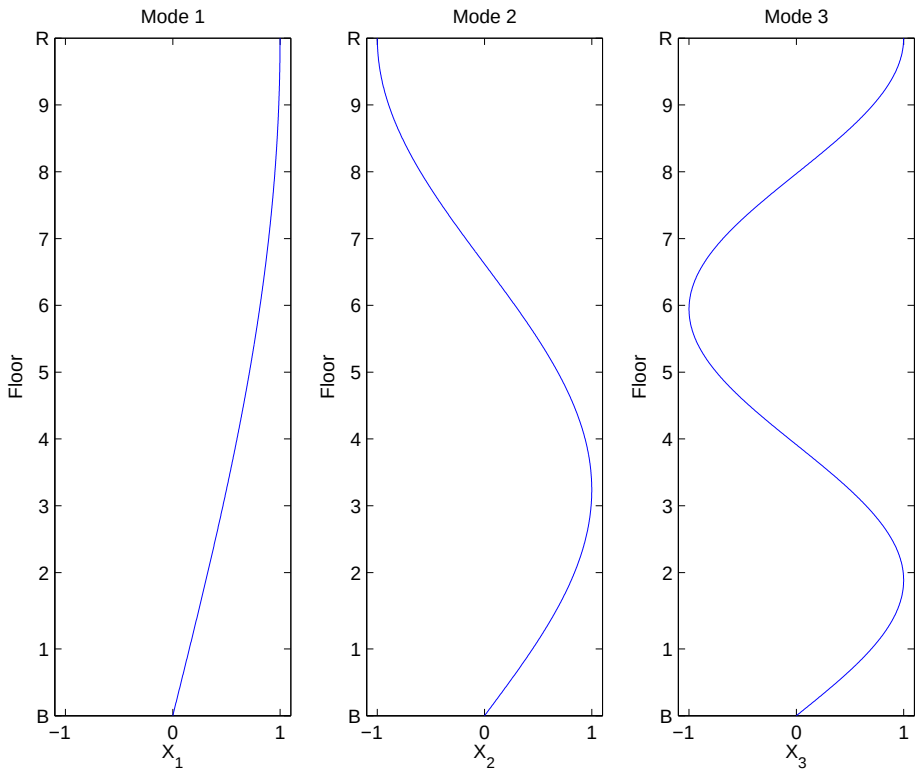

Figure B.14: From left to right, theoretical mode shapes for the fundamental mode (1st mode) and the first two overtones (2nd and 3rd modes) for a cantilevered shear beam. Mode shapes X_n are normalized such that the maximum displacement is equal to 1.

Theoretical shear beam behavior is as follows, with the deformed shape being portions of a sine curve:

$$X_n(z) = C_1 \left[(\sin \frac{(2n-1)\pi}{2} z) \right] \qquad n = 1, 2, 3...$$

The first three modes are plotted in Figure B.14.

B.6 Historical Summary of Millikan Library Studies

Adapted from Clinton (2004).

Tables B.5 and B.6 provide a summary of various studies into the frequencies and damping of Millikan Library. Table B.7 contains the references used to compile Tables B.5 and B.6. These studies include ambient and forced vibration testing as well as data recorded from earthquake ground motions.

Test	East - West		North - South		Torsional		Remark
	f_0 [ζ_0]	f_1 [ζ_1]	f_0 [ζ_0]	f_1 [ζ_1]	f_0 [ζ_0]	f_1 [ζ_1]	
1966-1967[1]	1.46-1.51 [0.7-1.7]	6.2	1.89-1.98 [1.2-1.8]	-	2.84-2.90 [0.9-1.6]	-	A,F,M
Mar 1967[2]	1.49 [1.5]	6.1	1.91 [1.6]	-	2.88	-	A
Apr 1968[3]	1.45	6.1	1.89	9.18	2.87	9.62	A
Jul 1969[4]	1.45	5.90	1.89	9.10	-	-	A
Sep 12 1970[5]	1.30-1.50	-	1.90-2.10	-	-	-	E (LC)
Sep 12 1970[6]	1.30	-	1.88	-	-	-	E (LC)
∼ M6.7 February 9 1971 San Fernando Earthquake (SF) @ 44km ∼							
Feb 9 1971[5]	1.00-1.50	-	1.50-1.90	-	-	-	E (SF)
Feb 9 1971[7]	0.82-1.43 [1.0-13.0]	-	-	-	-	-	E (SF)
Feb 9 1971[8]	1.02-1.11 [3.5-5.5]	-	-	-	-	-	E (SF)
Feb 9 1971[9]	1.03 [0.07]	4.98 [0.06]	1.61 [0.06]	7.81 [0.06]	-	-	E (SF)
Feb 9 1971[10]	1.02 [0.06]	4.93 [0.05]	1.61 [0.06]	7.82 [0.05]	-	-	E (SF)
Feb 9 1971[6]	1.00	-	1.64	-	-	-	E (SF)
Feb 1971[11]	1.27 [2.5]	5.35 [0.9]	1.8 [3]	9.02 [0.2]	2.65 [2]	9.65 [0.5]	A
Feb 1971[4]	1.30	-	-	-	-	-	A
Dec 1972[4]	1.37	-	1.77	-	-	-	M
Apr 1973[12]	1.28 [1.3]	-	-	-	-	-	A
1974[13]	1.21	-	1.76	-	-	-	F
Jul 1975[14]	1.21 [1.8]	-	1.79 [1.8]	-	-	-	F
May 1976[9]	1.27	-	1.85	-	2.65	-	A
∼ M6.1 October 1 1987 Whittier Narrows Earthquake (WN) @ 19km ∼							
Oct 1 1987[10]	0.932 [0.04]	4.17 [0.08]	1.30 [0.06]	6.64 [0.18]	-	-	E (WN)
Oct 1 1987[6]	1.00	-	1.33	-	-	-	E (WN)
Oct 4 1987[10]	0.98	-	1.43	-	-	-	E (WN M5.3)
Oct 16 1987[10]	1.20	-	1.69	-	-	-	E (WN M2.8)
May 1988[11]	1.18	-	1.70	-	-	-	F
∼ M5.8 June 28 1991 Sierra Madre Earthquake (SM) @ 18km ∼							
June 28 1991[6]	0.92	-	1.39	-	-	-	E (SM)
May 1993[15]	1.17	-	1.69	-	2.44	-	F
∼ M6.7 January 17 1994 Northridge Earthquake (N) @ 34km ∼							
Jan 17 1994[6]	0.94	-	1.33	-	-	-	E (N)
Aug 2002[18]	1.14 [2.28]	4.93	1.67 [2.39]	7.22	2.38 [1.43]	6.57	F

Table B.5: Summary of Millikan Library Modal Frequency and Damping Analysis Experiments 1967-1994. f_o and f_1 are the fundamental frequency and the first overtone in Hz. ζ_o and ζ_1 are the corresponding damping ratios in %. References are found in Table B.7. A: Ambient, M: Man Excited, F: Forced Vibration, E: Earthquake Motions [LC: Lytle Creek Earthquake].

Test	East - West		North - South		Torsional		Remark
	f_0 [ζ_0]	f_1 [ζ_1]	f_0 [ζ_0]	f_1 [ζ_1]	f_0 [ζ_0]	f_1 [ζ_1]	
1966-1967[1]	1.46-1.51	6.2	1.89-1.98	-	2.84-2.90	-	A,F,M
	[0.7-1.7]		[1.2-1.8]		[0.9-1.6]		
Mar 1967[2]	1.49 [1.5]	6.1	1.91 [1.6]	-	2.88	-	A
∼ M6.7 February 9 1971 San Fernando Earthquake (SF) @ 44km ∼							
Feb 9 1971[6]	1.00	-	1.64	-	-	-	E (SF)
May 1976[9]	1.27	-	1.85	-	2.65	-	A
∼ M6.1 October 1 1987 Whittier Narrows Earthquake (WN) @ 19km ∼							
Oct 1 1987[10]	0.932 [0.04]	4.17 [0.08]	1.30 [0.06]	6.64 [0.18]	-	-	E (WN)
Oct 1 1987[6]	1.00	-	1.33	-	-	-	E (WN)
Oct 4 1987[10]	0.98	-	1.43	-	-	-	E(WN M5.3)
Oct 16 1987[10]	1.20	-	1.69	-	-	-	E(WN M2.8)
May 1988[11]	1.18	-	1.70	-	-	-	F
∼ M5.8 June 28 1991 Sierra Madre Earthquake (SM) @ 18km ∼							
June 28 1991[6]	0.92	-	1.39	-	-	-	E (SM)
May 1993[15]	1.17	-	1.69	-	2.44	-	F
∼ M6.7 January 17 1994 Northridge Earthquake (N) @ 34km ∼							
Jan 17 1994[6]	0.94	-	1.33	-	-	-	E (N)
Jan 19 1994[15]	1.13	-	1.65	-	2.39	-	F
Jan 20 1994[15]	1.13	4.40-4.90	1.65	8.22-8.24	2.39	-	A
	[1.2-2.1]	[1.0]	[0.7-1.5]	[0.2-0.3]	[0.3-0.5]		F
May 1994[16]	1.15 [1.38]	-	1.67 [1.46]	-	2.4 [1.18]	-	F
May 1995[16]	1.15 [1.44]	-	1.68 [1.25]	-	2.42 [1.15]	-	F
May 1998[16]	1.17 [1.4]	-	1.70 [1.3]	-	2.46	-	F
May 1998[16]	-	-	1.68	1.5	-	-	M
May 2000[16]	1.15 [3]	-	1.66 [3]	-	2.41 [2.5]	-	F
May 2000[16]	-	-	1.72 [0.8]	-	-	-	A
May 2001[16]	1.11 [3.25]	-	1.63 [3.69]	-	2.31 [2.9]	-	F
May 2001[16]	-	-	1.71 [1.2]	-	-	-	M
Dec 2001[17]	1.12 [1.63]	-	1.63 [1.65]	-	2.34	-	F
Sep 9 2001[6]	1.16	-	1.68	-	-	-	E (BH M4.2)
Aug 2002[18]	1.14 [2.28]	4.93	1.67 [2.39]	7.22	2.38 [1.43]	6.57	F
Feb 22 2003[6]	1.07	-	1.61	-	-	-	E (BB M5.4)

Table B.6: Summary of Millikan Library Modal Frequency and Damping Analysis Experiments 1987-2003. f_o and f_1 are the fundamental frequency and the first overtone in Hz. ζ_o and ζ_1 are the corresponding damping ratios in %. References are found in Table B.7. A: Ambient, M: Man Excited, F: Forced Vibration, E: Earthquake Motions [BH: Beverly Hills Earthquake, BB: Big Bear Earthquake].

Footnote	Reference	Remarks
1	Kuroiwa (1967)	forced, ambient, man excitations — during and immediately after construction, Library not full
2	Blandford et al. (1968)	ambient
3	Jennings and Kuroiwa (1968)	ambient
4	Udwadia and Trifunac (1973)	ambient
5	Udwadia and Trifunac (1974)	Lytle Creek, San Fernando — based on transfer functions
6	Clinton (2004)	Earthquakes — estimated from strong motion records
7	Iemura and Jennings (1973)	San Fernando
8	Udwadia and Marmarelis (1976)	San Fernando — based on linear model
9	McVerry (1980)	SanFernando; ambient
10	Beck and Chan (1995)	SanFernando, Whittier MODEID
11	Teledyne-Geotech-West (1972)	ambient - 1mth after San Fernando — Also Vertical $f_0 = 3 - 4Hz$, high ζ.
12	Udwadia and Marmarelis (1976)	San Fernando
13	Foutch et al. (1975)	forced
14	Luco et al. (1987)	forced
15	Beck et al. (1994)	forced, ambient — Also Jan 20 Ambient test: EW3 at 7.83Hz
16	CE180 Caltech - various students	forced
17	Favela, personal communication	forced
18	EERL report, Bradford et al. (2004)	forced — Also EW3 at 7.83Hz

Table B.7: References which correspond to footnote numbers in Tables B.5 and B.6.

Appendix C

Time-Frequency Tools and Downloads

There are many online resources for time-frequency analysis. This appendix contains some useful collections of tools and examples as well as MATLAB® functions. (Links and code provided "as-is.")

C.1 Links

WAVELAB

`http://www-stat.stanford.edu/~wavelab/`

A collection of Matlab functions that contains a Wigner-Ville implementation, along with a very complete wavelet analysis toolbox. [Good online documentation for installing the .m files and setting up your path properly, but please note that some of the .mex files will not compile using modern versions of Matlab, and some routines will generate error messages when using obsolete commands/syntax.]

MATLAB LINK EXCHANGE: Signal Processing

`http://www.mathworks.com/matlabcentral/link_exchange/`

User-contributed toolboxes and .m files. Of particular interest is René Laterveer's wvd.m package. I have modified this package and include my version below.

TIME FREQUENCY TOOLBOX

`http://tftb.nongnu.org/`

This toolbox contains the most applicable functions for general time-frequency analysis. The Reduced Interference Distributions in this thesis were created from a largely unchanged "tfrridh.m" function, which stands for "Time Frequency Response, Reduced Interference Distribution, Hanning Smoothing Kernel." Other smoothing and TFR options are available and there is very thorough online documentation.

C.2 Downloads

Wigner-Ville Distribution

wvdc.m – This is my adaptation of R. Laterveer's wvd.m file. I have modified it for ease of input/output. Place the .m file in your path and use "help wvdc" for instructions. (May generate dimension errors in Matlab 6.) The WVD can be efficiently implemented using the FFT algorithm built into Matlab.

```
function [wv, ff, tt] = wvdc(x, res, win, sps);
% wvdc creates a Wigner-Ville spectrogram
%
% (wv,ff,tt)=wvdc(x,res,win,sps)
%
% x=    real input time series
% res=    resolution, number of samples between windows
%   (for full resolution:  1)
% win=    window, becomes length of frequency axis
%   (for full resolution:  length(x))
% sps=    samples per second of signal
%
% wv=   the W-V spectrum, each row represents a
%   frequency, each column a time instant
% ff=   frequency vector (optional)
% tt=   time vector (optional)
%
%   Display using:
%
%   imagesc(tt,ff,log10(abs(wv)));axis xy
%   or:
%   surf(tt,ff,log10(abs(wv)));shading interp
%
% ...of course modifying the abs or log10 as desired.
%
%           -Case Bradford, February 2005


%
%   Adapted from Rene Laterveer, 1999, wvd.m package available from:
%   http://www.mathworks.com/matlabcentral/link_exchange/
%     MATLAB/Signal_processing/
%
```

```
z=hilbert(x);
% make even number of points, at given resolution
npts = floor(floor(length(z)/res)/2)*2;
% make window an integer
win=floor(win);
% round window length down to nearest odd integer
oddwin = (floor((win-1)/2)*2)+1;
% half point (for indexing reasons we need it later, we're
% filling two columns per loop, so we only index through half)
halfwin  = (oddwin+1)/2-1;
% create tt and ff
tt=[0:npts-1]*res/sps;
ff=[0:(win-1)]*(sps/2)/(win-1);
% pad with zeros
z = [zeros(1,oddwin-1), z, zeros(1,oddwin-1)];
% initialize (important when creating large arrays)
wv = zeros(win,npts);
R = zeros(1, win);
idx = 1:halfwin;
for n=0:npts/2-1
  t = 2*n*res+oddwin;
  R(1) = z(t)*conj(z(t)) + i*z(t+res)*conj(z(t+res));
  v1 = z(t+idx).*conj(z(t-idx));
  v2 = z(t+res+idx).*conj(z(t+res-idx));
  R(idx+1) = v1+i*v2;
  R(win-idx+1) = conj(v1)+i*conj(v2);
  RF = fft(R, win);
  wv(:,2*n+1) = real(RF);
  wv(:,2*n+2) = imag(RF);
end
return;
```

Double Chirp

doublechirp.m – Creates a simple double chirp function as in Section 2.13.2.

```
function [yy,t] = doublechirp;
% [yy,tt] = doublechirp;
%
% Creates a double chirp function.
%
% http://ecf.caltech.edu/case/tfr/
%
% Modify the values in this file to create chirps of different
% slopes/amplitudes.
%
% -Case
A1=1; A2=1; T=.3;
ft1=200; f01=100;
ft2=400; f02=300;
df1dt=(ft1-f01)/T;
df2dt=(ft2-f02)/T;
t=[0:.001:.3];
yy=A1*cos(2*pi*(f01 + .5*df1dt*t).*t) ...
```

```
   + A2*cos(2*pi*(f02 + .5*df2dt*t).*t);
return;
```

Double Chirp WVD Example

dcexample.m – Sample script that will test that the wvdc and doublechirp commands are working correctly. This shows proper syntax for these commands.

```
[yy,tt]=doublechirp;
[wv,wvfrequency,wvtime]=wvdc(yy,1,length(yy)/2,1000);
figure;
subplot(2,1,1);
imagesc(wvtime,wvfrequency,wv);axis xy;colormap bone
subplot(2,1,2);
surf(wvtime,wvfrequency,wv);axis tight;shading interp;colormap bone
```

Read SAC2000 files into MATLAB: sac2mat

sac2mat.m – You can use this sac2mat.m file to read .sac files into Matlab. The syntax is: [data,header,station.name]=sac2mat('1409094992.CI.MIK.HLE.sac'); use "help sac2mat" for more information. The other sac2mat versions deal with little/big endian byte-ordering for windows machines and allow you to select your start and stop points.

```
function [data,header,kstnm] = sac2mat(sacfile);
% sac2mat  loads a SAC2000 file into Matlab, along with
% header information.
%  [data,header,kstnm] = sac2mat(sacfile);
%
%  sacfile must be a STRING, eg.
%     [fff,hhh,name]=sac2mat('dir1/file1.sac')
%
% Output:
% data= the data from the file
% header=the first 105 header variables, from the SAC Home Page
% http://www.llnl.gov/sac/
% http://www.llnl.gov/sac/SAC_Manuals/FileFormatPt1.html
% kstnm= KSTNM, the station name (string)
% (header and kstnm are optional)
%
% Some common/useful headers:
% header(1:3) DELTA,DEPMIN,DEPMAX
% header(57) DEPMEN
% header(6:7) B,E
% header(8) Event origin time (seconds relative to reference time)
% header(32:39) STLA,STLO,STEL,STDP,EVLA,EVLO,EVEL,EVDP
% header(51:54) DIST,AZ,BAZ,GCARC
% header(71:76)  NZYEAR,NZDAY,NZHOUR,NZMIN,NZSEC,NZMSEC
% header(80) NPTS
%      Case Bradford, 8 June 2004
sacfid = fopen(sacfile,'r');
if sacfid==-1;error='Not a valid path.'
```

```
return;end
% The first 70 header variables are floating point
header1 = fread(sacfid,70,'float32');
% The next 35 are integers (after that they're a mix of strings)
header2 = fread(sacfid,35,'int32');
% Outputs the number of points being read to the screen
header=[header1;header2];
npts = header(80)
% kstnm, station name, is a string
% stored in the 110th header variable
% kstnm = KSTNM (First 3 letters of the station name)
fseek(sacfid,4*110,-1);
kstnm = char(fread(sacfid,3)');
% Now read the data...
fseek(sacfid,158*4,-1);
data(1:npts) = fread(sacfid,npts,'float32');
status = fclose(sacfid);
return
```

sac2mata.m – Adjusts the start/stop points of a file. This version is useful when reading long files.

"help sac2mata" for more information on syntax.

```
function [data,header,kstnm] = sac2mata(sacfile,start,duration);
% sac2mata  loads a SAC2000 file into Matlab,
% along with header information.
%  [data,header,kstnm] = sac2mata(sacfile, start, duration);
%
%  sacfile must be a STRING, eg.
%     [fff,hhh,name]=sac2mata('dir1/file1.sac')
%
% sac2mata also takes two optional arguments:
%  start (INTEGER)
%   sets the starting offset for data, this defaults to 0
% duration - sets the duration for the data, this defaults to 'eof'
%  if duration='eof', then sac2mata reads to end of file
%  if duration is an INTEGER (start+duration < length of sac file)
%       then sac2mata reads from start to start+duration
%  eg. [fff,hhh,name]=sac2mata('dir1/file1.sac',31415,1000);
% ...this will read in 1000 points, starting at point 31415,
%   as long as the file to be read is less than
%   31415+1000=32425 points long.
%
% Output:
% data= the data from the file
% header=the first 105 header variables, from the SAC Home Page
% http://www.llnl.gov/sac/
% http://www.llnl.gov/sac/SAC_Manuals/FileFormatPt1.html
% kstnm= KSTNM, the station name (string)
% (header and kstnm are optional)
%
% Some common/useful headers:
% header(1:3) DELTA,DEPMIN,DEPMAX
% header(57) DEPMEN
% header(6:7) B,E
```

```
% header(8) Event origin time (seconds relative to reference time)
% header(32:39) STLA,STLO,STEL,STDP,EVLA,EVLO,EVEL,EVDP
% header(51:54) DIST,AZ,BAZ,GCARC
% header(71:76)  NZYEAR,NZDAY,NZHOUR,NZMIN,NZSEC,NZMSEC
% header(80) NPTS
%      Case Bradford, 8 June 2004
sacfid = fopen(sacfile,'r');
if sacfid==-1;error='Not a valid path.'
return;end
% The first 70 header variables are floating point
header1 = fread(sacfid,70,'float32');
% The next 35 are integers (after that they're a mix of strings)
header2 = fread(sacfid,35,'int32');
% Outputs the number of points being read to the screen
header=[header1;header2];
npts = header(80);
total_npts=npts
% Now check the duration/start values for logic:
if nargin==1;start=0;duration='eof';end;
if nargin==2;
if start > npts;error='Start point is after end of file.'
return;end
if start < 0;error='Start time cannot be negative.'
return;end
if isnan(start);error='Start time cannot be NaN.'
return;end
duration='eof';end;
if nargin==3;
if start > npts;error='Start point is after end of file.'
return;end
if start < 0;error='Start time cannot be negative.'
return;end
if isempty(start);
  start=0;
end
 if ischar(duration);
  if not(strcmp(duration,'eof'));
    error = 'Duration is an undefined string.'
                return;
                end
 elseif duration > (npts-start);
   error='Duration is past end-of-file.'
 return;
 elseif duration <= 0;
   error='Duration cannot be negative, or zero.'
 return;
 elseif isempty(duration);
   duration='eof';
 end
end
if duration=='eof';npts = npts-start;else;npts=duration;end;
npts=round(npts);
start=round(start);
number_read=npts
starting_at=start
% kstnm, station name, is a string
% stored in the 110th header variable
% kstnm = KSTNM (First 3 letters of the station name)
fseek(sacfid,110*4,-1);
```

```
kstnm = char(fread(sacfid,3)');
% Now read the data...
fseek(sacfid,158*4+start*4,-1);
data(1:npts) = fread(sacfid,npts,'float32');
status = fclose(sacfid);
return
```

sac2matl.m – Forces "little-endian" byte ordering when reading file.

```
function [data,header,kstnm] = sac2matl(sacfile);
% sac2mat  loads a SAC2000 file into Matlab, along with
% header information.
%  [data,header,kstnm] = sac2matl(sacfile);
%
%  sacfile must be a STRING, eg.
%     [fff,hhh,name]=sac2mat('dir1/file1.sac')
%
% Output:
% data= the data from the file
% header=the first 105 header variables, from the SAC Home Page
% http://www.llnl.gov/sac/
% http://www.llnl.gov/sac/SAC_Manuals/FileFormatPt1.html
% kstnm= KSTNM, the station name (string)
% (header and kstnm are optional)
%
% Some common/useful headers:
% header(1:3) DELTA,DEPMIN,DEPMAX
% header(57) DEPMEN
% header(6:7) B,E
% header(8) Event origin time (seconds relative to reference time)
% header(32:39) STLA,STLO,STEL,STDP,EVLA,EVLO,EVEL,EVDP
% header(51:54) DIST,AZ,BAZ,GCARC
% header(71:76)  NZYEAR,NZDAY,NZHOUR,NZMIN,NZSEC,NZMSEC
% header(80) NPTS
%      Case Bradford, 8 June 2004
sacfid = fopen(sacfile,'r','l');
if sacfid==-1;error='Not a valid path.'
return;end
% The first 70 header variables are floating point
header1 = fread(sacfid,70,'float32');
% The next 35 are integers (after that they're a mix of strings)
header2 = fread(sacfid,35,'int32');
% Outputs the number of points being read to the screen
header=[header1;header2];
npts = header(80)
% kstnm, station name, is a string
% stored in the 110th header variable
% kstnm = KSTNM (First 3 letters of the station name)
fseek(sacfid,4*110,-1);
kstnm = char(fread(sacfid,3)');
% Now read the data...
fseek(sacfid,158*4,-1);
data(1:npts) = fread(sacfid,npts,'float32');
status = fclose(sacfid);
return
```

sac2matb.m – Forces "big-endian" byte ordering.

```
function [data,header,kstnm] = sac2matb(sacfile);
% sac2mat  loads a SAC2000 file into Matlab, along with
% header information.
%  [data,header,kstnm] = sac2matb(sacfile);
%
%  sacfile must be a STRING, eg.
%     [fff,hhh,name]=sac2mat('dir1/file1.sac')
%
% Output:
% data= the data from the file
% header=the first 105 header variables, from the SAC Home Page
% http://www.llnl.gov/sac/
% http://www.llnl.gov/sac/SAC_Manuals/FileFormatPt1.html
% kstnm= KSTNM, the station name (string)
% (header and kstnm are optional)
%
% Some common/useful headers:
% header(1:3) DELTA,DEPMIN,DEPMAX
% header(57) DEPMEN
% header(6:7) B,E
% header(8) Event origin time (seconds relative to reference time)
% header(32:39) STLA,STLO,STEL,STDP,EVLA,EVLO,EVEL,EVDP
% header(51:54) DIST,AZ,BAZ,GCARC
% header(71:76)  NZYEAR,NZDAY,NZHOUR,NZMIN,NZSEC,NZMSEC
% header(80) NPTS
%      Case Bradford, 8 June 2004
sacfid = fopen(sacfile,'r','b');
if sacfid==-1;error='Not a valid path.'
return;end
% The first 70 header variables are floating point
header1 = fread(sacfid,70,'float32');
% The next 35 are integers (after that they're a mix of strings)
header2 = fread(sacfid,35,'int32');
% Outputs the number of points being read to the screen
header=[header1;header2];
npts = header(80)
% kstnm, station name, is a string
% stored in the 110th header variable
% kstnm = KSTNM (First 3 letters of the station name)
fseek(sacfid,4*110,-1);
kstnm = char(fread(sacfid,3)');
% Now read the data...
fseek(sacfid,158*4,-1);
data(1:npts) = fread(sacfid,npts,'float32');
status = fclose(sacfid);
return
```

Bibliography

Beck, J. L. (1996). System identification methods applied to measured seismic response. In *Eleventh World Conference on Earthquake Engineering, Acapulco, Mexico, Disc 4, Paper No. 2004*, Acapulco, Mexico.

Beck, J. L. and E. Chan (1995). Comparison of the response of Millikan Library to San Fernando and Whittier Narrows earthquakes.

Beck, J. L., B. S. May, and D. C. Polidori (3-5 August 1994). Determination of modal parameters from ambient vibration data for structural health monitoring. In *First World Conference on Structural Control*, Los Angeles, California, USA.

Blandford, R., V. R. McLamore, and J. Aunon (1968). Analysis of Millikan Library from ambient vibrations. Technical report, Earth Teledyne Co.

Boashash, B. (1988, September). Note on the Use of the Wigner Distribution for Time-Frequency Signal Analysis. *IEEE Transactions on Acoustics, Speech, and Signal Processing 36*(9), 1518–1521.

Boashash, B. (2003). *Time Frequency Signal Analysis and Processing*. ELSEVIER Ltd.

Bracewell, R. N. (2000). *The Fourier Transform and its Applications*. McGraw Hill Higher Education.

Bradford, S. C., J. F. Clinton, J. Favela, and T. H. Heaton (2004). Results of Millikan Library Forced Vibration Testing. Technical report, California Institute of Technology. http://resolver.caltech.edu/CaltechEERL:EERL-2004-03 .

Bradford, S. C., J. Yang, and T. H. Heaton (2006). Variations in the Dynamic Properties of Structures: The Wigner-Ville Distribution. In *100th Anniversary Earthquake Conference, April 18-22, 2006, commemorating the 1906 San Francisco Earthquake*, San Francisco, California.

Chopra, A. K. (1995). *Dynamics of Structures - Theory and Applications to Earthquake Engineering*, Chapter 11. Prentice Hall.

Clinton, J. F. (2004). *Modern Digital Seismology - Instrumentation and Small Amplitude Studies in the Engineering World*. Ph.D. thesis, California Institute of Technology. http://resolver.caltech.edu/CaltechETD:etd-05202004-225044 .

Clinton, J. F., S. C. Bradford, T. H. Heaton, and J. Favela (2006, February). The observed wander of the natural frequencies in a structure. *Bulletin of the Seismological Society of America 96*(1), 237–257.

Doebling, S., C. Farrar, M. Prime, and D. Shevitz (1996). Damage Identification and Health Monitoring of Structural and Mechanical Systems from Changes in their Vibration Characteristics: A Literature Review. *Los Alamos National Laboratory Report LA-13070-MS*.

Favela, J. (2004). *Energy Radiation From a Multi-Story Building*. Ph.D. thesis, California Institute of Technology. http://resolver.caltech.edu/CaltechETD:etd-06032004-143147 .

Feynman, R. P., R. B. Leighton, and M. Sands (1966). *The Feynman Lectures on Physics*, Volume III. Addison Wesley.

Flandrin, P. (1999). *Time Frequency / Time Scale Analysis*. Academic Press. Translated from the French, *Temps-fréquence*, Hermés, Paris, 1993.

Flandrin, P. and W. Martin (1997). *The Wigner Ville Spectrum of Nonstationary Random Signals*. "The Wigner Distribution: Theory and Applications in Signal Processing," edited by Mecklenbräuker, W. and Hlwatsch, F., ELSEVIER Ltd.

Foutch, D. A. (1976). *A Study of the Vibrational Characteristics of Two Multistorey Buildings*. Ph.D. thesis, California Institute of Technology, Earthquake Engineering Research Laboratory, Pasadena, California.

Foutch, D. A., J. E. Luco, M. D. Trifunac, and F. E. Udwadia (1975). Full scale, three dimensional tests of structural deformationduring forced excitation of a nine-storey reinforced concrete building. In *Proceedings, U.S. National Conference on Earthquake Engineering*, Ann Arbor, Michigan, pp. 206–215.

Hall, J. F. (1997). Seismic response of steel frame buildings to near source ground motions. Technical report, California Institute of Technology. http://resolver.caltech.edu/CaltechEERL:1997.EERL-97-05 .

http://tftb.nongnu.org/ (2006). Time-Frequency Toolbox, developed by François Auger, Olivier Lemoine, Paulo Gonçalvès and Patrick Flandrin.

Iemura, H. and P. C. Jennings (1973). Hysteretic response of a nine-storey reinforced concrete building during the san fernando earthquake. Technical report, Earthquake Engineering Research Laboratory, California Institute of Technology.

Iwan, W. D. (1966). A distributed-element model for hysteresis and its steady-state dynamic response. *American Society of Mechanical Engineers, Journal of Applied Mechanics* (33), 893–900.

Iwan, W. D. (1967). On a class of models for the yielding behavior of continuous and composite systems. *American Society of Mechanical Engineers, Journal of Applied Mechanics* (89), 612–617.

Jennings, P. C. (1971). Engineering Features of the San Fernando Earthquake of February 9, 1971. Technical report, Earthquake Engineering Research Laboratory, California Institute of Technology.

Jennings, P. C. and J. H. Kuroiwa (1968). Vibration and soil-structure interaction tests of a nine-storey reinforced concrete building. *Bulletin of the Seismological Society of America 58*(3), 891–916.

Kohler, M. D., T. H. Heaton, and S. C. Bradford (2006). Wave Propagation in Buildings. *Bulletin of the Seismological Society of America. in preparation.*

Kuroiwa, J. H. (1967). *Vibration Test of a Multistorey Building.* Ph.D. thesis, California Institute of Technology, Earthquake Engineering Research Laboratory, Pasadena, California.

Luco, J., M. Trifunac, and H. Wong (1987). On the apparent change in dynamic behavior of a 9- story reinforced-concrete building. *BULLETIN OF THE SEISMOLOGICAL SOCIETY OF AMERICA 77*(6), 1961–1983.

Luco, J. E., W. H. L., and T. M. D. (1986, September). Soil-structure interaction effects on forced vibration tests. Technical Report Report 86-05, University of Southern California, Department of Civil Engineering, Los Angeles, California.

Mallat, S. (1999). *A Wavelet Tour of Signal Processing.* Academic Press.

McVerry, G. H. (1980). *Frequency Domain Identification of Structural Models from Earthquake Records.* Ph.D. thesis, California Institute of Technology.

Meirovitch, L. (1986). *Elements of Vibration Analysis.* McGraw-Hill, Inc.

Papandreou-Suppappola, A. (2003). *Applications in Time-Frequency Signal Processing.* CRC Press.

Qian, S. (2002). *Time Frequency and Wavelet Transforms.* Prentice-Hall, Inc.

Rojahn, C. and P. N. Mork (1982). *An Analysis of Strong Motion Data From a Severly Damaged Structure – The Imperial County Services Building, El Centro, California.* in "The Imperial Valley, California, Earthquake of October 15, 1979," Geological Survery Professional Paper 1254, United States Government Printing Office, Washington.

Teledyne-Geotech-West (1972). Post earthquake vibration measurements: Millikan Library. Technical report, Teledyne Geotech West, Monrovia, California.

Todorovska, M. and Y. Al Rjoub (2006a). 1. Plain strain soil-structure interaction model for a building supported by a circular foundation embedded in a poroelastic half-space. *SOIL DYNAMICS AND EARTHQUAKE ENGINEERING 26*(6-7), 694–707.

Todorovska, M. and Y. Al Rjoub (2006b). 2. Effects of rainfall on soil-structure system frequency: examples based on poroelasticity and a comparison with full-scale measurements. *SOIL DYNAMICS AND EARTHQUAKE ENGINEERING 26*(6-7), 708–717.

Todorovska, M. and M. Trifunac (2006a). Earthquake damage detection in the Imperial County Services Building I: the data and time-frequency analysis. *SOIL DYNAMICS AND EARTHQUAKE ENGINEERING. submitted.*

Todorovska, M. and M. Trifunac (2006b). Earthquake damage detection in the Imperial County Services Building II: Analysis of novelties via wavelets. *SOIL DYNAMICS AND EARTHQUAKE ENGINEERING. submitted.*

Trifunac, M. D. (1972). Comparisons between ambient and forced vibration experiments. *Earthquake Engineering and Structural Dynamics 1*, 133–150.

Udwadia, F. E. and P. Z. Marmarelis (1976). The identification of building structural systems: I. the linear case. *BULLETIN OF THE SEISMOLOGICAL SOCIETY OF AMERICA 66*(1), 125–151.

Udwadia, F. E. and M. D. Trifunac (1973). Ambient vibration tests of a full-scale structures. In *Proceedings, Fifth World Conference on Earthquake Engineering*, Rome.

Udwadia, F. E. and M. D. Trifunac (1974). Time and amplitude dependent response of structures. *Int. J. Earthquake Engineering and Structural Dynamics 2*, 359–378.

Ville, J. (1948). Theorie et applications de la notion de signal analytique. *Cables et Transmissions 2A*(1), 61—74. I. Selin, translator, *"Theory and applications of*

the notion of complex signal," RAND Corporation Technical Report T-92, Santa Monica, CA (1958).

Wigner, E. (1932, June). On the quantum correction for thermodynamic equilibrium. *Physical Review 40*, 749—759.

Yang, J., T. H. Heaton, and J. Hall (2006). Simulated Nonlinear Response of High-rise Buildings for the 2003 Tokachi-oki Earthquake. In *100th Anniversary Earthquake Conference, April 18-22, 2006, commemorating the 1906 San Francisco Earthquake*, San Francisco, California.